

Fabrication and Characterization of Functional ALD Metal Oxide Thin Films for Solar Applications

THÈSE N° 7036 (2016)

PRÉSENTÉE LE 3 JUIN 2016

À LA FACULTÉ DES SCIENCES DE BASE

LABORATOIRE DE PHOTONIQUE ET INTERFACES

PROGRAMME DOCTORAL EN CHIMIE ET GÉNIE CHIMIQUE

ÉCOLE POLYTECHNIQUE FÉDÉRALE DE LAUSANNE

POUR L'OBTENTION DU GRADE DE DOCTEUR ÈS SCIENCES

PAR

Ludmilla STEIER

acceptée sur proposition du jury:

Prof. F. Nüesch, président du jury

Prof. M. Graetzel, Prof. K. Sivula, directeurs de thèse

Prof. J. Durrant, rapporteur

Prof. R. van de Krol, rapporteur

Prof. S. Haussener, rapporteuse



ÉCOLE POLYTECHNIQUE
FÉDÉRALE DE LAUSANNE

Suisse
2016

“Oui, mes amis, je crois que l'eau sera un jour employée comme combustible, que l'hydrogène et l'oxygène, qui la constituent, utilisés isolément ou simultanément, fourniront une source de chaleur et de lumière inépuisables et d'une intensité que la houille ne saurait avoir. Un jour, les soutes des steamers et les tenders des locomotives, au lieu de charbon, seront chargés de ces deux gaz comprimés, qui brûleront dans les foyers avec une énorme puissance calorifique. Ainsi donc, rien à craindre. Tant que cette terre sera habitée, elle fournira aux besoins de ses habitants, et ils ne manqueront jamais ni de lumière ni de chaleur, pas plus qu'ils ne manqueront des productions des règnes végétal, minéral ou animal. Je crois donc que lorsque les gisements de houille seront épuisés, on chauffera et on se chauffera avec de l'eau. L'eau est le charbon de l'avenir.”

Jules Verne, *L'île Mystérieuse*, 1874

ABSTRACT

Motivated to revolutionize our today's fossil fuels based energy production, my work concentrated on the investigation of promising low-cost materials for photoelectrochemical hydrogen production and photovoltaic electricity generation. Hydrogen presents a fully scalable energy storage solution while photovoltaics have the biggest potential for clean electricity generation. Both are combined in the hydrogen-based economy that will be introduced in Chapter 1. A clear way to achieve this revolutionary technological and societal goal is through fundamental understanding of the complex electronic properties of the most promising low-cost semiconductors offering strong visible light absorption. The modern fields of photoelectrochemical (PEC) water splitting and photovoltaics have a lot in common: materials, scientific concepts and theoretical background. In other words, their complementarity was a strong motivation for the interdisciplinary work presented in this thesis.

The main focus in this thesis is on hematite ($\alpha\text{-Fe}_2\text{O}_3$), which is a promising low-cost material offering visible light absorption and the chemical robustness for photoelectrochemical water oxidation. However, it has two major drawbacks: firstly, for a semiconductor, hematite has extremely low electron and hole mobilities. This makes it challenging to collect charges that are photo-generated deep within the hematite layer and far away from the surface. Secondly, water oxidation appears to be limited by trap states located in the mid band gap region.

Chapter 3 addresses these drawbacks showing that doping of hematite from the underlayer, surface passivation from annealing treatments and/or overlayers are all key parameters to consider for the design of more efficient iron oxide electrodes. By better understanding the underlying principles of over- and underlayers, I was able to design multilayered hematite photoanodes comprised of functional thin films to obtain a significant reduction in the water oxidation overpotential.

Whereas hematite thin film electrodes were fabricated by ultrasonic spray pyrolysis in Chapter 3, I introduce a new atomic layer deposition (ALD) route towards crystalline, highly photoactive, phase pure and impurity-free hematite films in Chapter 4. With this thin film model system I could precisely demonstrate that only the 10 nm thick space charge region of hematite is photoactive, which presents a major challenge when

considering that around 60-70 nm are needed to achieve sufficient light absorption as shown in Chapter 5. In light of this charge transport limitation, I propose and demonstrate new host-guest electrode designs that would be indispensable for the realization of high performance ALD hematite photoanodes. To complement these studies, I demonstrate in Chapter 5 the basis for an optoelectronic modeling of the hematite PEC device that helps identifying and eliminating major optical and electronic losses in the PEC cell.

In Chapter 6 my work on ALD SnO₂ as an electron selective layer (ESL) led to major advances in low-cost flat hybrid organic-inorganic perovskite solar cells. The tin oxide layer is found to resolve the problem of an energy band misalignment encountered with the previously used ALD TiO₂ ESL in addition to stabilizing the photovoltaic performance. Hysteresis-free solar conversion efficiencies of up to 18% have been achieved for flat devices paving the way towards low-cost flat film perovskite solar cells that will easily surpass the photovoltaic performance of polycrystalline silicon solar cells in the near future.

Keywords: Photoelectrochemical water oxidation, hematite, ultrasonic spray pyrolysis, atomic layer deposition (ALD), host-guest approach, electrochemical impedance spectroscopy, trap states, doping, interfacial functional layers, optical constants, SnO₂, electron selective contacts, hybrid organic-inorganic perovskite solar cells

ZUSAMMENFASSUNG

Heutzutage basiert unsere Energieversorgung sehr stark auf der Verbrennung von fossilen Energieträgern. Meine Doktorarbeit fokussiert sich auf die Untersuchung und Verbesserung zukunftsversprechender und kostengünstiger Materialien für eine CO₂-neutrale Energieversorgung auf Basis von Solarenergie. Solarenergie muss zunächst umgewandelt und anschließend gespeichert werden. Für die Energieumwandlung stellen Solarzellen eine der vielversprechendsten Kandidaten dar und ein Teil meines Doktorats konzentrierte sich auf die Entwicklung neuartiger und effizienter Solarzellen – der Perowskitsolarzellen. Der Großteil meines Doktorats beschäftigte sich jedoch mit der Wasserstoffgewinnung durch Photolyse, die Sonnenenergie in Wasserstoff umwandelt der dann gespeichert werden kann. Beide Forschungsfelder liegen eng beieinander und ergänzen sich daher – insbesondere Materialien, Konzepte und Arbeitstechniken betreffend. Das Konzept einer Wasserstoffwirtschaft sowie die Grundlagen der Photolyse werden in der Einleitung näher erörtert.

Die Photolyse hat 2 Teilreaktionen und ich habe einen Schwerpunkt auf die Wasseroxidation gesetzt. Dabei wählte ich das kostengünstige Hämatit (α -Fe₂O₃), das im sichtbaren Bereich des Lichtes absorbiert und die nötige chemische Stabilität aufweist, Wasser photoelektrochemisch zu oxidieren. Allerdings hat Hämatit zwei entscheidende Nachteile: erstens, für einen Halbleiter, ist die Ladungsträgermobilität sehr niedrig. Dies erschwert eine effiziente Extraktion photogenerierter Ladungsträger, insbesondere wenn sie fern von der Hämatitoberfläche erzeugt werden. Zweitens, die Überspannung für die Wasseroxidation hängt stark von Fallenzuständen ab, die sich in der Mitte der Bandlücke des Hämatits befinden und somit sehr aktive Rekombinationszentren bilden.

Kapitel 3 befasst sich mit dieser Problematik. Darin zeige ich, dass Hämatit durch eine darunterliegende dünne höhervalente Oxidschicht dotiert werden kann und dass Sintervorgänge sowie gezielte Oberflächenbeschichtungen diese Rekombinationszentren passivieren können. Mit Hilfe einer detaillierten Untersuchung dieser funktionellen Dünnschichten, konnte ich eine mehrschichtige Hämatit-Photoanode entwerfen, die eine deutlich niedrigere Überspannung für Wasseroxidation aufweist, wodurch der Gesamtprozess deutlich verbessert werden konnte.

Während in Kapitel 3 die Hämatit Dünnschichtelektroden durch Ultraschall-Sprühpyrolyse hergestellt wurden, schlage ich in Kapitel 4 eine neue Methode zur Atomlagenabscheidung (ALD) von kristallinen, photoaktiven und kontaminationsfreien Hämatitfilmen vor. In einer Untersuchung an dünnen Hämatitfilmen von präzise variierte Schichtdicke konnte ich zeigen, dass nur eine 10 nm dicke Raumladungsschicht photoaktiv ist. Dies stellt eine große Herausforderung dar, wenn man bedenkt, dass ein 60-70 nm dicker Hämatitfilm nötig ist um fast alle Photonen mit einer Energie grösser der Bandlücke zu absorbieren. Um dieses Dilemma zu umgehen, stelle ich Ansätze vor, 10 nm dünne Hämatitfilme auf geeigneten elektronenleitenden Nanostrukturen abzulagern. Dies garantiert eine verbesserte Lichtabsorption durch die Nanostruktur und gleichzeitig eine gute Ladungsträgerextraktion in der dünnen Hämatitschicht.

In Kapitel 5 werden die Grundlagen für eine optoelektronische Modellierung einer Photolysezelle gelegt und optische Verluste identifiziert.

Kapitel 6 zeigt meine Arbeit an ALD SnO₂ Elektronenakzeptorschichten, die zu großen Fortschritten im Wirkungsgrad der planaren organisch-anorganischen Perowskit-Solarzellen führte. Die Zinnoxidschicht half dabei das Problem einer Energiebarriere zwischen den Leitungsbändern der Absorbers und der konventionellen Elektronenakzeptorschicht zu beheben. Hysteresefreie Solarumwandlungswirkungsgrade von bis zu 18% wurden für planare Solarzellenkonfigurationen erreicht und ebnet den Weg in Richtung kostengünstiger flacher organisch-anorganischer Perowskit-Solarzellen, die schon bald die Photovoltaik-Leistung von polykristallinen Silizium-Solarzellen übertreffen werden.

Stichwörter: Photolyse, Hämatit, Ultraschall-Sprühpyrolyse, Atomlagenabscheidung (ALD), Elektrochemische Impedanzspektroskopie, Rekombinationszentren, Dotierung, Grenzflächenfunktionsschichten, optische Konstanten, SnO₂, ladungselektive Kontakte, hybride organisch-anorganische Perowskit-Solarzellen

LIST OF ABBREVIATIONS AND SYMBOLS

α	Absorption coefficient
A	Absorptance (in %)
ALD	Atomic layer deposition
AM	Air mass
APCE	Absorbed photon to current conversion efficiency
APCVD	Atmospheric pressure chemical vapor deposition
A_S	Electrode surface area
atm	atmosphere (= 1.013 bar)
C	Capacitance (in F)
CBD	Chemical bath deposition
CIGS	Copper-Indium-Gallium-Diselenide (solar cells)
CSP	Concentrated solar power
CVD	Chemical vapor deposition
δ	Phase angle
DMAMFc	<i>N,N</i> -Dimethylaminomethylferrocene
DOS	Density of states
DSC	Dye-sensitized solar cell
η_a	Overpotential at the anode
η_c	Overpotential at the cathode
η_F	Faradaic efficiency
η_{Sol}	Overpotential in solution
η_{STH}	Solar to hydrogen conversion efficiency
η_{PV}	Efficiency of the photovoltaic module
$\eta_{Electrolyzer}$	Efficiency of the Electrolyzer
E	Energy
\vec{E}	Electric field
e_0	Elementary charge (= $1.602 \cdot 10^{-19}$ C)
E_A	Energy level of acceptor impurities A (in eV)
E_{CB}	Energy of the edge of the conduction band (in eV)
E_D	Energy level of donor impurities D (in eV)
E_{EA}	Electron affinity (in eV)
E_F	Fermi level energy (in eV)
E_{Fn}	Quasi Fermi level energy of electrons under illumination (in eV)
E_{Fp}	Quasi Fermi level energy of holes under illumination (in eV)
E_g	Band gap energy (in eV)

E_{Redox}	Redox potential or electrolyte energy (in V)
E_V	Energy of the edge of the valence band (in eV)
ϵ_0	Permittivity of vacuum ($= 8.85419 \cdot 10^{-12} \text{ F m}^{-1}$)
ϵ_r	Relative dielectric constant
EDX	Energy-dispersive X-ray spectroscopy
EIS	Electrochemical impedance spectroscopy
EMA	Effective medium approximation
EQE	External quantum efficiency (= IPCE)
ESL	Electron selective layer
Φ	Photon flux (= number of photons per m^2 per s)
Φ_M	Work function of metal
Φ_{SC}	Work function of semiconductor
F	Faraday constant ($= 96\,485.333 \text{ As mol}^{-1}$)
$f(E)$	Occupancy of states
$\text{Fe}(\text{acac})_3$	Tris(acetylacetonato)iron(III)
FF	Fill factor (of an J-V curve)
FTO	Fluorine-doped tin oxide (F:SnO_2)
fs	Femtosecond
ΔG	Gibbs free energy
$g_C(E)$	Density of conduction band states
GCL	Gouy-Chapman layer
GDP	Gross domestic product
h	Planck constant ($= 6.62607004 \times 10^{-34} \text{ J s}$)
\hbar	$= h/2\pi$
H_f	Enthalpy of formation
HL	Helmholtz layer
HLW	High level (radioactive) waste
HOMO	Highest occupied molecular orbital
HR	High resolution
IHP	Inner Helmholtz plane
ILW	Intermediate level (radioactive) waste
IPCE	Incident photon to current conversion efficiency
IOP	Inverse opal
IR	Infrared region (700 nm – 1 mm)
ITO	Tin-doped indium oxide ($\text{Sn:In}_2\text{O}_3$)
J	Current density (in mA cm^{-2})
J_{ph}	Photocurrent (in mA cm^{-2})
J_{SC}	Short circuit current density (in mA cm^{-2})
k_B	Boltzmann constant ($= 1.380 \cdot 10^{-23} \text{ J K}^{-1}$)
λ	Wavelength (in nm or μm)
λ_m	Mean free path
LLW	Low level (radioactive) waste

LUMO	Lowest unoccupied molecular orbital
μ	Mobility (in $\text{cm}^2 (\text{Vs})^{-1}$)
m_c^*	Effective mass of electrons in the conduction band
m_v^*	Effective mass of holes in the valence band
MOF	Metal-organic framework
MS	Mott–Schottky
ν	Frequency (in s^{-1})
n	Number of electrons
N_A	Concentration of acceptor impurities = acceptor density (in cm^{-3})
NASA	National Aeronautics and Space Administration
N_C	Effective density of states in the conduction band
n_c	Number of electrons in the conduction band
N_D	Concentration of donor impurities = donor density (in cm^{-3})
n_i	Refractive index of layer i
N_P	Number of people on Earth (population)
OER	Oxygen evolution reaction
OHP	Outer Helmholtz plane
OM	Optical modeling
ψ	Wave function
P	Porosity
P_{incident}	Incident power density of solar irradiation (in mW cm^{-2})
PB	Photobleach
PCE	Power conversion efficiency
PEC	Photoelectrochemical
ps	Picosecond
PSC	Perovskite solar cell
p_v	Holes in the valence band
PV	Photovoltaic
PVD	Physical vapor deposition
q	Charge
ρ	Resistivity (in $\Omega \text{ cm}$)
R	Resistance (in Ω) or Reflectance (in %)
RC	Resistor-capacitor unit
RHE	Reversible hydrogen electrode
RoHS	Restriction of Hazardous Substances
σ	Conductivity (in S cm^{-1})
ΔS	Entropy
sat'd	saturated
SCLJ	Semiconductor/liquid junction
SEM	Scanning electron microscopy
STEM	Scanning transmission electron microscopy
STH	Solar-to-hydrogen conversion efficiency

T	Temperature (in K or °C) or Transmittance (in %)
t	Time
TA	Transient absorption
TCO	Transparent conductive oxide
TBTDEN	Tris(diethylamido)(<i>tert</i> -butylimido)niobium(V)
TBTDET	Tris(diethylamido)(<i>tert</i> -butylimido)tantalum(V)
TDMASn	Tetrakis(dimethylamino)tin(IV)
TDMAT	Tetrakis(dimethylamino)titanium(IV)
TEM	Transmission electron microscopy
TMA	Trimethylaluminium
T_t	Tunneling probability
UPS	Ultraviolet photoelectron spectroscopy
USP	Ultrasonic spray pyrolysis
UV	Ultra violet (10 – 400 nm)
V_{bias} or V	Applied bias potential (in V)
V_{fb}	Flat-band potential (in V)
V_{H}	Helmholtz potential (in V)
V_{O}	Oxygen vacancy
V_{OC}	Open circuit voltage (in V)
V_{Ph}	Photovoltage (in V)
V_{RHE}	Volts vs. RHE
Vis	Visible light region (400 – 700 nm)
ω	Angular frequency (in s^{-1})
W_{SC}	Depletion layer width (in nm)
XPS	X-ray photoelectron spectroscopy
Z	Impedance

TABLE OF CONTENTS

ABSTRACT	I
ZUSAMMENFASSUNG	III
LIST OF ABBREVIATIONS AND SYMBOLS	V
TABLE OF CONTENTS	IX
1 INTRODUCTION	1
1.1 World Energy Consumption	1
1.2 The Solar Potential	3
1.3 A Hydrogen Economy	4
1.4 Water Splitting	6
1.4.1 Semiconductor Fundamentals	9
1.4.2 Semiconductor-Metal Junction	12
1.4.3 Semiconductor-Electrolyte Junctions	14
1.4.4 Choice of the Semiconductor	17
1.5 References	21
2 THEORETICAL BACKGROUND FOR METHODS APPLIED IN THIS WORK	25
2.1 Impedance Spectroscopy	25
2.1.1 Measurement Principle	25
2.1.2 Semiconductor-Electrolyte Interface in the Dark and its Equivalent Circuit	27
2.1.3 Mott-Schottky Analysis	28
2.2 Atomic Layer Deposition	30
2.2.1 Principle	30
2.2.2 Demand on Precursors	33
2.3 References	35

3 UNDERSTANDING THE ROLE OF UNDERLAYERS AND OVERLAYERS IN THIN FILM HEMATITE PHOTOANODES	37
3.1 Introduction	38
3.1.1 Thin Film Hematite and the Use of Functional Layers	38
3.1.2 Electrochemical Impedance Spectroscopy for PEC Water Splitting with Photoanodes	39
3.2 Experimental	41
3.2.1 Substrate Cleaning	41
3.2.2 Deposition of Underlayers	41
3.2.3 USP of Iron Oxide	41
3.2.4 Overlayer Deposition	42
3.2.5 Catalyst Deposition	42
3.2.6 Photocurrent-Voltage Measurements	42
3.2.7 Impedance Measurements	43
3.2.8 X-Ray Photoelectron Spectroscopy	43
3.2.9 Scanning Electron Microscopy	43
3.3 Results	44
3.3.1 Role of the Underlayer in Hematite Thin Film Photoanodes	44
3.3.2 Role of Gallium Oxide Overlayer in Hematite Thin Film Photoanodes	50
3.3.3 Combination of Interfacial Layers with an Abundant Catalyst	55
3.4 Conclusions	56
3.5 References	57
4 LOW-TEMPERATURE ALD OF CRYSTALLINE AND PHOTOACTIVE ULTRATHIN HEMATITE FILMS FOR SOLAR WATER SPLITTING	63
4.1 The Significance of ALD for Hematite Photoanodes	64
4.2 Methods	65
4.2.1 Construction of the ALD-Setup	65
4.2.2 ALD of the Underlayer	69
4.2.3 Ellipsometry	69
4.2.4 TOF-ERDA	70
4.2.5 Electron Microscopy	70
4.2.6 X-Ray Diffraction	70
4.2.7 Raman Spectroscopy	70
4.2.8 Synthesis of the Nanowire Scaffold	70

4.2.9	Catalyst Deposition	71
4.2.10	Photoelectrochemical Characterization	71
4.2.11	UV-Vis Measurements	72
4.3	Results	73
4.3.1	Thoughts Behind the Choice of Precursors and Substrate Preparation	73
4.3.2	Growth Characteristics of Hematite	74
4.3.3	Hematite Film Purity	75
4.3.4	Crystallinity and Phase Purity	77
4.3.5	Photoelectrochemical Performance of As-Deposited ALD-Hematite Films	80
4.3.6	Examples of Host-Guest Hematite Photoanodes	86
4.4	Conclusions	92
4.5	References	94
5	QUANTITATIVE ANALYSIS OF OPTICAL LOSSES IN PHOTOELECTROCHEMICAL CELLS BASED ON HEMATITE PHOTOANODES	99
5.1	Introduction	100
5.1.1	Background of PEC Optical Modeling	100
5.1.2	Theory of Optical Modeling	101
5.2	Methods	103
5.2.1	Transmission Electron Microscopy	103
5.2.2	Ellipsometry and Sample Preparation	104
5.2.3	UV-Vis Measurements	104
5.2.4	Optical Modelling	105
5.3	Results	105
5.3.1	Extraction of Optical Parameters of the Tec15 Substrate	105
5.3.2	Optical Parameterization of Hematite	110
5.3.3	Optical Model of a Typical PEC Cell Employing a Thin Film Hematite Photoanode	113
5.4	Conclusion	116
5.5	References	117
6	HIGHLY EFFICIENT PLANAR PEROVSKITE SOLAR CELLS THROUGH BAND ALIGNMENT ENGINEERING	123

6.1	Introduction	124
6.2	Methods	125
6.2.1	Electron Selective Layer Preparation	125
6.2.2	Perovskite Precursor Solution and Film Preparation	125
6.2.3	Solar Cell Characterization	126
6.2.4	fs-Transient Absorption Spectroscopy	127
6.2.5	Band Gap Estimation Measurements	127
6.2.6	Photoelectron Spectroscopy	128
6.2.7	Electrochemical Measurements on ALD Tin Oxide Layers	128
6.2.8	ALD-SnO ₂ Characterization	129
6.3	Results	129
6.3.1	Probing the Presence of Pinholes in ALD Tin Oxide	129
6.3.2	Tin Oxide Based Flat Perovskite Devices	133
6.4	Conclusion	141
6.5	References	142
7	CONCLUSIONS AND OUTLOOK	145
7.1	Trap States in Hematite	145
7.2	With ALD Hematite Towards Host-Guest Architectures	148
7.3	Tin Oxide Electron-Selective Contact for Perovskite Solar Cells	150
7.4	References	151
8	APPENDIX	153
8.1	Derivation of Mott-Schottky Equation	153
8.2	References	156
	ACKNOWLEDGEMENTS	157
	CV	161

1 INTRODUCTION

1.1 WORLD ENERGY CONSUMPTION

In 2013, the world consumed 389 million TJ of energy, which is equivalent with an energy consumption rate of 12.3 TW.¹ Almost 80% of the energy was produced from fossil fuels (oil, coal and natural gas) and only 7% originated from renewable sources (hydro, wind, solar, geothermal, bioenergy) as shown in Figure 1.1a,b,c.^{1, 2} Oil clearly dominates the transport sector (Figure 1.1d) as the major oil refining products are gasoline, kerosene and diesel fuel. Coal with a share of more than 40% is the predominant fuel for electricity generation (Figure 1.1b) especially for industrial use (Figure 1.1e).

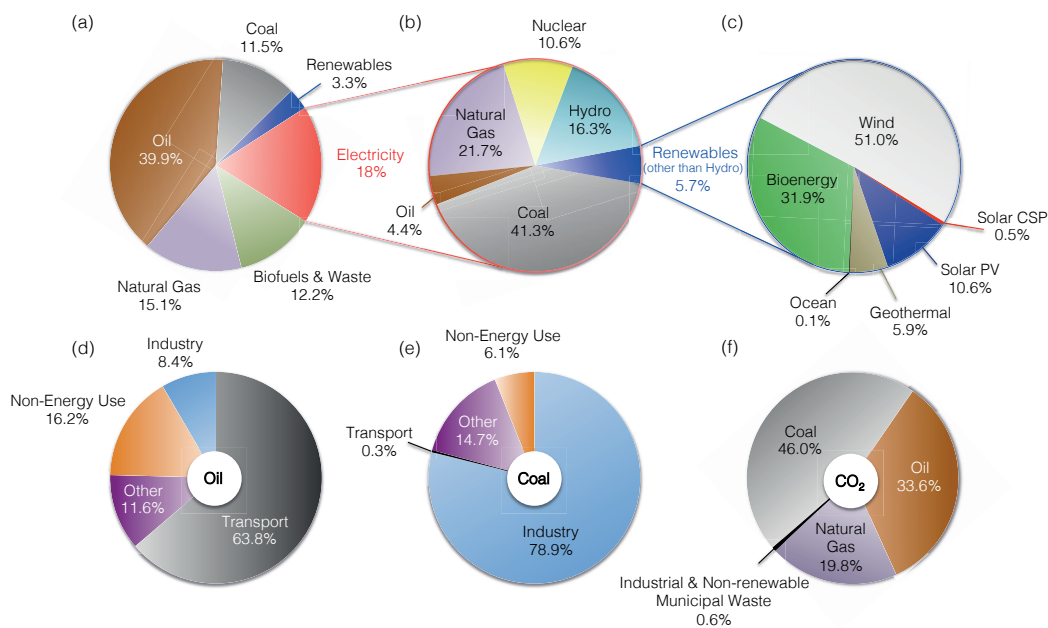


Figure 1.1 a) Fuel shares of the world final energy consumption of 389 million TJ in 2013. b) Fuel shares of world electricity consumption of 23'332 TWh in 2013. c) Renewable energy shares (excluding hydroelectric) for the world electricity consumption in 2013 (CSP = concentrated solar power). d) Shares of world oil and e) coal consumption with "Other" including agriculture, commercial and public services, residential, and non-specified others. f) Fuel shares of CO₂ emissions in 2013 (32'190 Mt CO₂) from fuel combustion excluding emissions from non-energy. Adapted from references ^{1, 2}.

The conventional way of electricity generation is based on turbines driving an electric

generator. In the case of coal, oil, nuclear, biomass, geothermal and solar thermal the produced heat then evaporates water to run a steam turbine. Gas turbines use natural gas combustion. Water turbines and wind turbines use hydro and wind power, respectively. Although the working principle of a turbine using heat, wind or water to power the electric generator is very similar, the outcome in terms of waste products is very different. In 2013, the combustion of fossil fuels emitted 32'190 Mt of CO₂ whereof 46% is allotted to coal and almost 34% to oil (Figure 1.1f). CO₂ along with methane and other pollutant gases persist in the atmosphere and absorb the solar infrared radiation that is reflected from the earth's surface. As in a greenhouse, the average temperature of the atmosphere and the oceans increases leading to severe climate changes.³ Hence, a timely decarbonization of our energy generation is important. Although nuclear power is rather CO₂ neutral, its radioactive waste has a major environmental impact persisting for centuries and even longer.⁴ A typical 1 GW nuclear power plant produces about 12 m³ of high-level (HLW) and 30 m³ of low- (LLW) and intermediate-level (ILW) radioactive waste every year.^{5,6} Scaling to the 441 nuclear power plants installed worldwide in 2014 with a net capacity of 383 GW,⁷ more than 4'200 m³ of HLW and 10'600 m³ of ILW and LLW is produced yearly. In addition, HLW often has to be calcined with added sugar to produce a more stable glass for long-term storage since it carries more than 95% of the total radioactivity produced. This so called vitrification process runs at a very high energy cost.⁸ The largest producers worldwide of nuclear energy are the United States and France.

Comparing CO₂ emissions between countries China (8'977.1 Mt), USA (5'119.7 Mt), India (1'868.6 Mt), Russia (1'543.1 Mt) and Japan (1'235.1 Mt) have the biggest obligation to reduce their emissions in the nearest future as, presently, they are the most polluting countries worldwide and are responsible for almost 60% of our global CO₂ emission. With currently 28% of our total global CO₂ emissions, China has a very central role in the energy policy of the future. With 1.37 billion people (1/5 of the worlds population) its demand for electricity represents 1/4 of the total globally produced electricity and 76% of this electricity is produced from coal resulting in the above-mentioned CO₂ emissions. However, China is producing also almost 1/4 of our global hydroelectricity and invested a record \$83.3 billion in renewable energy in 2014.⁹ The investment trend in renewables by China as well as Europe (\$57.5 billion), USA (38.3 billion), Japan (\$35.7 billion) and others is very promising for the decarbonization of our

future energy supply.

1.2 THE SOLAR POTENTIAL

In 2014, wind (\$99.5 billion) and solar (\$149.6 billion) accounted for 92% of the overall investment in renewable power and fuels, pointing to their great potential for a zero-emission future. Indeed, the sun is the biggest renewable energy resource available to our planet. In average, the earth receives a solar irradiation of 1366.1 W/m^2 , whereof about 50% are lost due to reflection and absorption in the atmosphere (clouds, aerosols etc.). With a total land surface of 149 million km^2 (with only half receiving sunlight at any one time), 183 million TJ are hitting the surface per hour. In view of our total annual energy demand in 2013 (389 million TJ), this means that the sun could cover all our *yearly* energy needs in about 2 *hours*! Thus, harvesting even just a fraction of this clean renewable energy is realistic given new technologies and societal/political changes.

Mankind has a big inertia towards drastic changes of habits. Using fossil fuels as energy source has been very convenient due to easy storage and transportation combined with their high energy density and low price. However, with limited fossil fuel stocks, global warming, steady population growth ($N_P = 7.1$ billion people in 2013 compared to 6.1 billion in 2000) and the rising standard of living in developing countries, the energy demand, E , will grow according to Equation (1.1).

$$E = N_P \times \frac{GDP}{N_P} \times \frac{E}{GDP} \quad (1.1)$$

All of these arguments must be the driving force needed for an economic and environmental revolution towards carbon neutral renewable energy supply. However, for the realization of the jump from 7% to 100% supply from renewable energy resources, we have to guarantee scalable storage and redistribution of energy. Photovoltaics can produce electricity with the scalability that we need, but due to the intermittence in solar irradiation, a constant, stable electricity supply is not possible *without a viable storage solution*. Evidently, an insecure electricity supply is unacceptable – especially in the industrial sector working 24/7 with high power demanding machines. Pumped-storage hydropower is a good strategy used nowadays to buffer the electricity grid. Especially in the United States, China and Europe pumped storage is well established and planned to be expanded in the future. To date, there are approximately 270 pumped-storage power

plants globally installed or about to be inaugurated in the next few years. With a total of 127 GW, it represents the highest capacity for energy storage to date.¹⁰ These numbers are expected to double in the near future but even then, this represents only a small fraction of energy needed to be stored once we transition to a solar driven economy.

1.3 A HYDROGEN ECONOMY

Fortunately, a hydrogen-based economy represents a scalable solution to the energy storage and distribution problem we are facing. Hydrogen is one of the most abundant elements on Earth and liquid hydrogen has the highest energy density of any fuel (Figure 1.2a) or battery (0.15 MJ/kg for lead acid and 0.5 MJ/kg for Li-Ion batteries). It is a transportable fuel that can be stored in small or TWh-quantities. For more than three decades, NASA (Cap Canaveral, Florida, USA) has been storing safely and economically $\sim 34'000 \text{ m}^3$ of liquid hydrogen used to fuel their space shuttle launches (Figure 1.2b).¹¹

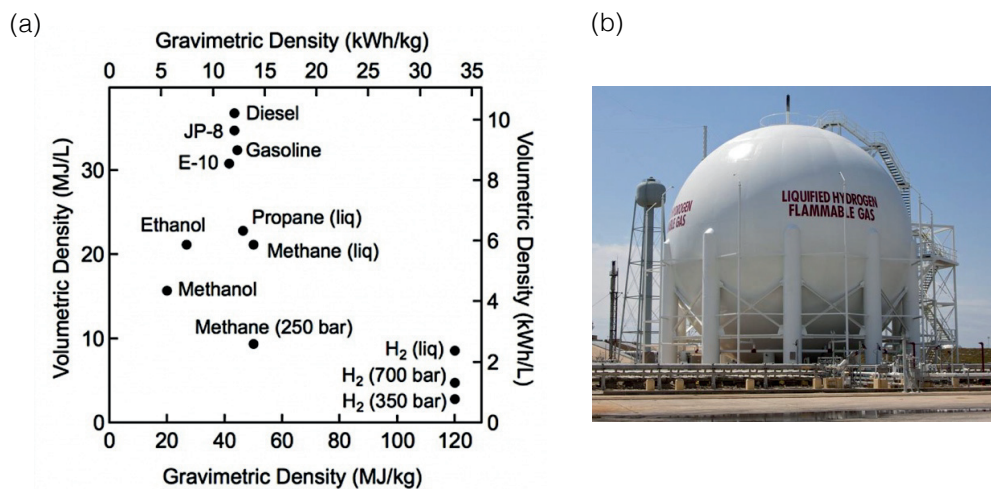


Figure 1.2 Hydrogen fuel. a) Volumetric and gravimetric energy densities of some fuels. Taken from reference 12. b) Liquid hydrogen stored at NASA.¹¹

In a hydrogen economy (Figure 1.3), a smart grid distributes electricity produced from renewable energy resources (sun, wind, water, geothermal and bioenergy). Excess electricity is then converted by electrolysis to hydrogen that can be stored in different forms such as compressed gas, liquid hydrogen, adsorbed hydrogen on, for example, metal-organic-frameworks (MOFs) or as metal hydride. On demand, hydrogen can then be reconverted in electricity via fuel cells. The hydrogen storage strategy would

compensate for the intermittency of solar irradiation or wind power and allow for a stable electricity grid. In addition, hydrogen can be directly produced with solar energy by photoelectrochemical splitting of water and can supply a surplus of hydrogen to cover the needs of our transportation system and chemical industry for example. Using a carbon monoxide/hydrogen gas mixture (syngas) all kinds of carbohydrates needed for the fabrication of polymers, cosmetics and prescription drugs for example can be synthesized via the Fischer-Tropsch process. Using nitrogen and hydrogen the synthesis of ammonia via the Haber-Bosch process is important for the fertilizer industry. Both are already established key processes in today's economy but the hydrogen is synthesized mainly via methane steam reforming at high temperatures and is neither renewable, nor carbon-neutral.

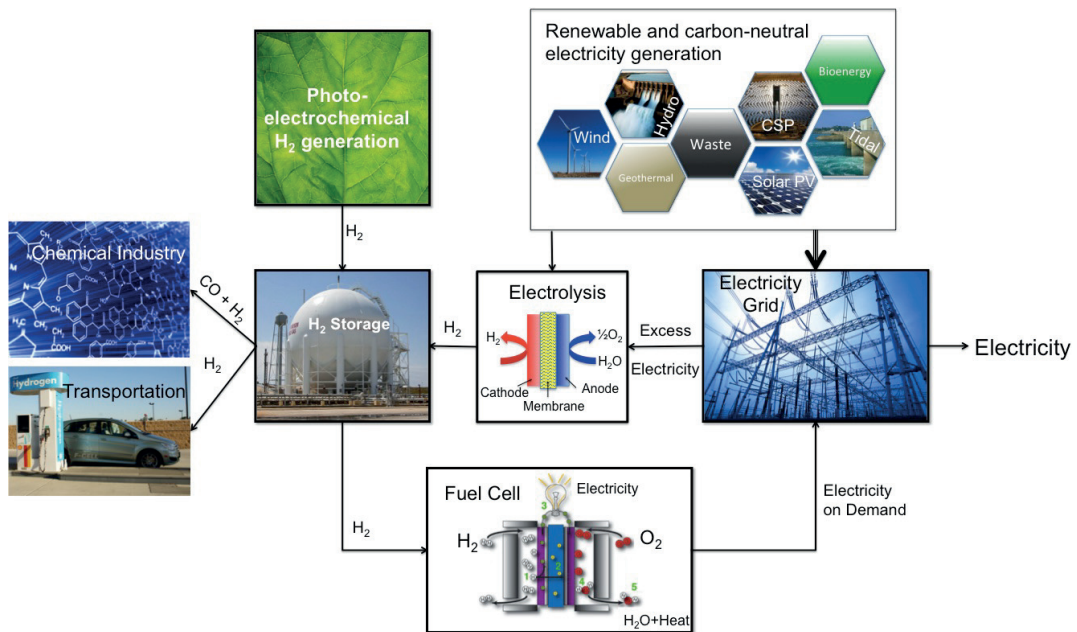


Figure 1.3 Schematic representation of significant aspects of a hydrogen economy based on renewable energy sources (wind, hydro, geothermal, waste, concentrated solar power (CSP), solar photovoltaics, tidal, biomass) that produce energy injected as electricity in the grid. Excess electricity can be stored in hydrogen produced cleanly by electrolysis. On demand, it can be recombined with oxygen in a fuel cell to produce clean electricity. In addition, hydrogen can be directly produced with solar energy by photoelectrochemical splitting of water and can supply a surplus of hydrogen to cover the needs of our transportation system and chemical industry for example.

Furthermore, the renewable hydrogen can also be distributed as a fuel for transportation. In 2015, the system cost of an automotive fuel cell was around 55 \$/kWh_{net}, which is 43% lower than 2006.¹³ The price-determining factor is the pricy Pt-based catalyst. Thus,

research towards low-cost catalysts using abundant materials is important, in order to further decrease cost. Nowadays, vehicles with fuel cell technology mainly from Honda, Hyundai, Daimler and BMW, are already on the market. Indeed, along with the decrease in system cost, prices of fuel cell vehicles (Toyota Mirai, \$58'333) have dramatically decreased in recent years to rival that of battery-based electric vehicles (Tesla Model S, \$71'100). In the San Francisco bay area the bus company AC Transit (USA) already uses 12 fuel cell busses on hydrogen.¹⁴ With the new ionic compressor developed by the Linde group (Germany), refueling of a vehicle with autonomy of approximately 500 km takes only 3 minutes.¹⁵ These short refueling times and high autonomies make a hydrogen fuel infrastructure highly attractive.

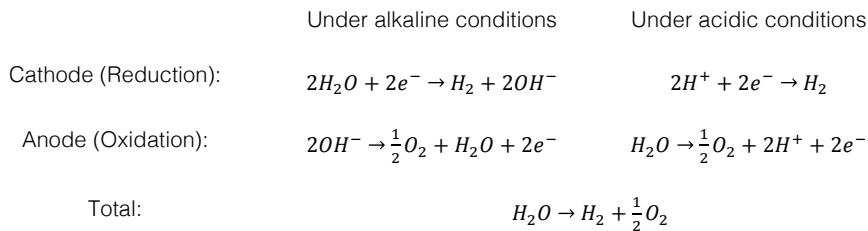
1.4 WATER SPLITTING

In such an economy, renewable hydrogen would be produced with an excess of electricity via electrolysis of water and/or more elegantly and potentially more cost-efficient via direct photolysis.

Water electrolysis is the decomposition of water into hydrogen and oxygen. According to thermodynamics given in Equation (1.2), the minimum free energy needed for this splitting reaction is $\Delta G = +237.18$ kJ/mol at 25 °C, which is equal to a required voltage of 1.23 V ($=\Delta G/nF$ for $n=2$ electrons with F being the Faraday constant).

$$\Delta G = \Delta H_f - T\Delta S = 286.03 \frac{\text{kJ}}{\text{mol}} - 0.163 \frac{\text{kJ}}{\text{mol}\cdot\text{K}} T[\text{K}] \quad (1.2)$$

However, in practice, this voltage is not enough to split water. Overpotential losses at the anode (η_a), cathode (η_c) and in solution due to ionic conductivity (η_{sol}) have to be considered such that the final applied voltage can be substantially higher than 1.23 V. Given the correct energetics, the following processes can occur depending on whether the reaction medium is alkaline or acidic:



In dark electrolysis, the energy needed is supplied by electricity (Figure 1.4a) that would in the future be entirely generated by renewables and hence, is an attractive way to produce carbon-neutral hydrogen. Indeed, even the photolysis community largely discusses the advantages of a “PV-electrolysis” concept, especially after Luo *et al.* recently demonstrated conversion efficiencies of 12.3% employing relatively inexpensive and highly abundant materials.¹⁶ PV-electrolysis has the advantage that hydrogen generation is decoupled from light absorption and hence theoretically higher solar-to-hydrogen (STH) efficiencies are possible if for example triple-junction solar cells are used. The efficiency is in this case simply the product of the separate process efficiencies:

$$\eta_{STH} = \eta_{PV} \times \eta_{Electrolyzer} \quad (1.3)$$

For a PV efficiency (η_{PV}) of 38% for triple-junction solar cells (non-concentrated) or 20% for cheaper alternatives such as polycrystalline silicon or perovskite solar cells, and typical electrolyzer efficiencies ($\eta_{Electrolyzer}$) between 75-80%, STH efficiencies between 15-30% are realistic.¹⁷ More on the development in dark electrolysis as well as corresponding life cycle assessments can be found elsewhere.¹⁸⁻²²

Photolysis is inspired by natural photosynthesis, which converts solar to chemical energy by light absorbers (chlorophyll) that use their absorbed energy to generate electrons for the reduction of CO₂ to energy dense sugars (Figure 1.4b). In analogy, direct photolysis (Figure 1.4c) uses semiconductors to absorb sunlight for the generation of electrons and holes used to drive the above reactions.

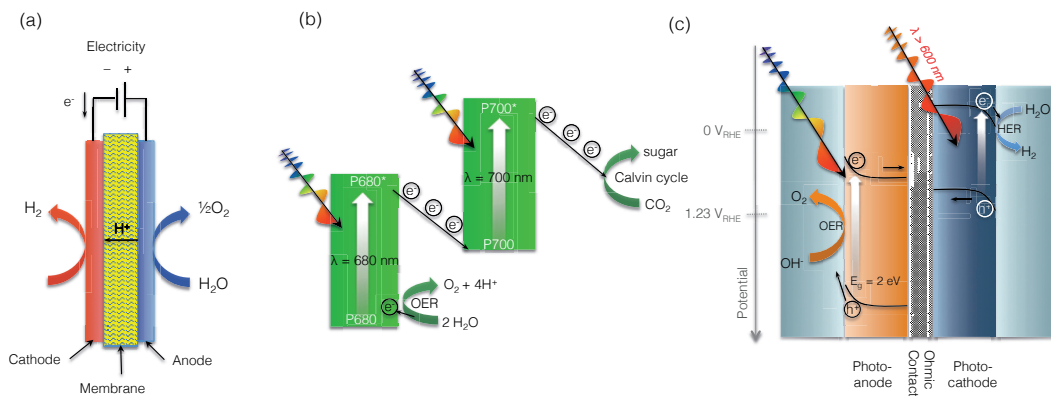


Figure 1.4 a) Principle of dark water electrolysis shown on the example of PEM (polymer electrolyte membrane) electrolysis. b) Z-scheme type of natural photosynthesis as an inspiration for c) the working principle of photoelectrochemical water splitting with a photoanode in tandem with a smaller band gap photocathode.

Photosynthesis uses pigments to absorb sunlight in the leaf. More specifically, the leaf has two different types of chlorophyll dyes – chlorophyll a and b – absorbing visible light of 700 nm and 680 nm, respectively (Figure 1.5a). With respect to the broad solar spectrum shown in Figure 1.5b, this is a very narrow absorption region, meaning that most of the energy rich visible light is not captured by the plant due to the limitation in the absorption coefficient of its dyes. In an artificial solar energy conversion system, such losses are unacceptable. For energy conversion efficiencies to be high, most of the visible and infrared (IR) light has to be efficiently absorbed. Dye-sensitized solar cells have shown to work efficiently with precisely engineered dyes adsorbed on mesoporous TiO_2 . Thus, these devices were able to capture most of the visible light due to the modified absorption coefficients of the synthetic dyes and the improved loading of these dyes on the nanostructured TiO_2 .^{23, 24}

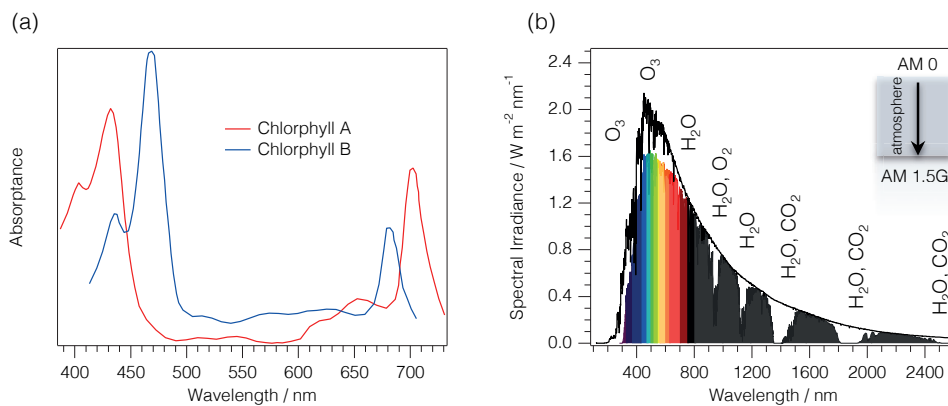


Figure 1.5 a) Absorption spectra of chlorophyll a and b. In the visible region, chlorophyll a absorbs around 700 nm and chlorophyll b around 680 nm as indicated also in Figure 1.4b. b) Solar irradiance outside atmosphere (AM 0) and at the Earth's surface (AM 1.5G, incident angle of 48°) after a reduction in the power of the solar radiation due to absorption (by water vapor, oxygen, CO_2 and ozone), scattering and reflection in the atmosphere. More on specifics of solar irradiation can be found elsewhere.²⁵

Besides strong visible light absorption, photoelectrode materials for PEC water splitting have to fulfill several other important criteria such as efficient charge transport, natural abundance of the constituent elements, low cost, non-toxicity and high stability under water splitting conditions.²⁶ The latter is very important to avoid corrosion/degradation processes of the photoabsorbers. Semiconductors are excellent light absorbers and some of them are chemically robust enough in alkaline or acidic media (necessary to increase the ionic conductivity of the solution). Similar to the light absorption process in a dye molecule, where an electron is excited from the highest occupied molecular orbital

(HOMO) to the lowest unoccupied molecular orbital (LUMO) (Figure 1.6, center), an electron can be excited from the valence band to the conduction band if the absorbed energy exceeds the band gap energy (Figure 1.6, right). Hence, in order to absorb most of the visible and near-IR irradiation (Figure 1.5b), small-band gap semiconductors are desired.

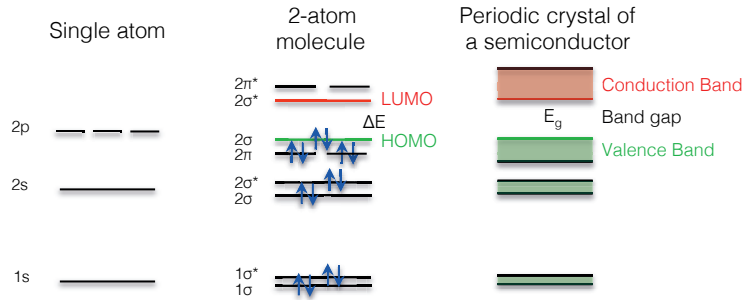


Figure 1.6 In a single atom the atomic orbitals are degenerate, meaning having equal energies (as the 2p orbitals shown left). In a molecule atoms are close enough to energetically interact with each other leading to a splitting in the energy of the molecular orbitals formed, which is a consequence of the Pauli exclusion principle stating that a maximum of 2 electrons with spin states $s^{+1/2}$ and $s^{-1/2}$ can occupy one state (the spin states are represented by the blue arrows in up and down direction). Electrons from each atomic orbital fill the molecular orbitals until the highest occupied molecular orbital (HOMO). Upon light absorption of light with an energy bigger than ΔE , an electron from the HOMO can be excited to the lowest unoccupied molecular orbital (LUMO). This excited state lasts only a split of a second (depending on the molecule). Projecting molecules of only a few atoms to periodic crystals of N atoms, energetic coupling of all the atomic orbitals leads to a quasi-continuum of states known as bands. The highest occupied band is the valence band and the lowest unoccupied band is the conduction band. In a semiconductor the valence and conduction bands are separated by a band gap with energy E_g . Depending on the band gap energy materials are classified into metals (no band gap, bands overlap), semiconductors and insulators ($E_g > 3$ eV).

1.4.1 SEMICONDUCTOR FUNDAMENTALS

In this subchapter the concept of Fermi level will be introduced leaning on semiconductor physics literature.²⁷ In thermal equilibrium, the number of electrons, n , in occupied conduction-band levels is given by the density of conduction band states $g_c(E)$ multiplied by the occupancy $f(E)$, integrated over the conduction band (Equation (1.4)).

$$n_c = \int_{E_C}^{\infty} g_c(E) \cdot f(E) dE \quad (1.4)$$

The density of states is given by

$$g_c(E) = \frac{\sqrt{2} (m_c^*)^{\frac{3}{2}}}{\pi^2 \hbar^3} \sqrt{E - E_C} \quad (1.5)$$

with m_C^* being the effective mass of electrons in the conduction band. The probability of occupying these states strongly depends on temperature and energy and is described by the Fermi-Dirac function that can be approximated by a Boltzmann term for $E - E_F \gg 3k_B T$

$$f(E) = \frac{1}{e^{\frac{E-E_F}{k_B T}} + 1} \approx e^{-\frac{E-E_F}{k_B T}} \quad (1.6)$$

where E_F is the Fermi energy of electrons. Defining N_C as the effective density of states in the conduction band,

$$N_C(T) \equiv 2 \left(\frac{2\pi m_C^* k_B T}{h^2} \right)^{\frac{3}{2}} \cdot M_C \quad (1.7)$$

with M_C being the number of minima in the conduction band. The number of electrons in the conduction band is given by

$$n_C = N_C(T) e^{-\frac{(E_C - E_F)}{k_B T}} \quad \text{or} \quad E_C - E_F = k_B T \ln \left(\frac{N_C(T)}{n_C} \right). \quad (1.8)$$

Similarly for the valence band holes, p_V :

$$p_V = N_V(T) e^{-\frac{(E_F - E_V)}{k_B T}} \quad \text{or} \quad E_F - E_V = k_B T \ln \left(\frac{N_V(T)}{p_V} \right). \quad (1.9)$$

Subtraction of Equation (1.8) from (1.9) gives the Fermi level, which is the electrochemical potential of charge carriers:

$$E_F = \frac{E_C + E_V}{2} + \frac{k_B T}{2} \ln \left(\frac{n_C N_V}{p_V N_C} \right) \quad (1.10)$$

For an intrinsic semiconductor ($n_C = p_V$), the Fermi level is located close to the middle of the band gap as shown in Figure 1.7a, since the effective mass of electrons is very close to the one of holes. For one minimum in the conduction band and with

$$\frac{N_V}{N_C} = \left(\frac{m_V^*}{m_C^*} \right)^{\frac{3}{2}} \quad (1.11)$$

the Fermi level of an intrinsic semiconductor is given by

$$E_F = \frac{E_C + E_V}{2} + \frac{3k_B T}{4} \ln \left(\frac{m_V^*}{m_C^*} \right). \quad (1.12)$$

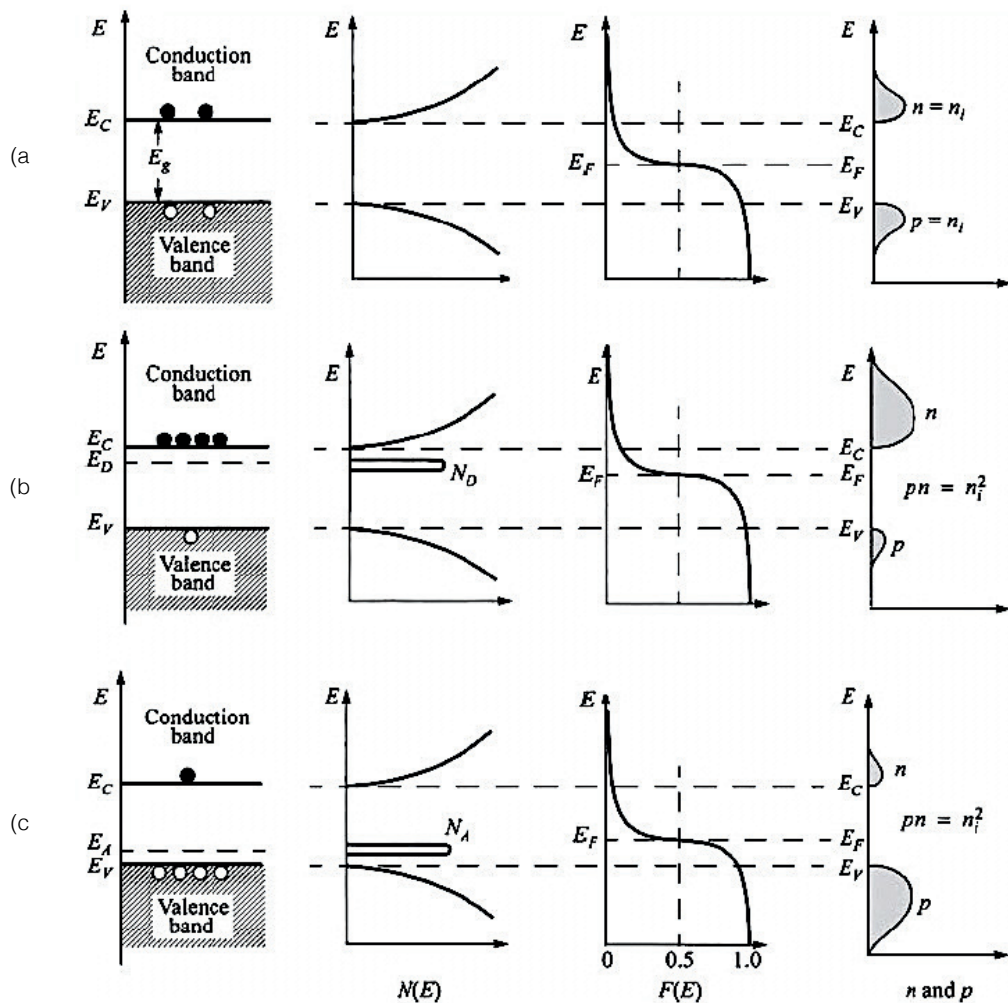


Figure 1.7 Schematic band diagram, density of states, Fermi-Dirac distribution, and carrier concentrations for (a) intrinsic, (b) n-type, and (c) p-type semiconductors at thermal equilibrium. The mass action law $pn = n_i^2$ is valid for all three cases. Taken from reference ²⁷.

The intrinsic carrier concentration of semiconductors such as silicon and gallium arsenide is very low at room temperature: Si ($E_g = 1.1$ eV, $n_i = 10^{10}$ cm⁻³), GaAs ($E_g = 1.4$ eV, $n_i = 3 \cdot 10^6$ cm⁻³). However, one of the most important properties of a semiconductor is that it can be doped with different types and concentrations of impurities to vary its resistivity. When a semiconductor is doped with donor or acceptor impurities, impurity energy levels are introduced that usually lie within the energy gap as shown in Figure 1.7b,c. A donor impurity has a *donor level* at energy E_D , which is defined as *being neutral if filled by an electron, and positive if empty*. Conversely, an *acceptor level* at energy E_A is *neutral if empty and negative if filled by an electron*. Depending on the impurity energy level and the lattice temperature, not all dopants are necessarily ionized. The concentration of all

donor impurities is defined as N_D and of the ionized as N_D^+ and similar for the acceptor impurities N_A and N_A^- .

The total negative charges (electrons and ionized acceptors) have to be balanced by the total positive charges (holes and ionized donors) to maintain charge neutrality:

$$N_D^+ + p = N_A^- + n \quad (1.13)$$

Due to the change in the carrier concentration upon doping with ionized donor impurities ($D \leftrightarrow D^+ + e^-$), the Fermi level shifts closer to the conduction band (Equation (1.10)) as the carrier concentration of electrons exceeds that of holes ($n_c \gg p_v$) and vice versa for doping with acceptor impurities resulting in n- and p-type semiconductors, respectively, as illustrated in Figure 1.7b,c.

1.4.2 SEMICONDUCTOR-METAL JUNCTION

Semiconductors have to be contacted to extract the photogenerated charge carriers in form of a current to either generate electricity as in a solar cell or just to shuttle electrons from the photoanode to the photocathode where they recombine with the holes in the p-type semiconductor (Figure 1.4c) while the minority carriers perform the water splitting reactions. Hence, the energetics at the contact are very important. When a metal contacts the semiconductor, the contact can either be ohmic (no potential barrier) or blocking due to a so-called Schottky barrier that forms. Figure 1.8 illustrates both contact types for the example of an n-type semiconductor. Helpful animations on solid-state junctions are given elsewhere.²⁸

In order to allow electrons to pass from the semiconductor to the metal contact, their work functions have to be well aligned. The work function, Φ , defines the energy required to completely remove an electron from the material to an infinite point in the vacuum and arrive there with zero energy. When the work function of the metal is smaller (Fermi level energetically higher) than that of the semiconductor, electrons will first flow from the metal to the conduction band of the semiconductor to lower their energy. For an n-type semiconductor, this leads to a downwards bending of the conduction band allowing electrons to pass this junction (Figure 1.8a).

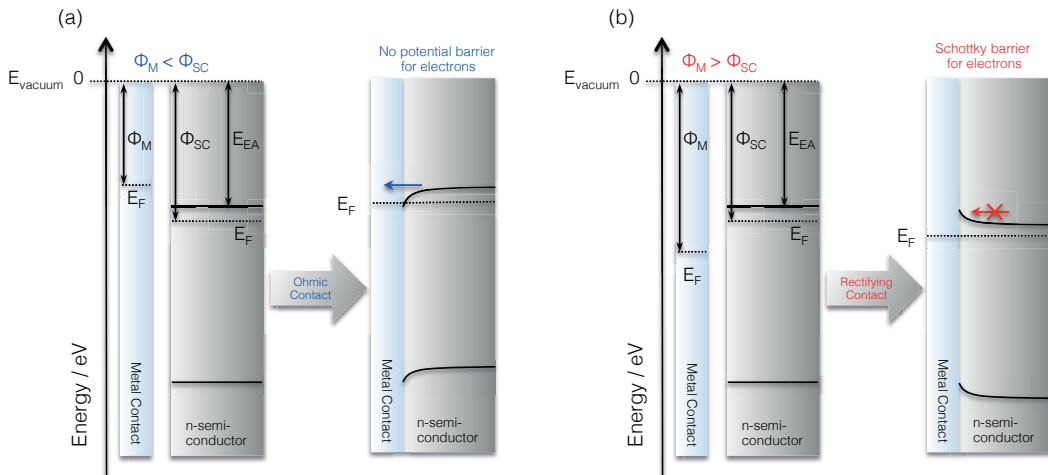


Figure 1.8 Formation of a) an ohmic contact or b) a Schottky barrier between the metal and the n-type semiconductor.

If, however, the work function of the metal is larger than of the semiconductor, the equilibration of the contacted system results in a Schottky barrier that hampers the electrons to pass. Still, there is a probability of tunneling through such a potential barrier, depending on the barrier thickness and height as well as on the electron effective mass as illustrated in Figure 1.9 and given by Equation (1.14).

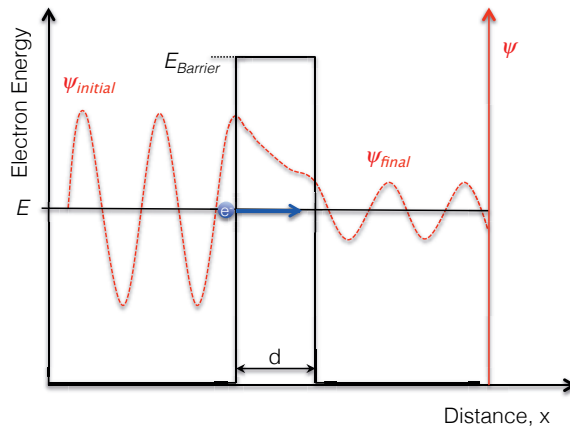


Figure 1.9 Wave functions and electron energy for an electron tunneling through a rectangular barrier.

The tunneling probability, T_t , decreases exponentially with barrier thickness d :

$$T_t = \frac{|\psi_{\text{final}}|^2}{|\psi_{\text{initial}}|^2} \propto e^{-2d\sqrt{\frac{2m_c^*(E_{\text{Barrier}}-E)}{\hbar^2}}} \quad (1.14)$$

1.4.3 SEMICONDUCTOR-ELECTROLYTE JUNCTIONS

1.4.3.1 IN THE DARK

Splitting water with a semiconductor photoelectrode needs a proper understanding of the semiconductor-electrolyte junction in the dark and under illumination. Figure 1.10 shows the change in band and Fermi level positions of an n-type semiconductor upon contact with an electrolyte in the dark. Upon contact, electrons flow from the semiconductor to the electrolyte to lower their chemical potential until equilibrium is reached ($E_F = E_{Redox}$). This results in an electron-depleted region of thickness W_{SC} (=space charge layer width) in the semiconductor near the semiconductor-electrolyte junction and induces an electric field, \vec{E} .

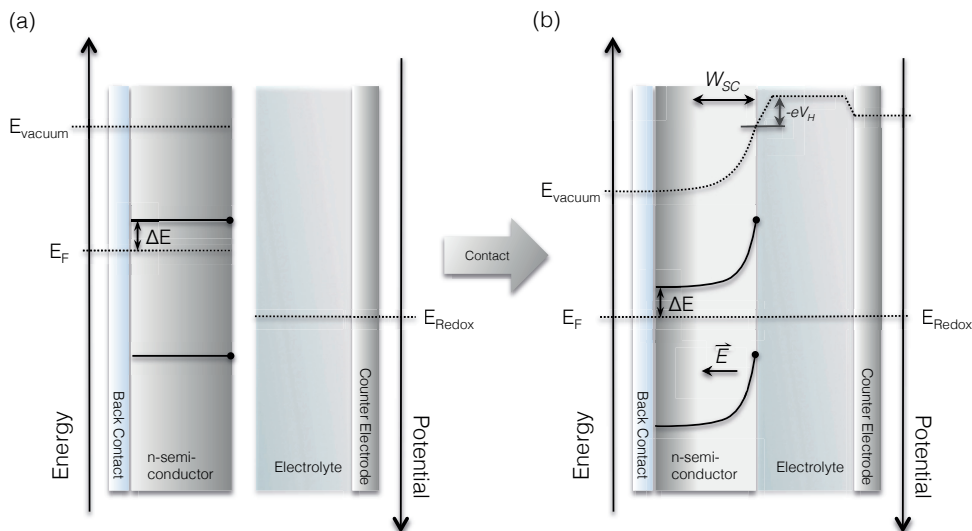


Figure 1.10 Energy band diagram of an n-type semiconductor a) before and b) after contact with an electrolyte in the dark.

On the electrolyte side, negative ions adsorb at the semiconductor surface to counterbalance the positive space charge (= ionized donor impurities) in the semiconductor. A detailed view on the electrical double layer forming at this interface as well as further details on the space charge region are given in Section 2.1.2 on impedance spectroscopy.

1.4.3.2 UNDER ILLUMINATION

Upon light absorption an electron is excited from the valence into the conduction band leaving behind a hole (= electron vacancy) in the valence band if the energy of light is

higher than the band gap energy:

$$E = h\nu = \frac{hc}{\lambda} \geq E_g \quad (1.15)$$

The additional electrons generated under light shift the Fermi level of electrons closer to the conduction band, which is accompanied by a weaker band bending. Given that there still persists an electric field, the just created charges can be separated: electrons flow (energetically downhill) to the back contact while holes accumulate at the semiconductor/electrolyte junction. This charge separation induces a gradient in the concentration of holes from the junction to the bulk of the semiconductor leading to a splitting of the Fermi energy into quasi Fermi levels for electrons, E_{Fn} , and holes, E_{Fp} , in the space charge region as illustrated in Figure 1.11 a.

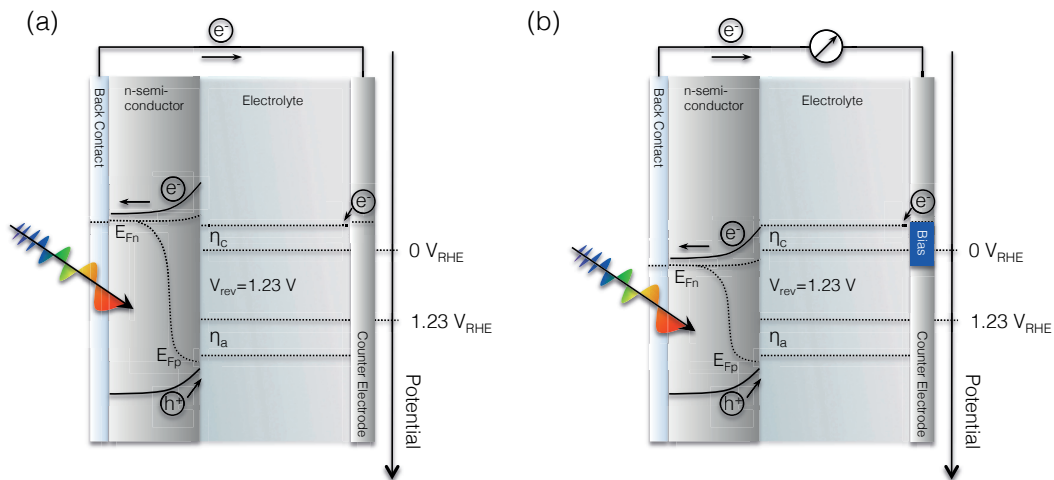


Figure 1.11 a) Ideal n-type semiconductor for standalone photoelectrochemical (PEC) water splitting with well aligned conduction and valence bands and a large enough Fermi level splitting to drive the water splitting reactions including the overpotentials at the cathode, η_c , and the photoanode, η_a . b) An n-type semiconductor with an insufficiently high Fermi level of electrons (and conduction band) and hence generates not enough photovoltage to drive both water splitting reactions. PEC water splitting can only be realized in a voltage bias assisted mode.

For standalone water splitting, the photoabsorber should provide a photovoltage of around 1.5 V considering the reversible potential of 1.23 V and the sum of the overpotentials ($=\eta_c+\eta_a$). Only few semiconductors have an energy band alignment that matches the water splitting potentials. TiO_2 fulfills this requirement and was the first material to be studied for solar water splitting in the early 1970's.^{29, 30} However, with a band gap of ~ 3.2 eV corresponding to a maximum absorption wavelength of 387 nm, it absorbs only a small fraction of solar irradiation resulting in a theoretical solar-to-

hydrogen (STH) conversion efficiency of only 4%. Unfortunately, most of the low-cost and stable* photoanode materials with band gaps between 1.5 and 2 eV have non-ideal positions of their conduction and valence bands (see Section 1.4.4). In this case, a voltage bias is needed to drive the reactions (Figure 1.11b). The bias voltage can be supplied by a photocathode³¹ or a solar cell³²⁻³⁶ in tandem with the photoanode. A detailed review summarizes recent advances in photoelectrochemical tandem cells for solar water splitting.³⁷

Another way of circumventing a non-ideal energy band alignment has been employed by NREL in 2001 and still holds the record STH efficiency of 16.4%.³⁸ The device is shown in Figure 1.12. Instead of externally connecting a solar cell to the PEC system, a *wireless* version of a solar cell tandem was applied using a double-junction GaInP₂/GaAs tandem photoanode. This configuration profits from the sum of the integrated photovoltages generated by the GaInP₂-np junction, V_{ph1} , and the GaAs-np junction, V_{ph2} , that is sufficiently high to achieve unassisted (= no voltage bias) water splitting.

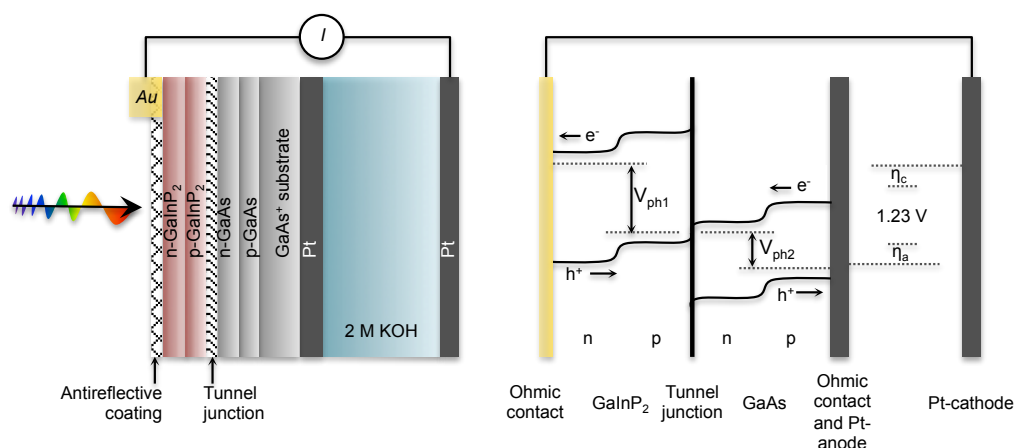


Figure 1.12 Schematic presentation of the components (left) and the energy band diagram (right) of the record np-GaInP₂/np-GaAs/Pt/KOH/Pt configuration for PEC water splitting. The band gap of GaInP₂ is 1.8 eV and that of GaAs is 1.4 eV. Adapted from reference³⁸.

To the present time, immersing state-of-the-art multi-junction solar cells has proven to achieve the highest solar-to-hydrogen conversion (STH) efficiencies (given by Equation (1.16)) for photoelectrochemical (PEC) water splitting.³⁸⁻⁴⁰

* A semiconductor is generally stable against oxidation by photogenerated holes if this oxidation potential lies lower than the valence band position or the O₂/H₂O potential. Likewise, a material is generally stable against reduction by photogenerated electrons if this reduction potential is higher than the conduction band position or the H⁺/H₂ potential.

$$\eta_{STH} = \frac{(1.23 V - V_{bias}) \times J_{ph} \left[\frac{mA}{cm^2} \right] \times \eta_F}{P_{incident} \left[\frac{mW}{cm^2} \right]} \quad (1.16)$$

With η_F being the faradaic efficiency and $P_{incident}$ the incident solar irradiation.

1.4.4 CHOICE OF THE SEMICONDUCTOR

As the voltage necessary to drive the water splitting reaction is around 1.5-1.6 V (depending on the overpotentials for water oxidation and reduction), it is challenging to find a material that precisely straddles these potentials with its quasi Fermi level positions and still broadly absorbs in the visible region (equivalent to a band gap of 1.5 - 2 eV). On the photoanode side, there are several semiconductors that absorb visible light as shown in Figure 1.13. Though GaAs and GaInP₂ have demonstrated record efficiencies for PEC water splitting (Figure 1.12), their production cost is too high for large-scale production. Besides, they need to be protected from solution, as they are not stable in aqueous media.⁴¹ Others such as silicon, indium and bismuth vanadates, sulphides, oxynitrides, nitrides and hybrid organic-inorganic perovskites are not stable under water splitting conditions. Besides, cadmium (in CdS and CdSe) and lead (in hybrid organic-inorganic perovskites) are under RoHS (Restriction of Hazardous Substances) regulations.

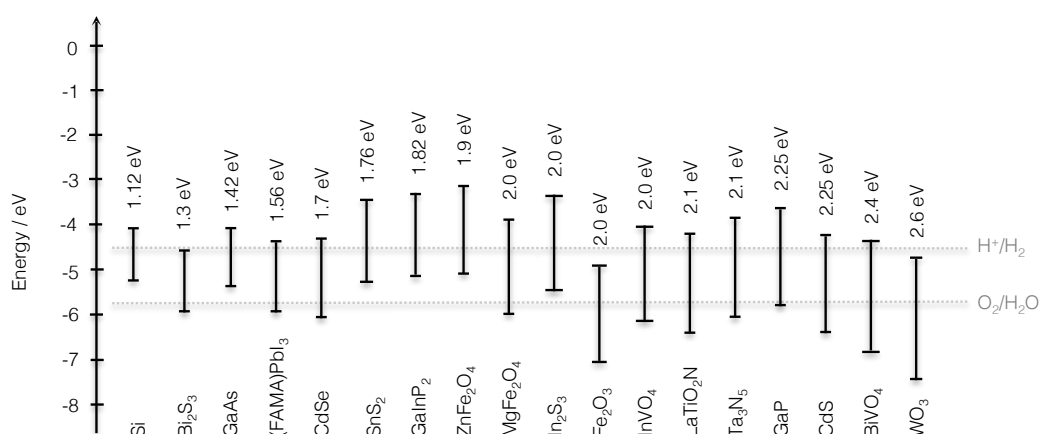


Figure 1.13 Band gaps and band positions of n-type semiconductors with band gaps between 1 eV and 2.6 eV. Adapted from references ^{24, 42-44}.

Though recent developments in protection layer engineering led to a significant stabilization of unstable materials,⁴⁵⁻⁴⁷ their stability would highly depend on the production process. Minor production errors could create pinholes in the protection

layer.⁴⁸ Hence, inherently stable materials are more favorable for long-term installations. Tungsten trioxide is stable in acidic medium but only absorbs the blue part of the visible region (due to its band gap of 2.6 eV). However, the iron-based compounds such as hematite and the ferrites are highly stable in neutral to alkaline medium. Furthermore, their elements are highly earth-abundant as seen in Figure 1.14 and the compounds are nontoxic. With band gaps of ~ 2.0 eV, they have the potential to reach STH conversion efficiencies of up to 16.8% when used as the bottom photoabsorber.^{17, 49}

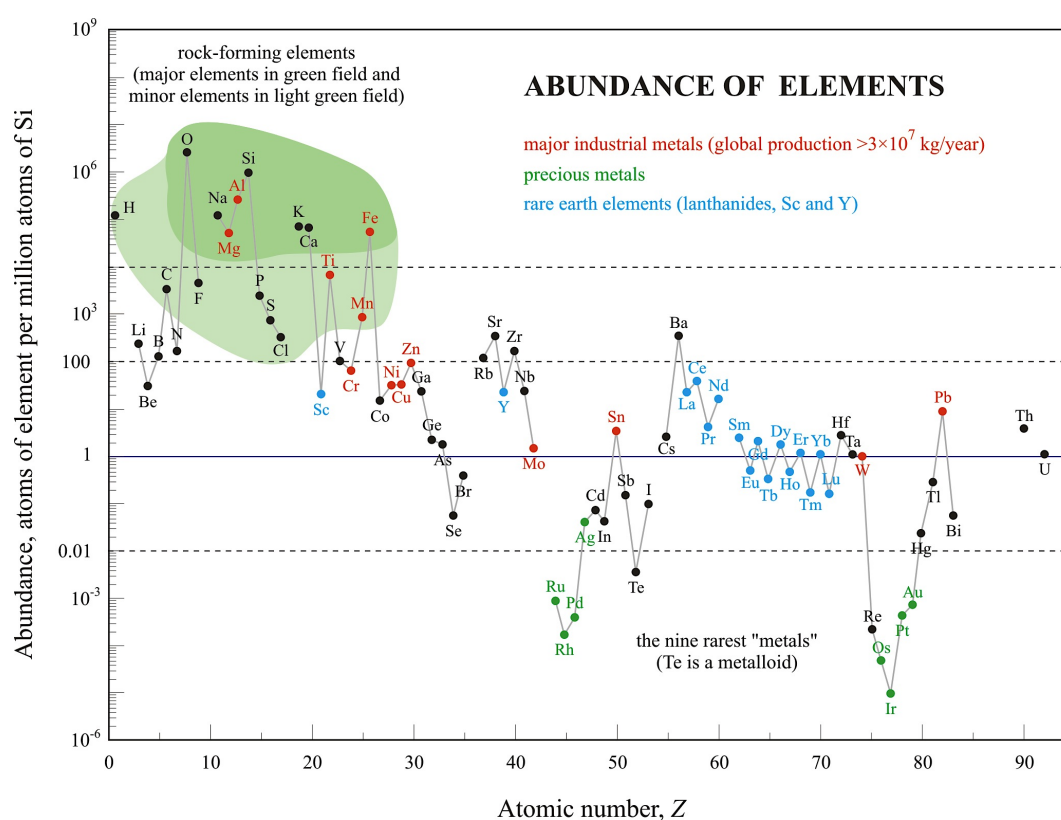


Figure 1.14 Relative abundance of elements in Earth's upper continental crust as a function of atomic number, Z . Taken from reference ⁵⁰.

Hematite ($\alpha\text{-Fe}_2\text{O}_3$) has a well-aligned valence band maximum for water oxidation and it fulfills almost all of the above-mentioned criteria for a suitable photoanode material.²⁶ However, it suffers from two major game-changing drawbacks:

Firstly, hematite's extremely low mobility of electrons ($\mu_n = 1.6 \cdot 10^{-2} \text{ cm}^2 (\text{Vs})^{-1}$ for Ti-doped hematite at 300 K) and orders of magnitude lower for holes ($\mu_p = 5.6 \cdot 10^{-6} \text{ cm}^2 (\text{Vs})^{-1}$ for Mg-doped p-type hematite)⁵¹ is in stark contrast with mobilities found for

example in silicon ($\mu_n = 100\text{-}1060 \text{ cm}^2 (\text{Vs})^{-1}$; $\mu_p = 150\text{-}500 \text{ cm}^2 (\text{Vs})^{-1}$ at 300 K) or GaAs ($\mu_n = 3000\text{-}8000 \text{ cm}^2 (\text{Vs})^{-1}$; $\mu_p = 180\text{-}400 \text{ cm}^2 (\text{Vs})^{-1}$ at 300 K).^{†27} The mobility is a function of the mean free path, λ_m , and the carrier effective mass, m^* ,

$$\mu = \frac{q\lambda_m}{\sqrt{3k_B T m^*}} \quad (1.17)$$

and is a determining parameter for the internal resistivity, ρ , and hence, the conductivity, σ , of a semiconductor given by

$$\sigma = \frac{1}{\rho} = q(\mu_n n + \mu_p p) \quad (1.18)$$

This makes it extremely challenging to collect holes that are photo-generated within the hematite layer (and far from the surface) especially when hematite is operated in water. As thin films absorb only a small fraction of light depending on their absorption coefficient,[‡] a myriad of works have focused on photoelectrode designs aiming at facilitating hole extraction at the hematite surface. Nanostructuring approaches have been applied to either the semiconductor itself⁵²⁻⁵⁴ or to an electron conductive host scaffold coated by a thin layer of the hematite guest absorber⁵⁵⁻⁵⁸ as illustrated in Figure 1.15.

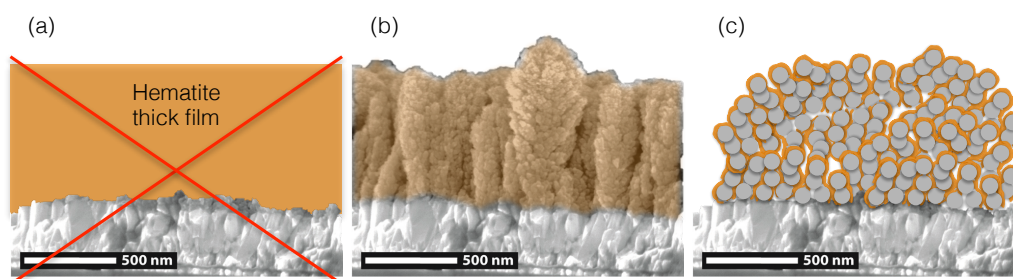


Figure 1.15 a) Thick film configuration most commonly employed for semiconductors with low resistivities. In this configuration hematite will heavily suffer from its low conductivity so that charge extraction will be inefficient. b) Cauliflower-nanostructured hematite (orange) on a FTO conductive substrate (grey). Adapted from reference ⁵⁹. c) Nanostructured electron conductive host scaffold (grey particles) coated with a hematite thin film (orange) corresponds to the host-guest configuration.

[†] For these materials, mobility decreases with increased carrier concentration. Values were taken for a carrier concentration range of $10^{14}\text{-}10^{18} \text{ cm}^{-3}$.

[‡] The light penetration depth is defined as the inverse of the absorption coefficient (α^{-1}). To absorb light up to 620 nm (equal to 2 eV), hematite thickness has to be roughly $1 \mu\text{m}$ as will be shown in Section 5.3.2. This is mainly due to the indirect band gap character in hematite: indirect transitions show rather weak light absorption

A nanostructured hematite photoanode design targets complete light absorption while simultaneously providing a short pathway for holes to the semiconductor-liquid junction, a combination that should result in higher photocurrents and better charge extraction efficiencies.

Here lies the first motivation and challenge for the work presented in this thesis: The objective to design a synthesis process that allows for a conformal and homogenous coating of a nanostructured conductive host scaffold with a photoactive hematite thin film. This work on hematite deposited by atomic layer deposition will be presented in Chapter 4 and the deposition method introduced in Section 2.2.⁶⁰

The second major drawback encountered in hematite lies in its extremely fast electron-hole recombination kinetics (some ps) that compete with the rather slow (up to 3 s) water oxidation reaction step.⁶¹⁻⁶³

In general, there are 3 different types of recombination shown in Figure 1.16:

- Band-to-band recombination that results in the emission of a photon and hence is radiative
- Auger recombination transferring the energy to another electron in the conduction band
- Nonradiative trap-assisted recombination through single-level traps (2-step process).

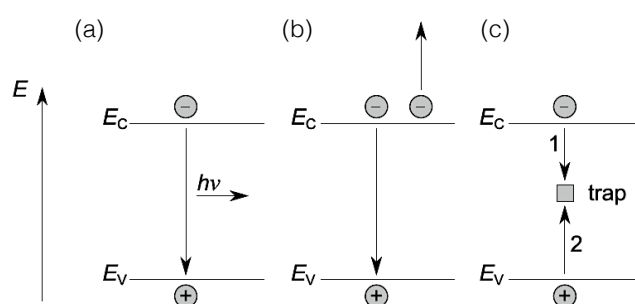


Figure 1.16 Recombination processes (the reverse are generation processes). (a) Band-to-band radiative recombination. (b) Auger recombination transferring the energy to another electron in the conduction band. (c) Nonradiative trap-assisted recombination through single-level traps (2-step process). Taken from reference ⁶⁴.

It was observed that hematite exhibits a deep donor level.^{61, 65-68} In Chapter 3 this deep trap level is identified and a method towards trap passivation will be presented. In the final conclusion in Chapter 7 the nature, role and importance of these traps is discussed.

1.5 REFERENCES

1. http://www.iea.org/publications/freepublications/publication/KeyWorld_Statistics_2015.pdf (accessed February 1, 2016).
2. <http://www.iea.org/Textbase/npsum/MTrenew2014sum.pdf> (accessed February 02, 2016).
3. IPCC. Climate Change 2014 Synthesis Report. http://www.ipcc.ch/pdf/assessment-report/ar5/syr/SYR_AR5_FINAL_full_wcover.pdf (accessed February 13, 2016).
4. Council, N. R. *Nuclear Wastes: Technologies for Separations and Transmutation* NATIONAL ACADEMY PRESS, Washington, D.C.: 1996.
5. http://www.kkl.ch/fileadmin/seiteninhalt/dateien/publikationen/2014_Faktenblatt_d.pdf (accessed February 4, 2016).
6. http://www.kernfragen.de/sites/default/files/media/publication/file/018basiswissen_0.pdf (accessed February 3, 2016).
7. http://www.kernfragen.de/sites/default/files/media/publication/file/atw2015_11_schnellstatistik.pdf (accessed February 5, 2016).
8. Agency, U. E. P. *Vitrification Technologies for Treatment of Hazardous and Radioactive Waste*. 1992.
9. <http://fs-unep-centre.org/publications/global-trends-renewable-energy-investment-2015> (accessed March 01, 2016).
10. Challenges and Opportunities for New Pumped Storage Development. http://www.hydro.org/wp-content/uploads/2014/01/NHA_PumpedStorage_071212b12.pdf (accessed February 13, 2016).
11. <http://www.nasa.gov/content/liquid-hydrogen-the-fuel-of-choice-for-space-exploration> (accessed February 13, 2016).
12. <http://energy.gov/eere/fuelcells/hydrogen-storage> (accessed February 12, 2016).
13. https://http://www.hydrogen.energy.gov/pdfs/15015_fuel_cell_system_cost_2015.pdf (accessed March 01, 2016).
14. H2 Infrastructure. http://www.the-linde-group.com/en/clean_technology/clean_technology_portfolio/hydrogen_as_fuel/building_hydrogen_refueling_infrastructure/index.html (accessed February 12, 2016).
15. Linde Standard Hydrogen Filling Station with Ic90 Compressor. <http://www.youtube.com/watch?v=usaQrCDORFY> (accessed February 12, 2016).
16. Luo, J. S.; Im, J. H.; Mayer, M. T.; Schreier, M.; Nazeeruddin, M. K.; Park, N. G.; Tilley, S. D.; Fan, H. J.; Gratzel, M. Water Photolysis at 12.3% Efficiency Via Perovskite Photovoltaics and Earth-Abundant Catalysts. *Science* **2014**, 345, 1593-1596.
17. Hu, S.; Xiang, C. X.; Haussener, S.; Berger, A. D.; Lewis, N. S. An Analysis of the Optimal Band Gaps of Light Absorbers in Integrated Tandem Photoelectrochemical Water-Splitting Systems. *Energy & Environmental Science* **2013**, 6, 2984-2993.
18. Shandarr, R.; Trudewind, C. A.; Zapp, P. Life Cycle Assessment of Hydrogen Production Via Electrolysis - a Review. *Journal of Cleaner Production* **2014**, 85, 151-163.
19. Pshenichnikov, A. G.; Kazarinov, V. E.; Naumov, I. P. Electrocatalytic Problems in Water Electrolysis. *Soviet Electrochemistry* **1991**, 27, 1375-1396.
20. Marini, S.; Salvi, P.; Nelli, P.; Pesenti, R.; Villa, M.; Berrettoni, M.; Zangari, G.; Kirov, Y. Advanced Alkaline Water Electrolysis. *Electrochimica Acta* **2012**, 82, 384-391.

21. Le Formal, F.; Bouree, W. S.; Prevot, M. S.; Sivula, K. Challenges Towards Economic Fuel Generation from Renewable Electricity: The Need for Efficient Electro-Catalysis. *Chimia* **2015**, 69, 789-798.
22. Carmo, M.; Fritz, D. L.; Merge, J.; Stolten, D. A Comprehensive Review on Pem Water Electrolysis. *International Journal of Hydrogen Energy* **2013**, 38, 4901-4934.
23. Mathew, S.; Yella, A.; Gao, P.; Humphry-Baker, R.; Curchod, B. F. E.; Ashari-Astani, N.; Tavernelli, I.; Rothlisberger, U.; Nazeeruddin, M. K.; Gratzel, M. Dye-Sensitized Solar Cells with 13% Efficiency Achieved through the Molecular Engineering of Porphyrin Sensitizers. *Nature Chemistry* **2014**, 6, 242-247.
24. Gratzel, M. Photoelectrochemical Cells. *Nature* **2001**, 414, 338-344.
25. <http://www.pveducation.org/pvcdrom> (accessed March 03, 2016).
26. van de Krol, R.; Liang, Y. Q.; Schoonman, J. Solar Hydrogen Production with Nanostructured Metal Oxides. *Journal of Materials Chemistry* **2008**, 18, 2311-2320.
27. Sze, S. M.; Ng, K. K. *Physics of Semiconductor Devices*. 3rd ed.; Wiley-Interscience: Hoboken, N.J., 2007; p x, 815 p.
28. <http://www.doitpoms.ac.uk/tlplib/semiconductors/index.php> (accessed March 03, 2016).
29. Boddy, P. J. Oxygen Evolution on Semiconducting TiO₂. *Journal of The Electrochemical Society* **1968**, 115, 199-208.
30. Fujishima, A.; Honda, K. Electrochemical Photolysis of Water at a Semiconductor Electrode. *Nature* **1972**, 238, 37-41.
31. Kim, J. H.; Kaneko, H.; Minegishi, T.; Kubota, J.; Domen, K.; Lee, J. S. Overall Photoelectrochemical Water Splitting Using Tandem Cell under Simulated Sunlight. *ChemSusChem* **2016**, 9, 61-66.
32. Arakawa, H.; Shiraishi, C.; Tatemoto, M.; Kishida, H.; Usui, D.; Suma, A.; Takamisawa, A.; Yamaguchi, T. Solar Hydrogen Production by Tandem Cell System Composed of Metal Oxide Semiconductor Film Photoelectrode and Dye-Sensitized Solar Cell - Art. No. 665003. *Solar Hydrogen and Nanotechnology II* **2007**, 6650, 65003-65003.
33. Brillet, J.; Yum, J. H.; Cornuz, M.; Hisatomi, T.; Solarska, R.; Augustynski, J.; Gratzel, M.; Sivula, K. Highly Efficient Water Splitting by a Dual-Absorber Tandem Cell. *Nature Photonics* **2012**, 6, 823-827.
34. Kim, J. H.; Jo, Y.; Kim, J. H.; Jang, J. W.; Kang, H. J.; Lee, Y. H.; Kim, D. S.; Jun, Y.; Lee, J. S. Wireless Solar Water Splitting Device with Robust Cobalt-Catalyzed, Dual-Doped BiVO₄ Photoanode and Perovskite Solar Cell in Tandem: A Dual Absorber Artificial Leaf. *ACS Nano* **2015**, 9, 11820-11829.
35. Park, J. H.; Bard, A. J. Photoelectrochemical Tandem Cell with Bipolar Dye-Sensitized Electrodes for Vectorial Electron Transfer for Water Splitting. *Electrochemical and Solid State Letters* **2006**, 9, E5-E8.
36. Shi, X.; Zhang, K.; Shin, K.; Ma, M.; Kwon, J.; Choi, I. T.; Kim, J. K.; Kim, H. K.; Wang, D. H.; Park, J. H. Unassisted Photoelectrochemical Water Splitting Beyond 5.7% Solar-to-Hydrogen Conversion Efficiency by a Wireless Monolithic Photoanode/Dye-Sensitized Solar Cell Tandem Device. *Nano Energy* **2015**, 13, 182-191.
37. Prévot, M. S.; Sivula, K. Photoelectrochemical Tandem Cells for Solar Water Splitting. *The Journal of Physical Chemistry C* **2013**, 117, 17879-17893.
38. Khaselev, O.; Bansal, A.; Turner, J. A. High-Efficiency Integrated Multijunction Photovoltaic/Electrolysis Systems for Hydrogen Production. *International Journal of Hydrogen Energy* **2001**, 26, 127-132.
39. Verlage, E.; Hu, S.; Liu, R.; Jones, R. J. R.; Sun, K.; Xiang, C. X.; Lewis, N. S.; Atwater, H. A. A Monolithically Integrated, Intrinsically Safe, 10% Efficient, Solar-Driven Water-Splitting System Based on

- Active, Stable Earth-Abundant Electrocatalysts in Conjunction with Tandem Iii-V Light Absorbers Protected by Amorphous TiO₂ Films. *Energy & Environmental Science* **2015**, *8*, 3166-3172.
40. Khaselev, O.; Turner, J. A. A Monolithic Photovoltaic-Photoelectrochemical Device for Hydrogen Production Via Water Splitting. *Science* **1998**, *280*, 425-427.
41. Khaselev, O.; Turner, J. A. Electrochemical Stability of P - Gainp₂ in Aqueous Electrolytes toward Photoelectrochemical Water Splitting. *Journal of The Electrochemical Society* **1998**, *145*, 3335-3339.
42. Marschall, R. Semiconductor Composites: Strategies for Enhancing Charge Carrier Separation to Improve Photocatalytic Activity. *Advanced Functional Materials* **2014**, *24*, 2421-2440.
43. Smith, W. A.; Sharp, I. D.; Strandwitz, N. C.; Bisquert, J. Interfacial Band-Edge Energetics for Solar Fuels Production. *Energy & Environmental Science* **2015**, *8*, 2851-2862.
44. Baena, J. P. C.; Steier, L.; Tress, W.; Saliba, M.; Neutzner, S.; Matsui, T.; Giordano, F.; Jacobsson, T. J.; Kandada, A. R. S.; Zakeeruddin, S. M., *et al.* Highly Efficient Planar Perovskite Solar Cells through Band Alignment Engineering. *Energy & Environmental Science* **2015**, *8*, 2928-2934.
45. Hu, S.; Shaner, M. R.; Beardslee, J. A.; Lichterman, M.; Brunenschwig, B. S.; Lewis, N. S. Amorphous TiO₂ Coatings Stabilize Si, Gaas, and Gap Photoanodes for Efficient Water Oxidation. *Science* **2014**, *344*, 1005-1009.
46. McDowell, M. T.; Lichterman, M. F.; Spurgeon, J. M.; Hu, S.; Sharp, I. D.; Brunenschwig, B. S.; Lewis, N. S. Improved Stability of Polycrystalline Bismuth Vanadate Photoanodes by Use of Dual-Layer Thin TiO₂/Ni Coatings. *Journal of Physical Chemistry C* **2014**, *118*, 19618-19624.
47. Paracchino, A.; Laporte, V.; Sivula, K.; Gratzel, M.; Thimsen, E. Highly Active Oxide Photocathode for Photoelectrochemical Water Reduction. *Nature Materials* **2011**, *10*, 456-461.
48. Didden, A.; Hillebrand, P.; Dam, B.; van de Krol, R. Photocorrosion Mechanism of TiO₂-Coated Photoanodes. *International Journal of Photoenergy* **2015**, *2015*, 8.
49. Murphy, A. B.; Barnes, P. R. F.; Randeniya, L. K.; Plumb, I. C.; Grey, I. E.; Horne, M. D.; Glasscock, J. A. Efficiency of Solar Water Splitting Using Semiconductor Electrodes. *International Journal of Hydrogen Energy* **2006**, *31*, 1999-2017.
50. http://www.periodni.com/rare_earth_elements.html (accessed March 05, 2016)
51. Gardner, R. F. G.; Sweett, F.; Tanner, D. W. Electrical Properties of Alpha Ferric Oxide .1. Impure Oxide. *Journal of Physics and Chemistry of Solids* **1963**, *24*, 1175-&.
52. Sivula, K.; Brillet, J.; Gratzel, M. Controlling Photo-Activity of Solution-Processed Hematite Electrodes for Solar Water Splitting. *Solar Hydrogen and Nanotechnology V* **2010**, 7770.
53. Sivula, K.; Zboril, R.; Le Formal, F.; Robert, R.; Weidenkaff, A.; Tucek, J.; Frydrych, J.; Gratzel, M. Photoelectrochemical Water Splitting with Mesoporous Hematite Prepared by a Solution-Based Colloidal Approach. *Journal of the American Chemical Society* **2010**, *132*, 7436-7444.
54. Li, L.; Yu, Y.; Meng, F.; Tan, Y.; Hamers, R. J.; Jin, S. Facile Solution Synthesis of Alpha-Fe₃.3h₂O Nanowires and Their Conversion to Alpha-Fe₂O₃ Nanowires for Photoelectrochemical Application. *Nano Letters* **2012**, *12*, 724-731.
55. Sivula, K.; Le Formal, F.; Gratzel, M. Wo₃-Fe₂O₃ Photoanodes for Water Splitting: A Host Scaffold, Guest Absorber Approach. *Chemistry of Materials* **2009**, *21*, 2862-2867.
56. Stefik, M.; Cornuz, M.; Mathews, N.; Hisatomi, T.; Mhaisalkar, S.; Gratzel, M. Transparent, Conducting Nb:Sno(2) for Host-Guest Photoelectrochemistry. *Nano Letters* **2012**, *12*, 5431-5435.
57. Lin, Y. J.; Zhou, S.; Sheehan, S. W.; Wang, D. W. Nanonet-Based Hematite Heteronanostructures for Efficient Solar Water Splitting. *Journal of the American Chemical Society* **2011**, *133*, 2398-2401.

-
58. Riha, S. C.; Klahr, B. M.; Tyo, E. C.; Seifert, S.; Vajda, S.; Pellin, M. J.; Hamann, T. W.; Martinson, A. B. F. Atomic Layer Deposition of a Submonolayer Catalyst for the Enhanced Photoelectrochemical Performance of Water Oxidation with Hematite. *Acs Nano* **2013**, *7*, 2396-2405.
59. Cornuz, M.; Gratzel, M.; Sivula, K. Preferential Orientation in Hematite Films for Solar Hydrogen Production Via Water Splitting. *Chemical Vapor Deposition* **2010**, *16*, 291-295.
60. Steier, L.; Luo, J. S.; Schreier, M.; Mayer, M. T.; Sajavaara, T.; Gratzel, M. Low-Temperature Atomic Layer Deposition of Crystalline and Photoactive Ultrathin Hematite Films for Solar Water Splitting. *Acs Nano* **2015**, *9*, 11775-11783.
61. Barroso, M.; Pendlebury, S. R.; Cowan, A. J.; Durrant, J. R. Charge Carrier Trapping, Recombination and Transfer in Hematite (Alpha-Fe₂O₃) Water Splitting Photoanodes. *Chemical Science* **2013**, *4*, 2724-2734.
62. Le Formal, F.; Pendlebury, S. R.; Cornuz, M.; Tilley, S. D.; Gratzel, M.; Durrant, J. R. Back Electron-Hole Recombination in Hematite Photoanodes for Water Splitting. *Journal of the American Chemical Society* **2014**, *136*, 2564-2574.
63. Pendlebury, S. R.; Wang, X. L.; Le Formal, F.; Cornuz, M.; Kafizas, A.; Tilley, S. D.; Gratzel, M.; Durrant, J. R. Ultrafast Charge Carrier Recombination and Trapping in Hematite Photoanodes under Applied Bias. *Journal of the American Chemical Society* **2014**, *136*, 9854-9857.
64. Tress, W. *Organic Solar Cells*. Springer International Publishing: Switzerland, 2014.
65. Steier, L.; Herraiz-Cardona, I.; Gimenez, S.; Fabregat-Santiago, F.; Bisquert, J.; Tilley, S. D.; Gratzel, M. Understanding the Role of Underlayers and Overlayers in Thin Film Hematite Photoanodes. *Advanced Functional Materials* **2014**, *24*, 7681-7688.
66. Ahmed, S. M.; Leduc, J.; Haller, S. F. Photoelectrochemical and Impedance Characteristics of Specular Hematite .1. Photoelectrochemical, Parallel Conductance, and Trap Rate Studies. *Journal of Physical Chemistry* **1988**, *92*, 6655-6660.
67. Horowitz, G. Capacitance Voltage Measurements and Flat-Band Potential Determination on Zr-Doped Alpha-Fe₂O₃ Single-Crystal Electrodes. *Journal of Electroanalytical Chemistry* **1983**, *159*, 421-436.
68. Leduc, J.; Ahmed, S. M. Photoelectrochemical and Impedance Characteristics of Specular Hematite .2. Deep Bulk Traps in Specular Hematite at Small Alternating-Current Frequencies. *Journal of Physical Chemistry* **1988**, *92*, 6661-6665.

2 THEORETICAL BACKGROUND FOR METHODS APPLIED IN THIS WORK

2.1 IMPEDANCE SPECTROSCOPY

Electrochemical impedance spectroscopy is a widely used technique for investigation of electrochemical processes at surfaces and interfaces.¹ To extract the parameters of the investigated system it is necessary to simulate and fit the data by an *equivalent circuit* based on a physical model of the system.

2.1.1 MEASUREMENT PRINCIPLE

During the impedance experiment, the *alternating current response*, $I(t)$ (Equation (2.1)), to a *small sinusoidal voltage perturbation*, $V(t)$ (Equation (2.2)), is measured during a frequency scan.

$$I(t) = I_0 e^{i(\omega t + \delta(\omega))} \quad (2.1)$$

$$V(t) = V_0 e^{i\omega t} \quad (2.2)$$

From the voltage to current ratio at a certain angular frequency, ω , the impedance, $Z(\omega)$, can be defined as:

$$Z(\omega) = \frac{V(t)}{I(t)} = \frac{V_0 e^{i\omega t}}{I_0 e^{i(\omega t + \delta(\omega))}} = \frac{V_0}{I_0} e^{-i\delta(\omega)} = |Z| e^{-i\delta(\omega)} \quad (2.3)$$

Applying the formula of Euler, the following is obtained from Equation (2.3):

$$Z(\omega) = |Z| \cos(\delta(\omega)) - i|Z| \sin(\delta(\omega)) = Z' - iZ'' \quad (2.4)$$

Equation (2.4) shows the two parts of impedance; the real, Z' , and the imaginary part, Z'' in the way impedance data is represented in *Nyquist* diagrams (Figure 2.1 left). Other useful graphical representations are *Bode* plots (Figure 2.1 right). They represent impedance in terms of magnitude, $|Z|$, and phase angle, δ , as functions of frequency on a logarithmic scale.

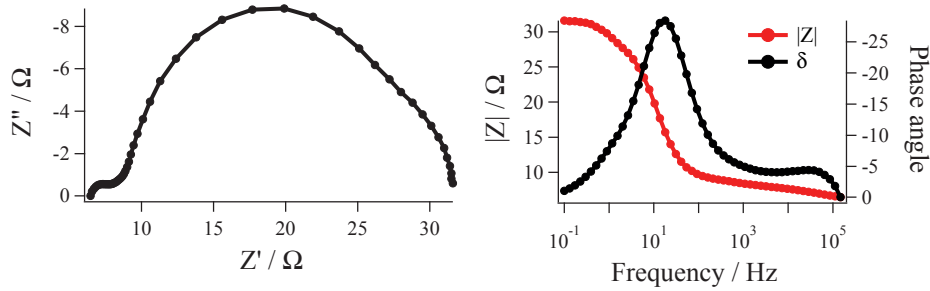


Figure 2.1 An example of a Nyquist plot (left) and Bode plots (right).

A phasor diagram nicely graphs the relationships among impedance, magnitude and phase angle (Figure 2.2).

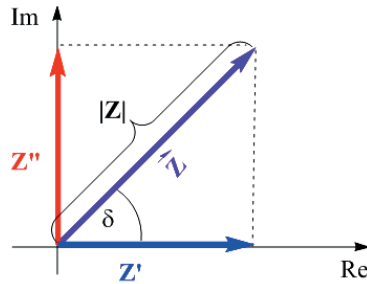


Figure 2.2 Phasor diagram showing the relationships among impedance, Z , magnitude, $|Z|$, and phase angle, δ . $Z' = |Z|\cos(\delta(\omega))$, $Z'' = |Z|\sin(\delta(\omega))$.

From Figure 2.2, the phase angle can be calculated according to Equation (2.5).

$$\delta = \arctan\left(\frac{Z''}{Z'}\right) \quad (2.5)$$

The impedance for an ohmic resistor, Z_R , is given by the resistance, R (Equation (2.6)); alternating current and voltage are in-phase ($\delta = \arctan(0) = 0$) in a pure ohmic circuit.

$$Z_R = R \quad (2.6)$$

In case of a capacitor, with a capacitance, C , the AC voltage lags the current by 90° ($\delta = \arctan(-\infty) = -90^\circ$) and the impedance, Z_C , is given by Equation (2.7).

$$Z_C = \frac{1}{i\omega C} = -i \frac{1}{\omega C} \quad (2.7)$$

2.1.2 SEMICONDUCTOR-ELECTROLYTE INTERFACE IN THE DARK AND ITS EQUIVALENT CIRCUIT

As shown in Figure 1.10, upon contact of an n-type semiconductor with an electrolyte in the dark, electrons flow from the semiconductor to the electrolyte to lower their chemical potential until equilibrium is reached ($E_F = E_{Redox}$). This results in an electron-depleted region of thickness W_{SC} (=space charge layer width) in the semiconductor near the semiconductor-electrolyte junction. The electrostatic potential, V_{SC} , in the space charge layer entails a band bending since the potential contributes a term, $-e_0V_{SC}$, to the energy.

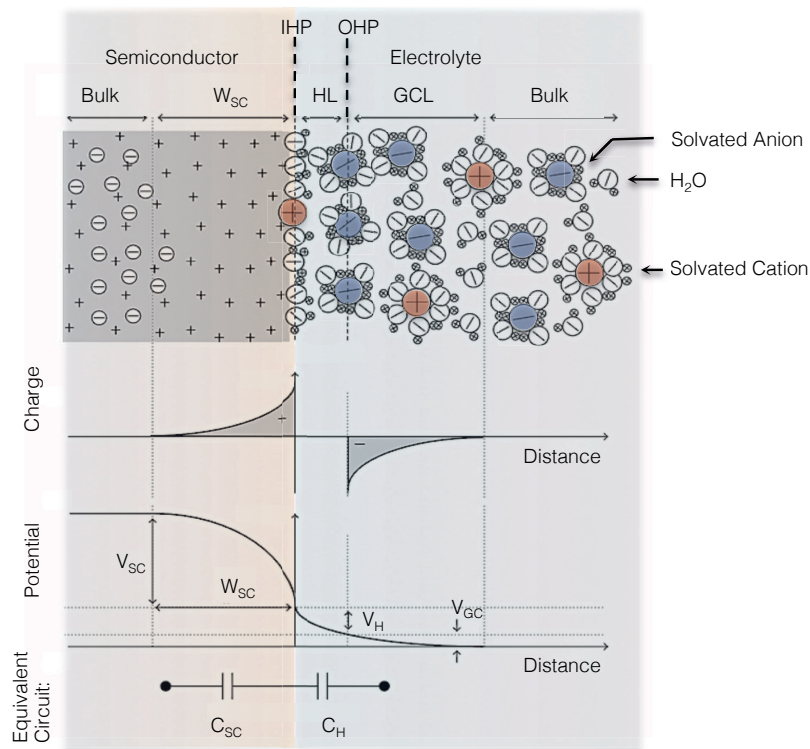


Figure 2.3 Formation of an electrical double layer at the semiconductor-electrolyte junction. Top: A schematic showing the depleted n-type semiconductor with a positively charged space-charge layer. The positive charge is balanced by solvated anions in the electrolyte at the outer Helmholtz plane (OHP) and in the Gouy-Chapman layer (GCL), both having an enriched concentration of solvated anions compared to the bulk electrolyte. Directly at the interface the solvent molecules (here H_2O) adsorb with aligned dipole moments at the semiconductor surface forming the inner Helmholtz plane (IHP). Across the Helmholtz layer (HL) and the GCL a potential drop ($V_H + V_{GC}$) is obtained. Adapted from reference ².

On the electrolyte side, the positive charge is balanced by solvated anions in the electrolyte at the outer Helmholtz plane (OHP) and in the Gouy-Chapman layer (GCL), both having an enriched concentration of negative charge compared to the bulk

electrolyte. According to this model, directly at the interface the solvent molecules (here H₂O) adsorb with aligned dipole moments at the semiconductor surface forming the inner Helmholtz plane (IHP). In solution, across the Helmholtz layer (HL) and the GCL also a small potential drop (V_H+V_{GC}) is obtained.

The equivalent circuit for this ideal capacitive system would consist of a solution resistance, $R_{Solution}$, in series with the two capacitances for each potential drop such that the sum of the capacitances is

$$\frac{1}{C_{bulk}} = \frac{1}{C_{SC}} + \frac{1}{C_H} \quad (2.8)$$

The Helmholtz capacitance is usually assumed to be much bigger than the space charge capacitance ($C_H \gg C_{SC}$) so that it becomes negligible in Equation (2.8). In parallel to the capacitances a resistance describes the charge transfer between the electrode and the electrolyte. The full equivalent circuit used for the fitting of impedance measurement data acquired for a hematite/electrolyte system is shown in Figure 2.4.

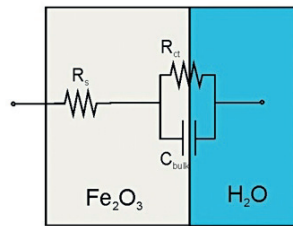


Figure 2.4 Physical schematic of the equivalent circuit for a hematite/electrolyte interface in the dark.

In the real measurement, additional to the solution resistance are all other series resistances due to e.g. cable and contact resistances contributing to the overall series resistance, R_S . For the PEC cell depicted in Chapter 5 (Figure 5.1) a typical series resistance of 25 Ω was measured.

2.1.3 MOTT-SCHOTTKY ANALYSIS

Mott-Schottky plots are widely used for the extraction of the charge carrier density, N_D , and the flat band potential, V_{Fb} , of the semiconductor. The latter allows estimating the conduction band position. The experiment is based on the fact that changing the voltage of the semiconductor artificially through the use of a potentiostat causes the

semiconductor and redox couple Fermi levels to separate, and hence the level of band bending owing to electron depletion in the semiconductor will change depending on the applied voltage. When the applied voltage is such that there is no band bending, or charge depletion (zero space charge), then the semiconductor is at its flat-band potential as shown in Figure 2.5b.

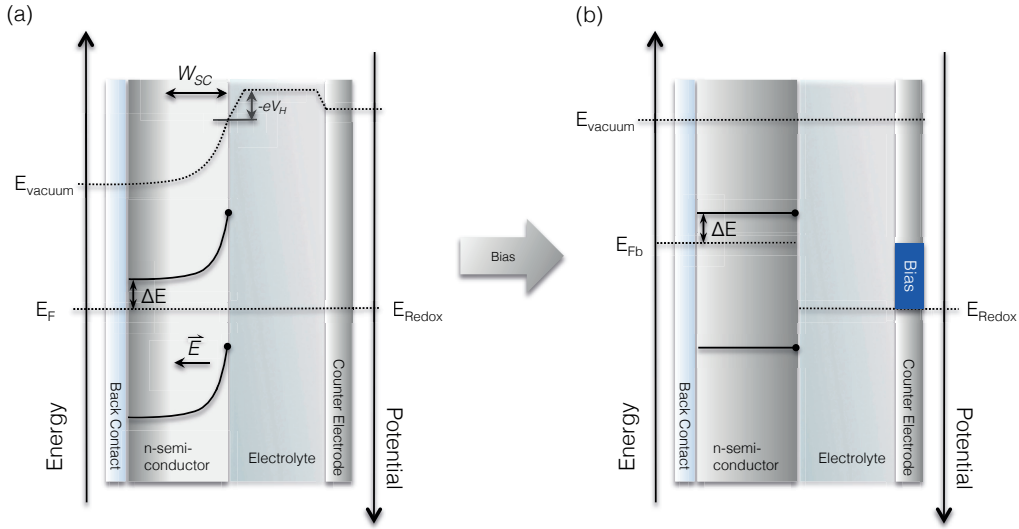


Figure 2.5 Semiconductor-liquid junction in the dark a) at equilibrium and b) upon voltage bias up to its flat band potential.

Thus, this variation in the applied voltage will significantly change the capacitance of the space charge layer and can be used for the extraction of the flat band position and the charge carrier density of the employed semiconductor according to the Mott-Schottky equation

$$\left(\frac{A_S}{C_{SC}}\right)^2 = \frac{2}{e\epsilon_r\epsilon_0 N_D} \left(V - V_{FB} - \frac{k_B T}{e}\right) \quad (2.9)$$

with C_{SC}/A_S being the surface area corrected space charge layer capacitance, ϵ_r the dielectric constant of the material and ϵ_0 the vacuum permittivity. V is the applied potential. The detailed derivation of the Mott-Schottky equation starting from the Poisson-Boltzmann equation can be found in the Appendix. In practice, impedance measurements are carried out in a broad potential range of interest and the results are fitted to the equivalent circuit shown in Figure 2.4. The fitted capacitance is plotted against the applied potential in a Mott-Schottky plot as shown in Figure 2.6. The charge density is extracted from the slope of the linear region and the flat band potential can be

calculated from the intercept at $(A_S/C_{SC})^2 = 0$.

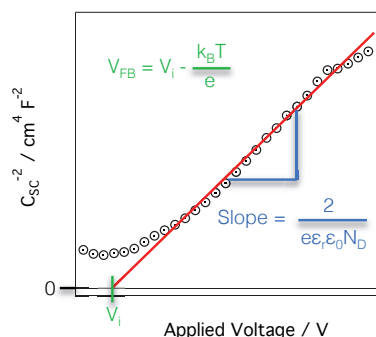


Figure 2.6 A typical Mott-Schottky plot of measured data (black circles) fitted in the linear region with a linear fit (red line) that is used for the calculation of the charge carrier density from the slope and the flat band potential from the intercept with the voltage axis at voltage V_i .

It was shown that linear Mott-Schottky plots can also be obtained when the Helmholtz capacitance is significant and hence, the Mott-Schottky equation stays valid even for highly doped materials.³

With the extracted charge carrier density and the flat band potential, the space charge layer width can be calculated according to Equation (2.10).

$$W_{SC} = \sqrt{\frac{2\epsilon_r\epsilon_0}{e_0N_D}(V_{bias} - V_{fb})} \quad (2.10)$$

2.2 ATOMIC LAYER DEPOSITION

Here, a summary of the most important characteristics of atomic layer deposition will be briefly discussed. For more profound information I recommend review articles by the group of Prof. Markku Leskelä and Prof. Steven M. George.^{4, 5 6}

2.2.1 PRINCIPLE

Atomic layer deposition (ALD) belongs to the family of vapor deposition methods and is a modification of chemical vapor deposition (CVD) where usually two reactants undergo a chemical reaction either in the gas phase or at a substrate surface. In CVD both precursors react instantly (or one precursor decomposes) once the necessary temperature for the reaction is provided, whereas in ALD the highly reactive precursors react in two

subsequent steps (half cycles) by saturating surface reactions and do not decompose. A typical ALD cycle is shown in Figure 2.7 for Al_2O_3 deposition.

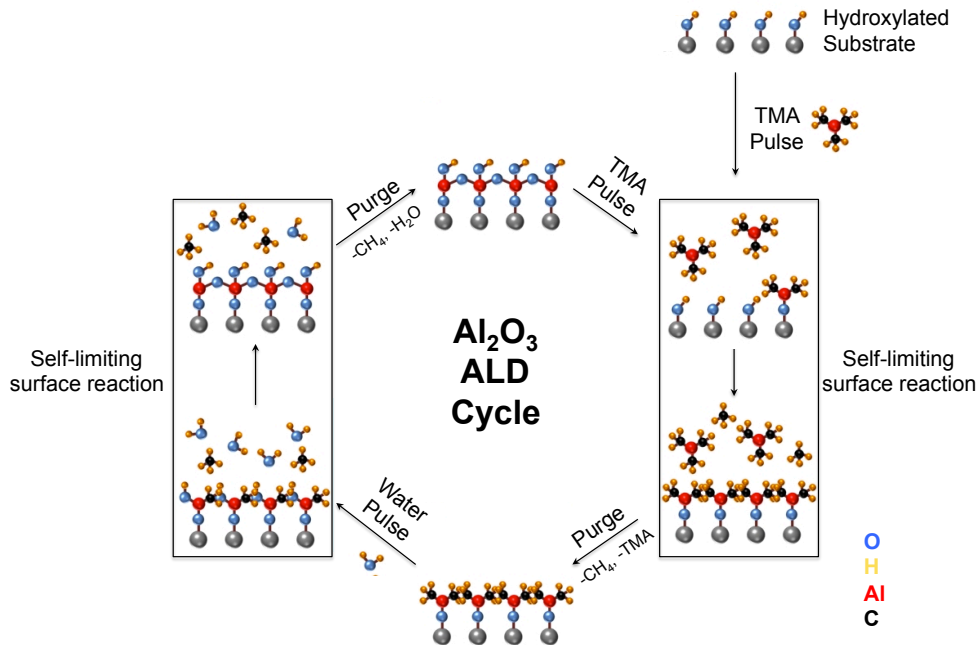


Figure 2.7 ALD deposition sequence shown on the example of Al_2O_3 formation with TMA (trimethylaluminium) and water. 1. During the metal precursor (here: TMA) pulse TMA reacts with the hydroxylated surface of a given substrate (chemisorption) in a saturating surface reaction. 2. Purging with inert gas removes the unreacted precursor (TMA) and the reaction byproducts (methane). 3. In the second half cycle during the water pulse water reacts with the surface until the reaction is saturated. 4. Another purge prepares the surface for a subsequent cycle of Al_2O_3 ALD. Repeating this cycle for a number of times leads to a layer-by-layer growth of thin films.

Through the self-limiting growth mechanism of ALD, film thickness is adjustable with atomic precision. Furthermore, since growth is surface controlled, coating porous materials of high aspect ratio with precisely the same thickness is very straightforward in ALD compared to alternative deposition methods such as sol-gel, physical vapor deposition (PVD) and CVD (Figure 2.8).

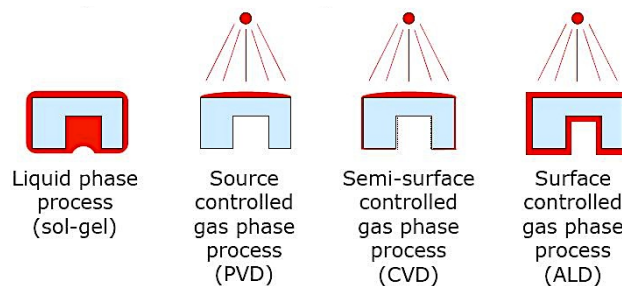


Figure 2.8 Coating thickness uniformity with different methods. Taken from reference ⁷.

It is desirable (not required though) to have a so-called “ALD window” for the deposition where the growth rate is more or less stable in a certain temperature range. In this temperature window undesirable features such as low reactivity or condensation at too low temperatures and decomposition or desorption of the precursors at too high temperatures can be avoided (Figure 2.9). However, it does not confirm the self-saturating character of the deposition, which requires monitoring the growth rate dependence on the precursor pulse length.

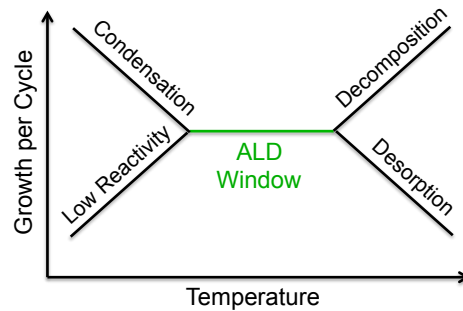


Figure 2.9 ALD temperature window.

The growth rate (commonly reported as “growth per cycle” in ALD) is rather low compared to other deposition processes including CVD. It is even lower when the actual deposition rate (thickness/time) is compared. However, this issue has been addressed in recent years and the development of a reactor, designed for sequential deposition as shown in Figure 2.10, could speed up the deposition process. For Al_2O_3 an actual deposition rate of 1.2 nm/s has been demonstrated.⁸ Beneq, which is one of the biggest ALD construction companies worldwide, followed up on this approach and has built a spatial ALD, the WCS 600, for roll-to-roll fabrication. It has a throughput of 400'000 m^2/year (calculated for a film thickness of 25 nm assuming a growth rate of roughly 1 Å/cycle).⁹

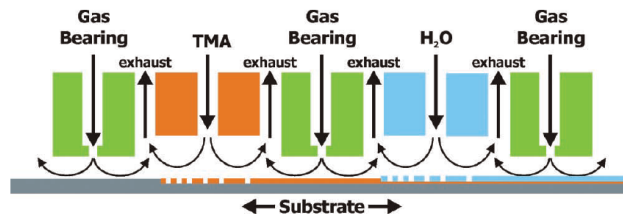


Figure 2.10 Schematic drawing of the spatial ALD reactor concept, where TMA and water half-reaction zones are separated by gas bearings. Moving the substrate underneath the reactor, the two half-reactions will take place subsequently to form an Al_2O_3 monolayer. Reprinted from reference ⁸.

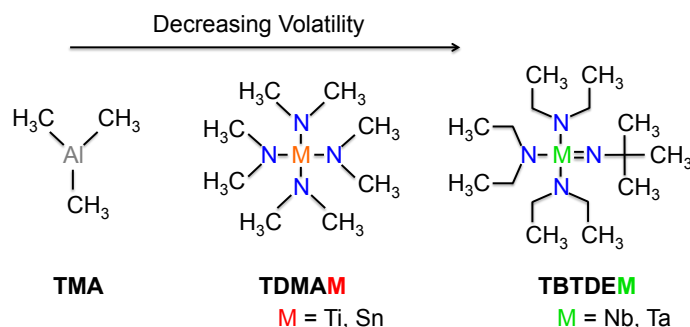
Therefore, with the spatial deposition approach and in view of the thicknesses of oxide layers of only a few tens of nanometers used in microelectronics, solar cell fabrication and water splitting, ALD absolutely represents a scalable fabrication method.

2.2.2 DEMAND ON PRECURSORS

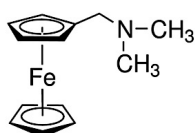
ALD is widely used for the fabrication of oxide, nitride and metal thin films but also processes for sulfides and ternary compounds have been developed.^{10,11} A recent review by Blanquart *et al.* covers the variety of precursors for thermal as well as for plasma enhanced ALD.⁶ Depending on the material to be fabricated, different hydrides are used (H_2O , H_2S , H_3N) but also oxidizers such as oxygen, hydrogen peroxide and ozone are employed for ALD of oxides.

In order to achieve reasonable deposition rates, precursors have to easily chemisorb on the substrate surface or rapidly react with the surface groups. Different metal reactants such as alkyls, halides, alkoxides, β -diketonates, cyclopentadienyls and alkyl amides are commonly employed in ALD. The precursor chemistry is the key process in ALD and the precursors can be gaseous, liquid or solid as long they are volatile enough and thermally stable. Furthermore, the byproducts from the ALD reaction have to be volatile in order to avoid physical vapor deposition of these byproducts that would contaminate the substrate surface. Trimethylaluminium (TMA) is the most studied ALD precursor mainly for two reasons: firstly, because Al_2O_3 thin films have been of interest for microelectronics since the 1970's and secondly, because TMA is highly volatile, thermally stable and forms gaseous methane as a byproduct. Hence, it represents the ideal precursor for ALD.

From my personal experience, reproducibility of the ALD process with precursors that have to be heated higher than 100 °C to attain the desired vapor pressure is sometimes difficult to maintain as thermal degradation in the precursor reservoir over the time of several depositions becomes an issue. For example, precursors such as TMA, diethylzinc and others that are volatile at room temperature, give the highest reproducibility. Also tetrakis(dimethylamino)titanium(IV) (TDMAT) and the tin equivalent TDMASn give very reliable depositions with precursor temperatures of 75 °C and 65 °C respectively. However, tris(diethylamido)(*tert*-butylimido)tantalum(V) (TBTDET) and its niobium equivalent, TBTDEN, suffer from partial degradation in the reservoir over time. Especially the volatility of TBTDET poses major challenges.



In this work I will present a low-temperature ALD process to obtain crystalline, phase-pure and photoactive hematite films that are deposited with (dimethylaminomethyl)ferrocene (DMAMFc) and ozone. More details will be given in Chapter 4.



DMAMFc

In summary Table 2.1, shows the advantages and drawbacks of ALD.

Table 2.1 Technical advantages and disadvantages of atomic layer deposition.

Advantages	Disadvantages
Precise film thickness control on the atomic scale	Low deposition rates
Film homogeneity	Dependence on the nature of the precursor so that the choice of materials for ALD is limited to precursor synthesis
Conformity	
Pinhole-free film deposition	Usually films are amorphous as-grown
Precise doping control	Expensive precursors for many materials

Though ALD was relatively recently introduced to the field of PEC water splitting, it has already enhanced research progress quite rapidly due to its precise control of the many parameters listed above. This makes it a valuable and powerful deposition technique for innovative research.

2.3 REFERENCES

1. Orazem, M. E.; Tribollet, B. *Electrochemical Impedance Spectroscopy*. Wiley: Hoboken, N.J., 2008; p xxxi, 523 p.
2. <http://www.hindawi.com/journals/apc/2011/786759/fig4/> (accessed March 03, 2016)
3. Albery, W. J.; O'Shea, G. J.; Smith, A. L. Interpretation and Use of Mott-Schottky Plots at the Semiconductor/Electrolyte Interface. *Journal of the Chemical Society, Faraday Transactions* **1996**, 92, 4083-4085.
4. Nicola Pinna, M. K. *Atomic Layer Deposition of Nanostructured Materials*. Wiley-VCH Verlag GmbH & Co. KGaA: 2012.
5. George, S. M. Atomic Layer Deposition: An Overview. *Chemical Reviews* **2010**, 110, 111-131.
6. Blanquart, T.; Niinisto, J.; Ritala, M.; Leskela, M. Atomic Layer Deposition of Groups 4 and 5 Transition Metal Oxide Thin Films: Focus on Heteroleptic Precursors. *Chemical Vapor Deposition* **2014**, 20, 189-208.
7. <http://nextbigfuture.com/2010/04/equipment-for-roll-to-roll-atomic-layer.html> (accessed March 08, 2016).
8. Poodt, P.; Lankhorst, A.; Roozeboom, F.; Spee, K.; Maas, D.; Vermeer, A. High-Speed Spatial Atomic-Layer Deposition of Aluminum Oxide Layers for Solar Cell Passivation. *Advanced Materials* **2010**, 22, 3564-+.
9. <http://www.beneq.com/wcs-600.html> (accessed March 08, 2016).
10. Bakke, J. R.; Jung, H. J.; Tanskanen, J. T.; Sinclair, R.; Bent, S. F. Atomic Layer Deposition of Cds Films. *Chemistry of Materials* **2010**, 22, 4669-4678.
11. Chong, Y. T.; Yau, E. M. Y.; Nielsch, K.; Bachmann, J. Direct Atomic Layer Deposition of Ternary Ferrites with Various Magnetic Properties. *Chemistry of Materials* **2010**, 22, 6506-6508.

3 UNDERSTANDING THE ROLE OF UNDERLAYERS AND OVERLAYERS IN THIN FILM HEMATITE PHOTOANODES

This chapter is adapted from a peer-reviewed article by Ludmilla Steier, Isaac Herraiz-Cardona, Sixto Gimenez, Francisco Fabregat-Santiago, Juan Bisquert, S. David Tilley and Michael Grätzel published 2014 in Advanced Functional Materials.¹

Recent research on photoanodes for photoelectrochemical water splitting has introduced the concept of under- and overlayers for the *activation* of ultrathin hematite films. Their effects on the photocatalytic behavior were clearly shown, however, the mechanism is thus far not fully understood. Herein, I analyze the contribution of each layer by means of electrochemical impedance spectroscopy, with the aim of obtaining a general understanding of surface and interface modifications and their influence on the hematite photoanode performance. This broad study shows that doping of hematite from the underlayer, surface passivation from annealing treatments and an overlayer are key parameters to consider for the design of more efficient iron oxide electrodes. Understanding the contribution of these layers enables a new design for ultrathin photoactive hematite films. Employing a combination of a gallium oxide overlayer with either niobium oxide or silicon oxide thin film underlayers is shown to achieve greatly improved photocurrent onset potentials for the photoelectrochemical oxidation of water using Co-Pi as a water oxidation catalyst. By better understanding the underlying principles of over- and underlayers, I was able to design multilayered hematite photoanodes comprised of functional thin films to obtain a significant reduction in water oxidation overpotential, such that less voltage bias is needed to drive the reaction. These encouraging results bode well for improving the efficiency of photoelectrochemical tandem cells as shown in Figure 1.4.

3.1 INTRODUCTION

3.1.1 THIN FILM HEMATITE AND THE USE OF FUNCTIONAL LAYERS

Considering the mandatory criteria of a photoanode material for PEC water splitting—such as a suitable band gap for the absorption of visible light, excellent aqueous stability, natural abundance of the constituent elements, low cost and non-toxicity, hematite (α - Fe_2O_3) is a very attractive candidate. However, for water splitting to occur efficiently with hematite, several processes must be addressed: facilitating majority charge carrier (electron) conduction to the back contact, improving charge transfer of photogenerated holes at the semiconductor-liquid junction (SCLJ), and passivating surface states, which act to diminish the photovoltage delivered by the hematite through surface recombination and/or band edge unpinning.^{2, 3} Due to the disaccord between hematite's short hole diffusion length (2 - 4 nm)⁴ and its two orders of magnitude larger absorption length, it is desirable to use films of a few nanometer thickness to allow for the photogenerated holes to reach the SCLJ before recombining with electrons. In order to provide a high surface area for efficient light harvesting even with very thin absorber films, nanostructuring approaches have been applied to either the semiconductor itself⁵⁻⁷ or to a host scaffold covered by the α - Fe_2O_3 guest absorber.⁸⁻¹⁰

So far, the successful realization of the host-guest approach is hampered by the low photo-activity of thin hematite layers in contact with the supporting electrode surface.⁸ Ultrathin hematite films prepared by different techniques like ultrasonic spray pyrolysis (USP), atmospheric pressure chemical vapor deposition (APCVD) and atomic layer deposition (ALD) on a F:SnO₂ (FTO) glass electrode have served as a model system to further investigate the carrier dynamics of hematite in contact with an aqueous electrolyte.¹¹⁻¹⁴ Particularly, regarding ALD hematite, the importance of surface states governing the charge transfer kinetics for water photo-oxidation has been recognized. A physical model of Fe_2O_3 explicitly including charge transfer through a surface state has successfully explained the mechanism of water photo-oxidation in this system.^{13, 15} Similar results have been obtained with APCVD hematite.^{16, 17} This information is essential to investigate and ameliorate the design of interfaces. Previous studies have shown that in the presence of underlayers such as SiO_x,¹⁸ TiO₂ and Nb₂O₅¹⁹ as well as

SnO_2 ²⁰ or Ga_2O_3 ²¹, the photo-activity of thin hematite photoanodes was increased. On the other hand, focusing on the semiconductor/electrolyte interface, catalysts such as Co-Pi²² and IrO_2 ^{16, 23} as well as functional overlayers such as Al_2O_3 , Ga_2O_3 and In_2O_3 were shown to succeed in shifting the onset to more negative potentials.^{24, 25} This improvement in the photocurrent onset potential is a key aspect to enable unassisted water splitting using tandem configurations²⁶ and therefore it is crucial to understand its nature. The function of overlayers for hematite photoanodes has been extensively debated^{22, 25, 27} and it was recently suggested that the role of these layers lies in the extension of the space charge region by surface state passivation rather than in surface catalysis.²¹

Herein I aim at further elucidating the effect of performance-enhancing underlayers and overlayers by a mechanistic study using electrochemical impedance spectroscopy (EIS) and physical modeling. I focus on thin hematite films employing a SiO_x or an Nb_2O_5 underlayer and a Ga_2O_3 overlayer prepared by spray pyrolysis, atomic layer deposition and chemical bath deposition, respectively.^{18, 19, 24} It is shown that the combination of the underlayers with a Ga_2O_3 overlayer yields a favorable shift in photocurrent onset potential towards 0.8 V versus the reversible hydrogen electrode (RHE), indicating an increase in the photovoltage that can be extracted from iron oxide for water oxidation. Furthermore, I apply Co-Pi as a water oxidation catalyst to further reduce the overpotential for water oxidation approaching the flat band potential of hematite.

3.1.2 ELECTROCHEMICAL IMPEDANCE SPECTROSCOPY FOR PEC WATER SPLITTING WITH PHOTOANODES

The physical model employed is conveyed by the equivalent circuit shown in Figure 3.1a and was detailed in previous studies.^{13, 15} Under illumination, the circuit consists of a capacitance of the bulk hematite, C_{bulk} , in parallel with a resistance related to the rate of trapping holes in surface states, R_{trap} , and a RC unit consisting of a charge transfer resistance from the surface states, $R_{\text{ct,trap}}$, in parallel with a capacitance of the surface states, C_{trap} . In all the samples tested in the present study, the photocurrent onset is coincident with the peak of the surface state capacitance and a valley for the charge transfer resistance from this surface state, $R_{\text{ct,trap}}$. As an illustrative example, Figure 3.1c shows the results for an USP Fe_2O_3 sample. This behavior clearly indicates that efficient hole transfer depends on surface states in USP hematite.

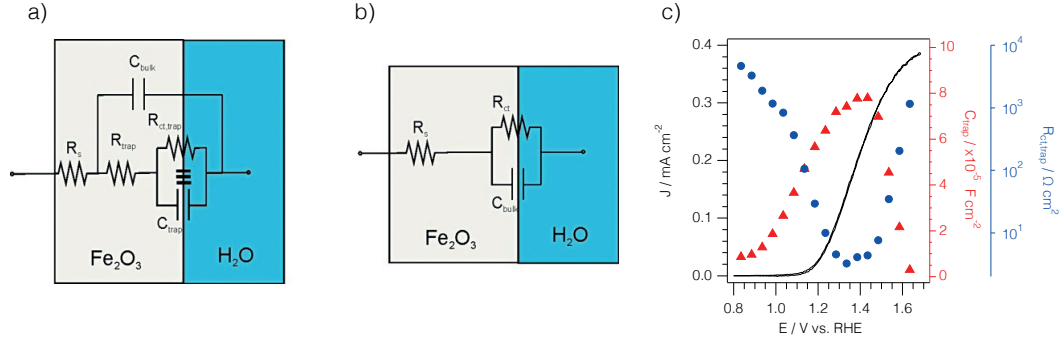


Figure 3.1 Physical equivalent circuit model employed under illumination (a) and in the dark (b) for photoelectrochemical water splitting with hematite. (c) Representative plot of a USP Fe_2O_3 photoanode showing that the photocurrent onset is coincident with the C_{trap} peak and the $R_{\text{ct,trap}}$ valley. This behavior has been systematically observed for all the samples analyzed in the present study.

The trap capacitance, C_{trap} , was extracted by fitting the experimental impedance spectra under illumination to the physical model detailed in Figure 3.1a using Constant Phase Elements (CPE) accounting for the non-ideal behavior of the capacitance. The impedance of the CPE can be written as:

$$Z = \frac{1}{Q (i\omega)^n} \quad (3.1)$$

In order to extract the trap capacitance, the Brug equation²⁸ was used:

$$C_{\text{trap}} = \left[\frac{Q}{((R_s + R_{\text{trap}})^{-1} + R_{\text{ct,trap}}^{-1})^{1-n}} \right]^{1/n} \quad (3.2)$$

In the dark, the surface state is not identified and the equivalent circuit employed consists of a simple RC circuit (Figure 3.1b) used for the Mott–Schottky (MS) analysis herein. As described in Section 2.1.3, plotting the surface area corrected space charge capacitance, $\left(\frac{C_{\text{bulk}}}{A_S}\right)$, versus the applied potential, V , according to Equation (2.9), the flat band potential, V_{FB} , as well as the charge carrier density, N_D , can be extracted from a linear fit of the linear region in a MS plot. Here, a dielectric constant of hematite of 32 was used as reported earlier.^{15, 29}

With the extracted charge carrier density and the flat band potential, the space charge layer width can be calculated according to Equation (2.10).

3.2 EXPERIMENTAL

3.2.1 SUBSTRATE CLEANING

All samples were prepared on high temperature resistant alumino-borosilicate glass coated with fluorine-doped tin oxide (FTO) serving as a transparent conducting oxide ($10 \times 10 \text{ cm}^2$, 10Ω , Solaronix, cut into $1.25 \text{ cm} \times 3.4 \text{ cm}$ substrates). The substrates were cleaned by successive ultra-sonication for 15 min with acetone, soap, water and 2-propanol as previously reported.¹⁸

3.2.2 DEPOSITION OF UNDERLAYERS

2 nm thick Nb_2O_5 , Ga_2O_3 and Al_2O_3 layers were deposited on the FTO by atomic layer deposition using a Savannah 100 instrument (Cambridge Nanotechnology). For Nb_2O_5 , (tert-butylimido)tris(diethylamino)niobium (TBTDEN, Digital Specialty Chemicals, 99.8%) and bidistilled water (AppliChem) were pulsed into a nitrogen flow (20 sccm, Carbagas, 99.9999% purity) at $150 \text{ }^\circ\text{C}$ with exposure times of 10 s, resulting in a growth rate of 0.56 \AA/cycle , estimated from ellipsometry measurements on a Si-wafer. Ga_2O_3 , was deposited using tris(dimethylamido)gallium(III) (98%, Aldrich) held at $130 \text{ }^\circ\text{C}$ and bidistilled water held at room temperature. The precursors were pulsed into a nitrogen flow of 10 sccm and exposed for 30 s to the FTO heated to $150 \text{ }^\circ\text{C}$. The growth rate of the Ga_2O_3 layer was estimated to be 1 \AA/cycle on a Si-wafer by ellipsometry. For Al_2O_3 , trimethylaluminium and water were pulsed into a nitrogen flow of 10 sccm and exposed for 30 s to the FTO heated to $150 \text{ }^\circ\text{C}$. The growth rate of the Al_2O_3 layer was estimated to be 1.7 \AA/cycle on a Si-wafer.

A silicon oxide underlayer was deposited at a surface temperature of $370 \text{ }^\circ\text{C}$ by spray pyrolysis (2 ml/sample of a 10 Vol.-% tetraethoxysilane (99.999%, Aldrich) solution in ethanol (99.9%, Fluka)).

3.2.3 USP OF IRON OXIDE

Iron oxide was deposited on cleaned FTO (or FTO coated by the underlayer) by ultrasonic spray pyrolysis (USP) at a surface temperature of $415 \text{ }^\circ\text{C}$ (10 mM $\text{Fe}(\text{acac})_3$ (99.9%) solution; 1 ml every 30 s, 12 ml/min). After deposition was complete, the

samples were held at 415 °C for 1 min prior to cooling down to room temperature. Annealed samples were heated in air or argon to 500 °C for 2 h with a heating and cooling rate of 10 °C/min.

3.2.4 OVERLAYER DEPOSITION

A gallium oxide layer was deposited by chemical bath deposition (CBD) (10 mM $\text{Ga}(\text{NO}_3)_3 \times x \text{H}_2\text{O}$ ($x = 6, 9$), 1 M Urea, 78 - 83 °C). 15 minutes after Urea addition the samples were rinsed with distilled water and annealed in air at 550 °C for 1 h together with their control samples (without Ga_2O_3).

ALD of Ga_2O_3 was performed under the same conditions as the Ga_2O_3 for the underlayer.

3.2.5 CATALYST DEPOSITION

Co-Pi was photo-electrodeposited under AM 1.5G simulated sunlight at 0.4 V vs. Ag/AgCl, KCl (sat'd) for 1000 s in a Co^{2+} enriched phosphate buffer solution (0.5 mM $\text{Co}(\text{NO}_3)_2 \times 6 \text{H}_2\text{O}$ in 0.1 M potassium phosphate buffer, pH 7).

3.2.6 PHOTOCURRENT-VOLTAGE MEASUREMENTS

Photocurrent measurements were performed in 1 M NaOH aqueous solution (pH 13.6) using a three-electrode configuration, with a Pt wire counter electrode and an Ag/AgCl, KCl (sat'd) reference electrode. Simulated sunlight was generated from a 450 W xenon lamp (Osram, ozone free) passed through a KG3 filter (3 mm, Schott) with a measured intensity equivalent to standard AM 1.5G sunlight (100 mWcm^{-2} , spectrally corrected) at the sample face masked to 0.5 cm^2 . Without a catalyst, the potential was swept in positive direction at a scan rate of 20 mV s^{-1} (after it was proven that the sweeps did not differ from scans at lower scan rates). In the presence of Co-Pi, cyclic voltammograms were taken at a scan rate of 1 mV/s. Higher scan rates showed capacitive behavior (and a more negative potential onset due to the capacitive current).

3.2.7 IMPEDANCE MEASUREMENTS

Impedance measurements for Mott-Schottky analysis were carried out in the dark with the same three-electrode cell in 1 M NaOH solution. Full impedance spectra were measured with a SP-300 (BioLogic Science Instruments) at frequencies from 1 MHz to 0.1 Hz with a sinusoidal potential perturbation of 25 mV. The range of the bias potential was equal to that of the photocurrent measurements (0.6 – 1.7 V vs. RHE). The capacitance was extracted from the fit to the equivalent circuit shown in Figure 3.3b using Zview (Scribner Associates).

Impedance spectra under illumination were acquired with a FRA equipped PGSTAT-30 potentiostat from Autolab. The electrodes were illuminated using a 300 W Xe lamp, where the light intensity was adjusted with a thermopile to 100 mW cm⁻². EIS measurements were carried out by applying a 20 mV AC signal and scanning in a frequency range between 100 kHz and 50 mHz, at different applied bias.

All potentials have been referenced to the reversible hydrogen electrode (RHE):

$$V_{\text{RHE}} = V_{\text{Ag/AgCl}} + 0.197 \text{ V} + 0.059 \text{ V} \cdot \text{pH}.$$

3.2.8 X-RAY PHOTOELECTRON SPECTROSCOPY

X-ray photoelectron spectroscopy (XPS) data were collected by Axis Ultra (Kratos analytical, Manchester, UK) under ultra-high vacuum condition (<10⁻⁸ Torr), using a monochromatic Al K_α X-ray source (1486.6 eV), in the laboratory of Chemical Metallurgy at EPFL. The source power was maintained at 150 W (10 mA, 15 kV). The emitted photoelectrons were sampled from a square area of 750×350 μm. Gold (Au 4f_{7/2}) and copper (Cu 2p_{3/2}) lines at 84.0 eV and 932.6 eV, respectively, were used for calibration, and the adventitious carbon 1s peak at 285 eV as an internal standard to compensate for any charging effects.

3.2.9 SCANNING ELECTRON MICROSCOPY

Scanning electron microscopy (SEM) secondary electron images were acquired with a Merlin microscope (Zeiss).

3.3 RESULTS

I first focus on the electrochemical contribution of the SiO_x or the Nb_2O_5 underlayers to the activation of hematite photoanodes before exploring the role of the Ga_2O_3 overlayer.

3.3.1 ROLE OF THE UNDERLAYER IN HEMATITE THIN FILM PHOTOANODES

Figure 3.2 shows typical current density–voltage (J – V) curves and their corresponding MS plots of as prepared (a-b) and air-annealed (c-d) thin hematite films employing Nb_2O_5 , SiO_x or no underlayer.

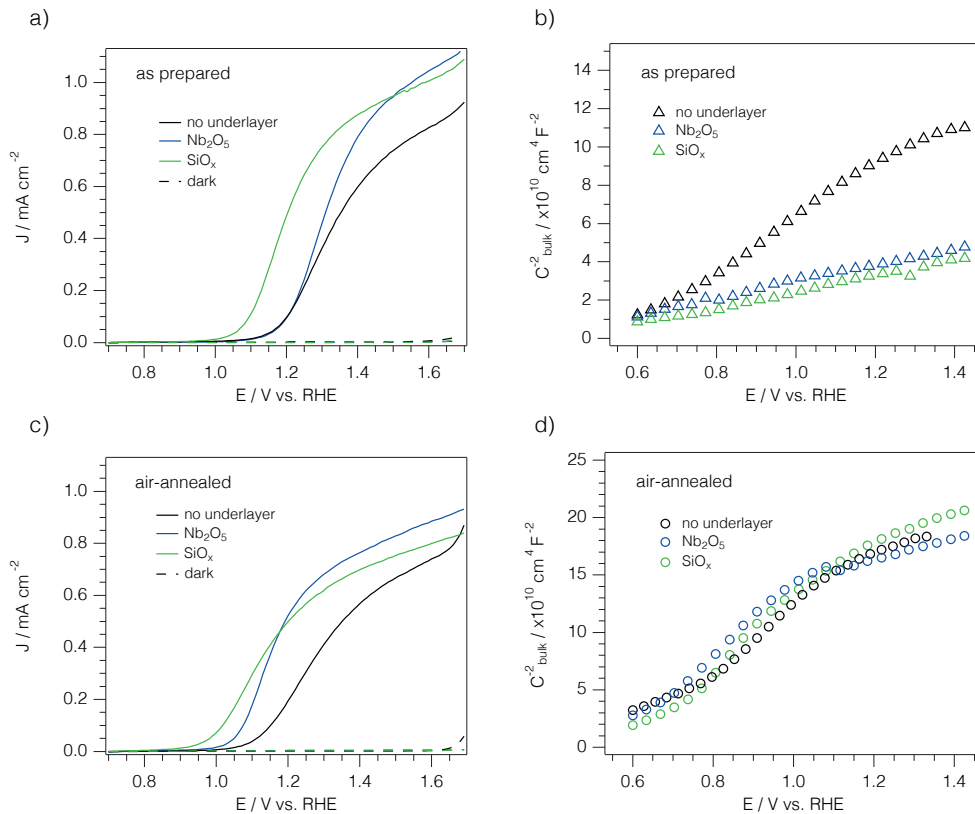


Figure 3.2 Current Density–Voltage curves (left) and Mott–Schottky measurements (right) of hematite photoanodes employing an Nb_2O_5 (blue), a SiO_x (green) or no underlayer (black) compared in an “as prepared” state (a-b) and after 2 h of annealing in air at 500 °C (c-d). J – V measurements were obtained in the dark (dashed lines) and under AM 1.5G simulated solar illumination (100 mW cm^{-2} , solid lines). The corresponding MS measurements were carried out in the dark. The electrolyte was 1 M NaOH (pH 13.6).

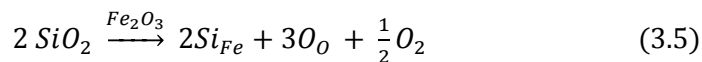
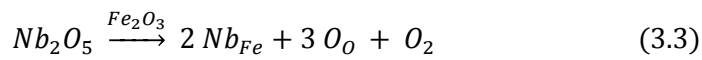
Due to space charge layer limitations, these samples were chosen to be thicker for EIS

measurements (approximately 30 nm) and therefore the enhancement of photoactivity due to the employed underlayer compared to ultrathin hematite films (where these underlayers revive the photoelectrical performance of the photoanodes) is less dramatic.^{18, 19} The photocurrent plateau is remarkably higher for the underlayer treated hematite samples and has been attributed to a change in film morphology in the case of a SiO_x underlayer¹⁸ and to a hole blocking effect in the case of the Nb₂O₅ underlayer.¹⁹ In addition to these observations, here, I find a doping contribution from these underlayers (obtained from MS analysis). Representative results of the MS analysis based on at least 3 samples of each kind are summarized in Table 3.1.

Table 3.1 Representative results for flat band potential, E_{FB} , charge carrier concentration, N_D , and space charge width, W_{SC} (at 1.23 V), from EIS measurements in the dark. Sample thicknesses varied between approximately 19 nm or 30 nm but W_{SC} did not exceed film thickness.

		no underlayer	Nb ₂ O ₅ underlayer	SiO _x underlayer
As-prepared	E_{FB} / V vs. RHE	0.60	0.45	0.46
	N_D / 10 ¹⁹ cm ⁻³	3.00	6.53	7.27
	W_{SC} / nm	8.63	6.50	6.14
Air-annealed	E_{FB} / V vs. RHE	0.51	0.54	0.60
	N_D / 10 ¹⁹ cm ⁻³	1.31	1.27	1.22
	W_{SC} / nm	13.9	13.8	13.6
Ar-annealed	E_{FB} / V vs. RHE	0.25	0.32	
	N_D / 10 ¹⁹ cm ⁻³	4.50	8.70	
	W_{SC} / nm	8.78	6.08	

It is also directly visible from the slope of the MS plots shown in Figure 3.2b that the SiO_x and the Nb₂O₅ layers have a higher charge carrier density and serve as doping agents for hematite according to the following proposed defect mechanisms:



Charge carrier concentrations increase by a factor of 2 when an underlayer is present ($N_D \approx 7 \cdot 10^{19}$ cm⁻³). Ultrathin hematite films (approximately 10-15 nm) employing these

underlayers also measured in the context of this work even show a three times higher donor density ($N_D \approx 2.0 \cdot 10^{20} \text{ cm}^{-3}$), which can be attributed to gradient doping from the underlayer with a stronger doped region near the underlayer. XPS measurements confirmed the presence of the dopant atoms at the hematite surface in thicker (>30 nm) samples, where the underlying substrate is not seen (Figure 3.3).

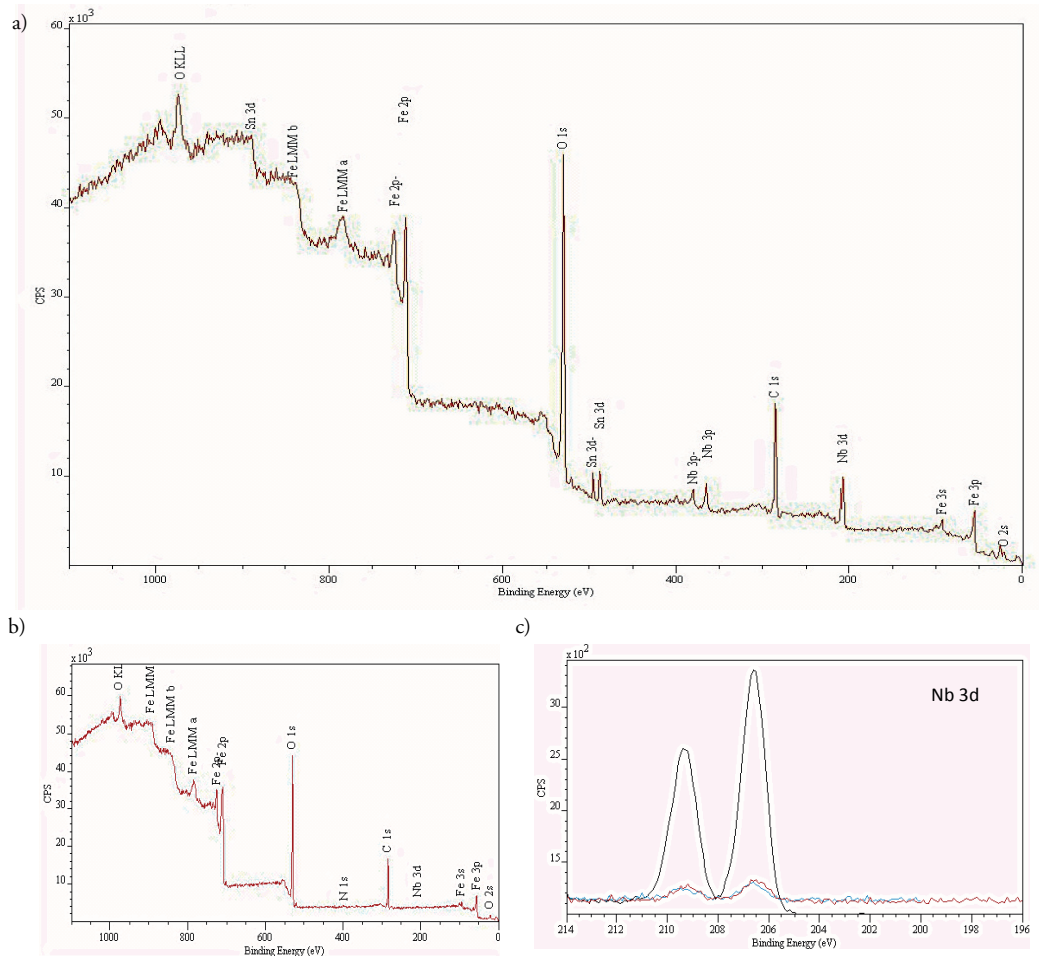


Figure 3.3 a) X-ray Photoelectron spectrum of thin (<10 nm) hematite films deposited on Nb_2O_5 (2 nm thick) coated F:SnO_2 (borosilicate glass). b) X-ray Photoelectron spectrum of a thick (>30 nm) hematite photoanode. c) Comparison of the Nb 3d doublets detected in the thin (black) and the thick hematite photoanode before (light blue) and after annealing (red).

The increase in electron density in doped hematite films is correlated with an increase in the photocurrent plateaus (Figure 3.2a). The calculated space charge layer width, W_{SC} , (Equation (2.10)) is several nanometers shorter for the Nb- and Si-doped samples than for the samples without an underlayer (Figure 3.4). Thus, the higher photocurrents can be explained by a stronger band bending in the surface region of the film, and therefore

improved charge separation in the space charge layer, which leads to reduced recombination at the hematite surface.

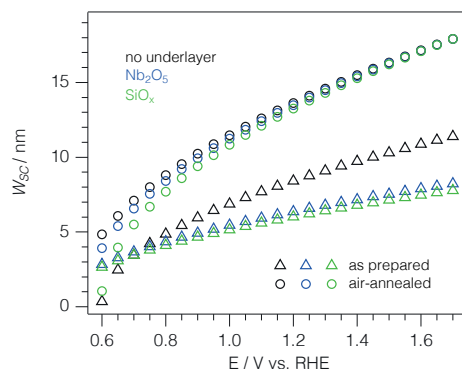


Figure 3.4 Calculated space charge layer width versus applied potential for as prepared (filled triangles) and air-annealed samples (hollow circles) employing an Nb_2O_5 (blue), a SiO_x (green) or no underlayer (black). Flat band potential and charge carrier density data was taken from Table 3.1.

The contribution of the doping effect is especially visible in ultrathin hematite photoanodes while the influence on film morphology and/or surface state passivation³⁰ becomes predominant in thicker hematite films if the doping level is sufficiently high to allow for high conductivity. Figure 3.5a shows the influence of the Nb_2O_5 underlayer compared to Al_2O_3 and Ga_2O_3 underlayers (all underlayers 2 nm thick) on the J–V performance of approximately 10 nm hematite photoanodes. It is observed that the underlayers with a 3-valent cation (Al^{3+} and Ga^{3+}) improve slightly the photocurrent of the completely inactive hematite anode (black) most likely due to their influence on the uniformity of the grown hematite film. However, Nb_2O_5 clearly revives the hematite electrode of the same thickness due to its doping effect. The thickness is confirmed by absorbance measurements in Figure 3.5b. With USP as deposition technique, it cannot be excluded that Nb_2O_5 also has a morphological influence on the hematite film formation, though it is not the predominant effect in thin films. It is likely that the “dead-layer-effect” is overcome for Nb_2O_5 due to the introduction of band bending in the ultrathin (10 nm) hematite layer. For thicker hematite films of approximately 30 nm thickness, which exceed the thickness where the so-called “dead layer effect” is seen, the Ga_2O_3 underlayer shows a more negative onset potential than the Nb_2O_5 underlayer while maintaining the same photocurrent plateau (Figure 3.5c).

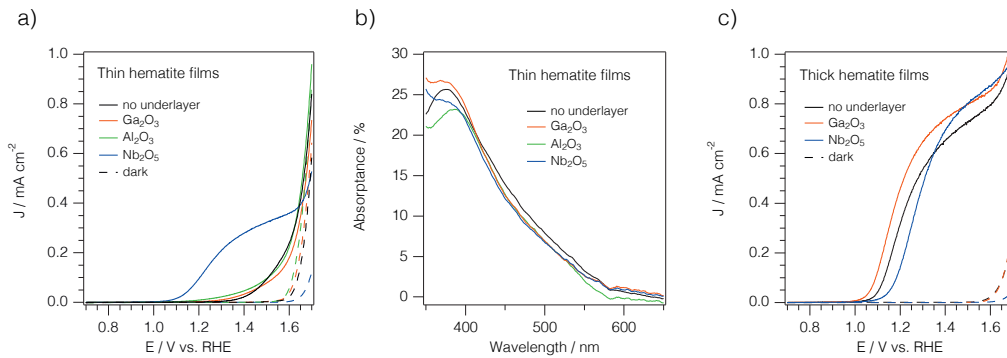


Figure 3.5 J–V performance of ultrathin hematite anodes (approximately 10 nm) employing a Ga₂O₃ (orange), Al₂O₃ (green) and Nb₂O₅ (blue) or no underlayer (black) and b) their corresponding absorbance spectra. C) J–V measurements of equivalent thicker hematite anodes (approximately 30 nm). J–V measurements were obtained in the dark (dashed lines) and under AM 1.5G simulated solar illumination (100 mWcm⁻², solid lines). The electrolyte was 1 M NaOH (pH 13.6).

This phenomenon points to a surface state passivation effect that is dominating the onset potential,³⁰ and is consistent with the results obtained in Figure 3.2c where the Nb₂O₅ treated film improves its photocurrent onset potential after air-annealing, but suffers from a decreased photocurrent plateau due to a decreased conductivity (Figure 3.2d). The same effect is observed for the SiO_x underlayer (compare Figure 3.2a and c). The effect of annealing on surface state passivation is further analyzed in the context of our Ga₂O₃ overlayer.

The extracted charge carrier density from the MS plots takes both doping effects into account: the n-doping from the oxide underlayers (when present) as well as the n-doping of hematite by oxygen vacancies. The latter's influence on the doping level is visible in annealing experiments performed in air (bottom part of Figure 3.2). Figure 3.2d shows that all three samples suffer from a severe decrease in doping density and equilibrate around practically the same value of $N_D \approx 1.3 \cdot 10^{19} \text{ cm}^{-3}$. Again, the decrease in charge carrier density and the increase in the space charge layer width correlate with a lower plateau current (200 $\mu\text{A cm}^{-2}$ decrease for the samples employing an underlayer and 100 $\mu\text{A cm}^{-2}$ decrease for the standard hematite, Figure 3.2c). I hypothesized that the decrease in charge carrier concentration was due to filling of oxygen vacancies by oxygen during the air-annealing process. I therefore carried out annealing experiments under argon atmosphere. Indeed, the data shown in Figure 3.6 demonstrate oxygen-dependent photoanode behavior. In contrast to the air-annealed hematite samples where the charge carrier concentration and photocurrent plateau are decreased, annealing in argon

atmosphere results in a higher carrier concentration as seen in the MS plots for samples both without and with extrinsic doping from an underlayer (Figure 3.6b and (d) respectively).

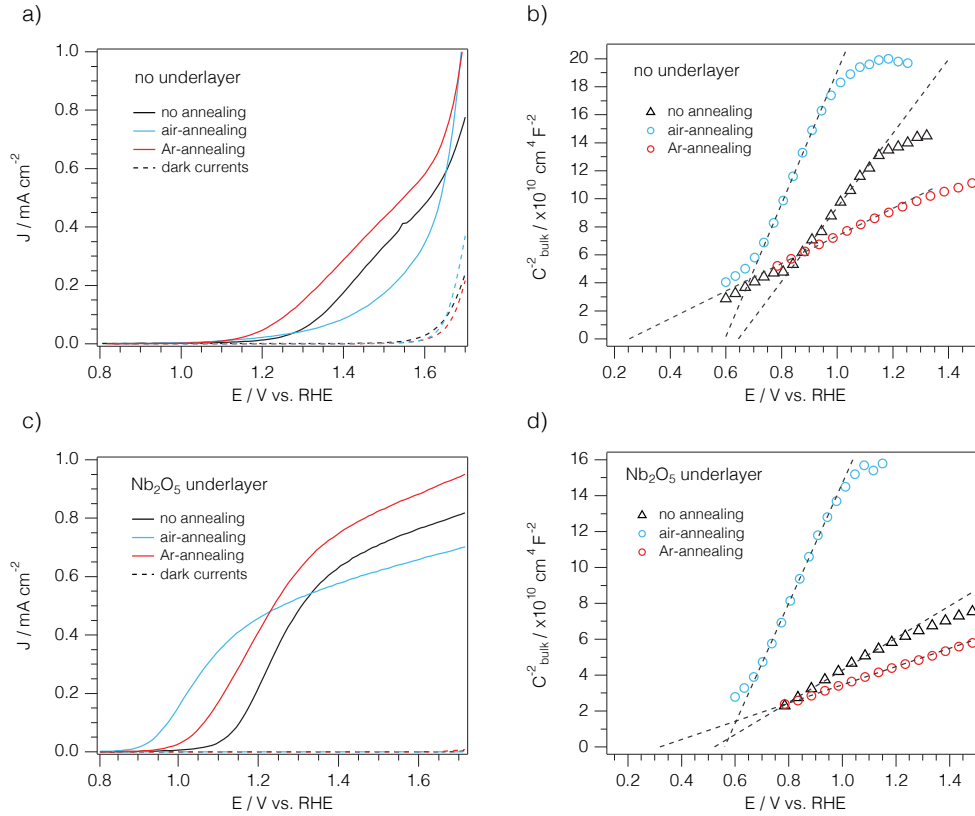
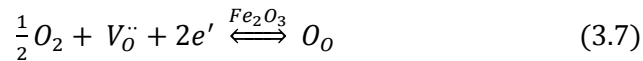


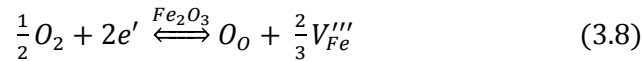
Figure 3.6 J–V curves (left) and MS measurements (right) of thin hematite photoanodes employing no underlayer (a-b) or a 2 nm Nb₂O₅ underlayer (c-d) measured after annealing in air (light blue) or in argon (red) and compared to the as prepared samples (black) of approximately 19 nm thick. Photocurrent was measured under AM 1.5G simulated solar illumination (100 mWcm⁻²). Dark current measurements are shown in dashed lines ((a) and (c)). MS measurements were carried out in the dark. The electrolyte was 1 M NaOH (pH 13.6).

In the case of a hematite film without any foreign dopant, this behavior can be explained by the defect equilibrium formed by oxygen vacancies, ($V_{O}^{\bullet\bullet}$) (Equation (3.7)). The degree of doping by oxygen vacancies in hematite is known to be dependent on oxygen partial pressure according to $n_c \propto p_{O_2}^{-\frac{1}{6}}$ resulting from applying the mass action law on the following equilibrium equation:



The annealing in argon therefore forms additional oxygen vacancies due to the reduced oxygen partial pressure, while annealing in air fills the vacancies that are normally present. Comparing the resulting J–V curves with the results obtained from MS analysis, the same correlation is observed in the sense that the more highly doped film in the case of argon annealing shows a higher photocurrent plateau compared to the non-annealed and air-annealed samples. However, it seems that the oxygen vacancies are a mixed blessing in the sense that they increase the plateau current but increase the voltage onset for photo-oxidation of water as well.

In the case of Nb- or Si-doped hematite the defect equilibrium during annealing in air involves formation of cation vacancies according to Equation (3.8):



During the annealing process in air, oxygen can be incorporated as O^{2-} in the hematite lattice (O_O). The excess oxygen in the lattice created in this manner is then compensated by cation vacancies, (V_{Fe}'''), according to Equation (3.8). Cation vacancies are surrounded by anions and therefore are strong recombination centers for holes resulting in lower photocurrents in the J–V measurements (Figure 3.6c). In the case of annealing in oxygen-free atmosphere at temperatures that allow ion mobility, the hematite film is further doped from the underlayer, as this doping is sensitive to the oxygen partial pressure (Equations (3.3)–(3.6)). Hence, the increase in charge carrier concentration after annealing in argon atmosphere (red circles in Figure 3.6d) is resulting from additional electronic doping from the underlayer. These results show the tunable intrinsic doping level of hematite to be kept in mind for the preparation of standardized hematite thin films prepared by different deposition techniques.

3.3.2 ROLE OF GALLIUM OXIDE OVERLAYER IN HEMATITE THIN FILM PHOTOANODES

In the following I aimed at further improving the photocurrent onset potential and chose Ga_2O_3 as an abundant material previously reported to give a *remarkable* shift towards more negative potentials.²⁴ Ga_2O_3 was deposited as an overlayer onto the annealed samples by chemical bath deposition (CBD) as well as by atomic layer deposition (ALD) followed by annealing in air (as post-annealing in argon deteriorated the anode

performance and no annealing induced resistive photocurrent curves). The morphology of Ga_2O_3 overlayers is shown in Figure 3.7a,b,e.

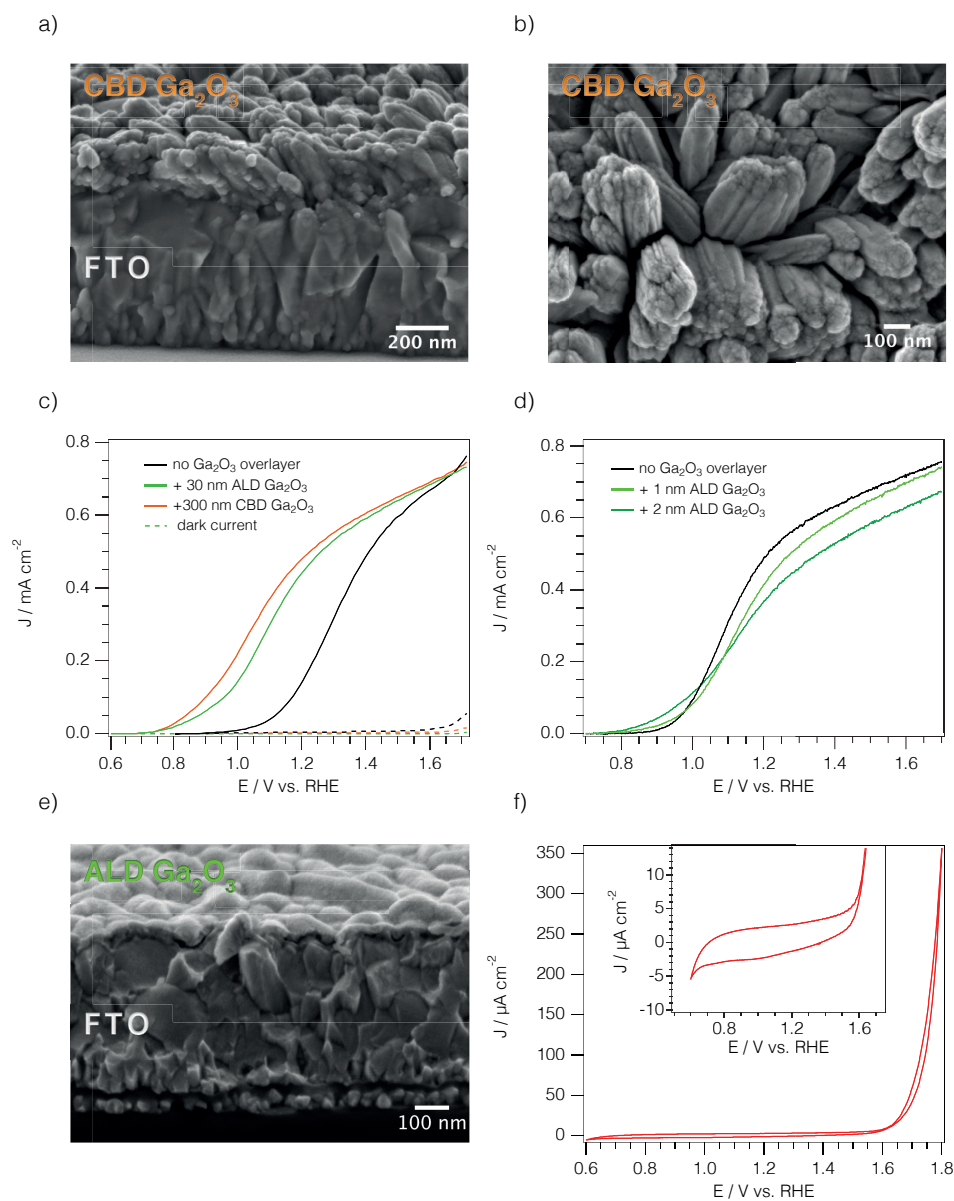


Figure 3.7 (a) Cross-sectional and (b) top-view SEM images of the CBD Ga_2O_3 structure on a (barely visible) ultrathin (approximately 16 nm) hematite layer deposited on FTO glass. c) J-V curves of Nb-doped hematite photoanodes employing no overlayer (black), a CBD Ga_2O_3 overlayer (orange) or a 30 nm thick ALD Ga_2O_3 (light green). d) J-V comparison with very thin films of ALD Ga_2O_3 . e) Cross-sectional SEM of a USP thin film hematite photoanode coated with 30 nm Ga_2O_3 by ALD. f) Cyclic voltammogram (CV) under light chopping of a CBD Ga_2O_3 film on Tec15 glass. The inset shows a magnification of the same CV. Neither a catalytic nor a photocatalytic effect is seen. All samples were heated to 550 °C after Ga_2O_3 deposition together with the control sample without any underlayer and measured under AM 1.5G solar irradiation (100 mWcm^{-2}) with a KG3 filter with a UV-cut-off at 300 nm (solid lines) and in the dark (dotted lines) in 1 M NaOH.

CBD Ga₂O₃ shows trunk formation with trunks on the order of 150 – 300 nm depending on deposition time. ALD Ga₂O₃ shows a uniform coating of 30 nm in thickness. Both, thick Ga₂O₃ overlayers deposited either by CBD or by ALD shift the photocurrent onset potential 200 mV more negative (Figure 3.7c). This shift is not visible with only a few nanometers of Ga₂O₃ (Figure 3.7d). Furthermore, omitting the annealing treatment, the electrodes with the Ga₂O₃ overlayer deposited either by ALD or CBD showed resistive J–V behavior. This observation supports the hypothesis that the hematite surface must be exposed to the solution and that the annealing process is mandatory to form cracks in the ALD as well as in the CBD grown Ga₂O₃ overlayers, and that suppression of the back reaction at the SCLJ is not the predominant mechanism of the CBD-Ga₂O₃ overlayer (as opposed to what was reported for Al₂O₃²⁵ and SnO₂³¹ on hematite nanoparticles).

To exclude any catalytic effect caused by the thick Ga₂O₃ layers, I deposited Ga₂O₃ directly onto FTO glass, omitting the hematite layer. The results shown in Figure 3.7f confirm that neither catalytic nor photocatalytic effects were observed for Ga₂O₃ deposited on F:SnO₂(Tec15) glass. As seen in Figure 3.7c, upon addition of the Ga₂O₃ overlayer the photocurrent onset potential is shifted by 200 mV, reaching 0.8 V vs. RHE. Such onset potentials have been obtained by using a catalyst³² or by employing alternative structures such as buried p-n homo-¹⁴ or hetero-junction hematite photoanodes¹² for improved band bending and better charge extraction. Also high temperature treatments have shown improved photocurrent onset potentials that were attributed to surface state passivation.³⁰

Now, the question of the role of the thick Ga₂O₃ overlayer rises and is investigated in Figure 3.8. Light-chopping experiments performed with these photoanodes show that Ga₂O₃ remarkably suppresses transient peaks especially in the photocurrent onset region (Figure 3.8a). The reduction of the photocurrent transients is either observed with water oxidation catalysts that have better charge-transfer properties than hematite, or in case of surface state passivation. As any photocatalytic effect of the Ga₂O₃ itself was excluded (Figure 3.7f), the assumption of surface passivation was investigated. Figure 3.8b shows the density of surface states (DOS) at a given potential measured under illumination. The DOS was extracted from the trap capacitance, C_{trap} , using Equation (3.9)

$$C_{trap} = q \cdot DOS \quad (3.9)$$

where C_{trap} was extracted from the equivalent circuit presented in Figure 3.1a using Equation (3.2).

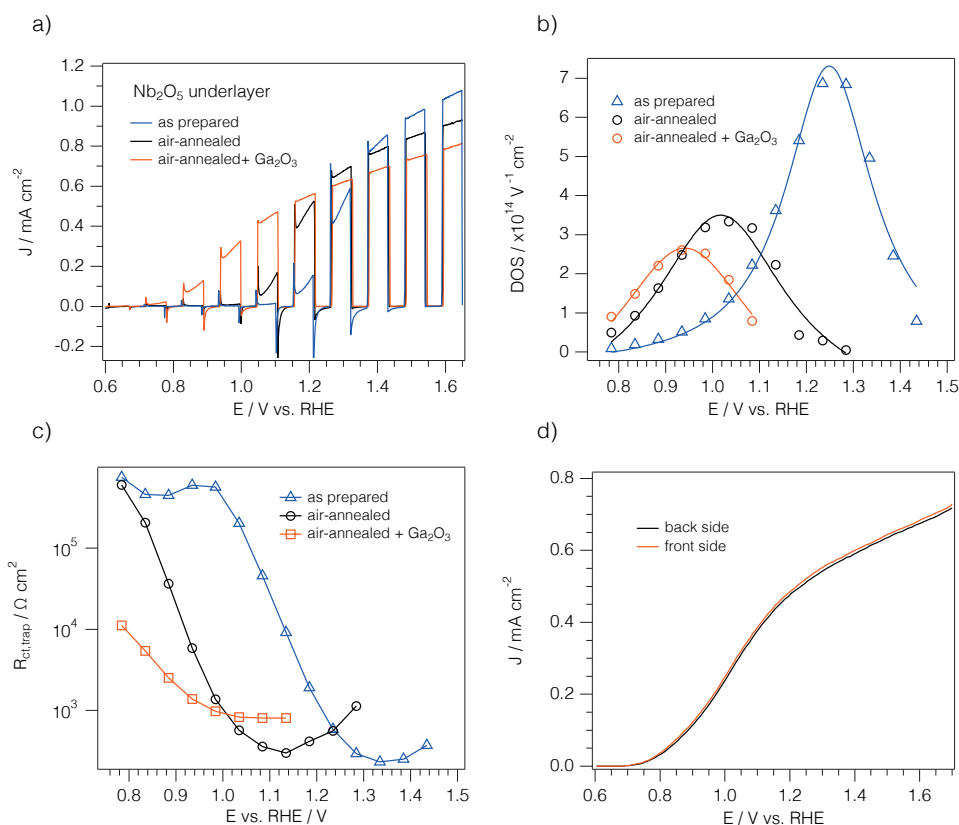


Figure 3.8 (a) Light chopping experiments of fresh (blue) and air-annealed (black) 30 nm thick Nb-doped hematite photoanodes as well as air-annealed Nb-doped hematite employing a CBD Ga₂O₃ overlayer (orange). (b) Potential dependent density of surface states (DOS) curves extracted from C_{trap} for the samples in (a). A Lorentzian fit for each sample guides the eye. (c) Corresponding charge transfer resistance from the surface states, $R_{\text{ct,trap}}$, shows a minimized resistance at earlier applied potentials in presence of a Ga₂O₃ overlayer. (d) MS plots of the air-annealed samples shown in (a) measured in the dark. The electrolyte was 1 M NaOH (pH 13.6).

From the density of surface states representation it is shown that surface passivation is evident for air-annealed samples (black hollow circles) and then further passivation is observed in the presence of a Ga₂O₃ overlayer (orange hollow squares). Interestingly, the potential position of the DOS peaks changes (along with the photocurrent onset) from 1.25 V_{RHE} for the fresh sample[§] to 1.02 V for the air-annealed sample and 0.94 V in the case of a Ga₂O₃ overlayer after annealing. The shift of the DOS maxima in Figure 3.8b after air-annealing (blue hollow triangles compared to black hollow circles) coincides

[§] 1.35 V_{RHE} for as-prepared hematite electrodes with no underlayer (Data not shown here).

with the approximately 200 mV photocurrent onset potential shift observed in Figure 3.8a (blue and black curves) as well as in Figure 3.6c (light blue compared to black line). This relation is illustrated in Figure 3.9. The onset of photocurrent occurs as soon as half of the surface states are emptied of electrons. When the surface states are empty, surface recombination of the trapped electrons with holes from the valence band is decreased and hence, the hole transfer across the hematite/electrolyte interface is facilitated. Therefore, the onset of the photocurrent is observed. Once the surface states are completely emptied, a change in the photocurrent-voltage slope is observed and the photocurrent starts plateauing. Surface states located energetically higher, allow for an earlier photocurrent onset potential as they are emptied at less applied bias and the photocurrent plateau region is reached at more negative potentials too. The change in density and energetic position of these states is most likely due to the decrease in oxygen vacancies at the surface during annealing in ambient air as is confirmed by our MS experiments (Figure 3.6).

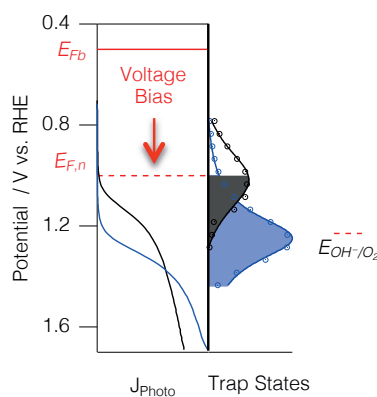


Figure 3.9 Energetic alignment of the trap states and the photocurrent curves (J_{Photo}) for Nb-doped hematite photoanodes before (black) and after air-annealing (blue). The data is taken from Figure 3.8b and Figure 3.6c for direct comparison. Also indicated is the measured flat band potential, E_{Fb} , and the quasi-Fermi level of electrons, $E_{F,n}$, under illumination.

With a Ga_2O_3 overlayer, a subsequent surface state passivation (orange squares in Figure 3.8b) as well as an additional 200 mV shift in photocurrent onset towards more negative potentials (Figure 3.8a) is observed. Again, part of this shift can be correlated with the shift of the energetic position of the DOS maxima of approximately 100 mV after Ga_2O_3 deposition. This behavior is also correlated to the shift of the minimum of the charge transfer resistance ($R_{\text{ct,trap}}$) as shown in Figure 3.8c, clearly indicating that the trap state is dominating the hole transfer kinetics for water oxidation, and that the effect of the Ga_2O_3

overlayer is affecting the energetic distribution of the trap state. With the MS analysis in Figure 3.8d, I ruled out any potential shift that would be caused by a shift of hematite's flat band potential which is in good agreement with previous studies.²¹ The surface state passivation could result from a decreased oxygen vacancy concentration at the hematite surface by the Ga₂O₃ overlayer that is less prone to oxygen vacancy formation than Fe₂O₃ itself.

3.3.3 COMBINATION OF INTERFACIAL LAYERS WITH AN ABUNDANT CATALYST

Finally, I sought to further improve the photocurrent onset potential through the addition of a water oxidation catalyst to our multilayer hematite photoanodes. As the hematite surface was only accessible through cracks in the Ga₂O₃ overlayer, photoelectrodeposition was the most efficient technique to deposit the catalyst (spin-coating of catalysts, for example, was unsuccessful). Thus, I photoelectrodeposited Co-Pi onto the Nb-doped hematite photoanode (with Ga₂O₃ overlayer) and could indeed obtain an additional 100 mV shift in the onset potential to more negative than 0.75 V vs. RHE (Figure 3.10a). Co-Pi photo-electrodeposition on a control Nb-doped hematite electrode without our Ga₂O₃ overlayer showed a 150 mV more positive photocurrent onset potential as seen in Figure 3.10b which is in good agreement with the literature.²²

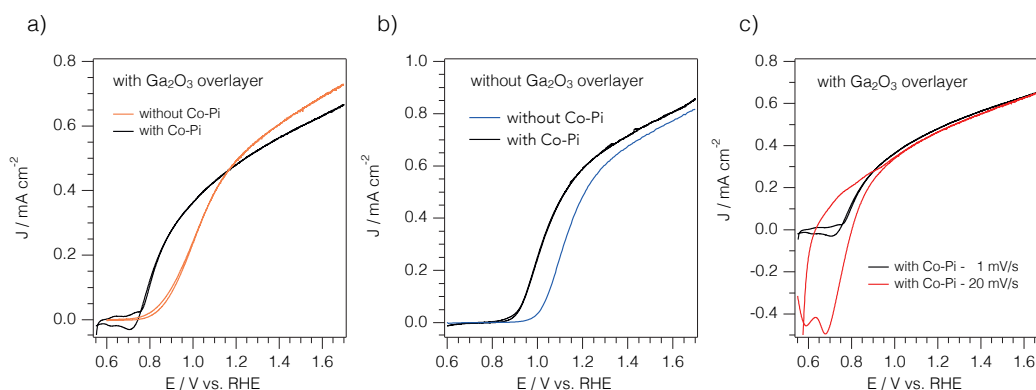


Figure 3.10 Photocurrent measurements of Nb-doped hematite thin films a) employing a CBD grown Ga₂O₃ overlayer with (black) and without (orange) a Co-Pi photo-electrodeposited catalyst compared to b) the control Nb-doped hematite electrode annealed in air at 500 °C without the Ga₂O₃ overlayer before (blue) and after Co-Pi photo-electrodeposition (black). c) Influence of the scan rate on the measured photocurrent onset potential. Cyclic voltammetric scans were carried out with simulated AM 1.5G (100 mWcm⁻²) light and were illuminated from the FTO side. The electrolyte was 1 M NaOH (pH 13.6).

It should be noted here, that higher scan rates showed capacitive behavior and a more negative potential onset due to the capacitive current (Figure 3.10c). Hence, it was important to scan slowly to obtain the same photocurrent onset potential for both scan directions that represents the real photocurrent onset potential.

With this electrode design, the overpotential for water oxidation was substantially lowered, and a mere 200 mV of bias relative to the flat band is required for the photocurrent onset ($V_{FB} = 0.54$ V vs. RHE for air-annealed Nb-doped thin hematite films (Table 3.1)).

3.4 CONCLUSIONS

Using impedance spectroscopy analysis and physical modeling, I could show that doping from underlayers into hematite thin films prepared by ultrasonic spray pyrolysis plays an important role in their performance, in addition to the influence of the underlayers on film growth and suppression of electron-hole recombination at the FTO/SC interface as already reported. Both the Nb_2O_5 and the SiO_x underlayers that were investigated herein induce an increase in n-doping in the hematite film. The increase in electron density is correlated with an increase in the photocurrent plateaus of the doped films. This is attributed to a stronger electric field in the surface region caused by stronger band bending in the thinner space charge layer enabling better charge separation and reduced recombination at the hematite/solution interface.

Furthermore, I showed that hematite, which tends to be n-doped by oxygen vacancies, is sensitive to the annealing environment. Oxygen present in the atmosphere tends to fill oxygen vacancies during the annealing process leading to a decrease in the photocurrent plateau. It was shown that annealing in oxygen-free atmosphere increases the carrier concentration in the film most probably due to subsequent doping from the underlayer increasing the photocurrent plateau. Additionally, annealing Nb-doped hematite films to 500 °C or 550 °C in air shifts the photocurrent onset to more negative potentials, which was attributed to surface state passivation.

Finally, I have shed light on the nature of the favorable photocurrent onset potential shift when adding a Ga_2O_3 overlayer. There seem to be two causes for this 200 mV shift. First, the energetic position of the trap states shifts 100 mV negatively, which can partially explain the observed potential shift. Second, the absolute value of the peak in the density

of surface together with the photocurrent transient experiments clearly indicate that passivation of surface states takes place, enabling a greater photovoltage to be extracted from the iron oxide.

In summary, this study provides insights into two major concepts to improve the catalytic performance of thin hematite films for photo-electrochemical water splitting. Firstly, the conductivity of hematite and band bending dominate the increase in the photocurrent plateau, while the photocurrent onset potential is dominated by surface state passivation (Figure 3.11).

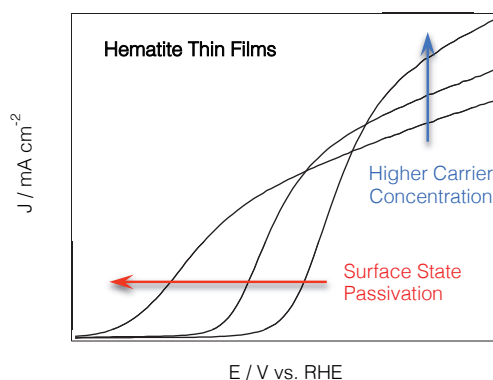


Figure 3.11 Illustration of the mechanisms dominating the photocurrent plateau (blue) and the photocurrent onset potential (red) in a J–V curve of thin film hematite photoanodes for photoelectrochemical water splitting.

As an example of these two concepts a novel multilayered hematite thin film photoanode design employing Nb_2O_5 and/or SiO_x underlayers combined with the Ga_2O_3 overlayer was developed. An onset potential of 0.8 V vs. RHE without any water oxidation catalyst was first reached and shifted more negative than 0.75 V vs. RHE with Co-Pi as a catalyst, while maintaining a high photocurrent plateau and using cheap, abundant and non-toxic materials.

3.5 REFERENCES

1. Steier, L.; Herraiz-Cardona, I.; Gimenez, S.; Fabregat-Santiago, F.; Bisquert, J.; Tilley, S. D.; Gratzel, M. Understanding the Role of Underlayers and Overlayers in Thin Film Hematite Photoanodes. *Advanced Functional Materials* **2014**, *24*, 7681-7688.
2. Sivula, K.; Le Formal, F.; Gratzel, M. Solar Water Splitting: Progress Using Hematite ($\alpha\text{-Fe}_2\text{O}_3$) Photoelectrodes. *ChemSuschem* **2011**, *4*, 432-449.

3. Duret, A.; Gratzel, M. Visible Light-Induced Water Oxidation on Mesoscopic Alpha-Fe₂O₃ Films Made by Ultrasonic Spray Pyrolysis. *Journal of Physical Chemistry B* **2005**, 109, 17184-17191.
4. Kennedy, J. H.; Frese, K. W. Photo-Oxidation of Water at Alpha-Fe₂O₃ Electrodes. *Journal of The Electrochemical Society* **1978**, 125, 709-714.
5. Sivula, K.; Brillet, J.; Gratzel, M. Controlling Photo-Activity of Solution-Processed Hematite Electrodes for Solar Water Splitting. *Solar Hydrogen and Nanotechnology V* **2010**, 7770.
6. Sivula, K.; Zboril, R.; Le Formal, F.; Robert, R.; Weidenkaff, A.; Tucek, J.; Frydrych, J.; Gratzel, M. Photoelectrochemical Water Splitting with Mesoporous Hematite Prepared by a Solution-Based Colloidal Approach. *Journal of the American Chemical Society* **2010**, 132, 7436-7444.
7. Li, L.; Yu, Y.; Meng, F.; Tan, Y.; Hamers, R. J.; Jin, S. Facile Solution Synthesis of Alpha-Fe₃O₄ Nanowires and Their Conversion to Alpha-Fe₂O₃ Nanowires for Photoelectrochemical Application. *Nano Letters* **2012**, 12, 724-731.
8. Sivula, K.; Le Formal, F.; Gratzel, M. WO₃-Fe₂O₃ Photoanodes for Water Splitting: A Host Scaffold, Guest Absorber Approach. *Chemistry of Materials* **2009**, 21, 2862-2867.
9. Stefik, M.; Cornuz, M.; Mathews, N.; Hisatomi, T.; Mhaisalkar, S.; Gratzel, M. Transparent, Conducting Nb:Sno(2) for Host-Guest Photoelectrochemistry. *Nano Letters* **2012**, 12, 5431-5435.
10. Lin, Y. J.; Zhou, S.; Sheehan, S. W.; Wang, D. W. Nanonet-Based Hematite Heteronanostructures for Efficient Solar Water Splitting. *Journal of the American Chemical Society* **2011**, 133, 2398-2401.
11. Cowan, A. J.; Barnett, C. J.; Pendlebury, S. R.; Barroso, M.; Sivula, K.; Grätzel, M.; Durrant, J. R.; Klug, D. R. Activation Energies for the Rate-Limiting Step in Water Photooxidation by Nanostructured α -Fe₂O₃ and TiO₂. *Journal of the American Chemical Society* **2011**, 133, 10134-10140.
12. Mayer, M. T.; Lin, Y. J.; Yuan, G. B.; Wang, D. W. Forming Heterojunctions at the Nanoscale for Improved Photoelectrochemical Water Splitting by Semiconductor Materials: Case Studies on Hematite. *Accounts of Chemical Research* **2013**, 46, 1558-1566.
13. Klahr, B.; Gimenez, S.; Fabregat-Santiago, F.; Bisquert, J.; Hamann, T. W. Electrochemical and Photoelectrochemical Investigation of Water Oxidation with Hematite Electrodes. *Energy & Environmental Science* **2012**, 5, 7626-7636.
14. Lin, Y.; Xu, Y.; Mayer, M. T.; Simpson, Z. I.; McMahon, G.; Zhou, S.; Wang, D. Growth of P-Type Hematite by Atomic Layer Deposition and Its Utilization for Improved Solar Water Splitting. *Journal of the American Chemical Society* **2012**, 134, 5508-5511.
15. Klahr, B.; Gimenez, S.; Fabregat-Santiago, F.; Hamann, T.; Bisquert, J. Water Oxidation at Hematite Photoelectrodes: The Role of Surface States. *Journal of the American Chemical Society* **2012**, 134, 4294-4302.
16. Badia-Bou, L.; Mas-Marza, E.; Rodenas, P.; Barea, E. M.; Fabregat-Santiago, F.; Gimenez, S.; Peris, E.; Bisquert, J. Water Oxidation at Hematite Photoelectrodes with an Iridium-Based Catalyst. *Journal of Physical Chemistry C* **2013**, 117, 3826-3833.
17. Braun, A.; Sivula, K.; Bora, D. K.; Zhu, J. F.; Zhang, L.; Gratzel, M.; Guo, J. H.; Constable, E. C. Direct Observation of Two Electron Holes in a Hematite Photoanode During Photoelectrochemical Water Splitting. *Journal of Physical Chemistry C* **2012**, 116, 16870-16875.
18. Le Formal, F.; Grätzel, M.; Sivula, K. Controlling Photoactivity in Ultrathin Hematite Films for Solar Water-Splitting. *Advanced Functional Materials* **2010**, 20, 1099-1107.

19. Hisatomi, T.; Dotan, H.; Stefik, M.; Sivula, K.; Rothschild, A.; Gratzel, M.; Mathews, N. Enhancement in the Performance of Ultrathin Hematite Photoanode for Water Splitting by an Oxide Underlayer. *Advanced Materials* **2012**, *24*, 2699-2702.
20. Liang, Y. Q.; Enache, C. S.; van de Krol, R. Photoelectrochemical Characterization of Sprayed Alpha-Fe₂O₃ Thin Films: Influence of Si Doping and SnO₂ Interfacial Layer. *International Journal of Photoenergy* **2008**.
21. Barroso, M.; Mesa, C. A.; Pendlebury, S. R.; Cowan, A. J.; Hisatomi, T.; Sivula, K.; Gratzel, M.; Klug, D. R.; Durrant, J. R. Dynamics of Photogenerated Holes in Surface Modified Alpha-Fe₂O₃ Photoanodes for Solar Water Splitting. *Proc Natl Acad Sci U S A* **2012**.
22. Klahr, B.; Gimenez, S.; Fabregat-Santiago, F.; Bisquert, J.; Hamann, T. W. Photoelectrochemical and Impedance Spectroscopic Investigation of Water Oxidation with "Co-Pi"-Coated Hematite Electrodes. *Journal of the American Chemical Society* **2012**, *134*, 16693-16700.
23. Tilley, S. D.; Cornuz, M.; Sivula, K.; Grätzel, M. Light-Induced Water Splitting with Hematite: Improved Nanostructure and Iridium Oxide Catalysis. *Angewandte Chemie International Edition* **2010**, *49*, 6405-6408.
24. Hisatomi, T.; Le Formal, F.; Cornuz, M.; Brillet, J.; Tétreault, N.; Sivula, K.; Grätzel, M. Cathodic Shift in Onset Potential of Solar Oxygen Evolution on Hematite by 13-Group Oxide Overlayers. *Energy & Environmental Science* **2011**, *4*, 2512.
25. Le Formal, F.; Tétreault, N.; Cornuz, M.; Moehl, T.; Grätzel, M.; Sivula, K. Passivating Surface States on Water Splitting Hematite Photoanodes with Alumina Overlayers. *Chemical Science* **2011**, *2*, 737.
26. Brillet, J.; Cornuz, M.; Le Formal, F.; Yum, J. H.; Gratzel, M.; Sivula, K. Examining Architectures of Photoanode-Photovoltaic Tandem Cells for Solar Water Splitting. *Journal of Materials Research* **2010**, *25*, 17-24.
27. Barroso, M.; Cowan, A. J.; Pendlebury, S. R.; Gratzel, M.; Klug, D. R.; Durrant, J. R. The Role of Cobalt Phosphate in Enhancing the Photocatalytic Activity of Alpha-Fe₂O₃ toward Water Oxidation. *J Am Chem Soc* **2011**, *133*, 14868-14871.
28. Brug, G. J.; Vandeneeden, A. L. G.; Sluytersrehabach, M.; Sluyters, J. H. The Analysis of Electrode Impedances Complicated by the Presence of a Constant Phase Element. *Journal of Electroanalytical Chemistry* **1984**, *176*, 275-295.
29. Glasscock, J. A.; Barnes, P. R. F.; Plumb, I. C.; Bendavid, A.; Martin, P. J. Structural, Optical and Electrical Properties of Undoped Polycrystalline Hematite Thin Films Produced Using Filtered Arc Deposition. *Thin Solid Films* **2008**, *516*, 1716-1724.
30. Zandi, O.; Hamann, T. W. Enhanced Water Splitting Efficiency through Selective Surface State Removal. *Journal of Physical Chemistry Letters* **2014**, *5*, 1522-1526.
31. Spray, R. L.; McDonald, K. J.; Choi, K. S. Enhancing Photoresponse of Nanoparticulate Alpha-Fe₂O₃ Electrodes by Surface Composition Tuning. *Journal of Physical Chemistry C* **2011**, *115*, 3497-3506.
32. Du, C.; Yang, X. G.; Mayer, M. T.; Hoyt, H.; Xie, J.; McMahon, G.; Bischooping, G.; Wang, D. W. Hematite-Based Water Splitting with Low Turn-on Voltages. *Angewandte Chemie-International Edition* **2013**, *52*, 12692-12695.

The short hole diffusion length in hematite demands the use of thin films for efficient charge extraction. To guarantee full light absorption, however, thick films of the photoabsorber material are necessary.

*“Look deep into nature and you will understand everything better”
Albert Einstein said.*

So how did nature overcome similar limitations? Not necessary to search on the nanoscale – just look around – at the trees that grow tall and branched to allow a maximum of leaves to absorb sunlight and you will identify the idea of the branched tree structure carrying its leaves.



A similar scaffold is needed for the hematite photoabsorber.

Ultrasonic spray pyrolysis is a useful technique to investigate thin hematite films on flat substrates as a model system but is not capable of homogeneously coating a nanostructured scaffold. With atomic layer deposition (ALD), however, a conductive scaffold/photoabsorber design is possible and full light absorption can be reconciled with maximum charge extraction.

4 LOW-TEMPERATURE ALD OF CRYSTALLINE AND PHOTOACTIVE ULTRATHIN HEMATITE FILMS FOR SOLAR WATER SPLITTING

This chapter is adapted from a peer-reviewed article by Ludmilla Steier, Jingshan Luo, Marcel Schreier, Matthew T. Mayer, Timo Sajavaara and Michael Grätzel published 2015 in ACS Nano.¹

In this chapter, I first present the design and construction of my atomic layer deposition (ALD) setup and then, introduce a low-temperature ALD route to deposit phase pure, crystalline and highly photoactive hematite ($\alpha\text{-Fe}_2\text{O}_3$) films at 230 °C without the need for post-annealing. Prior to the elaboration of this method, the majority of ALD hematite routes required annealing treatments at more than 500 °C to obtain a photoactive film. However, this high-temperature treatment would for example not be possible in the fabrication of a p-n junction. With transmission electron microscopy I demonstrate homogenous and conformal deposition of crystalline hematite on a high aspect ratio nanostructured substrate. These as-deposited $\alpha\text{-Fe}_2\text{O}_3$ films are investigated as photoanodes for photoelectrochemical water oxidation and found to be highly photoactive. Combined with a TiO_2 underlayer and a low-cost $\text{Ni}(\text{OH})_2$ catalyst, hematite films of less than 10 nm in thickness reached photocurrent densities of 0.3 mA cm^{-2} at 1.23 V vs. RHE and a photocurrent onset potential of less than 0.9 V vs. RHE, previously unseen for films this thin and without high temperature annealing. Furthermore, in a thickness-dependent photoelectrochemical analysis, I identify that a hematite thickness of only 10 nm yields the highest internal quantum efficiency when using a suitable underlayer such as TiO_2 that induces doping of the hematite film and reduces electron/hole recombination at the back contact. It is shown that at high bias potentials, photocurrent density and quantum efficiency proportionally increase with light absorption in hematite films thinner than 10 nm and are limited by the space charge layer width in thicker films. Thus, I propose to focus on 10 nm thick hematite films for future developments on suitable nanostructured conductive scaffolds.

4.1 THE SIGNIFICANCE OF ALD FOR HEMATITE PHOTOANODES

Apart from being a well-explored material in gas-sensors² and Li-Ion batteries,^{3, 4} hematite (α -Fe₂O₃) is also one of the very few truly stable semiconductor materials for photoelectrochemical (PEC) water oxidation^{5, 6} that does not require any protection layer engineering.⁷ With a suitable band gap of 2 eV and a well-positioned valence band for water oxidation, it is an appealing material for solar water splitting – especially because it fulfills the major requirements for industrial production by being earth-abundant, non-toxic, and inexpensive.

However, the application of hematite as a photoanode for water splitting is hampered by sluggish electron transport via polaron hopping⁸ and short carrier lifetimes.^{9, 10} These charge transport limitations force the photoanode design towards thin films deposited on high surface area nanostructured conductive scaffolds.¹¹⁻¹³ In such a nanostructured photoanode design, recombination losses within the thin absorber material are minimized while light absorption is adaptable by the adjustment of the nanostructure thickness. Though thin hematite films deposited by, for example, ultrasonic spray pyrolysis have reached high photoactivities on flat substrates,^{14, 15} this method is incapable of homogeneously depositing within a mesoporous structure. For this purpose atomic layer deposition (ALD) is ideal as it can deposit uniform and conformal films onto high aspect ratio nanostructures.¹⁶ ALD of transition metal oxides has first been demonstrated using metal acetamidinates as precursors,¹⁷ soon followed up by the deposition of hematite using Fe(thd)₃/O₃,^{18, 19} Fe₂(O^tBu)₆/H₂O^{20, 21} and Fe(Cp)₂/O₂.²² Unfortunately, these approaches suffered from low growth rates, commercially unavailable precursors and/or from elevated deposition temperatures. Martinson *et al.* introduced a Fe(Cp)₂/O₃ ALD process at 200 °C with a growth rate of 0.14 nm/cycle matching the rate of the high temperature deposition with Fe(Cp)₂/O₂ and being much faster than with the oxygen/ozone mixture introduced earlier.^{23, 24} Recently, the deposition temperature has been decreased to as low as 150 °C using *tert*-butyl ferrocene and O₂ plasma.²⁵ However, these as-deposited iron oxide films are amorphous and require high temperature annealing to crystallize, a step which greatly increases the energy demand for synthesis and will hinder its application on substrates or scaffolds not compatible with high temperatures. Meanwhile, a very interesting route for photoactive hematite films in their as-deposited

state has been introduced using FeCl_3 and water.²⁶ As observed in earlier studies,² FeCl_3 induces island growth resulting in crystalline Fe_2O_3 . At deposition temperatures around 235 °C, however, $\gamma\text{-Fe}_2\text{O}_3$ and high Cl contamination were observed in the as-grown films – the latter being responsible for the decrease in photoactivity after annealing.

Here, I present a novel low-temperature ALD route towards highly photoactive, crystalline, homogenous and pure hematite films in their as-grown state using *N,N*-(dimethylaminomethyl)ferrocene (DMAMFc) and ozone. DMAMFc was introduced recently as a suitable hematite precursor at temperatures between 325 – 450 °C with growth rates around 0.14 nm/cycle, similar to the growth characteristics obtained with ferrocene.²⁷ In the ALD process described herein, I was able to decrease the growth temperature to 230 °C and control the dose of the precursors to form phase-pure and crystalline hematite films *in situ* with extremely low levels of carbon contamination. These hematite films show photoelectrochemical activities that are remarkable for films this thin (≤ 10 nm) and without any high-temperature processing step. Avoiding high temperature annealing, hematite could be explored in pn junction configurations for water splitting without the risk of destroying the junction with a high-temperature treatment.

4.2 METHODS

4.2.1 CONSTRUCTION OF THE ALD-SETUP

Iron contamination in ALD grown films for photoelectrochemical and photovoltaic devices is often undesired especially in the field of high efficiency research. To circumvent this issue, I decided to construct an ALD setup that would be dedicated to the deposition of hematite. To avoid cross-contamination and to offer high flexibility in ALD recipes, I chose a “shower-head” design with three separate precursor lines for the iron precursor (Fe-Line), for other wide band gap metal oxide precursors (M-Line) and a separate line for the oxidizer (O-Line) as shown in Figure 4.1a. Separating the pathway of the oxidizer from the metal precursor pathway has also the advantage of low oxide deposition in the lines. Nevertheless, to allow for an easy dismantling of the ALD for cleaning, I used ¼” VCR Swagelok connectors with metal o-rings that enable leak-free reassembling. All 3 lines can be heated separately up to 450 °C and are equipped with 7 thermocouples (Type K) to control and check the temperature at several positions. Two

more thermocouples control and check the temperature of the hotplate. The hotplate consists of a resistive heating cartridge made of Kanthal (FeCrAl alloy, CMT Rickenbach SA, Switzerland) embedded in a heat insulator ceramic and covered with a 100 mm × 100 mm × 10 mm aluminum nitride ceramic plate ($170 \text{ Wm}^{-1}\text{K}^{-1}$, Ceramtec, Germany). AlN is the ideal material for hotplates in corrosive environments as it is conducting heat almost as well as copper metal²⁸ and is chemically much more robust. Even under harsh oxidizing conditions such as ozone exposure in the ALD chamber, an Al_2O_3 passivation layer forms and protects the AlN bulk material at moderate temperatures ($<700 \text{ }^\circ\text{C}$).²⁹

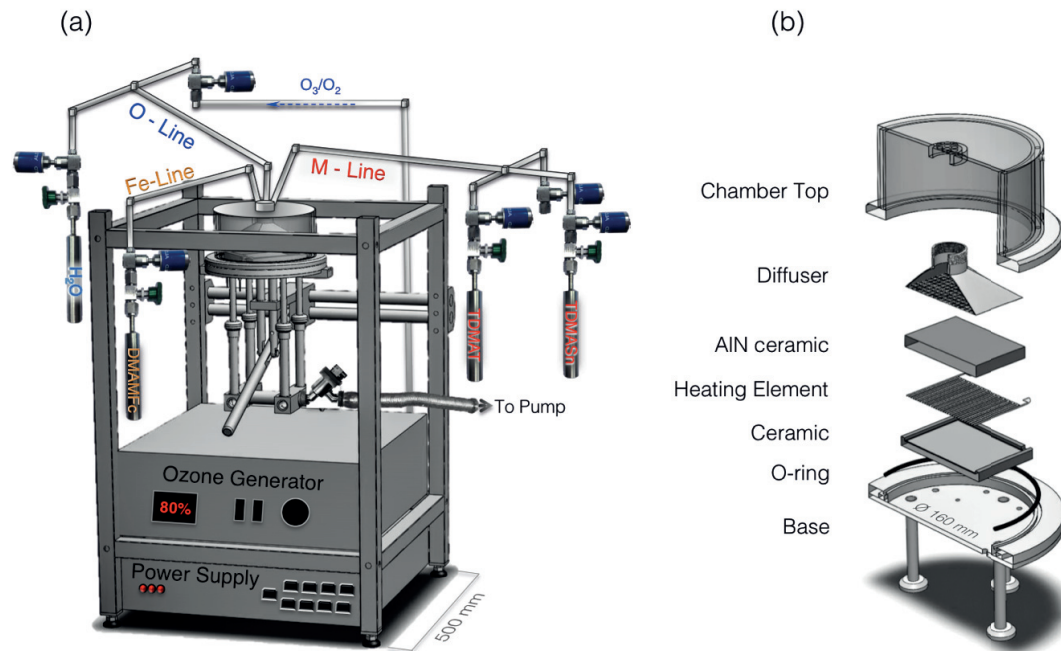


Figure 4.1 a) Schematic representation of the home-built ALD setup with a “shower-head” design with 3 separate precursor lines for iron precursors (Fe-Line), for other wide band gap metal oxide precursors such as TiO_2 and SnO_2 (M-Line) and a separate line for the oxidizer (O-Line). The setup is equipped with an ozone generator and a power supply for the heating of the hotplate, the precursor cylinders and lines. b) Cross-sectional exploded view of the ALD chamber with its components. The ensemble of ceramic, resistive heating element and AlN ceramic form the hotplate of the chamber.

To prevent deformation of the heating element and electrical shorts during deposition, I deposited an insulating layer of 200 nm Al_2O_3 by ALD (Figure 4.2a). With this modification, the hotplate could be used as designed up to 500 °C.

To prevent smooth samples like Si wafer sliding off the hotplate during deposition and to rapidly cool down the hotplate in between depositions, I designed a stainless steel frame

that could pass through compressed air for cooling (Figure 4.2b).

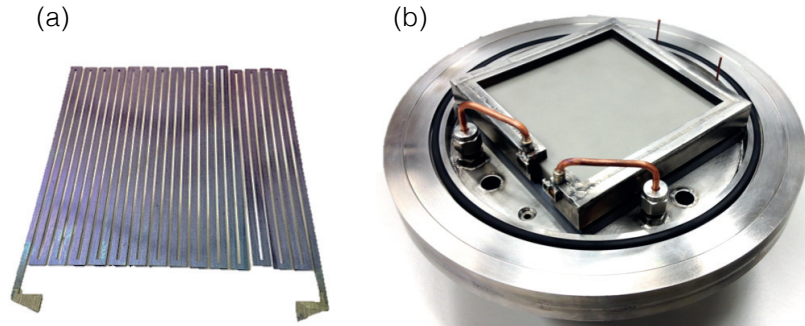


Figure 4.2 a) Designed resistive heating made of Kanthal insulated with 200 nm of Al₂O₃ by ALD leading to the purple-bluish color. b) Bottom of the ALD chamber with the hotplate embedded in a stainless steel frame that keeps the samples from sliding off the hotplate and enables air-flow inside the frame to accelerate cooling of the hotplate if needed.

In addition, the diffuser (Figure 4.1b) filled with glass beads prevented a displacement of samples on the hotplate even during strong ozone pulses.

For the precursor supply, compatibility with a Savannah 100 ALD apparatus (Cambridge Nanotech) already in use in our laboratory had to be maintained. Hence, I chose the same precursor cylinders from Swagelok to have a collection of precursors for both ALDs. Most of the ALD metal precursors have to be heated to attain the desired vapor pressure. In view of the fabrication delay and cost of commercial heating jackets by for example BriskHeat®, low-cost custom heating jackets were fabricated in-house as shown in Figure 4.3. The cylinder was wrapped in a thin glass fiber cloth and enclosed in a metal grid to give the jacket shape. Then a heating cord (Horst, Germany) was curled around the metal grid and a thermocouple (Type K) fixated to contact the metal cylinder inside the jacket. The heating cord was wrapped in a 0.8 cm thick heat insulating glass fiber layer (Horst, Germany) and covered with a second more robust glass fiber cloth (Horst, Germany). A heat resistive glass fiber tape (Horst, Germany) kept the jacket closed. Due to the tape and the thick glass fiber insulation, the heating of the jackets were limited to a maximum temperature of 200 °C.

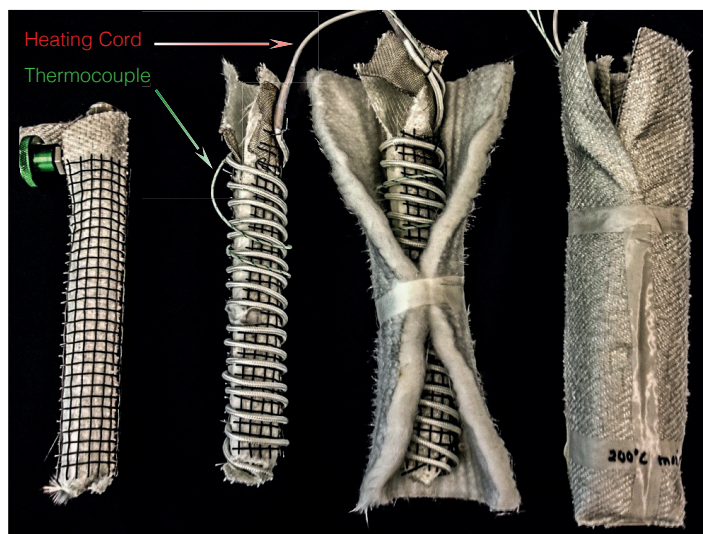


Figure 4.3 Fabrication steps of custom heating jackets for the ALD precursor cylinders. The cylinder is wrapped in a thin glass fiber cloth and enclosed in a metal grid to give the jacket shape. Then a heating cord is curled around the metal grid and a thermocouple (type K) is fixated to contact the metal cylinder inside the jacket. The heating cord is insulated by a 0.8 cm thick glass fiber layer and wrapped in a second more robust glass fiber cloth. A heat resistive (up to 200 °C) glass fiber tape keeps the jacket closed.

From the cylinder, the precursor is pulsed through a 3-way ALD valve (Swagelok) into a stream of the inert carrier gas that can be either nitrogen or argon in this ALD (the carrier gas lines were omitted in the drawing of Figure 4.1a). The electro-pneumatic solenoid (held under 7 bar of compressed air) enables a precise pulsing with a minimum pulse time of 0.01 s.

The ALD is operated by a powerful Labview software developed in-house in collaboration with Frédéric Gummy (EPFL). Via a real-time CompactRio (National Instruments) it controls the air solenoids (24 VDC) of 7 ALD valves and of a stop valve (Genesis Angle Inline Valve, KF 25, Nor-Cal, USA), the mass flow controller for the carrier gas (Type 1479B01312CR1BM, MKS Instruments, Germany), the pressure gauge (APGX-H-NW16, Edwards), the power supply for the heating (custom made by Patrick Favre and Frédéric Gummy) and the ozone generator (AC-2015, InUSA Corp., USA). A screenshot of the interface is shown in Figure 4.4.

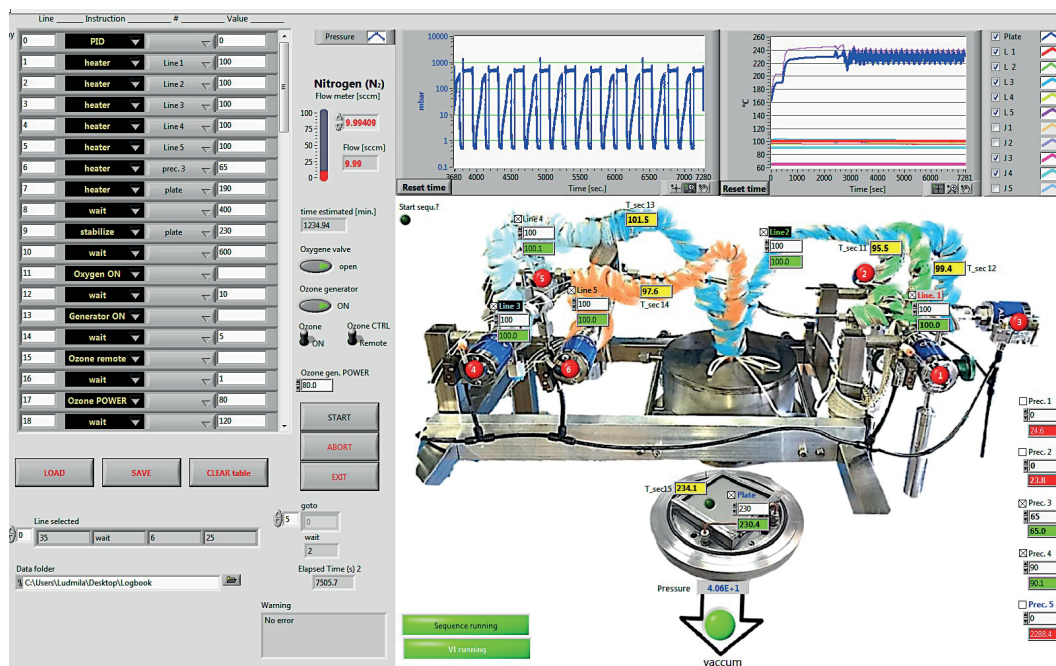


Figure 4.4 Screenshot of the interface of the ALD software that controls ALD heating, precursor pulsing, carrier gas flow and the ozone generator via a real-time module. The software also reads all temperatures measured by the thermocouples and the chamber pressure via the pressure gage.

4.2.2 ALD OF THE UNDERLAYER

Tetrakis(dimethylamino)titanium (TDMAT, Sigma Aldrich) and pure H₂O were used as precursors to deposit TiO₂ on F:SnO₂ substrates in the same ALD setup at 170 °C and a N₂ flow of 5 sccm. TDMAT was held at 75 °C and H₂O at room temperature. The growth rate was 0.06 nm/cycle as measured by ellipsometry on a Si-wafer.

4.2.3 ELLIPSOMETRY

Film thicknesses, refractive index (n) and extinction coefficient (k) parameters of the ALD Fe₂O₃ and TiO₂ layers were evaluated using spectroscopic ellipsometry (Sopra GES 5E, France). The range of photo energies used in the study was between 250–890 nm. I fitted the obtained spectra using a Tauc-Lorentz dispersion law (WinElli II software) and extracted the thickness of the deposited layers. Fe₂O₃ was analyzed on Si wafer substrates and on quartz glass substrates. Importantly, no difference in the dispersion law could be observed between the as-deposited and annealed Fe₂O₃ films indicating that the as-deposited films are pure hematite.

4.2.4 TOF-ERDA

In the TOF-ERDA measurements a beam of 7.5 MeV $^{35}\text{Cl}^{4+}$ ions was used as described elsewhere.³⁰ The high depth resolution was obtained by tilting the sample so that the angle between the incident beam and sample surface was 4–6 degrees.

4.2.5 ELECTRON MICROSCOPY

TEM measurements were carried out with a Technai Osiris (FEI, USA) with a built-in EDX unit. Secondary electron images were acquired with a Merlin microscope equipped with an EDX detector (Zeiss).

4.2.6 X-RAY DIFFRACTION

XRD Data was recorded using an X'Pert MPD PRO (Panalytical) X-ray diffractometer equipped with a ceramic tube (Cu anode, $\lambda=1.54060 \text{ \AA}$), a secondary graphite (002) monochromator and a RTMS X'Celerator detector (1D-mode, Panalytical). Measurements were carried out in the Bragg-Brentano geometry. The automatic divergence slit and antiscatter slit were adjusted to 0.982 and scans were carried out from $2\theta = 32.5^\circ$ to 39.0° at a rate of $0.003^\circ \text{ min}^{-1}$ using a step size of 0.03° .

4.2.7 RAMAN SPECTROSCOPY

Raman spectra were obtained with a confocal Raman microscope XploRa Plus (Horiba, USA), where the excitation line was provided by an Nd:YAG (doubled) laser (532 nm).

4.2.8 SYNTHESIS OF THE NANOWIRE SCAFFOLD

The TiO_2 nanowire arrays on F:SnO₂ substrate were synthesized by a hydrothermal method modified from previous report.³¹ In a typical process, the F:SnO₂ substrates were first cleaned with Deconex and deionized water for 15 min, sequentially, and then dried with compressed air. The precursor was prepared by adding 2.5 ml titanium butoxide to a well-mixed solution of 90 ml HCl and 90 ml H₂O. Then the whole mixture was stirred until the solution became clear. After that, the mixture was poured into a Teflon-liner stainless steel autoclave with the F:SnO₂ substrates placed at an angle against the wall

with the conductive side facing down. The hydrothermal growth was conducted at 150 °C for 6 h in an electric oven. After that, the samples were rinsed with deionized water and dried with compressed air.

4.2.9 CATALYST DEPOSITION

A Ni(OH)₂ catalyst was deposited by dipping the samples for 5 min in 1 M NaOH solution, then 3 min in 0.3 M Ni(NO₃)₂ aqueous solution and a third time in 1 M NaOH for a few seconds. All solutions were kept at room temperature. Subsequently, the samples were rinsed with deionized water and dried in an air stream.

4.2.10 PHOTOELECTROCHEMICAL CHARACTERIZATION

Photoelectrochemical measurements were performed in 1 M NaOH aqueous solution (pH 13.6) using a three-electrode configuration, with a Pt wire counter electrode and a Ag/AgCl, KCl (sat'd) reference electrode. Simulated sunlight was generated from a 450 W xenon lamp (Osram, ozone free) passed through a KG3 filter (3 mm, Schott) with a measured intensity equivalent to standard AM 1.5G sunlight (100 mWcm⁻², spectrally corrected) at the sample surface masked to 0.5 cm². IPCE measurements were carried out in the same solution and three-electrode configuration described above. The photoanode potential was fixed at 1.53 V *vs.* RHE and the photocurrent was measured while illuminating with monochromatic light of varying wavelength. The light originated from a 300 W Xe lamp passed through a single grating monochromator. The device photocurrent at each wavelength was compared to the photocurrent on a calibrated Si diode to determine the IPCE. EIS measurements were carried out in the dark with the same three-electrode cell in 1 M NaOH solution. Full impedance spectra were measured with a SP-200 (BioLogic Science Instruments) at frequencies from 1 MHz to 0.1 Hz with a sinusoidal potential perturbation of 25 mV. The range of the bias potential was 0.6-1.7 V *vs.* RHE. The capacitance was extracted from the fitting according to the standard RC circuit shown in Figure 2.4 fitted with Zview (Scribner Associates). Charge carrier density, N_D , was extracted from the slope of the linear region in a Mott-Schottky plot according to Equation (2.9) with a surface area corrected for roughness by a factor of 1.26 as obtained from Figure 4.5. The space charge layer width, W_{SC} , was calculated

according to Equation (2.10). All potentials have been referenced to the reversible hydrogen electrode (RHE) by the expression: $V_{\text{RHE}} = V_{\text{Ag/AgCl}} + 0.197 \text{ V} + 0.059 \text{ V} \cdot \text{pH}$.

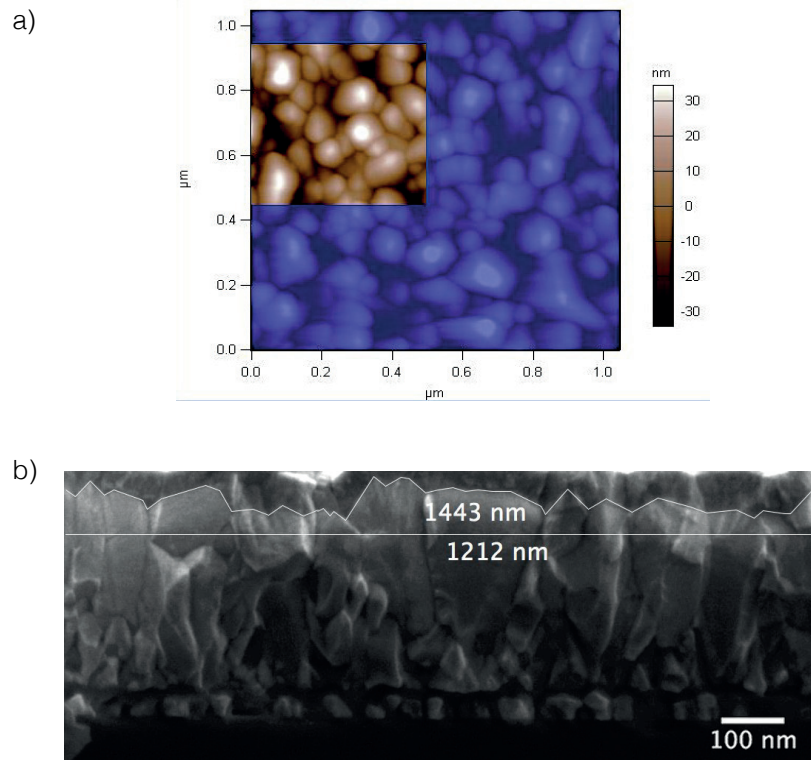


Figure 4.5 a) Atomic force micrograph of a F:SnO₂ substrate (TCO22-15, Solaronix SA, Switzerland) coated with 8 nm of ALD hematite. In an exemplary area of 250 x 250 nm, a ratio of the actual scanned area to the projected area was found to be 1.26. b) SEM cross-section micrograph of a F:SnO₂ substrate shows a roughness factor of 1.2 which is in good agreement with the results obtained from AFM.

4.2.11 UV-VIS MEASUREMENTS

For absorption measurements, samples were rinsed with ethanol and water and dried with compressed air to assure a dust free area. Then, they were sandwiched between two quartz slides that had been wetted with a droplet of water to obtain the following assembly: quartz-water-sample-water-quartz to mimic the PEC conditions. Inserting this sandwiched assembly in the beam path of the integrating sphere of the UV-3600 spectrometer (Shimadzu Scientific Instruments, USA), direct transmission and diffuse as well as total reflectance were measured under front (electrode-electrolyte) or back illumination (substrate-electrolyte). Absorbance was calculated with respect to the FTO blank as previously proposed.¹⁴

4.3 RESULTS

4.3.1 THOUGHTS BEHIND THE CHOICE OF PRECURSORS AND SUBSTRATE PREPARATION

I chose *N,N*-(dimethylaminomethyl)ferrocene (DMAMFc) as the iron precursor as it is a commercially available (98%+, Alfa Aesar or 96%, Sigma Aldrich), inexpensive and easy to handle liquid with a boiling point of 92 °C at 0.5 mmHg (0.7 mbar). As the base pressure in the ALD chamber was around 0.5 mbar under 20 sccm of N₂ flow, the DMAMFc stainless steel bubbler was heated to 90 °C. Temperatures up to 148 °C also gave homogenous iron oxide growth albeit with reduced photoactivity as seen in Figure 4.6.

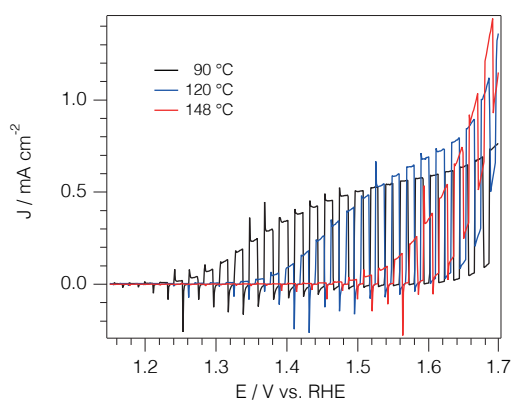


Figure 4.6 Current Density–Voltage curves under chopped illumination of as grown hematite films deposited on TiO₂ coated F:SnO₂ varying the precursor temperature from 90 °C to 148 °C. Film characteristics are given in Table 1. Measurements were carried out with simulated AM 1.5G (100 mWcm⁻²) light with a scan rate of 10 mV/s in 1 M NaOH (pH 13.6).

The oxidation state of iron in hematite is Fe³⁺, but in the ferrocene precursor the iron is in its Fe²⁺ state. Hence, it needs a strong oxidizer during the ALD process to oxidize Fe²⁺ to Fe³⁺. The most commonly used oxidizers for thermal ALD are oxygen, hydrogen peroxide and ozone. Their oxidation strength follows the electrochemical potential listed in Table 4.1. For ALD of hematite I chose ozone, as it is the strongest oxidizer. In the ozone generator AC-2025 (IN USA Inc., United States) fed with oxygen gas (99.9995% pure, Carbagas) a relatively high ozone concentration of 13% in O₂ could be reached.

Table 4.1 Oxidation strength of the most commonly used oxidizing precursors for thermal ALD.

Oxidizer	Electrochemical Potential / V
Oxygen	1.23
Hydrogen Peroxide	1.78
Ozone	2.08

In order to allow for pinhole-free and homogenous flat hematite films on FTO (F:SnO₂) glass (TCO22-15, Solaronix SA, Switzerland), the substrates were first wiped with acetone and then cleaned for 10 min in piranha solution (H₂SO₄/H₂O₂ = 3:1) prior to loading into the ALD. The piranha solution oxidizes any organics present and provides a clean and hydrophilic surface.

4.3.2 GROWTH CHARACTERISTICS OF HEMATITE

A highly optimized ALD to directly formed phase pure and highly photoactive hematite during the deposition is presented herein. ALD was performed in exposure mode, employing the sequence [*DMAMFc-Pulse/Exposure/Purge//O₃-Pulse/Exposure/Purge*] with pulse times fixed at 0.02 s for DMAMFc and 0.01 s for ozone while varying the exposure time of each. Because the Fe-precursor needs a certain time to re-establish its vapor pressure, the duration of one cycle was adjusted to 180 s. Growth characteristics of hematite ALD at 230 °C were investigated *ex-situ* by ellipsometry measurements on Si substrates and are presented in Figure 4.7. A thin layer of ALD TiO₂ was deposited onto Si to mimic the substrates for most of the other depositions used in this study. In Figure 4.7a,b growth saturation is observed for both precursor exposures. A constant growth rate of 0.25 ± 0.01 Å/cycle was calculated from the slope in Figure 4.7c, when using chamber and precursor temperatures of 230 °C and 90 °C, respectively. I found that higher growth rates up to 0.4 Å/cycle could be achieved by elevating the temperature of the precursor to increase its vapor pressure (Figure 4.7d), but heating the precursor higher than 125 °C led to films with decreased photoactivity (Figure 4.6). Thus, I continued to operate in a sub-saturation regime, where the saturation is limited by the precursor amount.

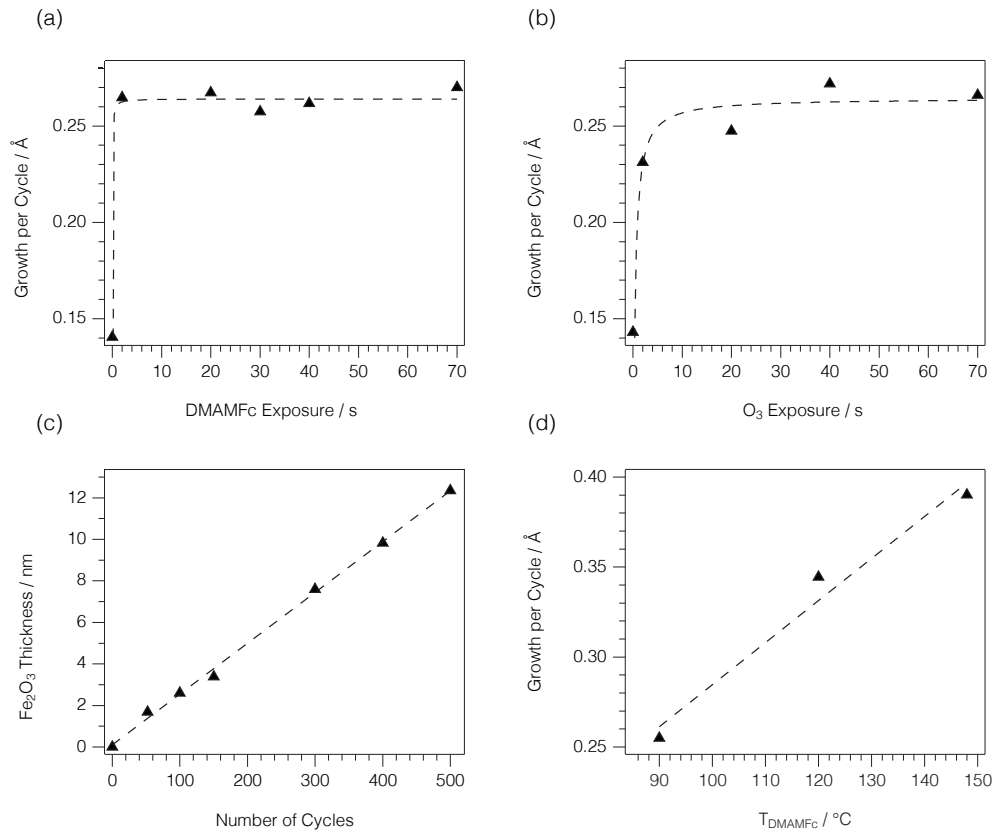


Figure 4.7 Growth characteristics of Fe₂O₃ deposited at 230 °C with DMAMFc and O₃ as measured by ellipsometry. Saturated growth demonstrated for a) DMAMFc in a 0.02s/Xs/(90-X)s//0.01s/70s/20s mode and b) O₃ exposure times in a 0.02s/70s/20s//0.01s/Xs/(90-X)s mode. Dashed lines represent a Langmuir type fit. c) Linear growth of Fe₂O₃ with number of cycles for 0.02s/70s/20s//0.01s/70s/20s mode. Dashed line represents the linear fit. d) Growth rate dependence on the precursor temperature varying from the standard 90 °C as presented in a)-c) to 148 °C in a 0.02s/70s/20s//0.01s/70s/20s mode.

4.3.3 HEMATITE FILM PURITY

To exclude that the photoactivity is affected by carbon contamination at elevated precursor temperatures, time-of-flight coupled elastic recoil detection analysis (TOF-ERDA) was performed on samples deposited at three different precursor temperatures on Si substrates coated with a thin TiO₂ layer (1.5 nm) or bare Si. TOF-ERDA results are given in Figure 4.8 for four different hematite samples that are detailed in Table 4.2.

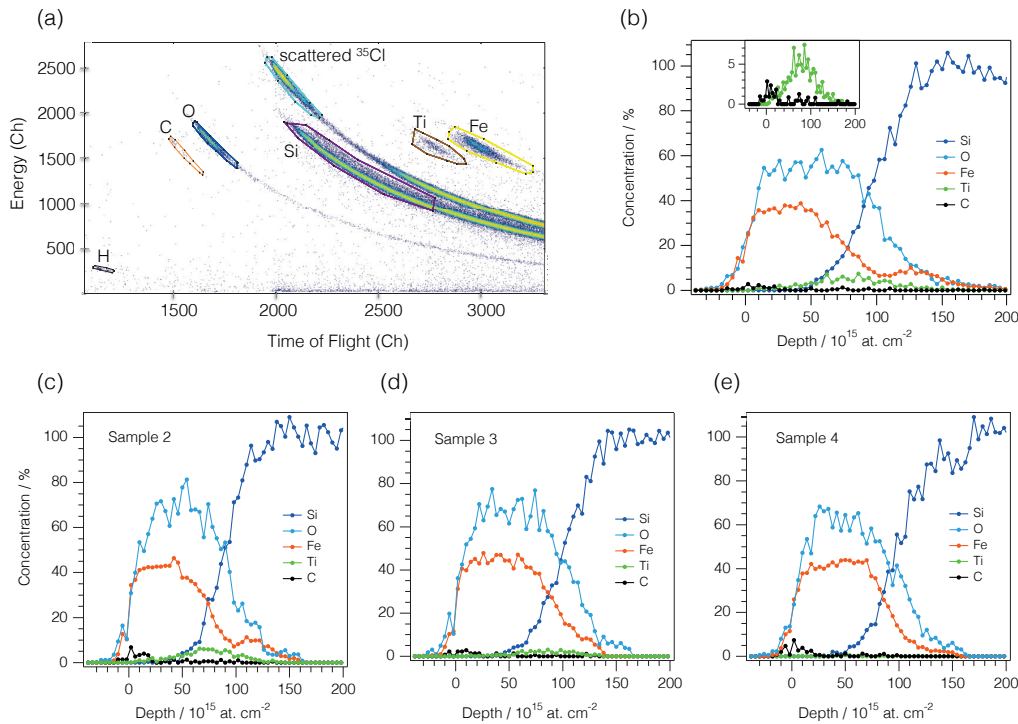


Figure 4.8 TOF-ERDA results. a) Time of flight signals of all detected elements in sample 1. Single carbon atoms are detected showing the very low contamination in the hematite film. b) Corresponding concentration depth profile of sample 1 obtained from (a). The depth profile of Fe was obtained from the scattered ³⁵Cl beam. The small hump around $125 \cdot 10^{15}$ at. cm⁻² is due to scattering from Ti instead of Fe. The inset zooms on the C and Ti concentration. c)-e) Concentration depth profiles of samples 2-4. Sample 4 did not have a TiO₂ underlayer and no Ti was detected.

Table 4.2 Film composition (Fe/O ratio) and carbon contamination (C) of hematite thin films deposited by DMAMFc/O₃ ALD on either TiO₂ coated silicon or bare silicon at different precursor temperatures, T_{prec} resulting in slightly different thicknesses, d , for 300 cycles. Films were measured with TOF-ERDA in their as-deposited state and the atom percentages were extracted from the flat plateau region of the Fe concentration (Figures b-e).

Sample	1	2	3	4
Substrate	TiO ₂ /Si	TiO ₂ /Si	TiO ₂ /Si	Si
T_{prec} / °C	90	125	148	148
d / nm	8.9	10.3	11.6	11.8
Fe/O ratio	2 : 2.96	2 : 3.14	2 : 3.0	2 : 2.96
C / at. %	0.2±0.1	0.3±0.2	0.3±0.1	0.2±0.1

TOF-ERDA is a powerful technique for depth profiling light elements such as C, H and O in a film containing heavy atoms. Its detection limit is on the order of 0.1 at.%, or $1 \cdot 10^{14}$ at. cm⁻² as an areal density for thin films.³² Table 4.2 shows that the carbon

concentration in all four samples is extremely low (~0.2 at.%) and just in the range of the detection limit of TOF-ERDA. Indeed, only trace carbon is observed in the raw TOF-ERDA data, primarily occurring at the hematite surface (at zero depth in Figure 4.8b-e). It should be noted that the given values represent upper estimates for carbon concentration in the film. No other elements except for H, Ti from the underlayer and Si from the substrate were detected. The hydrogen content is as low as the carbon content and most hydrogen is found to be on the surface. Furthermore, Fe/O ratios of about 2:3 were measured in all four samples confirming direct ALD of Fe₂O₃ at 230 °C. Profiting from the very high detection limit of TOF-ERDA, I could show that this low-temperature ALD process forms remarkably pure Fe₂O₃ films with negligible contamination from byproducts of the low-cost metal-organic precursor. The low level of carbon contamination is most likely achieved due to the use of ozone in the ALD process that successfully oxidizes carbon residues formed during the deposition.

4.3.4 CRYSTALLINITY AND PHASE PURITY

To examine the quality of the ALD films and their coating characteristics, hematite was deposited onto vertically aligned crystalline TiO₂ nanowires (NWs) of 1 – 2 μm in length (aspect ratio of ~13-25) grown hydrothermally on F:SnO₂ substrates.^{31, 33} Though from the point of view of band alignment, TiO₂ is not suitable for hematite, here, these rutile TiO₂ NWs are supposed to mimic a nanostructured F:SnO₂ substrate (rutile), that would be the optimal material for a highly conductive nanostructured scaffold. Figure 4.9a shows the cross-sectional scanning electron microscopy (SEM) image of these TiO₂ NWs coated with a thin layer of ALD-deposited Fe₂O₃. The energy-dispersive X-ray spectroscopy (EDX) element mapping shown in Figure 4.9b confirms the homogenous coverage by Fe₂O₃ throughout the entire sample. However, in SEM-EDX, the X-rays are detected from a large interaction volume within the material, and hence, the spatial resolution is only on the order of a few microns.³⁴ Therefore, I further investigated the quality of the Fe₂O₃ thin film deposition on a single TiO₂ NW by scanning transmission electron microscopy (STEM) coupled with EDX analysis. Elemental mapping on a single nanowire shows complete and conformal coverage with a hematite film of constant thickness (Figure 4.9d-f).

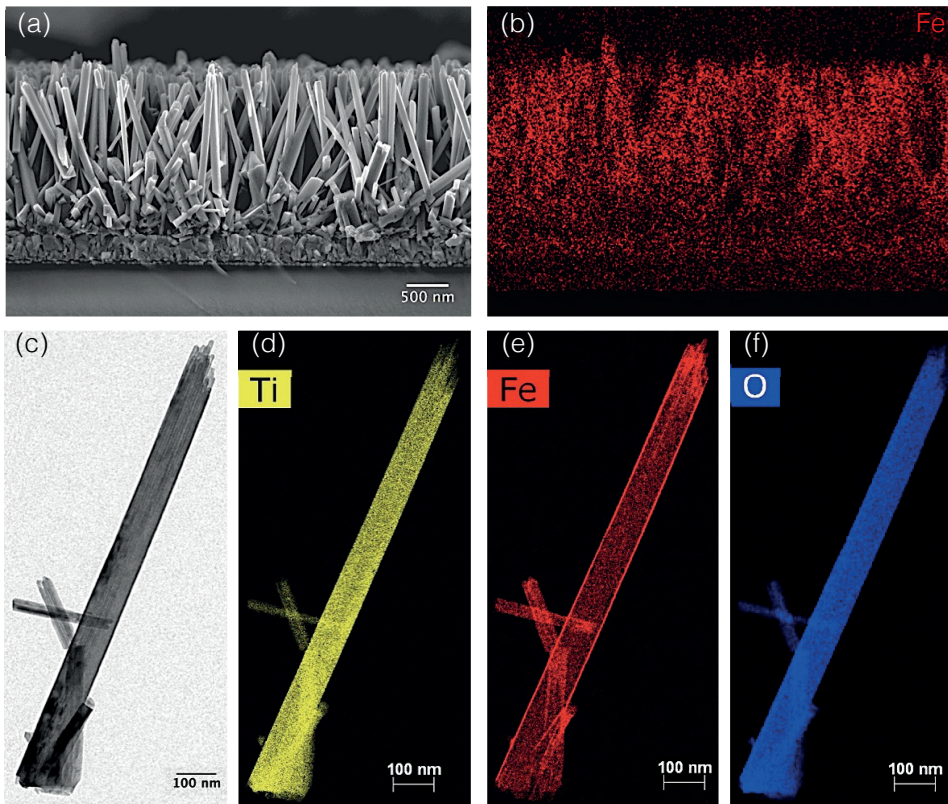


Figure 4.9 a) Cross-sectional SEM and b) SEM-EDX images of TiO_2 NWs grown on F:SnO_2 and coated with 300 cycles of Fe_2O_3 in the $0.02\text{s}/70\text{s}/20\text{s}/0.01\text{s}/70\text{s}/20\text{s}$ mode at a precursor temperature of 90°C . c) Bright-field-TEM image of a single TiO_2 NW coated with Fe_2O_3 . d)-f) STEM-EDX elemental mapping of titanium, iron and oxygen of the wire shown in c).

High-resolution TEM images taken at the edge of the same nanowires confirm the crystalline nature of the as-deposited (Figure 4.10a) and post-annealed hematite films (Figure 4.10b). The film thicknesses were found to be in excellent agreement with that measured by ellipsometry and UV-vis absorption spectroscopy on planar substrates – indicating that there is a sufficient amount of the precursor to homogeneously cover a nanostructure despite the limitation in dose time. From the micrographs it can be observed that the Fe_2O_3 deposition is highly uniform leading to crystalline films with a low degree of roughness. The Fe_2O_3 film growth seems to follow a Stranski–Krastanov growth mechanism where a layer-by-layer growth is competing with nucleation and grain formation in contrast to a Volmer-Weber type mechanism where grain formation is predominant, as was observed for hematite ALD with FeCl_3 and water.²⁶ In Figure 4.10, layer-by-layer growth is predominant showing only a few grains formed (indicated by red arrows). The grain size is on the same scale as the film thickness. Additionally, no grain

boundaries perpendicular to the substrate, which could act as charge transport barriers across the film could be observed in the micrographs.

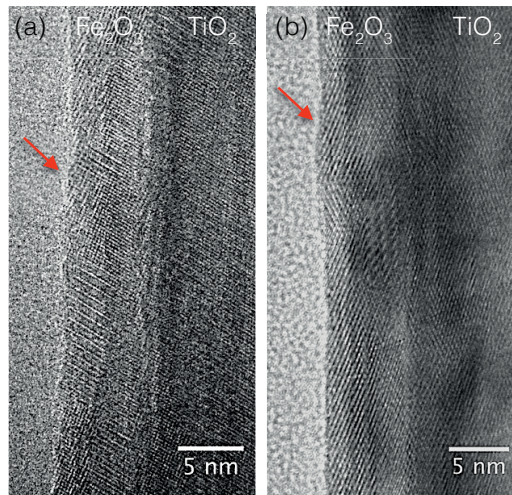


Figure 4.10 HR-TEM bright-field images of the Fe_2O_3 - TiO_2 interface of a) as-deposited and b) Fe_2O_3 annealed at 500 °C for 30 min in air.

The crystallinity of the as-deposited hematite was investigated by X-ray diffraction on films with a thickness of ~ 20 nm (Figure 4.11), confirming the presence of crystalline Fe_2O_3 grown on TiO_2 -coated F: SnO_2 substrates.

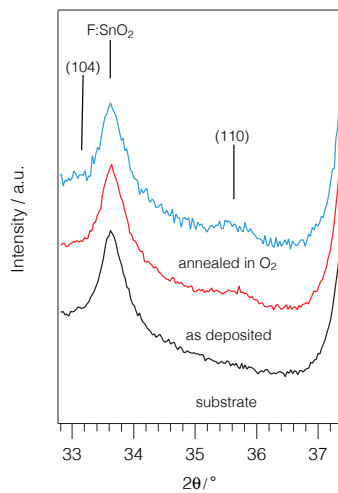


Figure 4.11 X-ray diffraction analysis of as deposited (red) and oxygen annealed hematite films (blue) compared to the F: SnO_2 substrate coated with 1.5 nm of TiO_2 (black).

Phase determination was carried out by Raman spectroscopy which is able to distinctly differentiate between iron oxide phases such as hematite, maghemite and magnetite.³⁵

Figure 4.12 shows the Raman spectra of the substrate material and the hematite samples in their as-deposited and annealed states compared to the reference spectrum of hematite (RRUFF ID R050300).^{36,37} The Raman spectra of annealed and as-deposited ALD films are essentially identical and can be well matched with hematite's reference spectrum, confirming that the as-deposited ALD films are phase-pure hematite and do not undergo phase transitions after annealing in oxygen at 500 °C.

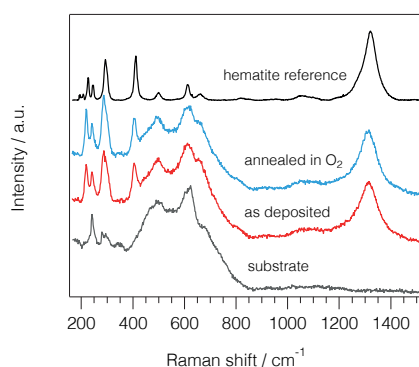


Figure 4.12 Raman spectra of as-deposited (red) and oxygen annealed (blue) ALD hematite films compared to a hematite reference spectrum (black, RRUFF ID R050300). The substrate was F:SnO₂ coated with 1.5 nm TiO₂ (grey).

4.3.5 PHOTOELECTROCHEMICAL PERFORMANCE OF AS-DEPOSITED ALD-HEMATITE FILMS

The data presented thus far confirms the low-temperature ALD of pure and crystalline hematite films with very good aspect ratio coverage within a nanostructured scaffold material. To investigate their intrinsic photoelectrochemical performance, I deposited hematite films on F:SnO₂ substrates coated with a 1.5 nm TiO₂ underlayer. The presence of TiO₂ is motivated by previous work on hematite thin films using functional layers such as SiO₂,¹⁵ SnO₂,³⁸ TiO₂ or Nb₂O₅¹⁴ that prevent electron-hole recombination at the back contact and serve as dopant sources, thereby enhancing the photoelectrochemical performance of thin film hematite photoelectrodes.³⁹ Hematite films of different thicknesses were deposited at a precursor temperature of 90 °C and deposition temperature of 230 °C. Directly after deposition, without any further processing, these films show comparably²⁶ high photoactivities of up to 0.7 mA cm⁻² and 0.5 mA cm⁻² at 1.53 V vs. RHE with and without the use of an underlayer, respectively (Figure 4.13a,b).

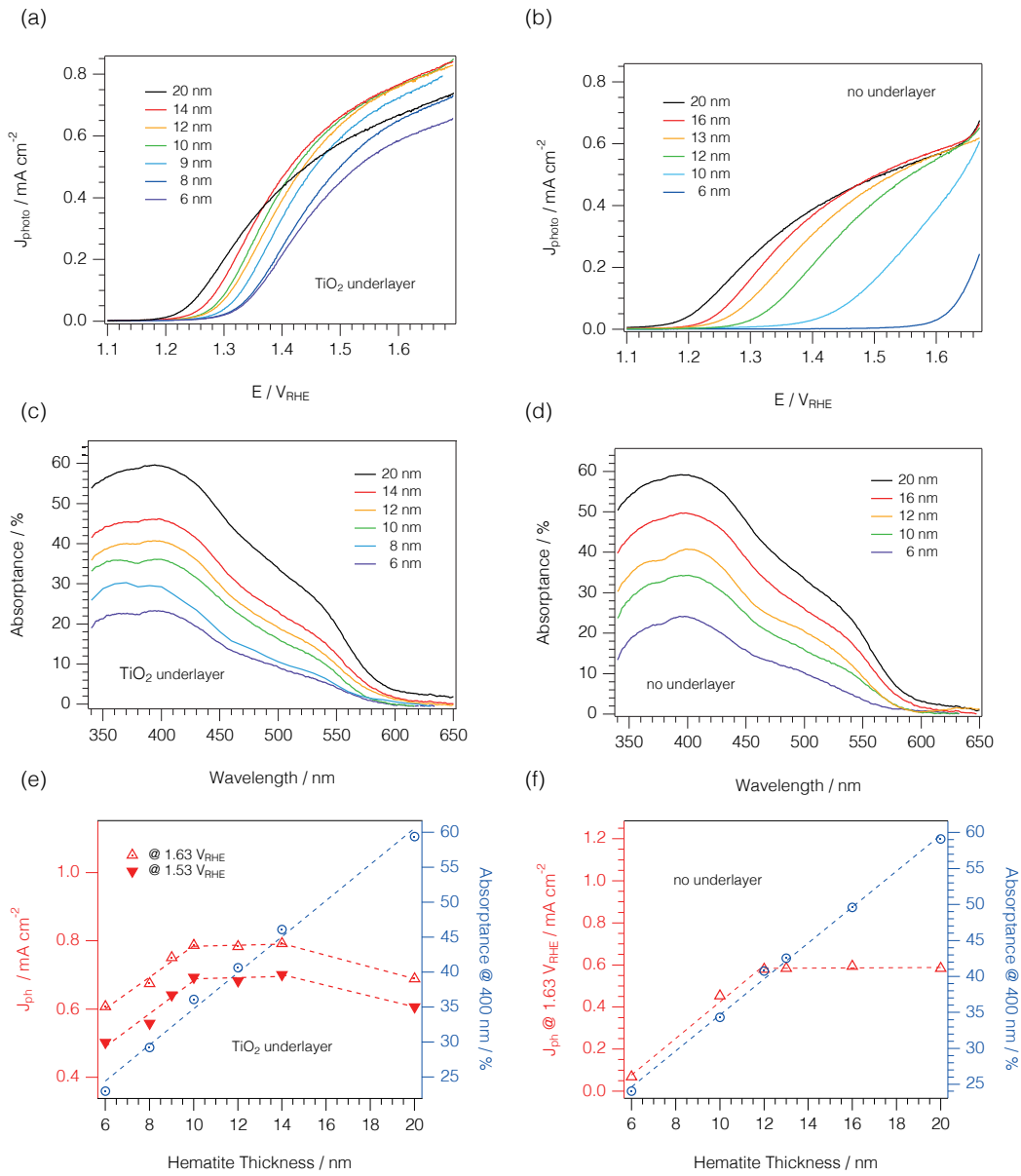


Figure 4.13 Thickness dependent photoelectrochemical analysis on as-deposited hematite thin film photoanodes deposited by DMAMFc/ O_3 ALD. Samples were illuminated from the F:SnO_2 side and measured in 1 M NaOH (pH 13.6). a) Photocurrent density-voltage curves of films deposited on TiO_2 (1.5 nm) coated and b) bare F:SnO_2 substrates. c) Wavelength dependent absorbance measurements of hematite films of different thicknesses employing a TiO_2 underlayer and d) without an underlayer. e) Photocurrent densities of films deposited on TiO_2 (1.5 nm) coated F:SnO_2 substrates extracted at 1.53 V and 1.63 V vs. RHE from J–V measurements shown in (a). Absorbance was taken at a wavelength of 400 nm from the measurements in (c). f) Photocurrent densities of films deposited on F:SnO_2 substrates extracted at 1.63 V vs. RHE from J–V measurements in (b). Absorbance was taken at a wavelength of 400 nm from the measurements in (d).

For this study, film thicknesses were similar for samples with and without an underlayer

as seen in the absorbance spectra (Figure 4.13c,d). This allows for a direct and precise comparison thanks to the precision of ALD. When omitting the use of an underlayer, thicker films are necessary to reach similar photocurrents. For example, only 6 nm hematite deposited on TiO₂-coated F:SnO₂ is sufficient to reach the same photoactivity as a 12 nm film deposited on bare F:SnO₂. This trend has been observed in previous studies where the underlayer strongly enhanced the photoactivity of thin hematite films due to hole blocking and doping.^{39,40} Furthermore, a linear increase in photocurrent is observed for film thicknesses up to 10 nm when a TiO₂ underlayer is present (Figure 4.13e) and up to 12 nm without the underlayer (Figure 4.13f). This linear increase goes in hand with a linear increase in absorbance of these films. Interestingly, for thicker films, the photocurrent plateaus even though thicker films absorb proportionally more light. In the case of hematite films deposited on a TiO₂ layer, the photocurrent even decreases for films as thick as 20 nm approaching the highest photocurrents of the films without any underlayer. Moving towards 3D nanostructured electrode designs, it is crucial to use thin hematite films that are entirely photoactive such that the maximum photocurrent can be extracted from the thinnest possible films to avoid parasitic light absorption. With the aim to find the thinnest and most efficient hematite film, Figure 4.14 shows an extensive thickness dependent study for hematite films in the range of 6 – 20 nm employing a TiO₂ underlayer. The absorbed photon-to-electron conversion efficiency (APCE) is a useful metric to quantify the efficiency of the thin films. In order to see a thickness dependent trend in the quantum efficiencies, values at 400 nm (which is around the absorption maximum of hematite) were extracted from the wavelength dependent quantum efficiency spectra shown in Figure 4.14a,b and plotted against the film thickness (Figure 4.14c). The incident photon-to-current efficiency, IPCE, confirms the observed trend in photocurrent in Figure 4.13e reaching a plateau at 10 nm. The APCE, which relates the generated current to the amount of absorbed photons, is found to peak at a hematite thickness of 10 nm. Thus, I can conclude that the optimal film thickness, meaning the thinnest hematite film with minimal parasitic absorption, is on the order of 10 nm. To further investigate why that is the case, I performed a Mott-Schottky analysis on the same batch of samples used for the photocurrent, absorbance and quantum efficiency studies. From Figure 4.14d, I obtained a flat band potential of $V_{FB} = 0.4 \text{ V vs. RHE}$ and a thickness dependent charge carrier density profile (Figure 4.14e).

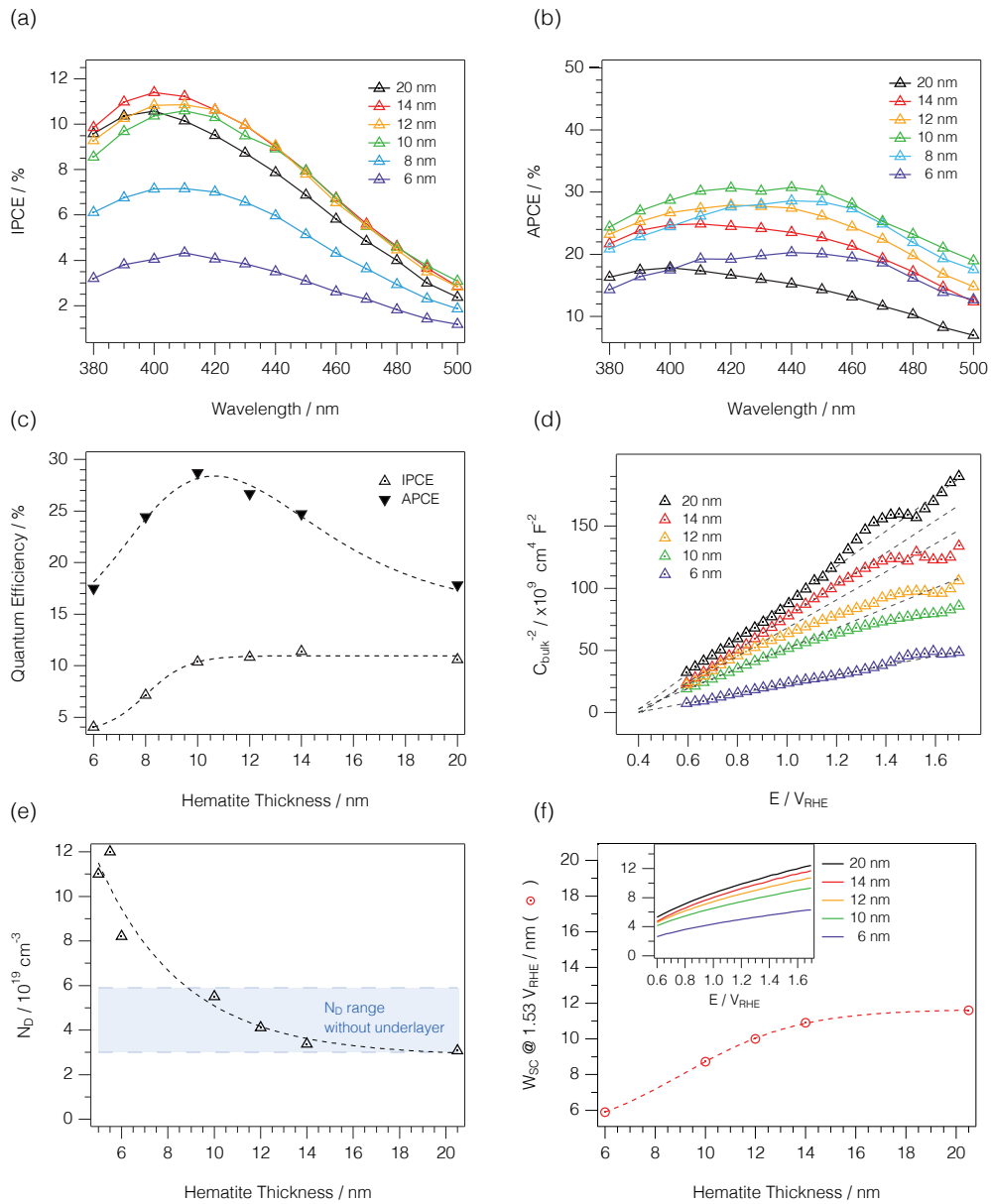


Figure 4.14 Thickness dependent photoelectrochemical analysis on as-deposited hematite thin film photoanodes deposited by DMAMFc/O₃ ALD. Samples were illuminated from the F:SnO₂ side and measured in 1 M NaOH (pH 13.6). a) IPCE measured at 1.53 V vs. RHE and b) APCE for different thicknesses of hematite calculated from the IPCE in a) and the absorptance data in Figure 4.13c. c) Quantum efficiencies measured at 1.53 V vs. RHE and 400 nm. d) Mott-Schottky analysis of impedance measurements carried out in the dark. The electrode area was corrected for the roughness of the F:SnO₂ substrate that was obtained from AFM measurements and cross-sectional SEM images shown in Figure 4.5. The linear region was fitted to extract the flat band potential (V_{FB}) and the charge carrier density (N_{D}). e) Charge carrier density extracted from the analysis in d) for different film thicknesses of hematite. The charge carrier density range for hematite films without an underlayer is indicated in blue. f) Space charge layer width calculated from the flat band potential and charge carrier densities extracted from (d) according to Equation (2.10).

The charge carrier concentration, N_D , decreases with increasing hematite thickness as dopants diffuse from the underlayer in the hematite film. At thicknesses exceeding 10 nm, N_D approaches values measured for my ALD hematite samples without an underlayer, indicating that the Ti dopant diffusion is restricted to the first 10 nm from the underlayer. This would explain the decrease in IPCE for the 20 nm samples and the similar value obtained for samples with and without TiO₂ underlayer (Figure 4.13e,f). The calculated space charge layer width, W_{SC} , is shown in Figure 4.14f. The electric field increases with applied potential, reaching a maximum width of 10-12 nm at 1.53 V vs. RHE. For films in the range of 10-14 nm, the space charge region covers 90-80% of the film at high bias potentials. For a 20 nm thick film, the space charge region represents only 60% of the total thickness. Only 60% of such a film has an electric field for efficient transport and separation of charges. In the other 40%, carriers are likely lost to recombination. Indeed, films thicker than 10 nm absorb a higher number of photons, they are unable to convert them into additional photocurrent since the carriers photo-generated deep within the film cannot reach the surface before recombining with electrons.

Comparing again these ALD hematite films with and without underlayers, the minimum thickness to obtain the maximum possible thin film performance increases to 12 nm when no underlayer is used. The presence of an underlayer is found to effectively reduce the buffer layer of hematite needed to block holes generated close to the back contact from recombining at the F:SnO₂/hematite interface. The maximum photocurrent at high bias potentials remains almost 30% lower as compared to the TiO₂ modified hematite films. Thickness-dependent charge collection efficiencies on ALD grown hematite films have previously pointed to an optimal hematite thickness of around 20 nm.^{41, 42} Here, however, I demonstrate optimal film thicknesses of 10 nm and 12 nm for thin hematite films with and without an underlayer, respectively, that still show comparable or improved photocurrent density plateaus as well as IPCEs.^{41, 43-45} This improved performance is believed to originate from a better F:SnO₂/hematite interface due to the slow formation of crystalline hematite during the ALD process and an even better interface when a functional layer such as TiO₂ is introduced. Furthermore, these ALD hematite films show higher charge carrier densities compared to previous literature ($N_D = 7 \cdot 10^{18} \text{ cm}^{-3}$).³⁸ Higher carrier densities increase the conductivity of the film, and hence may minimize the impact of recombination processes due to an improved charge transport.

To improve the photocurrent onset potential of the as-deposited hematite films high-temperature annealing is usually explored in the literature. Also these ALD hematite films show a shift in photocurrent onset potential of negative 200 mV (Figure a compare black and blue curves) after annealing in oxygen at 500 °C for 30 min. However, a high-temperature annealing step results in a systematic decrease in photocurrent at higher applied potentials. I found that a similar improvement of the onset potential could be obtained by deposition of a Ni(OH)₂ surface catalyst by a simple room-temperature dip-coating process, thereby reaching even slightly better photocurrent onset potentials compared to the 500 °C annealed sample without requiring the thermal treatment (Figure 4.15a). This suggests that the late onset of the as-deposited films is mostly a result of the surface, which may feature dangling bonds or surface defects, which affect the semiconductor-liquid junction, forming surface states. The presence of surface states pinned to a certain potential was observed earlier and is also supported by the data in the inset in Figure 4.14f, where a space charge layer of 5 nm is present at low potentials but no photocurrent is observed before 1.2 V as seen in Figure 4.13a. After catalyst loading, the photocurrent onset potential shifts 300 mV more negative leading to excellent photocurrent densities of 0.3 mA cm⁻² at 1.23 V *vs.* RHE and 0.7 mA cm⁻² at 1.53 V *vs.* RHE for hematite films of only 8 nm in thickness without the need for post-annealing (Figure 4.15a, compare black and red curves). I found that alternative techniques such as electrodeposition⁴⁶ and chemical bath deposition⁴⁷ led to strong darkening of the electrode due to deposition of a thick catalyst layer even if very short deposition times were used. Interestingly, the photocurrent of an 8 nm thin film could be enhanced by the Ni(OH)₂ catalyst to reach photocurrent densities demonstrated for 10-14 nm thick hematite films herein. Such photocurrents had not thus far been obtained for such thin ALD hematite films grown at low-temperature. The as-deposited catalyst layer is found to increase the absorption of the photoanode by only 1% (Figure 4.15b). Furthermore, this catalyst treatment on low-temperature as-deposited hematite films yields photocurrent onset potentials that have previously been achieved only on catalyst-treated annealed hematite films.⁴⁴ Omitting the high-temperature annealing step allows to maintain higher photocurrent plateaus, likely due to a preservation of the charge carrier density distribution in the film.

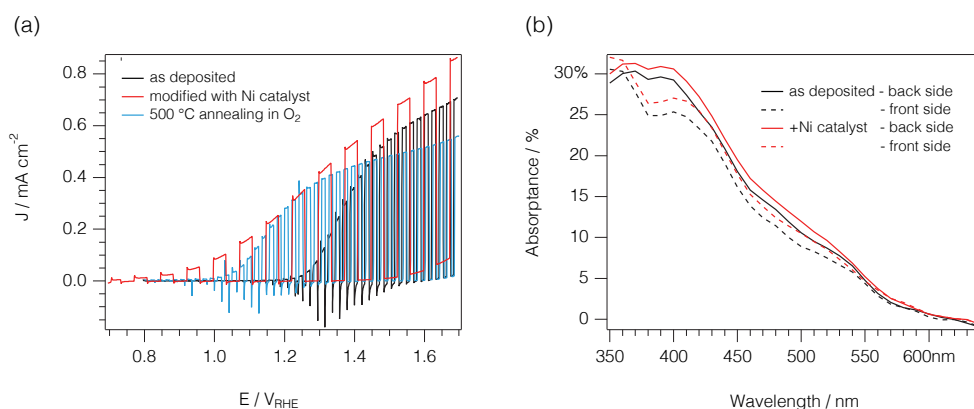


Figure 4.15 a) Current density–potential curves under chopped illumination of as-deposited ALD hematite without any modification (black) and with a $\text{Ni}(\text{OH})_2$ catalyst treatment (red) compared to the unmodified high temperature annealed hematite photoanode (blue). Measurements were carried out with simulated AM 1.5G (100 mWcm^{-2}) light with a scan rate of 10 mV/s for the unmodified and 1 mV/s for the catalyst treated photoanodes. The samples were illuminated from the F:SnO_2 side. The electrolyte was 1 M NaOH (pH 13.6). b) Absorbance of the as-deposited ALD hematite film before (black) and after a Ni catalyst treatment (red) for light hitting first the glass surface (back side) or the hematite/catalyst surfaces (front side). Absorbance calculated after T. Hisatomi *et al.*¹⁴

The advantages of achieving the deposition of a highly active thin-film hematite photoanode without exceeding $230 \text{ }^\circ\text{C}$ in the synthetic steps are at least twofold. First, the energy required for synthesis of active and phase pure material can be significantly reduced, which is important for optimizing the cost and scalability of the technology. Second, the lower temperature opens the possibility of depositing onto a broader range of heat-sensitive substrates, such as onto polymer-based substrates to construct flexible devices, or onto other photoabsorber devices in the construction of multi-junction tandems for driving complete water splitting.

4.3.6 EXAMPLES OF HOST-GUEST HEMATITE PHOTOANODES

The ALD method for hematite thin films is exemplified by fabrication of high-aspect ratio host-guest photoanodes. Three different approaches will be outlined in the following and the results analyzed, compared and evaluated.

TiO_2 nanowire array

The TiO_2 nanowires (NWs) demonstrated as a scaffold material in Figure 4.9 were specifically chosen given a) their single-crystal rutile structure that could mimic the FTO crystal structure as FTO would be the optimal material for a highly conductive

nanostructured scaffold and b) these single crystal nanowires were easily delaminated from the FTO substrate for TEM analysis. However, given the conduction band offset between rutile TiO_2 and hematite, a Schottky barrier contact is formed which would hinder injection from the Fe_2O_3 into the host TiO_2 . With that said, covering the inactive nanowire with a TCO shell could make this nanostructure a useful template for high aspect ratio transparent conductive oxide (TCO) deposition. Indeed, SnO_2 which has a well-aligned conduction band with hematite does not grow in such high density nanowire array so it needs a template be used as high surface area host material. It is very difficult to hydrothermally grow micron thick high aspect ratio SnO_2 nanostructures and examples in literature are sparse.^{48, 49} Different procedures to fabricate SnO_2 nanosheets were tested but did not result in good photoelectrochemical performance. Figure 4.16a-c show the fabrication details of this TiO_2 -core/TCO-shell architecture.

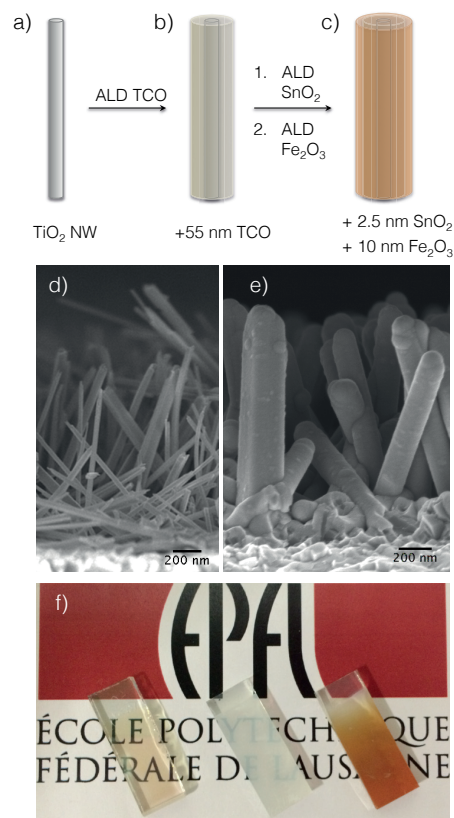


Figure 4.16 Host-guest nanowire architecture. Top: Schematic representation of the fabrication method for a hematite photoanode based on a TCO-coated nanowire array. a) A rutile TiO_2 nanowire is b) coated with 55 nm TCO and subsequently with c) 2.5 nm SnO_2 and 10 nm hematite by ALD. Middle: SEM micrographs of the d) TiO_2 nanowire array deposited using 2.1 mL titanium butoxide. e) TCO-coated TiO_2 nanowire array from d). f) Photograph of a typical ALD hematite thin film on FTO glass (left) compared to the host-guest architecture shown in c) (right). In the middle the TiO_2 nanowire array from d) is shown.

The TiO₂ NWs, which I grew sparser to avoid a formation of a compact blocking TiO₂ layer at the FTO surface, were coated by a recently developed ALD based TCO. This TCO with conductivities up to 300 S/cm was 55 nm thick and was deposited in a conformal manner on the TiO₂ NW template. SEM images in Figure 4.16d and e show the TiO₂ nanowire array before and after TCO ALD respectively. The thickness of the TCO layer was chosen to be thick enough as to minimize the sheet resistance of the coated nanowire. After the deposition of the TCO layer, I deposited a 2.5 nm thick SnO₂ interfacial layer serving as hole blocking layer as well as a doping source for the hematite thin film as discussed before. Finally, the TCO-covered NWs were coated with hematite by ALD as described before. The resulting hematite host-guest photoelectrode is pictured in in Figure 4.16f (right) next to a flat hematite film (left) and the blank TiO₂ NW array. The photoelectrochemical performance is shown in Figure 4.17. Figure 4.17a shows the current density-potential curves under chopped illumination for as-deposited ALD hematite on the TiO₂-NW-TCO array compared to a flat FTO substrate.

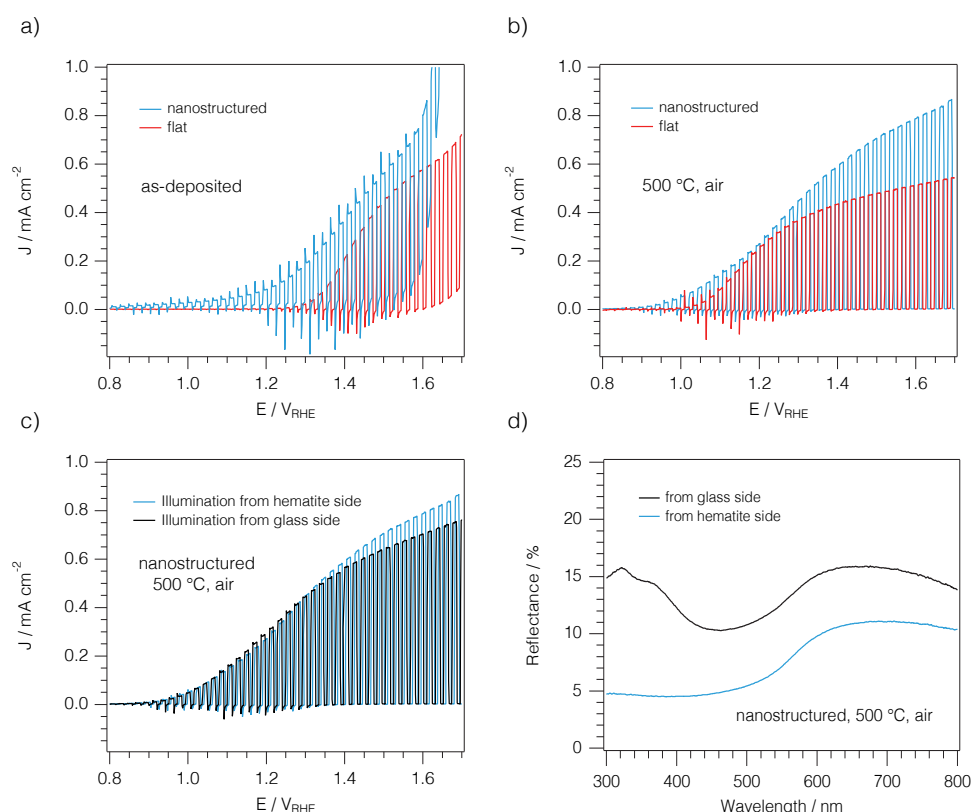


Figure 4.17 Current density-potential curves under chopped illumination of a) as-deposited and b) annealed ALD hematite on a flat FTO substrate (red) and the TiO₂-NW-TCO array (blue). c) Current density-potential curves and d) reflectance measurements of the TiO₂-NW-TCO-hematite electrode from both illumination directions: electrolyte/hematite (blue) and electrolyte/FTO-glass (black).

The nanostructured photoanode shows an earlier photocurrent onset, however, the increase in current density is found to be minor compared to the flat film photoanode shown in red. Interestingly, after annealing at 500 °C in air, the nanostructured photoanode maintains its current density at high potentials compared to the unannealed sample whereas the flat thin film photoanode suffers from the typical decrease in plateau photocurrent as seen also in Figure 4.15. Another point worth noting is that the dark current of both samples (flat and nanostructured) decreases upon calcination at 500 °C such that the photocurrent is approaching a plateau for the annealed films. Comparing the photocurrent at 1.23 V_{RHE}, the TiO₂-NW-TCO nanostructure reaches a photocurrent very similar to the flat film and hence, did not give the desired advantage of higher current densities at the water oxidation potential. Figure 4.17c compares the photocurrent densities of the nanostructured photoanode under different illumination directions: firstly, from the electrolyte/hematite interface and secondly, from the glass-substrate direction. Both illumination directions result in very similar current-density-potential profiles with the only difference that illumination from the electrolyte/hematite interface results in slightly improved photocurrent at high applied potentials. Figure 4.17d shows however, that this difference in photocurrent on the order of 10% is caused by reflection losses that are also 10% higher for the glass backside.

Clearly, the photocurrent response of this type of host-guest photoelectrode did not scale with the increased surface area, which infers that there might be a combination of bottleneck-characteristics for this nanostructure leading to the weak photoelectrochemical performance. These might include:

1. Since the core TiO₂ nanowire is electrochemically inactive, the final projected active area that is in direct contact with the FTO covered substrate is drastically reduced.
2. Though many of the nanowires are well aligned perpendicularly to the substrate, the majority are growing significantly tilted. In the most extreme scenario, where the nanowire is strongly tilted, light absorption will be comparable to that of only two superimposed thin hematite films.
3. The recombination within the TCO and at the TCO/TiO₂ interface might lead to considerable losses.

Inverse opal architecture

A more promising host-guest architecture is the inverse opal (IOP) nanostructure.⁵⁰ Compared to the nanowires that grow always with the same height of 1.4 μm on average (independent precursor concentration in solution) the inverse opal nanostructure is adaptable both in thickness and porosity. The surface area is highly increased and the opals can be grown in a highly ordered manner that could result in beneficial photonic properties or in a disordered structure to enhance light scattering within the inverse opal scaffold.

In collaboration with Dr. Philippe Labouchère and Dr. Nicolas Tétreault inverse opal scaffolds were prepared starting from PMMA spheres as shown in Figure 4.18a-d. In summary, a dispersion of PMMA spheres (\varnothing 500 nm) in isopropanol was doctor bladed on a FTO substrate to form a disordered opal template. Then, 27 nm of SnO_2 were deposited within the opal template pores by ALD. Then the top SnO_2 layer was removed by reactive ion etching (RIE) to reveal the underlying PMMA template to enable its vaporization during the subsequent heat treatment at 500 $^\circ\text{C}$ and avoid cracks. Finally, I deposited a thin interfacial layer of either Nb_2O_5 or TiO_2 by ALD followed by ALD of hematite. The cross-sectional SEM view in Figure 4.18e shows a 6 μm thick IOP structure that is highly disordered. The cross-sectional view (Figure 4.18f) of the SnO_2 IOP coated with hematite shows the detailed multilayer stack through some broken spheres. Subtracting the total wall thickness from the SnO_2 thickness yielded an estimated hematite thickness between 5-8 nm. The photoelectrochemical performance of the IOP structured hematite photoanodes employing Nb_2O_5 or TiO_2 interfacial layers is compared to the flat film performance with the same interfacial layers in Figure 4.18g. Firstly, a doubling of the photocurrent density is achieved with the IOP structured hematite photoanode employing a Nb_2O_5 interfacial layer, whereas the photocurrent density of the equivalent IOP structure employing a TiO_2 interfacial layer is comparable to the performance of a flat film with either of these interfacial layers. Based on the results obtained in Chapter 3 and in this chapter, this strongly suggests that the Nb^{5+} from the Nb_2O_5 interfacial layer is necessary to dope the SnO_2 (while at the same time doping the hematite) and enhance its conductivity. The equivalent Ti^{4+} is not able to n-dope tin oxide. Also in this IOP nanostructure, illumination from the glass side yields lower photocurrent responses for either of the interfacial layers. This is most likely due to similar reflectance losses as shown in Figure 4.17d for the nanowire scaffold.

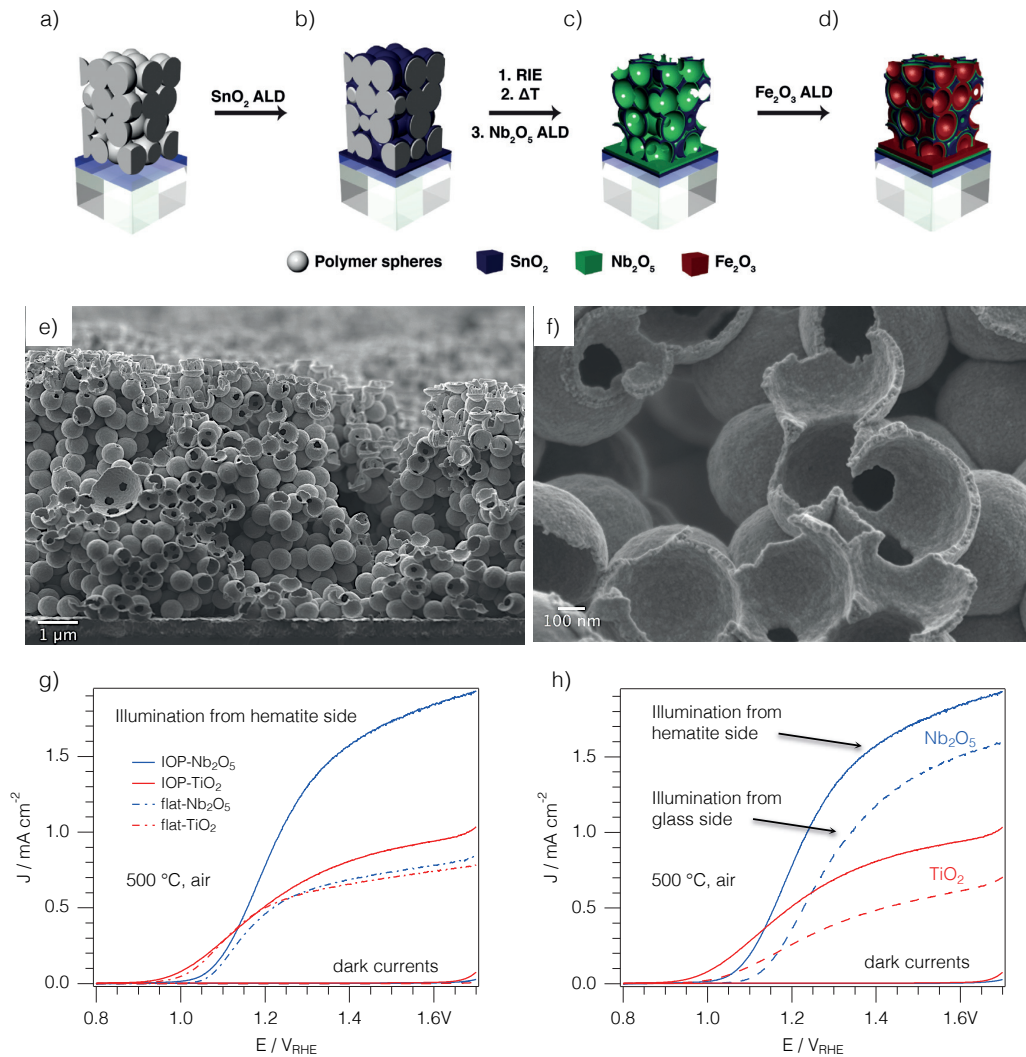


Figure 4.18 Characteristics of a hematite host-guest photoanode employing the inverse opal architecture. a)-d) Schematic representation of the fabrication method for the 3D inverse opal host-guest structure made by sequential atomic layer depositions of the host (SnO_2) and photoabsorber (Fe_2O_3) layers. SEM images of the IOP-hematite photoanode in e) cross-sectional and f) detailed view. The Fe_2O_3 layer was on the order of 5-8 nm making it difficult to see on the micrographs. The thickness of the SnO_2 ALD layer deposited on the PMMA spheres was measured to be 27 nm. The thickness of the hematite was estimated from more detailed SEM images on open spheres with exposed IOP wall cross-sections subtracting the thickness of the SnO_2 layer from the measured thickness of the IOP wall. Current density-potential curves of annealed hematite photoanodes with Nb_2O_5 and TiO_2 interfacial layers comparing the effects of g) nanostructure and h) illumination direction on the photoelectrochemical performance.

The result achieved in this study compares very well to what has been reported by Riha *et al.* with ALD hematite or by others with alternative deposition techniques of hematite.⁵¹⁻

Since the scaffold material has to be conductive enough to transport the electrons efficiently to the back contact without major recombination losses at the interface with hematite, highly conducting transparent oxides would be more suitable than surface doped SnO_2 . Hence, my most recent research was focusing on ITO ($\text{Sn}:\text{In}_2\text{O}_3$) IOPs fabricated by the group of Prof. Erwin Reisner.⁵⁴ The first results on the photoelectrochemical response of the ITO IOP structured hematite photoanode compared to the flat thin film photoanode are shown in Figure 4.19a. I used a 2.5 nm SnO_2 interfacial layer sandwiched between the ITO and hematite. The photocurrent onset of the as-deposited hematite films compares very well to the annealed SnO_2 IOP structures in the previous study and the photocurrent exceeds $1 \text{ mA}/\text{cm}^2$ at potentials higher than $1.4 \text{ V}_{\text{RHE}}$. These results are very promising and are subject to optimization at the moment. The reflection of this IOP scaffold seems to be reduced (but is still present) compared to the SnO_2 IOPs, which might result from the granular feature of the ITO as seen in Figure 4.19b.

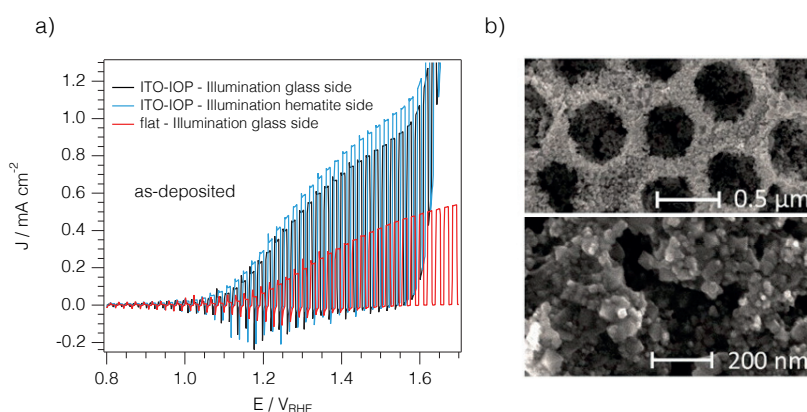


Figure 4.19 a) Current density-potential curves under chopped illumination of as-deposited ALD hematite films on an ITO-IOP scaffold illuminated from the glass side (black) or from the hematite side (blue) and compared to the flat hematite film on FTO (red). b) SEM micrographs of the ITO IOP scaffold reprinted from reference ⁵⁴.

4.4 CONCLUSIONS

In this work I demonstrated a new ALD route producing conformal, smooth, crystalline and phase pure hematite films at $230 \text{ }^\circ\text{C}$ in a fully low-temperature process. It was shown that ALD using DMAMFc and ozone as precursors produces hematite films with exceptionally low levels of carbon contamination (below 0.2 at.%). These high quality films are ideal to study the material's properties on flat model systems and to directly

transfer the knowledge to nanostructured host-guest devices. Applying a TiO_2 underlayer as a dopant source and as a hole blocking layer, a hematite film thickness of only 10 nm was identified as the maximum path length for efficient charge collection, reaching photocurrent densities of up to 0.8 mA cm^{-2} . Such high photocurrents have so far not been demonstrated for hematite films this thin. We found that for films thicker than 10 nm the photoelectrochemical performance was limited by the space charge layer width, while for thinner films, light absorption was the limiting factor. Even without the use of an underlayer, hematite film thicknesses of only 12 nm are sufficient to reach photocurrents comparable with those reported in literature for films almost twice as thick. Efficient charge transport is most likely facilitated by the crystalline and ordered nature of the as-grown hematite films and a better interface between the F:SnO_2 and the hematite film due to my ALD process. Combined with a low-cost Ni(OH)_2 catalyst deposited *via* a facile dip-coating method, the need for an annealing step was successfully avoided, enabling a synthesis process of Fe_2O_3 which at no point exceeds $230 \text{ }^\circ\text{C}$. The development of this low-temperature method can be expected to broaden the application variety of hematite as it could for example be used in pn junction configurations with preserved junction interface.

Going towards nanostructured hematite photoanodes is shown not to be straightforward in order to achieve photocurrent responses linearly proportional with increased surface area. With that said a $6 \mu\text{m}$ thick inverse opal nanostructure gives current densities approaching 2 mA/cm^2 – about double the photocurrent density of a thin hematite film in a flat electrode configuration. It would be helpful to be able to predict the optical and electronic losses when going from a flat thin film to a nanostructured and much more complicated system. The inverse opals structure yielded so far the best results and is hence, the most promising for future host-guest architectures with hematite. Inverse opals have been widely developed in the field of photonic crystals and host-guest materials, which means there is a vast array of detailed fabrication procedures available encompassing the fabrication of a wide range of functional optical and electronic materials. Thus the IOP scaffold is greatly appealing for future research on affordable high efficiency photoelectrochemical water splitting.

4.5 REFERENCES

1. Steier, L.; Luo, J. S.; Schreier, M.; Mayer, M. T.; Sajavaara, T.; Gratzel, M. Low-Temperature Atomic Layer Deposition of Crystalline and Photoactive Ultrathin Hematite Films for Solar Water Splitting. *Acs Nano* **2015**, *9*, 11775-11783.
2. Aronniemi, M.; Saino, J.; Lahtinen, J. Characterization and Gas-Sensing Behavior of an Iron Oxide Thin Film Prepared by Atomic Layer Deposition. *Thin Solid Films* **2008**, *516*, 6110-6115.
3. Chen, J.; Xu, L.; Li, W.; Gou, X. α -Fe₂O₃ Nanotubes in Gas Sensor and Lithium-Ion Battery Applications. *Advanced Materials* **2005**, *17*, 582-586.
4. Luo, J.; Xia, X.; Luo, Y.; Guan, C.; Liu, J.; Qi, X.; Ng, C. F.; Yu, T.; Zhang, H.; Fan, H. J. Rationally Designed Hierarchical TiO₂@Fe₂O₃ Hollow Nanostructures for Improved Lithium Ion Storage. *Advanced Energy Materials* **2013**, *3*, 737-743.
5. Brillet, J.; Yum, J. H.; Cornuz, M.; Hisatomi, T.; Solarska, R.; Augustynski, J.; Gratzel, M.; Sivula, K. Highly Efficient Water Splitting by a Dual-Absorber Tandem Cell. *Nature Photonics* **2012**, *6*, 823-827.
6. Tilley, S. D.; Cornuz, M.; Sivula, K.; Grätzel, M. Light-Induced Water Splitting with Hematite: Improved Nanostructure and Iridium Oxide Catalysis. *Angewandte Chemie International Edition* **2010**, *49*, 6405-6408.
7. Hu, S.; Shaner, M. R.; Beardslee, J. A.; Lichterman, M.; Brunenschwig, B. S.; Lewis, N. S. Amorphous TiO₂ Coatings Stabilize Si, Gaas, and Gap Photoanodes for Efficient Water Oxidation. *Science* **2014**, *344*, 1005-1009.
8. Iordanova, N.; Dupuis, M.; Rosso, K. M. Charge Transport in Metal Oxides: A Theoretical Study of Hematite α -Fe₂O₃. *The Journal of Chemical Physics* **2005**, *122*, 144305.
9. Pendlebury, S. R.; Wang, X.; Le Formal, F.; Cornuz, M.; Kafizas, A.; Tilley, S. D.; Grätzel, M.; Durrant, J. R. Ultrafast Charge Carrier Recombination and Trapping in Hematite Photoanodes under Applied Bias. *Journal of the American Chemical Society* **2014**, *136*, 9854-9857.
10. Frese, K. W.; Kennedy, J. H. Extrinsic Hole Lifetimes for N-Type α -Fe₂O₃ from Photocurrent Transients. *Journal of The Electrochemical Society* **1978**, *125*, C160-C160.
11. Sivula, K.; Le Formal, F.; Gratzel, M. WO₃-Fe₂O₃ Photoanodes for Water Splitting: A Host Scaffold, Guest Absorber Approach. *Chemistry of Materials* **2009**, *21*, 2862-2867.
12. Stefik, M.; Cornuz, M.; Mathews, N.; Hisatomi, T.; Mhaisalkar, S.; Gratzel, M. Transparent, Conducting Nb:Sno(2) for Host-Guest Photoelectrochemistry. *Nano Letters* **2012**, *12*, 5431-5435.
13. Riha, S. C.; Vermeer, M. J. D.; Pellin, M. J.; Hupp, J. T.; Martinson, A. B. F. Hematite-Based Photo-Oxidation of Water Using Transparent Distributed Current Collectors. *Acs Applied Materials & Interfaces* **2013**, *5*, 360-367.
14. Hisatomi, T.; Dotan, H.; Stefik, M.; Sivula, K.; Rothschild, A.; Gratzel, M.; Mathews, N. Enhancement in the Performance of Ultrathin Hematite Photoanode for Water Splitting by an Oxide Underlayer. *Advanced Materials* **2012**, *24*, 2699-2702.
15. Le Formal, F.; Grätzel, M.; Sivula, K. Controlling Photoactivity in Ultrathin Hematite Films for Solar Water-Splitting. *Advanced Functional Materials* **2010**, *20*, 1099-1107.
16. Leskela, M.; Ritala, M. Atomic Layer Deposition (Ald): From Precursors to Thin Film Structures. *Thin Solid Films* **2002**, *409*, 138-146.
17. Lim, B. S.; Rahtu, A.; Gordon, R. G. Atomic Layer Deposition of Transition Metals. *Nature Materials* **2003**, *2*, 749-754.

18. Nilsen, O.; Lie, M.; Foss, S.; Fjellvag, H.; Kjekshus, A. Effect of Magnetic Field on the Growth of Alpha-Fe₂O₃ Thin Films by Atomic Layer Deposition. *Applied Surface Science* **2004**, *227*, 40-47.
19. Lie, M.; Fjellvåg, H.; Kjekshus, A. Growth of Fe₂O₃ Thin Films by Atomic Layer Deposition. *Thin Solid Films* **2005**, *488*, 74-81.
20. Bachmann, J.; Jing, J.; Knez, M.; Barth, S.; Shen, H.; Mathur, S.; Gosele, U.; Nielsch, K. Ordered Iron Oxide Nanotube Arrays of Controlled Geometry and Tunable Magnetism by Atomic Layer Deposition. *Journal of the American Chemical Society* **2007**, *129*, 9554-+.
21. Lin, Y. J.; Zhou, S.; Sheehan, S. W.; Wang, D. W. Nanonet-Based Hematite Heteronanostructures for Efficient Solar Water Splitting. *Journal of the American Chemical Society* **2011**, *133*, 2398-2401.
22. Rooth, M.; Johansson, A.; Kukli, K.; Aarik, J.; Boman, M.; Harsta, A. Atomic Layer Deposition of Iron Oxide Thin Films and Nanotubes Using Ferrocene and Oxygen as Precursors. *Chemical Vapor Deposition* **2008**, *14*, 67-70.
23. Martinson, A. B. F.; DeVries, M. J.; Libera, J. A.; Christensen, S. T.; Hupp, J. T.; Pellin, M. J.; Elam, J. W. Atomic Layer Deposition of Fe₂O₃ Using Ferrocene and Ozone. *Journal of Physical Chemistry C* **2011**, *115*, 4333-4339.
24. Escrig, J.; Bachmann, J.; Jing, J.; Daub, M.; Altbir, D.; Nielsch, K. Crossover between Two Different Magnetization Reversal Modes in Arrays of Iron Oxide Nanotubes. *Physical Review B* **2008**, *77*, 214421.
25. Ramachandran, R. K.; Dendooven, J.; Detavernier, C. Plasma Enhanced Atomic Layer Deposition of Fe₂O₃ Thin Films. *Journal of Materials Chemistry A* **2014**, *2*, 10662-10667.
26. Klug, J. A.; Becker, N. G.; Riha, S. C.; Martinson, A. B. F.; Elam, J. W.; Pellin, M. J.; Proslie, T. Low Temperature Atomic Layer Deposition of Highly Photoactive Hematite Using Iron(III) Chloride and Water. *Journal of Materials Chemistry A* **2013**, *1*, 11607-11613.
27. Kukli, K.; Dimri, M. C.; Tamm, A.; Kemell, M.; Käämbre, T.; Vehkamäki, M.; Puttaswamy, M.; Stern, R.; Kuusik, I.; Kikas, A., *et al.* Structural and Magnetic Studies on Iron Oxide and Iron-Magnesium Oxide Thin Films Deposited Using Ferrocene and (Dimethylaminomethyl)Ferrocene Precursors. *ECS Journal of Solid State Science and Technology* **2013**, *2*, N45-N54.
28. Slack, G. A.; Tanzilli, R. A.; Pohl, R. O.; Vandersande, J. W. The Intrinsic Thermal-Conductivity of Aln. *Journal of Physics and Chemistry of Solids* **1987**, *48*, 641-647.
29. Gu, Z.; Edgar, J. H.; Speakman, S. A.; Blom, D.; Perrin, J.; Chaudhuri, J. Thermal Oxidation of Polycrystalline and Single Crystalline Aluminum Nitride Wafers. *Journal of Electronic Materials* **2005**, *34*, 1271-1279.
30. Laitinen, M.; Rossi, M.; Julin, J.; Sajavaara, T. Time-of-Flight – Energy Spectrometer for Elemental Depth Profiling – Jyväskylä Design. *Nuclear Instruments and Methods in Physics Research Section B: Beam Interactions with Materials and Atoms* **2014**, *337*, 55-61.
31. Luo, J.; Ma, L.; He, T.; Ng, C. F.; Wang, S.; Sun, H.; Fan, H. J. TiO₂/(Cds, Cdse, Cdses) Nanorod Heterostructures and Photoelectrochemical Properties. *The Journal of Physical Chemistry C* **2012**, *116*, 11956-11963.
32. Doyle, B. L.; Peercy, P. S. Technique for Profiling 1h with 2.5 - Mev Van De Graaff Accelerators. *Applied Physics Letters* **1979**, *34*, 811-813.
33. Liu, B.; Aydil, E. S. Growth of Oriented Single-Crystalline Rutile TiO₂ Nanorods on Transparent Conducting Substrates for Dye-Sensitized Solar Cells. *Journal of the American Chemical Society* **2009**, *131*, 3985-3990.

34. <http://www.ammr.org.au/myscope/analysis/eds/> (accessed January 12, 2016)
35. de Faria, D. L. A.; Venâncio Silva, S.; de Oliveira, M. T. Raman Microspectroscopy of Some Iron Oxides and Oxyhydroxides. *Journal of Raman Spectroscopy* **1997**, *28*, 873-878.
36. Glasscock, J. A.; Barnes, P. R. F.; Plumb, I. C.; Bendavid, A.; Martin, P. J. Structural, Optical and Electrical Properties of Undoped Polycrystalline Hematite Thin Films Produced Using Filtered Arc Deposition. *Thin Solid Films* **2008**, *516*, 1716-1724.
37. <http://rruff.info/Hematite/R050300> (accessed April 2015)
38. Liang, Y. Q.; Enache, C. S.; van de Krol, R. Photoelectrochemical Characterization of Sprayed Alpha-Fe₂O₃ Thin Films: Influence of Si Doping and SnO₂ Interfacial Layer. *International Journal of Photoenergy* **2008**.
39. Steier, L.; Herraiz-Cardona, I.; Gimenez, S.; Fabregat-Santiago, F.; Bisquert, J.; Tilley, S. D.; Grätzel, M. Understanding the Role of Underlayers and Overlayers in Thin Film Hematite Photoanodes. *Advanced Functional Materials* **2014**, *24*, 7681-7688.
40. Zandi, O.; Beardslee, J. A.; Hamann, T. Substrate Dependent Water Splitting with Ultrathin α -Fe₂O₃ Electrodes. *The Journal of Physical Chemistry C* **2014**, *118*, 16494-16503.
41. Klahr, B. M.; Martinson, A. B. F.; Hamann, T. W. Photoelectrochemical Investigation of Ultrathin Film Iron Oxide Solar Cells Prepared by Atomic Layer Deposition. *Langmuir* **2011**, *27*, 461-468.
42. Dotan, H.; Kfir, O.; Sharlin, E.; Blank, O.; Gross, M.; Dumchin, I.; Ankonina, G.; Rothschild, A. Resonant Light Trapping in Ultrathin Films for Water Splitting. *Nature Materials* **2013**, *12*, 158-164.
43. Klahr, B.; Gimenez, S.; Fabregat-Santiago, F.; Bisquert, J.; Hamann, T. W. Electrochemical and Photoelectrochemical Investigation of Water Oxidation with Hematite Electrodes. *Energy & Environmental Science* **2012**, *5*, 7626-7636.
44. Klahr, B.; Gimenez, S.; Fabregat-Santiago, F.; Bisquert, J.; Hamann, T. W. Photoelectrochemical and Impedance Spectroscopic Investigation of Water Oxidation with "Co-Pi"-Coated Hematite Electrodes. *Journal of the American Chemical Society* **2012**, *134*, 16693-16700.
45. Lin, Y. J.; Xu, Y.; Mayer, M. T.; Simpson, Z. I.; McMahon, G.; Zhou, S.; Wang, D. W. Growth of P-Type Hematite by Atomic Layer Deposition and Its Utilization for Improved Solar Water Splitting. *Journal of the American Chemical Society* **2012**, *134*, 5508-5511.
46. Xia, X.; Tu, J.; Zhang, Y.; Chen, J.; Wang, X.; Gu, C.; Guan, C.; Luo, J.; Fan, H. J. Porous Hydroxide Nanosheets on Preformed Nanowires by Electrodeposition: Branched Nanoarrays for Electrochemical Energy Storage. *Chemistry of Materials* **2012**, *24*, 3793-3799.
47. Xia, X.; Luo, J.; Zeng, Z.; Guan, C.; Zhang, Y.; Tu, J.; Zhang, H.; Fan, H. J. Integrated Photoelectrochemical Energy Storage: Solar Hydrogen Generation and Supercapacitor. *Sci. Rep.* **2012**, *2*.
48. Her, Y. C.; Wu, J. Y.; Lin, Y. R.; Tsai, S. Y. Low-Temperature Growth and Blue Luminescence of SnO₂ Nanoblades. *Applied Physics Letters* **2006**, *89*.
49. Zhang, L.; Wu, H. B.; Lou, X. W. Growth of SnO₂ Nanosheet Arrays on Various Conductive Substrates as Integrated Electrodes for Lithium-Ion Batteries. *Materials Horizons* **2014**, *1*, 133-138.
50. Tétreault, N.; Arsenaault, É.; Heiniger, L.-P.; Soheilnia, N.; Brillet, J.; Moehl, T.; Zakeeruddin, S.; Ozin, G. A.; Grätzel, M. High-Efficiency Dye-Sensitized Solar Cell with Three-Dimensional Photoanode. *Nano Letters* **2011**, *11*, 4579-4584.

-
51. Shi, X.; Zhang, K.; Shin, K.; Moon, J. H.; Lee, T. W.; Park, J. H. Constructing Inverse Opal Structured Hematite Photoanodes Via Electrochemical Process and Their Application to Photoelectrochemical Water Splitting. *Physical Chemistry Chemical Physics* **2013**, 15, 11717-11722.
 52. Yoon, K. Y.; Lee, J. S.; Kim, K.; Bak, C. H.; Kim, S. I.; Kim, J. B.; Jang, J. H. Hematite-Based Photoelectrochemical Water Splitting Supported by Inverse Opal Structures of Graphene. *Acs Applied Materials & Interfaces* **2014**, 6, 22634-22639.
 53. Riha, S. C.; Klahr, B. M.; Tyo, E. C.; Seifert, S.; Vajda, S.; Pellin, M. J.; Hamann, T. W.; Martinson, A. B. F. Atomic Layer Deposition of a Submonolayer Catalyst for the Enhanced Photoelectrochemical Performance of Water Oxidation with Hematite. *ACS Nano* **2013**, 7, 2396-2405.
 54. Mersch, D.; Lee, C.-Y.; Zhang, J. Z.; Brinkert, K.; Fontecilla-Camps, J. C.; Rutherford, A. W.; Reisner, E. Wiring of Photosystem II to Hydrogenase for Photoelectrochemical Water Splitting. *Journal of the American Chemical Society* **2015**, 137, 8541-8549.

5 QUANTITATIVE ANALYSIS OF OPTICAL LOSSES IN PHOTOELECTROCHEMICAL CELLS BASED ON HEMATITE PHOTOANODES

This chapter is based on the work in collaboration with Peter Cendula, Paolo Losio and Jürgen Schuhmacher from Institute of Computational Physics, ZHAW, Winterthur. I was working on the experimental characterization of the hematite photoanodes and the FTO substrate by means of ellipsometry, UV-Vis spectroscopy, TEM analysis and PEC analysis. The ZHAW Team developed the optical model of light propagation through the coherent and incoherent layers in the PEC cell.

The optical losses in a photoelectrochemical (PEC) cell play a substantial role in achieving high overall solar-to-hydrogen conversion efficiencies, but their quantitative analysis is sparse partially because the optical losses cannot be measured directly in an experiment and their quantification requires accurate knowledge of the optical constants of all individual layers. In this work, a detailed analysis of the optical losses of a typical PEC cell is presented. Based on spectroscopic measurements, an optical model of both coherent and incoherent layers is developed. The optical model is verified for hematite photoanodes fabricated by atomic layer deposition (ALD). The optical model is a valuable tool for detailed optical loss analysis of a PEC cell and prerequisite for a coupled optoelectronic model of a PEC device.

5.1 INTRODUCTION

5.1.1 BACKGROUND OF PEC OPTICAL MODELING

Since the band edges of hematite and most of the absorbers used in photoelectrochemical (PEC) water splitting, do not straddle the water reduction and oxidation electrochemical potentials, unassisted water splitting would only be possible in a dual light absorber design.¹⁻⁵ In such a design, light absorption of the two semiconductors has to be optimized and parasitic optical losses outside of the semiconductors have to be minimized in order to achieve the highest quantum efficiencies. As experimental methods cannot provide direct access to the absorptances in the individual layers of a PEC cell, optical modeling (OM) is a powerful tool to analyze the wavelength-dependent absorptance of each layer. Contrary to other solar cell technologies, only few reports can be found in the literature on the modeling and quantification of optical losses in a typical PEC cell.⁶⁻⁸ Han *et al.* optimized quantum efficiencies for PEC water splitting for a BiVO₄ photoanode in tandem with amorphous silicon double junction solar cells.^{3,9} Furthermore, Döscher *et al.* studied the effect of light absorption in aqueous electrolytes of different thicknesses on the solar-to-hydrogen (STH) efficiency limitations.¹⁰ Though light absorption in the electrolyte layer was extensively studied in that study, absorption by other layers of the PEC cell was not taken into account. Some recent studies focused on the hematite layer and reported on the increase in light absorption in the absorber by light trapping through back-reflectors¹¹ or nanocone arrays.¹² So far, literature on modeling of fluid flow, electrochemistry or charge transport in PEC water splitting is based only on simple Lambert-Beer light absorption, thereby neglecting coherence in thin films¹³⁻¹⁶ or disregarding optical processes completely.^{17, 18}

This chapter focuses on the optical characterization of hematite thin films deposited by atomic layer deposition as a basis for the development of a model of light propagation in a PEC cell, which is capable of quantifying optical losses in all layers present in a typical PEC cell. Light propagation is described in coherent layers (thickness comparable to the wavelength of light) with the transfer-matrix method¹⁹ and in incoherent layers (thickness larger than the wavelength of light) by ray-tracing geometrical optics.²⁰ To obtain a good overlap of the simulated and measured results with the optical model, an accurate and detailed optical characterization of the individual layers is essential. Therefore, the first

step in this work is to extract all wavelength-dependent refractive indices and extinction coefficients from spectroscopic ellipsometry and UV-Vis spectroscopy measurements and then to implement them in the optical model in the second step. The proper parameterization of the optical constants is confirmed with the ability of the optical model to reproduce the UV-Vis responses of various samples. After this validation, the optical model is applied to calculate spectrally resolved optical losses in the PEC cell and to obtain total integrated optical losses by reflection, transmission and absorption outside of the semiconductor. The charge generation rate from the OM shows limitations of the Lambert-Beer law and can be used in coupled optoelectronic PEC models.

5.1.2 THEORY OF OPTICAL MODELING

In a typical PEC cell as shown on the right of Figure 5.1, light is interacting with multiple layers of different optical properties. First the light is passing through a quartz window of 4 mm in width.

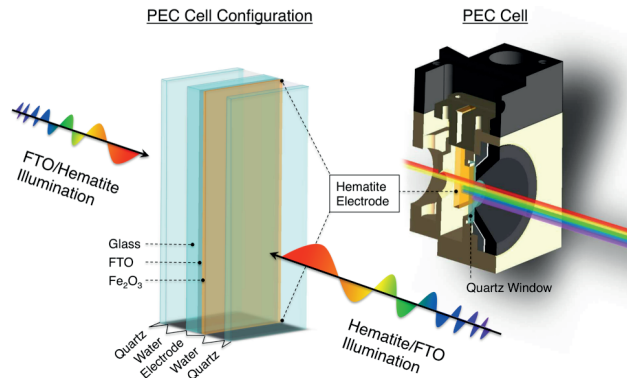


Figure 5.1 Schematic of the light path through a typical photoelectrochemical (PEC) cell (shown in cross-sectional view). The sequence of layers (quartz/water/electrode/water/quartz) represents the sequence during a PEC measurement. This “PEC cell configuration” was used for all UV-Vis measurements and simulations in this work. Thicknesses of the layers are scaled for the purpose of presentation.

Then it traverses a 0.4 mm thick electrolyte layer. Although water oxidation with hematite photoanodes is usually tested in alkaline aqueous electrolytes such as NaOH, here, all UV-vis measurements were performed with pure water to avoid crystallization of NaOH in the thin water layer. Hence, optical properties of the actual electrolyte are assumed to be equal to those of water.²¹ After having passed the quartz window and the electrolyte, light is hitting the electrode surface and is partially or fully absorbed by the

photoactive layers. The optical model accounts for both illumination directions that are shown in Figure 5.1.

- a) Hematite/FTO illumination direction
- b) FTO/hematite illumination direction

In case (a), light impinges first on the photo-absorber (here hematite) and then passes the FTO substrate. In case (b), light passes first the FTO-substrate before reaching the photo-absorber. All layers shown in Figure 5.1 are included during optical modeling with accurate complex index of refraction

$$\tilde{n}_l(\lambda) = n_l(\lambda) + ik_l(\lambda) \quad (5.1)$$

where n_l and k_l are the wavelength dependent refractive indices and extinction coefficients of layer l respectively. The n and k values of each layer cannot be extracted directly but rather have to be calculated indirectly from the dielectric constant ϵ_l that consists of the real (ϵ_r) and imaginary part (ϵ_i) according to Equation (5.2).

$$\epsilon_l(\lambda) = \epsilon_{r,l}(\lambda) + i\epsilon_{i,l}(\lambda) = \tilde{n}_l^2(\lambda) \quad (5.2)$$

Once the dielectric constants are extracted from ellipsometry measurements, n and k data of each layer can be calculated using Equations (5.3) and (5.4).

$$\epsilon_{r,l}(\lambda) = n_l^2(\lambda) - k_l^2(\lambda) \quad (5.3)$$

$$\epsilon_{i,l}(\lambda) = 2n_l(\lambda)k_l(\lambda). \quad (5.4)$$

The wavelength dependent absorption coefficient $\alpha(\lambda)$ of layer l is computed from the extinction coefficient by

$$\alpha_l(\lambda) = \frac{4\pi k_l(\lambda)}{\lambda} \quad (5.5)$$

The optical model treats light propagation and absorption in coherent layers with the transfer-matrix method, calculating the propagation of the electric field in the multilayer stack by matrix operations derived from Fresnel equations of all interfaces in the cell.¹⁹ Optical propagation in incoherent layers is described by following geometric light rays and their reflections and transmissions (including attenuation in absorbing media) in the multilayer cell recursively until their intensity drops below a certain threshold. The

energy conservation is fulfilled during optical modeling and it holds

$$R_{tot}(\lambda) + \sum_l A_l(\lambda) + T_{tot}(\lambda) = 1 \quad (5.6)$$

where R_{tot} is the total reflectance, A_l denotes absorptance of layer l and T_{tot} is the total transmittance.^{19, 22} The rough/porous layer is described with the Bruggemann effective medium approximation²³

$$p \frac{n_a^2 - n_e^2}{n_a^2 + 2n_e^2} + (1 - p) \frac{n_b^2 - n_e^2}{n_b^2 + 2n_e^2} = 0 \quad (5.7)$$

where medium a is enclosed in medium b with fraction p (porosity) and the resulting effective medium has an effective refractive index n_e . The presented optical losses can be quantified also in terms of photocurrent, if ideal conversion of every photon to separated electron-hole pair is assumed. The photocurrent loss by reflection, transmission and absorption is calculated by integrating the product of R_{tot} , T_{tot} and A_l with the incident spectral photon flux $\phi(\lambda)$ [$s^{-1} m^{-2}$] of AM 1.5G illumination

$$\{j_R, j_{A_l}, j_T\} = e \int_{\lambda} \{R_{tot}(\lambda), A_l(\lambda), T_{tot}(\lambda)\} \phi(\lambda) d\lambda \quad (5.8)$$

where $e = 1.602 \cdot 10^{-19}$ C is the electronic charge.

Here, I present a the optical characterization of each layer in the PEC cell shown in Figure 5.1, as a basis for the development of an optical model to account for all optical losses in a PEC device. Identifying the optical losses in the PEC system will help minimizing losses in the final photocurrent of the PEC device and allow for a proper calculation of current matched dual-absorber tandem devices.

5.2 METHODS

5.2.1 TRANSMISSION ELECTRON MICROSCOPY

TEM measurements of the FTO substrate (TCO22-15, Solaronix SA, Switzerland) were carried out on a Technai Osiris (FEI, USA) with a built-in EDX unit. To avoid charging of the sample, a thick Au layer was sputtered using a DP650 (Alliance Concept). A thin TEM lamella was prepared with a Focused Ion Beam to obtain a cross-section of the FTO substrate.

5.2.2 ELLIPSOMETRY AND SAMPLE PREPARATION

Ellipsometry measurements of the FTO substrate as well as of the hematite layer were carried out on a Sopra GES 5E variable angle ellipsometer in the wavelength range of 0.25–1.2 μm . Prior to the measurement, the FTO substrate was wiped with acetone and cleaned for 10 min in piranha solution ($\text{H}_2\text{SO}_4/\text{H}_2\text{O}_2 = 3:1$). For the determination of the optical constants of the Tec glass, the SnO_2 was etched with nascent hydrogen generated by the reaction of Zn powder with an aqueous HCl solution (2 M). Hematite was deposited on FTO, Si wafer and quartz substrates by atomic layer deposition as described in Chapter 4. These samples were rinsed with water only. Optical constants of hematite were determined on Si wafer and on quartz substrates and no difference in the dispersion law was observed for as-deposited and annealed Fe_2O_3 films. The obtained spectra of the Tec glass and the hematite were fitted with WinElli II software.

5.2.3 UV-VIS MEASUREMENTS

Transmission and diffuse as well as total reflectance measurements were carried out with a UV-3600 spectrometer (Shimadzu Scientific Instruments, USA) equipped with an integrating sphere. Samples were cleaned as described in 5.2.2. To mimic the conditions in a typical PEC cell, most samples were measured in a “PEC Cell Configuration” as shown in Figure 5.1 where the sample is sandwiched between two quartz slides that have been wetted with a droplet of water. Only some measurements were performed in an “air/sample/air” configuration. For the band gap determination from diffuse reflectance measurements, hematite was deposited on the TiO_2 nanowires described in Chapter 4 to ensure a good scattering signal. An absorption coefficient equivalent was calculated after Kubelka-Munk according to

$$F(R) = \frac{(1-R)^2}{2R} \quad (5.9)$$

where R is the diffuse reflectance. The band gap was determined from Tauc plots according to

$$\alpha h\nu = A(h\nu - E_g)^{\frac{n}{2}} \quad (5.10)$$

with $n = 1$ for a direct allowed transition and $n = 4$ for an indirect band gap.

5.2.4 OPTICAL MODELLING

Optical model calculations were implemented using the SCOUT software.^{24,25} The data was then exported to SETFOS²⁶ for the optical modeling of the PEC cell.

5.3 RESULTS

In this study, the electrode is a thin film hematite photoanode as described in Chapters 3 and 4. Briefly, a thin layer of hematite is coated by ALD on a conductive FTO substrate. As shown in Chapters 3 and 4, hematite shows much higher photoactivity in the presence of a thin oxide interfacial layer. Hence, also for the OM herein, a thin (1.5 nm) layer of TiO_2 is implemented and the final configuration is shown in Figure 5.2a. The conductive FTO substrate itself has a multilayer structure of the following: float glass/ SnO_2 / SiO_2 /F: SnO_2 . A detailed view is shown in Figure 5.2b,c.

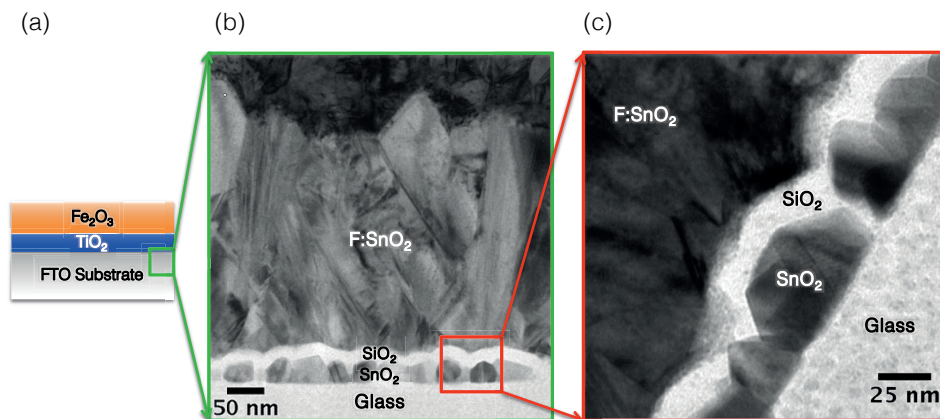


Figure 5.2 Photoanode layer composition. a) Sketch of the thin film hematite photoanode. b) TEM micrograph in cross-sectional view of the FTO substrate. c) Detailed TEM view on the SnO_2 and SiO_2 layers of the substrate.

5.3.1 EXTRACTION OF OPTICAL PARAMETERS OF THE TEC15 SUBSTRATE

The extraction of the n,k parameters of the F: SnO_2 layer is facilitated if the approximate thicknesses of each layer are known in order to initialise values of the fitting parameters. Therefore, average thicknesses were extracted from the TEM micrographs in Figure 5.2 (Table 5.1.) that were used in the fitting of the FTO substrate.

Table 5.1 Average thicknesses of the FTO substrate. F:SnO₂, SiO₂ and SnO₂ thicknesses are taken from the TEM micrographs in Figure 5.2b,c from 10 different points.

Layer	Glass	SnO ₂	SiO ₂	F:SnO ₂
Thickness	2.25 mm	27.8 ± 7.7 nm	15.3 ± 1.9 nm	314 ± 29 nm

5.3.1.1 FLOAT GLASS

First, I determined the optical constants of the float glass layer from an etched FTO substrate. The n, k data of the extracted refractive index and extinction coefficient are shown in Figure 5.3a and are compared to a reference Pilkington low iron Optiwhite™ glass with very similar transmission characteristics.²⁷ The extinction coefficient is similar to the Pilkington glass. In the FTO fitting, n, k parameters of Pilkington Optiwhite glass were compared to the parameters of Tec glass measured in this work. The optical constants from this work allowed for a better fit confirming their accuracy. Transmittance and reflectance of the etched Tec glass are shown in Figure 5.3b for illumination either from the etched side or from the backside of the FTO substrate. The total reflectance ($R_{\text{diffuse}} + R_{\text{specular}}$) is higher when the sample is illuminated from the glass backside leading to a 2.5% loss in transmittance.

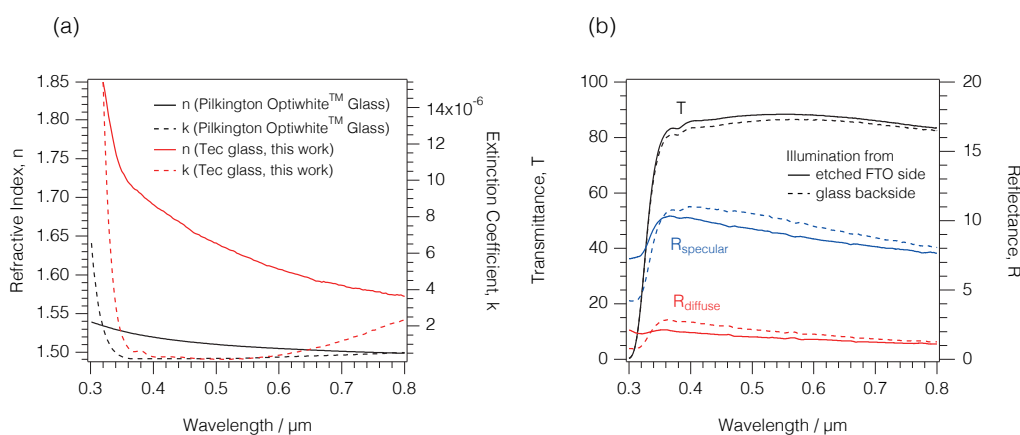


Figure 5.3 Optical characterization of the float glass used in Tec15 substrates. F:SnO₂ and SnO₂ layers were etched for these measurements. a) Optical constants of float glass measured in this work compared to referenced optical constants of Pilkington Optiwhite glass.²⁷ b) UV-vis measurements obtained with an integrating sphere. The specular reflectance was calculated from the measured total and diffuse reflectance according to $R_{\text{total}} = R_{\text{specular}} + R_{\text{diffuse}}$.

The float glass was fitted with a modified Cauchy dispersion law. The refractive index and the extinction coefficient were calculated with the following equations

$$n = A + \frac{B}{\lambda} + \frac{C}{\lambda^2} \tag{5.11}$$

$$k = D + \frac{E}{\lambda} + \frac{F}{\lambda^2} \tag{5.12}$$

Table 5.2 Fitting parameters for the modified Cauchy law for fitting of the float glass in Tec15 samples.

A	B	C	D	E	F
1.508	4.96E-03	4.611E-04	3.184E-06	-9.931E-07	8.830E-08

5.3.1.2 SILICON DIOXIDE LAYER

Optical constants of the SiO₂ thin film that is part of the FTO substrate, were adapted from the refractive index database, to avoid any fitting errors of the SiO₂ layer that is rough and 20x thinner than the F:SnO₂ that is to be characterized. Figure 5.4 shows the refractive index of SiO₂ thin films measured by Gao *et al.* that is in very good agreement with the fitted n values of the SiO₂ layer in a Tec15 substrate measured by Chen.^{27, 28}

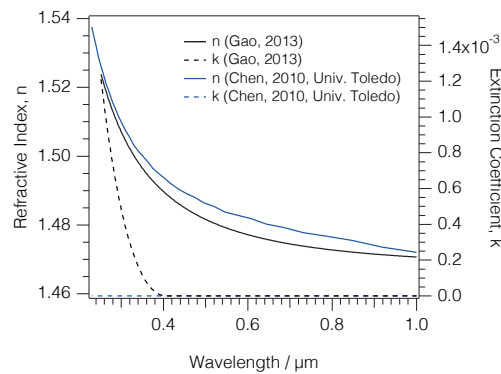


Figure 5.4 Optical constants of SiO₂ thin films adapted from Gao *et al.* and Chen.^{27, 28}

5.3.1.3 INTRINSIC TIN OXIDE LAYER

For the intrinsic SnO₂ layer, optical constants of several references were compared with the fitted results of this work. The refractive indices obtained in this work overlap very well with the ones measured by Chen.²⁷ However, they are slightly lower than the refractive indices measured by Reddaway *et al.* and Rankhshani *et al.*, which could result from different properties of the SnO₂ used in the different works.^{29, 30}

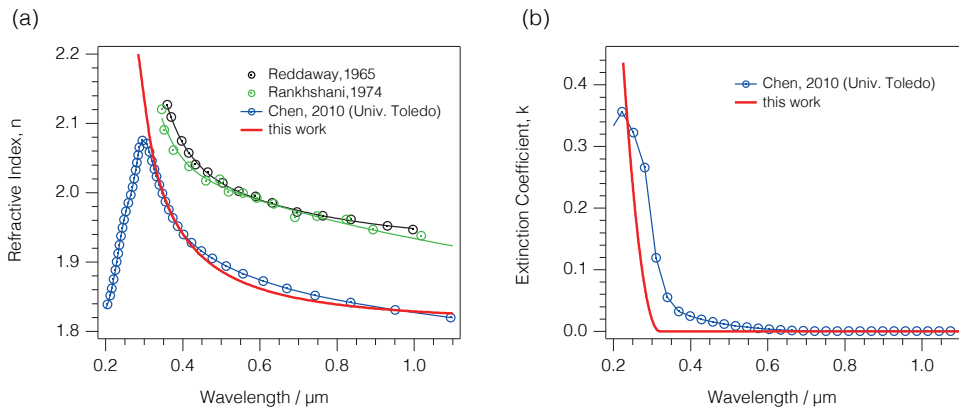


Figure 5.5 Optical constants of intrinsic crystalline SnO_2 . a) Refractive index and b) extinction coefficient of SnO_2 adapted from references ^{27, 29, 30}

Furthermore, while in Chen's work and herein the SnO_2 layer is less than 30 nm, the thinnest layer that Reddaway *et al.* investigated was 31 μm thick and in the case of Rankhshani *et al.* films were on the order of 300 nm.

Moreover, as visible by the black interruptions in the EDX spectrum in Figure 5.6a, the intrinsic thin SnO_2 layer in the Tec15 substrate is not continuous and rough relative to its layer thickness. As seen in Figure 5.6b, the thin SiO_2 layer covers the partially exposed glass and intermixes with the SnO_2 . This inhomogeneity in the SnO_2 layer could lead to the slight deviations in the refractive indices for different SnO_2 samples. From Figure 5.6b, a roughness factor of 1.013 was estimated, that is slightly lower than determined in Figure 4.5.

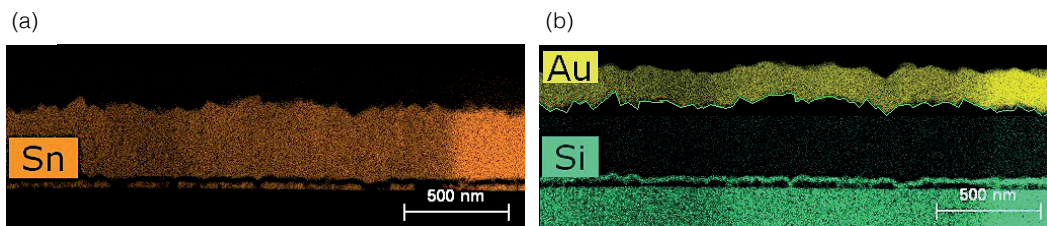


Figure 5.6 TEM-EDX analysis of a FIB lamella of the FTO substrate coated with a gold layer to avoid charging of the sample under the electron beam. a) X-ray signal of tin (Sn). b) X-ray signal of silicon (Si) superimposed with the X-ray signal of gold (Au). The interface between the gold and the FTO was measured against the projected length and the surface roughness factor was determined to be 1.013 that is even lower than determined in Figure 4.5.

The intrinsic SnO_2 film was modeled combining a constant dielectric term and OJL model.³¹ The OJL model is an interband (valence to conduction band) optical transition model with assumed parabolic bands and tail states exponentially decaying into the band

gap. The parameters of the OJL model are the gap energy E_0 , the tail state exponent 'gamma', the strength of the transition and a decay parameter necessary to enforce zero imaginary part at high frequencies.

5.3.1.4 EXTRACTION OF OPTICAL PARAMETERS OF THE FLUORINE DOPED TIN OXIDE LAYER

The doped SnO_2 film was approximated by combining the dielectric function of intrinsic SnO_2 with a Drude model and an additional harmonic oscillator. The Drude model accounts for the free carriers in metals and highly doped semiconductors such as transparent conductive oxides. Roughness of the F: SnO_2 layer was modeled with a Bruggemann effective medium approximation (EMA).²³ The thicknesses of the FTO-Air EMA, doped FTO, SiO_2 , intrinsic FTO were also fitting parameters and are listed in Table 5.3 and are in very good agreement with the thicknesses in Table 5.1 obtained from the TEM images in Figure 5.2. The fitting parameters for the F: SnO_2 layer are listed in Table 5.4.

Table 5.3 Layer stack used in the extraction of optical parameters of the F: SnO_2 layer.

Layer	Material	Thickness / nm
FTO-Air-EMA	50% FTO-doped, 50% Vacuum	27.0
FTO (doped)	FTO-doped	327.0
SiO_2	SiO_2 fused (DB)	17.4
SnO_2	FTO-intrinsic	28.1
Glass	Float glass	2.20E+06

Table 5.4 F: SnO_2 fit parameters.

Dielectric Background		OJL		Drude		Harmonic Oscillator	
Real	1.19	Strength	0.99	Plasma Freq. (1/cm)	6331.2	Resonance freq. (1/cm)	30248.1
Im	0	Gap Energy (1/cm)	31280.6	Damping (1/cm)	179983.8	Oscillator strength (1/cm)	3816.2
		Gamma (1/cm)	153.4			Damping (1/cm)	9292.1
		Decay factor (1/cm)	45346.2				

The fitted n , k parameters are shown in Figure 5.7.

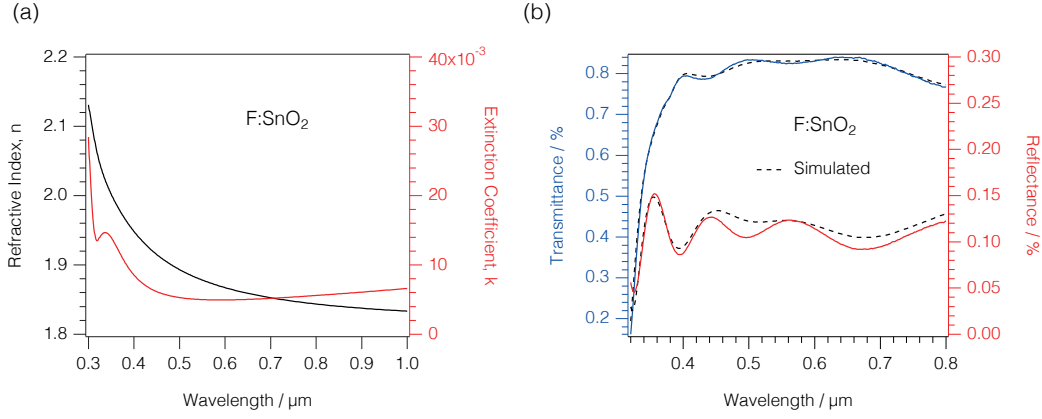


Figure 5.7 a) Extracted optical constants of crystalline F:SnO₂ used for b) the simulation of transmittance and reflectance data of the FTO substrate with the layer stack listed in Table 5.3.

5.3.2 OPTICAL PARAMETERIZATION OF HEMATITE

For the determination of the optical constants of hematite, thin Fe₂O₃ films were measured by ellipsometry on Si wafer substrates and on quartz substrates to facilitate the fitting. The dispersion law for hematite is based on a Tauc-Lorentz law following Equations (5.13) and (5.14)

$$\varepsilon_i(E) = \begin{cases} \frac{AE_0C(E-E_g)^2}{E[(E^2-E_g^2)^2+C^2E^2]} & , E > E_g \\ 0 & , E \leq E_g \end{cases} \quad (5.13)$$

$$\varepsilon_r(E) = \varepsilon_r(\infty) + \frac{2}{\pi} P \int_{E_g}^{\infty} \frac{\xi \varepsilon_i(\xi)}{\xi^2 - E^2} d\xi \quad (5.14)$$

where A is the strength of the peak, E_0 the peak central energy, C the broadening of the peak, E_g the optical band gap of the material and P the Cauchy principal value.³² For the fitting of hematite, a Tauc-Lorentz dispersion law with 5 oscillators was established on a 14 nm thick ALD hematite layer and was verified on several thinner hematite films (Table 5.5).

With the Tauc-Lorentz dispersion law shown in Table 5.5, the measured polarization change in the ellipsometry measurement could be fitted with a correlation coefficient of $R^2=0.996$ (Figure 5.8a). The resulting refractive index and extinction coefficient of hematite are shown in Figure 5.8b.

Table 5.5 Fitting parameters for the Tauc-Lorentz law for fitting of thin ALD hematite films.

	Peak 1	Peak 2	Peak 3	Peak 4	Peak 5	E _g	ε _r (∞)
A	38.28	2.86E-02	0.277	57.66	37.77	1.98	2.66
E ₀	4.792	3.864	3.754	2.918	2.290		
C	2.939	0.205	1.173	0.952	0.417		

The n,k data obtained from the ellipsometry fit is in very good agreement with the optical constants kindly provided by Filmetrics for comparison (Figure 5.8c) as well as with the dielectric constants measured by Galuza *et al.* (Figure 5.8d) and others.³³⁻³⁵

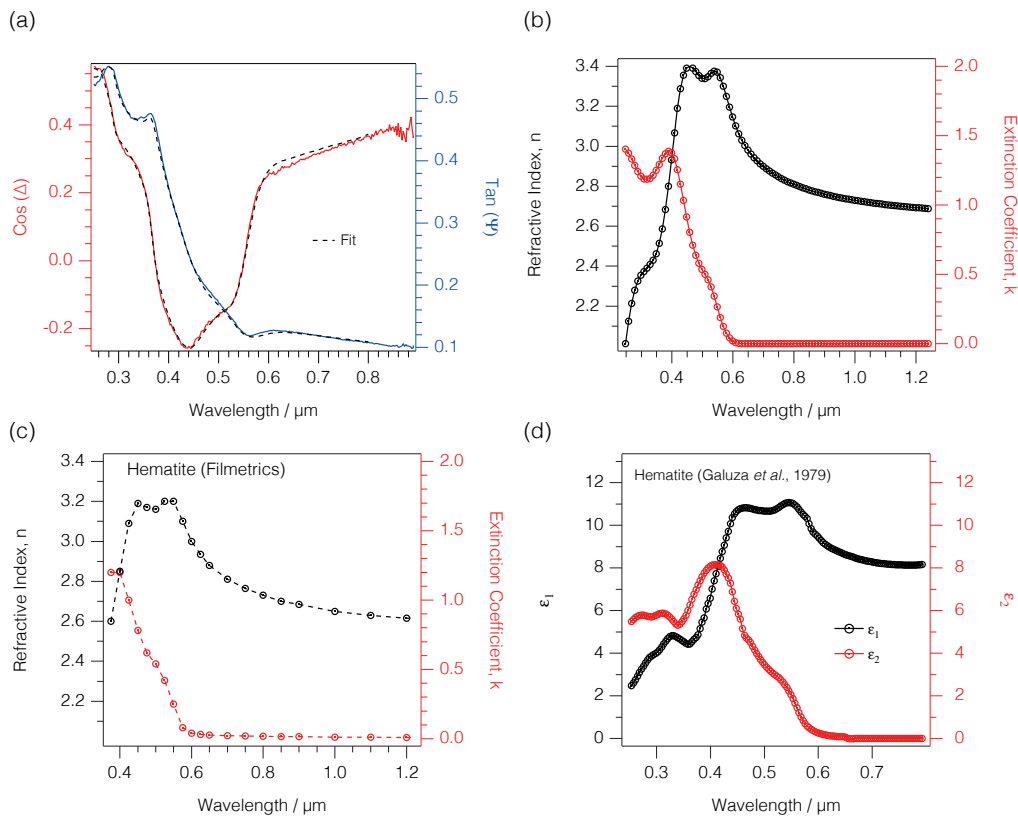


Figure 5.8 a) Raw data (red, blue) and fit (black dotted lines) of the ellipsometry measurement of a 14 nm hematite film on a TiO₂-coated Si wafer. R²=0.996. b) Calculated refractive index and extinction coefficient of the ALD hematite in this work. c) Reference optical constants of hematite from the Filmetrics database.³³ d) Dielectric constants of hematite adapted from Galuza *et al.*³⁴

In order to verify the Tauc-Lorentz law for hematite (Table 5.5), I wanted to compare the band gap that results from the dispersion law with the band gap, which can be obtained

from the diffuse reflectance spectrum of hematite opaque films. A TiO_2 nanowire array was coated with a thin layer of ALD hematite in order to get a nanostructured and opaque hematite sample. From the fitted extinction coefficient, k , of the 14 nm thick hematite films, the absorption coefficient was calculated according to Equation (5.5) and is shown in Figure 5.9a. The resulting Tauc plot shown in Figure 5.9b, gives an indirect band gap of 2.0 eV and a direct band gap of 2.6 eV for these thin ALD hematite films. The indirect band gap of 2.0 eV is in very good agreement with the band gap obtained from diffuse reflectance measurements on the nanostructured hematite sample (Figure 5.9c,d). The Tauc plot was constructed using the Kubelka-Munk transformation according to Equations (5.9) and (5.10). Thus, I could confirm that the established Tauc-Lorentz dispersion law for hematite is accurate.

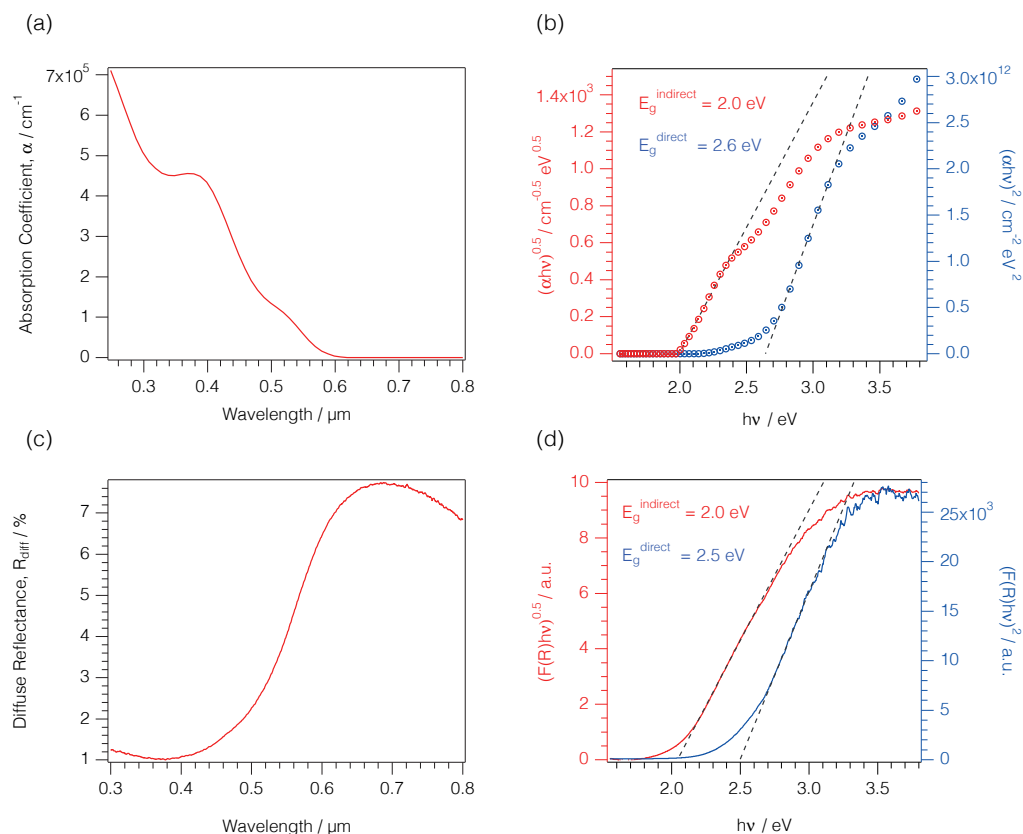


Figure 5.9 a) Absorption coefficient of hematite calculated from the fitted extinction coefficient in Figure 5.8b. b) Tauc plot of the direct in indirect band transition in the thin ALD hematite films. c) Diffuse reflectance spectrum of a thin ALD hematite film deposited on the TiO_2 nanowire array as shown in Figure 4.9. d) Tauc plot of the Kubelka-Munk transformed diffuse reflectance from c) according to Equations (5.9) and (5.10).

With the absorption coefficient, the light penetration depth in hematite was calculated

according to Equation (5.15) and is shown in Figure 5.10.

$$\text{Light Penetration depth} = \alpha^{-1} \quad (5.15)$$

It shows that in order to absorb fully until the band edge, the hematite layer has to be at least $1 \mu\text{m}$ thick. Knowing the charge transport limitations in hematite, it poses a major challenge for the realization of a nanostructured hematite photoanode.

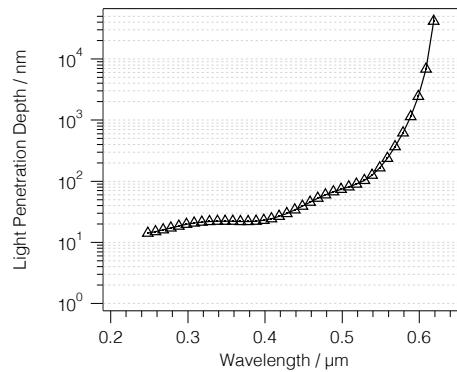


Figure 5.10 Light penetration depth ($=\alpha^{-1}$) in hematite calculated from the extracted absorption coefficient shown in Figure 5.9a.

5.3.3 OPTICAL MODEL OF A TYPICAL PEC CELL EMPLOYING A THIN FILM HEMATITE PHOTOANODE

With all the optical constants collected in Sections 5.3.1 and 5.3.2, the PEC device (here the hematite photoanode in the PEC cell as shown in Figure 5.1) can be analyzed for its optical losses.

In the PEC cell configuration, hematite is deposited on TiO_2 coated Tec15 glass and surrounded by electrolyte and quartz windows from both sides as depicted in Figure 5.1. Since the hematite used here is $\sim 10 \text{ nm}$ thin and RMS roughness of the Tec15 glass is on the order of $\sim 30 \text{ nm}$, spectroscopic ellipsometry data are strongly influenced by the roughness and cannot be used in combination with R,T data to determine a suitable effective medium approximation of our layer stack. Instead, all R,T data from three nominal hematite thicknesses (12, 16, 20 nm) and Tec15 in PEC configuration were used to determine the PEC cell optical model.

In Hematite/FTO illumination direction, the layer stack is composed of quartz/water/graded:water- Fe_2O_3 / Fe_2O_3 /graded: TiO_2 -FTO/FTO stack/water/quartz. The

graded layer is a sequence of 5 sublayers, the dielectric constants of each sublayer are obtained by using a Bruggemann EMA material approximation with a linear variation of the relative composition from the first to the second material. The fitting parameters and their extracted values are summarized in Table 5.6 and the comparison of the simulated and measured data is shown in Figure 5.11.

Table 5.6 Fitted thicknesses for the quartz/water/graded:water-Fe₂O₃/Fe₂O₃/graded:TiO₂-FTO/FTO stack/water/quartz stack. For the different thicknesses of 12, 16 and 20 nm of hematite, 0.7, 1.4 and 7.1 nm were obtained for the "bulk" Fe₂O₃ layer while the thickness of the gradient:Fe₂O₃-H₂O layer was kept constant.

Material	Thickness / nm
SnO ₂	28.1
SiO ₂	17.4
FTO	334
Gradient FTO-TiO ₂	3.5
Fe ₂ O ₃ (ALD)	0.7, 1.4, 7.1
Gradient Fe ₂ O ₃ -H ₂ O	21.1

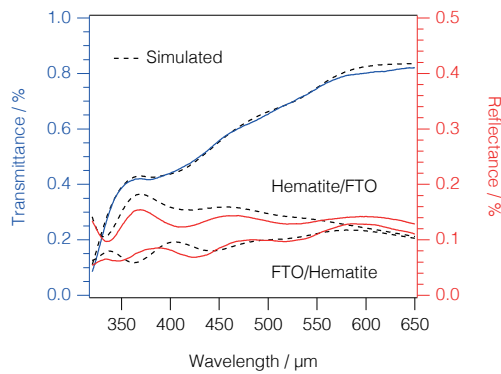


Figure 5.11 Measured (solid lines) and simulated (black broken lines) transmittance (blue) and reflectance (red) data. Simulated data was attained using a quartz/water/graded:water-Fe₂O₃/Fe₂O₃/graded:TiO₂-FTO/FTO stack/water/quartz stack.

The fit of T is satisfactory and the fit of R misses some features due to the pronounced effect of roughness. The effective thickness of every material in the graded layer is 50% of its total thickness. Hence we obtained total hematite thicknesses from bulk hematite layer and 1/2 of graded layer 11.25, 11.95 and 17.65 nm, in qualitative agreement with 'nominal' hematite thicknesses of 12, 16 and 20 nm.

Valuable insight into the optical losses through parasitic absorptances in the individual layers is presented in Figure 5.12. The calculated absorptances in the individual layers, A_l , the reflectance, R_{tot} and transmittance, T_{tot} for FTO/hematite and hematite/FTO illumination are shown in stacked diagrams and fulfill the energy conservation criterion (Equation (5.6)). For each wavelength a different ratio of illumination energy is reflected, absorbed in individual layers or transmitted through the PEC cell and strongly depends on the illumination direction.

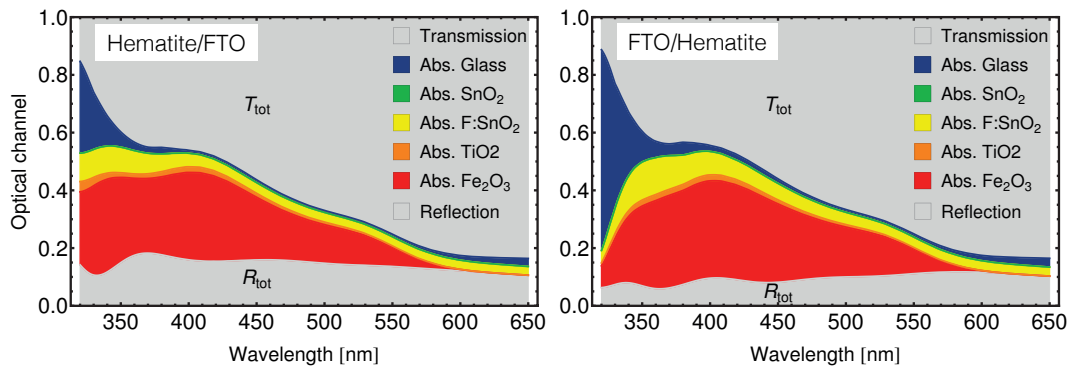


Figure 5.12 Detailed optical loss analysis of a PEC cell with a) FTO/hematite illumination and b) hematite/FTO illumination. The calculated total reflectance, the absorptances in each layer and the total transmittance are stacked and colored in the graphs.

For hematite/FTO illumination, Figure 5.12a, hematite absorbs $\sim 20\%$ of the light for wavelengths between 320 - 400 nm before its absorptance decreases to zero the closer the wavelength approaches its band gap energy ($\lambda = 620$ nm for $E_g = 2.0$ eV). A nearly constant absorption of $\sim 10\%$ can be seen in the F:SnO₂ layer over the whole wavelength range doubling to 20% in the blue region. In the blue region also glass absorption is large (up to $\sim 20\%$ for wavelengths < 350 nm). The absorption in water and quartz is negligible in the presented data. For FTO/hematite illumination, Figure 5.12b, the absorptance in hematite for wavelengths < 400 nm is smaller compared to hematite/FTO illumination due to much stronger absorption in float glass which stands in the FTO/hematite light path before hematite. Absorption in F:SnO₂ for FTO/hematite illumination is slightly larger than for Hematite/FTO illumination. Reflectance for both Hematite/FTO and FTO/hematite illumination accounts for 10-20% of the losses but the interference fringes of F:SnO₂ are more pronounced for the hematite/FTO illumination.

A decrease in reflectance losses from $\sim 20\%$ to $\sim 4\%$ could be achieved by using anti-reflective catalyst layers or nanostructuring approaches that usually decrease reflectance

losses from the hematite/FTO illumination direction as seen in Figure 4.17d.

5.4 CONCLUSION

In this chapter an optical model of light absorption in all layers in a typical PEC cell device was presented. Light propagation in the incoherent layers was described by geometrical ray tracing and in the coherent layers by the transfer-matrix method. A detailed UV-Vis and ellipsometry characterization of each layer of the PEC cell stack (quartz, water, float glass, SnO₂, SiO₂, F:SnO₂, Fe₂O₃) supplied the necessary optical parameters for the model. The ALD hematite used in this study was found to have a band gap of 2.0 eV and an absorption coefficient of $\sim 4.55 \cdot 10^5 \text{ cm}^{-1}$ at a wavelength of 380 nm. The light penetration depth in mind, the hematite layer has to be at least 60-70 nm thick to absorb sufficiently. Indeed, a 12 nm thick layer absorbs only 15-18% of the light due to its thickness and 64% are lost due to transmission (Table 5.7). Compared to the amount of absorbed light the optical loss due to reflection is considerable (10-15%). Furthermore, 4-5% are lost due to the absorption of FTO and finally 1-2% due to the absorption of the glass used.

Table 5.7 Qualitative values of photocurrents computed from Equation (5.8) stored by various optical processes for 12 nm ALD hematite. The sum of these respective channels gives the maximum possible photocurrent for hematite of 12.5 mA cm⁻².

Optical process	Hematite/FTO Illumination		FTO/Hematite Illumination	
	Loss / %	Loss in mA/cm ²	Loss / %	Loss in mA/cm ²
Reflection	15	1.82	10	1.22
Absorption Quartz	0	0	0	0
Absorption Water	0	0	0	0
Absorption Hematite	15	1.87	18	2.24
Absorption SnO ₂ :F	4	0.47	5	0.65
Absorption Glass	1	0.16	2	0.27
Transmission	64	7.84	64	7.84

If every photon would be converted to an electron-hole pair that is collected at the contacts (APCE=1), such a 12 nm thin hematite electrode should result in current densities between 1.8-2.2 mA cm⁻², depending on the illumination direction. The

measured current densities are around $0.6\text{-}0.7\text{ mA cm}^{-2}$, in other words, one third of the value obtained from the optical modeling. This is in very good agreement with the measured APCE values in Figure 4.14b,c of $\sim 30\%$.

In future, an opto-electronic model is desirable that accounts also for the electronic losses due to, for example, recombination processes. Data shown in Section 4.3.5 represents a good basis for the development of such an opto-electronic model. So far, with the set of information for these individual layers, a wavelength-dependent optical loss analysis of the complete PEC cell was achieved and the optical losses caused by each layer could be calculated separately, which is not possible with direct measurements.

5.5 REFERENCES

1. Brillet, J.; Cornuz, M.; Le Formal, F.; Yum, J. H.; Gratzel, M.; Sivula, K. Examining Architectures of Photoanode-Photovoltaic Tandem Cells for Solar Water Splitting. *Journal of Materials Research* **2010**, *25*, 17-24.
2. Brillet, J.; Yum, J. H.; Cornuz, M.; Hisatomi, T.; Solarska, R.; Augustynski, J.; Graetzel, M.; Sivula, K. Highly Efficient Water Splitting by a Dual-Absorber Tandem Cell. *Nature Photonics* **2012**, *6*, 823-827.
3. Abdi, F. F.; Han, L. H.; Smets, A. H. M.; Zeman, M.; Dam, B.; van de Krol, R. Efficient Solar Water Splitting by Enhanced Charge Separation in a Bismuth Vanadate-Silicon Tandem Photoelectrode. *Nature Communications* **2013**, *4*.
4. Prevot, M. S.; Sivula, K. Photoelectrochemical Tandem Cells for Solar Water Splitting. *Journal of Physical Chemistry C* **2013**, *117*, 17879-17893.
5. van de Krol, R.; Liang, Y. Q. An N-Si/N-Fe₂O₃ Heterojunction Tandem Photoanode for Solar Water Splitting. *Chimia* **2013**, *67*, 168-171.
6. Dennler, G.; Forberich, K.; Ameri, T.; Waldauf, C.; Denk, P.; Brabec, C. J.; Hingerl, K.; Heeger, A. J. Design of Efficient Organic Tandem Cells: On the Interplay between Molecular Absorption and Layer Sequence. *Journal of Applied Physics* **2007**, *102*.
7. Dennler, G.; Forberich, K.; Scharber, M. C.; Brabec, C. J.; Tomis, I.; Hingerl, K.; Fromherz, T. Angle Dependence of External and Internal Quantum Efficiencies in Bulk-Heterojunction Organic Solar Cells. *Journal of Applied Physics* **2007**, *102*.
8. Ding, K. N.; Kirchartz, T.; Pieters, B. E.; Ulbrich, C.; Ermes, A. M.; Schicho, S.; Lambertz, A.; Carius, R.; Rau, U. Characterization and Simulation of a-Si:H/Mu C-Si:H Tandem Solar Cells. *Solar Energy Materials and Solar Cells* **2011**, *95*, 3318-3327.
9. Han, L. H.; Abdi, F. F.; Rodriguez, P. P.; Dam, B.; van de Krol, R.; Zeman, M.; Smets, A. H. M. Optimization of Amorphous Silicon Double Junction Solar Cells for an Efficient Photoelectrochemical Water Splitting Device Based on a Bismuth Vanadate Photoanode. *Physical Chemistry Chemical Physics* **2014**, *16*, 4220-4229.

10. Doscher, H.; Geisz, J. F.; Deutsch, T. G.; Turner, J. A. Sunlight Absorption in Water - Efficiency and Design Implications for Photoelectrochemical Devices. *Energy & Environmental Science* **2014**, *7*, 2951-2956.
11. Dotan, H.; Kfir, O.; Sharlin, E.; Blank, O.; Gross, M.; Dumchin, I.; Ankonina, G.; Rothschild, A. Resonant Light Trapping in Ultrathin Films for Water Splitting. *Nature Materials* **2013**, *12*, 158-164.
12. Wang, K. X. Z.; Wu, Z. F.; Liu, V.; Brongersma, M. L.; Jaramillo, T. F.; Fan, S. H. Nearly Total Solar Absorption in Ultrathin Nanostructured Iron Oxide for Efficient Photoelectrochemical Water Splitting. *Acs Photonics* **2014**, *1*, 235-240.
13. Andrade, L.; Lopes, T.; Ribeiro, H. A.; Mendes, A. Transient Phenomenological Modeling of Photoelectrochemical Cells for Water Splitting - Application to Undoped Hematite Electrodes. *International Journal of Hydrogen Energy* **2011**, *36*, 175-188.
14. Berger, A.; Newman, J. An Integrated 1-Dimensional Model of a Photoelectrochemical Cell for Water Splitting. *Journal of the Electrochemical Society* **2014**, *161*, E3328-E3340.
15. Cendula, P.; Tilley, S. D.; Gimenez, S.; Bisquert, J.; Schmid, M.; Gratzel, M.; Schumachert, J. O. Calculation of the Energy Band Diagram of a Photoelectrochemical Water Splitting Cell. *Journal of Physical Chemistry C* **2014**, *118*, 29599-29607.
16. Park, H. S.; Ha, H. W.; Ruoff, R. S.; Bard, A. J. On the Improvement of Photoelectrochemical Performance and Finite Element Analysis of Reduced Graphene Oxide-BiVO₄ Composite Electrodes. *Journal of Electroanalytical Chemistry* **2014**, *716*, 8-15.
17. Carver, C.; Ulissi, Z.; Ong, C. K.; Dennison, S.; Kelsall, G. H.; Hellgardt, K. Modelling and Development of Photoelectrochemical Reactor for H₂ Production. *International Journal of Hydrogen Energy* **2012**, *37*, 2911-2923.
18. Haussener, S.; Xiang, C. X.; Spurgeon, J. M.; Ardo, S.; Lewis, N. S.; Weber, A. Z. Modeling, Simulation, and Design Criteria for Photoelectrochemical Water-Splitting Systems. *Energy & Environmental Science* **2012**, *5*, 9922-9935.
19. Macleod, H. A. *Thin-Film Optical Filters*. 4th ed.; CRC Press/Taylor & Francis: Boca Raton, FL, 2010; p xviii, 782 p.
20. Krč, J. *Optical Modeling and Simulation of Thin-Film Photovoltaic Devices*. p xiii, 258 pages.
21. <http://refractiveindex.info/database/main/H2O/Hale.yml> (accessed January 14, 2016)
22. Wenger, S.; Schmid, M.; Rothenberger, G.; Gentsch, A.; Gratzel, M.; Schumacher, J. O. Coupled Optical and Electronic Modeling of Dye-Sensitized Solar Cells for Steady-State Parameter Extraction. *Journal of Physical Chemistry C* **2011**, *115*, 10218-10229.
23. Bruggeman, D. A. G. Berechnung Verschiedener Physikalischer Konstanten Von Heterogenen Substanzen. I. Dielektrizitätskonstanten Und Leitfähigkeiten Der Mischkörper Aus Isotropen Substanzen. *Annalen der Physik* **1935**, *416*, 636-664.
24. Theiss, W. Model Meets Measurement – the Challenges of Optical Spectrum Simulation Facing Real Thin Film Deposition. In *Proceedings of the International Conference on Coating on Glass and Plastics*, Dresden, Germany, 2006.
25. <http://wtheiss.com/?c=1&content=scout> (accessed March 10, 2016).
26. SETFOS 4.0 <http://www.fluxim.com/> (accessed January 19, 2016)
27. Chen, J. Spectroscopic Ellipsometry Studies of II-VI Semiconductor Materials and Solar Cells Dissertation University of Toledo 2010.

-
28. Gao, L.; Lemarchand, F.; Lequime, M. Refractive Index Determination of SiO₂ Layer in the Uv/Vis/Nir Range: Spectrophotometric Reverse Engineering on Single and Bi-Layer Designs. *Journal of the European Optical Society-Rapid Publications* **2013**, *8*.
 29. Reddaway, S. F.; Wright, D. A. Optical Properties of Tin Oxide Crystals. *British Journal of Applied Physics* **1965**, *16*, 195-8.
 30. Rakhshani, A. E.; Makdisi, Y.; Ramazaniyan, H. A. Electronic and Optical Properties of Fluorine-Doped Tin Oxide Films. *Journal of Applied Physics* **1998**, *83*, 1049-1057.
 31. OLeary, S. K.; Johnson, S. R.; Lim, P. K. The Relationship between the Distribution of Electronic States and the Optical Absorption Spectrum of an Amorphous Semiconductor: An Empirical Analysis. *Journal of Applied Physics* **1997**, *82*, 3334-3340.
 32. Jellison, G. E.; Modine, F. A. Parameterization of the Optical Functions of Amorphous Materials in the Interband Region. *Applied Physics Letters* **1996**, *69*, 371-373.
 33. Karlsson, B.; Ribbing, C. G.; Roos, A.; Valkonen, E.; Karlsson, T. Optical-Properties of Some Metal-Oxides in Solar Absorbers. *Physica Scripta* **1982**, *25*, 826-831.
 34. Galuza, A. I.; Eremenko, V. V.; Kirichenko, A. P. Kramers-Kronig Analysis of Reflection Spectra of Hematite. *Fizika Tverdogo Tela* **1979**, *21*, 1125-1129.
 35. Dotan, H.; Kfir, O.; Sharlin, E.; Blank, O.; Gross, M.; Dumchin, I.; Ankonina, G.; Rothschild, A. Resonant Light Trapping in Ultrathin Films for Water Splitting. *Nat Mater* **2012**.

*All truths are easy to understand once they are discovered;
the point is to discover them.*

Galileo Galilei

6 HIGHLY EFFICIENT PLANAR PEROVSKITE SOLAR CELLS THROUGH BAND ALIGNMENT ENGINEERING

This chapter is adapted from the work by Juan Pablo Correa Baena, Ludmilla Steier, Wolfgang Tress, Michael Saliba, Stefanie Neutzner, Taisuke Matsui, Fabrizio Giordano, Ajay Ram Srimath Kandada, Shaik M. Zakeeruddin, Annamaria Petrozza, Antonio Abate, Mohammad Khaja Nazeeruddin, Michael Grätzel and Anders Hagfeldt published 2015 in Energy and Environmental Science and implements unpublished data acquired in collaboration with Prof. Ladislav Kavan (J. Heyrovsky Institute of Physical Chemistry of the ASCR). Juan Pablo and myself worked in equal contribution together on this project and hence I will use the we-form.¹

Thin film solar cells comprise a number of technologies based on different photovoltaic materials such as GaAs, CIGS and CdTe. Recently, organic-inorganic perovskites have emerged as an exciting new photovoltaic material, which is solution processable and cost-effective. In just a few years, perovskite solar cells (PSCs), based on methyl ammonium lead iodide (MAPbI₃) and modifications, have made impressive advances with maximum power conversion efficiencies (PCEs) moving from 3.8% in 2009¹ to certified efficiencies above 20% in 2015 surpassing state-of-the-art polycrystalline single junction cells.²³ The most current record PCEs of 17.9%, 20.1% and 21.0% were achieved using a mesoporous TiO₂ electron extraction layer.^{2, 4, 5} However, using a compact semi-crystalline TiO₂ layer deposited by atomic layer deposition (ALD) only poor performance was observed. Thus, we proposed the use of alternative electron selective layers, such as SnO₂, to overcome the injection barrier that was measured at the TiO₂ and perovskite interface. With my low temperature ALD grown SnO₂, a barrier free conduction band alignment for the SnO₂/perovskite interface could be demonstrated that allowed us to achieve stabilized PCEs of over 18% with remarkably high voltages up to 1.14 V, and in addition, a record high V_{oc} of 1.19 V for this type of PSCs. The fabrication of these devices avoids high-temperature steps, which is desirable for process upscaling, tandem configurations and applications for light weight flexible solar cells.

6.1 INTRODUCTION

Solution processed, hybrid organic-inorganic perovskite materials were studied by Mitzi et al. in the 1990s and were recognized as excellent semiconducting materials.⁶ It was not, however, until Miyasaka and coworkers pioneered the work on dye-sensitized solar cell applications in 2009, that the material started to be recognized by the photovoltaic community.⁷ Since then, a myriad of works has been published exploring different device configurations. The currently highest reported PCE value of over 20% was achieved using a thin layer of mesoporous TiO₂.² In this architecture, the perovskite material, infiltrates a mesoporous TiO₂ layer which is sandwiched between a hole transporting layer (HTL, typically doped 2,2',7,7'-tetrakis(*N,N'*-di-*p*-methoxyphenylamine)-9,9'-spirobifluorene (Spiro-OMeTAD) or polytertiary arylamine (PTAA)) and an electron selective layer (ESL, typically TiO₂).

From the earlier works, it was realized that the perovskite absorber material transports both holes and electrons.⁸⁻¹⁰ Naturally, this led towards the investigation of a thin film perovskite configuration with only a compact TiO₂ as the ESL.¹¹ However, these devices exhibit poor charge collection efficiency¹² and low open circuit voltage.^{13, 14} Especially for fast voltage sweeps, this device architecture shows pronounced hysteresis of the J-V curve^{12, 14, 15} and to our knowledge no PCE of over 18% in this architecture has been reported with a stabilized power output. Xing et al. showed that planar devices using PCBM as the ESL and methyl ammonium lead iodide (MAPbI₃) as the absorbing and transporting material, had a much improved stabilized power output behavior when compared to TiO₂ ESL, which they linked to the improved interfacial charge transfer. Wojciechowski and co-workers showed that modifying the TiO₂ surface with fullerene derivatives can work towards high efficiency PSCs.¹⁴ Recent works have shown the potential of SnO₂-based ESLs,¹⁶⁻¹⁹ but so far these devices have not shown high efficiency with stabilized power output.

Using a low temperature ALD process to fabricate SnO₂ ESLs, we demonstrate that planar PSCs can achieve stabilized PCEs of above 18% with voltages exceeding 1.14 V. It is shown that this is not the case for the planar ALD TiO₂. We choose SnO₂ considering the favorable alignment of the conduction bands of the perovskite materials and the ESL and show an energy mismatch in the case of TiO₂. Thus, using SnO₂, which has a deeper conduction band, enables the fabrication of planar devices with high efficiencies, long

term air stability and improved stabilized power output, while keeping the processing at low temperatures ($< 120\text{ }^{\circ}\text{C}$), which is key for process upscaling and high efficiency tandem devices.²⁰

6.2 METHODS

6.2.1 ELECTRON SELECTIVE LAYER PREPARATION

F:SnO₂ substrates were first wiped with acetone, and then cleaned for 10 min in piranha solution (H₂SO₄/H₂O₂ = 3:1) followed by 10 min in a plasma cleaner prior to ALD deposition.

Atomic layer deposition (ALD) of semi-crystalline TiO₂²¹ was carried out in a Savannah ALD 100 instrument (Cambridge Nanotech Inc.) at 120 °C using tetrakis(dimethylamino)titanium(IV) (TDMAT, 99.999% pure, Sigma Aldrich) and H₂O₂. TDMAT was held at 75 °C and H₂O₂ at room temperature. The growth rate was 0.07 nm/cycle at a N₂ flow rate of 5 sccm as measured by ellipsometry.

SnO₂ was deposited at 118 °C in the home-built ALD setup presented in Section 4.2.1 using Tetrakis(dimethylamino)tin(IV) (TDMASn, 99.99%-Sn, Strem Chemicals INC) and ozone at a constant growth rate of 0.065 nm/cycle measured by ellipsometry. TDMASn was held at 65 °C. Ozone was produced by an ozone generator (AC-2025, IN USA Incorporated) fed with oxygen gas (99.9995% pure, Carbagas) producing a concentration of 13% ozone in O₂. Nitrogen was used as a carrier gas (99.9999% pure, Carbagas) with a flow rate of 10 sccm.

Nb₂O₅ was deposited in the home-built ALD setup at 170 °C and a carrier gas flow rate of 20 sccm using (tert-butylimido)bis(diethylamino)Niobium (TBTDEN, Digital Specialty Chemicals, Canada) and ozone with a constant growth rate of 0.06 nm/cycle. TBTDEN was held at 130 °C.

6.2.2 PEROVSKITE PRECURSOR SOLUTION AND FILM PREPARATION

Before perovskite deposition, the ALD layers were treated with UV ozone for 10 min to remove by-products from the deposition process. The perovskite films were deposited

from a precursor solution containing FAI (1 M), PbI_2 (1.1 M, TCI Chemicals), MABr (0.2 M) and PbBr_2 (0.2 M, AlfaAesar) in anhydrous DMF:DMSO 4:1 (v:v, Acros). The perovskite solution was spin-coated in a two-step program; first at 1000 rpm for 10 s and then at 4000 rpm for 30 s. During the second step, 100 μL of chlorobenzene were poured on the spinning substrate 15 s prior the end of the program. The substrates were then annealed at 100 °C for 1 h in a nitrogen filled glove box.

The spiro-OMeTAD (Merck) solution (70 mM in chlorobenzene) was spun at 4000 rpm for 20 s. The spiro-OMeTAD was doped at a molar ratio of 0.5, 0.03 and 3.3 with bis(trifluoromethylsulfonyl)imide lithium salt (Li-TFSI, Sigma Aldrich), tris(2-(1H-pyrazol-1-yl)-4-tert-butylpyridine)-cobalt(III)tris(bis(trifluoromethylsulfonyl)imide) (FK209, Dyenamo) and 4-tert-Butylpyridine (TBP, Sigma Aldrich), respectively.²²⁻²⁴ As a last step 70-80 nm of gold top electrode were thermally evaporated under high vacuum.

6.2.3 SOLAR CELL CHARACTERIZATION

A ZEISS Merlin HR-SEM was used to characterize the morphology of the device cross-section. The solar cells were measured using a 450 W xenon light source (Oriel). The spectral mismatch between AM 1.5G and the simulated illumination was reduced by the use of a Schott K113 Tempax filter (Präzisions Glas & Optik GmbH). The light intensity was calibrated with a Si photodiode equipped with an IR-cutoff filter (KG3, Schott) and it was recorded during each measurement. Current-voltage characteristics of the cells were obtained by applying an external voltage bias while measuring the current response with a digital source meter (Keithley 2400). The voltage scan rate was 10 mV s⁻¹ and no device preconditioning was applied before starting the measurement, such as light soaking or forward voltage bias applied for long time. The starting voltage was determined as the potential at which the cells furnished 1 mA in forward bias, no equilibration time was used. The cells were masked with a black metal mask limiting the active area to 0.16 cm² and reducing the influence of the scattered light. It is important to note that the devices achieved the highest efficiency and stabilized currents after 1 week of preparation.

The EQE spectra were measured under constant white light bias with an intensity of 10 mW cm⁻² supplied by a LED array. The superimposed monochromatic light was chopped at 2 Hz. The homemade system comprises a 300 W Xenon lamp (ICL Technology), a Gemini-180 double-monochromator with 1200 grooves/mm grating

(Jobin Yvon Ltd) and a lock-in amplifier (SR830 DSP, Stanford Research System). The EQE integration was performed according to the following equation

$$J_{sc} = \int_{\lambda_1}^{\lambda_2} q \cdot \phi \cdot EQE \, d\lambda \quad (6.1)$$

with λ being the wavelength, q the elementary charge and ϕ the photon flux calculated from the ratio of the AM1.5 G spectral irradiance and the photon energy.

6.2.4 FS-TRANSIENT ABSORPTION SPECTROSCOPY

A Coherent Micra Ti:Sapphire oscillator in conjunction with a Coherent RegA 9040 amplifier (800 nm central wavelength, 40 fs pulse duration and 250 kHz repetition rate) was used to generate pump and probe light. The 520 nm pump beam was generated in a coherent collinear optical parametric amplifier; the probe resulted from white light generation in a sapphire plate. The delay between the two pulses was controlled by a motorized delay-stage and the signal was detected using a photodiode with monochromator, connected to a Stanford Instruments Lock-in Amplifier SR830. During the measurements, the pump beam of 1.6 nJ excitation power was focused on approximately 1 mm² device area. To monitor the current in short-circuit condition, the devices were connected to an Agilent B2912A source/measure unit. All measurements were set up in reflection geometry, measuring double transmission by reflecting the probe beam from the back electrode of the device. To prevent degradation during laser illumination, all measurements were carried out in vacuum, using a continuous flow static exchange gas cryostat (Oxford Instruments Optistat CF).

6.2.5 BAND GAP ESTIMATION MEASUREMENTS

The band gap of the perovskite materials (Supplementary Figure S3) was determined from diffuse reflectance measurements in a wavelength range of 300–900 nm carried out with a UV-3600 spectrometer (Shimadzu Scientific Instruments, USA) that was equipped with an integrating sphere. For these measurements, a thick layer of perovskite was deposited on a quartz slide (Ted Pella, USA) to ensure a good scattering signal. An absorption coefficient equivalent was calculated after Kubelka-Munk according to

$$F(R) = \frac{(1-R)^2}{2R} \quad (6.2)$$

where R is the diffuse reflectance. The band gap was determined from Tauc plots according to

$$\alpha h\nu = A(h\nu - E_g)^{\frac{n}{2}} \quad (6.3)$$

with $n = 1$ for a direct band gap material.

The band gaps of SnO_2 and TiO_2 were confirmed by spectroscopic ellipsometry measurements (GES 5E, Sopra S.A., France) in the wavelength range of 250–890 nm on 100 nm thick layers deposited on Si by ALD as described above. The obtained spectra were fitted using a Tauc-Lorentz dispersion law (WinElli II software) to extract the band gap and thickness of the deposited layers. The results were in very good agreement with transmittance measurements performed on films deposited on quartz as well as with literature values.

6.2.6 PHOTOELECTRON SPECTROSCOPY

The XPS and UPS measurements were performed on a PHI5000 VersaProbe instrument. The UPS radiation was generated by a He-gas discharge lamp (He I α at 21.22 eV). The electron binding energy scale was calibrated using the Fermi edge of clean silver. Samples were prepared in the same way as for the devices for the 2 perovskites on ESLs of SnO_2 and TiO_2 , which were deposited on FTO glass.

6.2.7 ELECTROCHEMICAL MEASUREMENTS ON ALD TIN OXIDE LAYERS

Electrochemical experiments were carried out in a one-compartment cell using Autolab Pgstat-30 equipped with the FRA module (Ecochemie) controlled by the GPES-4 software. The reference electrode was Ag/AgCl (sat. KCl). The electrolyte solutions were purged with Ar, and the measurement was carried out under Ar atmosphere in a closed electrochemical cell. Impedance spectra were measured at varying potentials, which were scanned typically from 1.3 V to -0.3 V vs. Ag/AgCl and back. Impedance spectra were evaluated using Zview (Scribner) software. Electrolytes, solvents and redox-active molecules were of the standard quality (p.a. or electrochemical grade) purchased from Aldrich or Merck and used as received.

6.2.8 ALD-SNO₂ CHARACTERIZATION

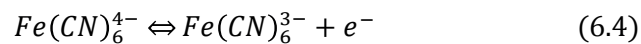
Transmission electron microscopy (TEM) measurements were carried out with a FEI CM12 microscope (Philips, Netherlands) and a Technai Osiris (FEI, USA) in dark field and bright field as well as in high-angle annular dark-field (HAADF) modes. Cross-section lamellae for TEM were prepared with a Zeiss NVision 40 CrossBeam with focused ion beam (FIB). Hall measurements were carried out with an Ecopia HMS 3000 Hall setup (supplied by Microworld) with a magnetic field of 0.54 T in a 4-point configuration measuring an area of 1 cm². The SnO₂ layer was deposited on microscope glass and contacted via soldered contacts of InSn (Microworld).

6.3 RESULTS

TiO₂ was the most employed electron selective layer in perovskite solar cells until now and hence, it is well characterized in literature.²⁵ In the following, our new electron selective material - SnO₂ - will be characterized in a similar way to TiO₂ in order to draw some interesting conclusions for these materials.

6.3.1 PROBING THE PRESENCE OF PINHOLES IN ALD TIN OXIDE

The pinhole-defects in our SnO₂ blocking layer were investigated by the cyclic voltammetry of the Fe(CN)₆^{3-/4-} redox couple.^{25, 26} According to the redox reaction (6.4),



a rectifying contact should suppress the oxidation of the redox species and only show the reduction peak corresponding to electron flow through the layer. If it is not the case, a metal like behavior is seen showing both oxidation and reduction peaks in the cyclic voltammogram. If pinholes are present in the selective contact, the underlying FTO (which is a degenerate F:SnO₂ semiconductor that behaves like a metal) will be able to oxidize and reduce the redox species.

Figure 6.1 shows that the blocking ability of the ALD SnO₂ films is perfect for all layers of varying thicknesses between 2-100 nm. Their corresponding voltammograms exhibit solely the onset of ferricyanide reduction at a potential of ~0 V (vs. Ag/AgCl, KCl sat'd) but no anodic charge of ferrocyanide oxidation at potentials as high as 1.2 V is recorded.

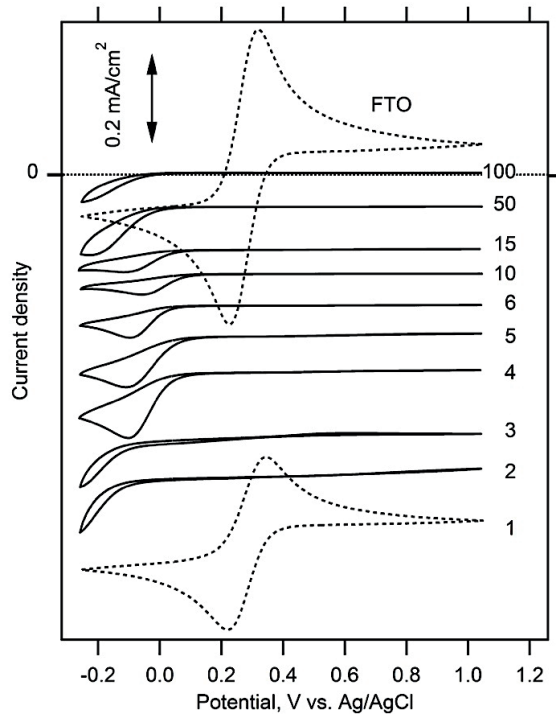


Figure 6.1 Cyclic voltammograms at bare FTO electrode (dashed line) and that covered by SnO_2 layers made by ALD. The layer thickness (in nm) is labeled in annotations. Scan rate: 50 mV/s. The electrolyte solution is 1 mM $\text{K}_4\text{Fe}(\text{CN})_6$ + 1 mM $\text{K}_3\text{Fe}(\text{CN})_6$ in aqueous 0.5 M KCl, pH 2.5. The voltammograms (except 'FTO' and '100') are offset for clarity.

In other words, there are no detectable pinholes exposing the FTO underneath the SnO_2 layer. Furthermore, the voltammograms confirm that our ALD- SnO_2 film behaves like an ideally rectifying interface already at the thickness of 2 nm. Solely the 1 nm thick film shows pinholes, which expose part of the FTO surface to the electrolyte solution and hence show a cyclic voltammogram similar to FTO though with a reduced peak current.

Assuming linear diffusion towards the FTO/electrolyte solution interface, the effective pinhole area can be calculated from the voltammetric peak current, I_p . It is given by the Randles-Sevcik equation

$$I_p = k \cdot n^{3/2} \cdot A \cdot c \cdot D^{1/2} \cdot v^{1/2} \quad (6.5)$$

where $k = 2.69 \cdot 10^5 \text{ C mol}^{-1} \text{ V}^{-1/2}$, n is the number of electrons appearing in the half-reaction for the redox couple, A is the electrode area, D is the diffusion coefficient and v is the scan rate. Specific diffusion fields might develop around pinholes in real electrodes, for example, the microelectrode-like pinholes can show spherical diffusion and sigmoidal-shaped voltammograms,^{27, 28} but these fields may also merge to form a single

planar diffusion layer. For the 1 nm thick SnO₂ layer (Figure 6.1), the applicability of Equation (6.5) is corroborated by the scan-rate ($v^{1/2}$) dependence of I_p (not shown) and the Nernstian peak-shaped voltammogram.^{25, 28} Under these assumptions, the effective pinhole area equals

$$\frac{A_u}{A_0} = \frac{j_p}{j_{o,FTO}} \quad (6.6)$$

where A_u is the uncovered area of FTO on a partially blocking electrode, A_0 is the total electrode area, j_p is the peak current density at the actual blocking electrode and $j_{p,FTO}$ is the current density at the clean FTO electrode. The 1 nm thick SnO₂ layer gives a ratio of $A_u/A_0 = 59\%$, which compares favorably to the blocking function of ALD TiO₂ films that were used in the perovskite study (with A_u/A_0 of 79% or 87%, depending on the synthetic conditions).²⁵ The ALD-TiO₂ films actually required thicknesses of 3-5 nm for demonstrating blocking behavior comparable to our 2 nm thick SnO₂.

The excellent blocking behavior of such thin SnO₂ ALD films is a big advantage for their use as rectifying contacts in solar cells, water splitting electrodes and others.

With respect to the photoconductivity of MAPbI₃ ($4 \times 10^{-5} - 3 \times 10^{-4}$ S/cm) measured on Al₂O₃, ZrO₂ and TiO₂,²⁹ the dark conductivity of our low-temperature ALD SnO₂ layers of $8.4 \cdot 10^{-3}$ S/cm is sufficiently high (left column of Table 6.1). Hence, there is no bottleneck for the electron transport to the FTO contact.

Table 6.1 Hall measurement results of as-deposited ALD-SnO₂ films of 36 nm deposited on microscope glass.

Charge carrier density / cm ⁻³	$-2.46 \cdot 10^{16}$
Mobility / cm ² (Vs) ⁻¹	2.1
Resistivity / Ω cm	$1.2 \cdot 10^2$
Conductivity / S cm ⁻¹	$8.4 \cdot 10^{-3}$

Since the record holding perovskite solar cells are based on mesoporous TiO₂ electron selective contacts, it appears to be tempting to try the SnO₂ ALD layer also with mesoporous oxide nanoparticles. However, the low-temperature ALD deposited SnO₂ loses all its blocking ability upon annealing at 450 °C, which is the temperature used during the annealing process of the mesoporous layer. Cyclic voltammetry measurements

with the same $\text{Fe}(\text{CN})_6^{3-/4-}$ redox couple used for measurements in Figure 6.1 confirmed the complete loss in rectifying character upon annealing. The results in Figure 6.2 show that after calcination at 450 °C, the electrode has the same metallic electrochemical response as the uncoated FTO substrate regardless the SnO_2 layer thickness.

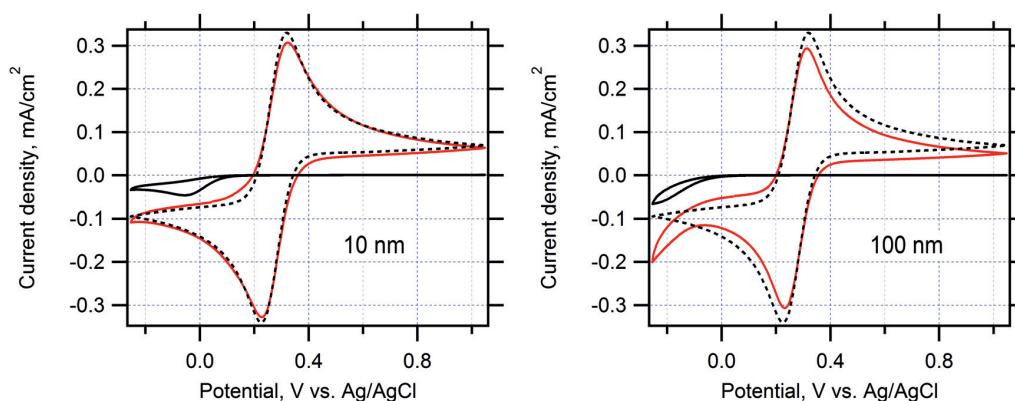


Figure 6.2 Cyclic voltammograms on bare FTO electrode (dashed line) and that covered by SnO_2 layers made by ALD (black full line). Red line is for the same sample calcined at 450 °C in air. The layer thickness (in nm) is labeled in annotations. Scan rate: 50 mV/s. The electrolyte solution is 1 mM $\text{K}_4\text{Fe}(\text{CN})_6$ + 1 mM $\text{K}_3\text{Fe}(\text{CN})_6$ in aqueous 0.5 M KCl, pH 2.5.

The observed metallic behavior of the SnO_2 electrodes after annealing is much stronger than observed for the ALD TiO_2 .²⁵ This could either be due to doping of the SnO_2 layer from the underlying F: SnO_2 (FTO) substrate, or, due to the crystallization of the amorphous layer upon annealing which could induce grain formation.

Hence, I investigated both samples in top view by scanning electron microscopy and in cross-sectional view by transmission electron microscopy as presented in Figure 6.3. This study confirms the formation of grains (Figure 6.3c) upon annealing of the low-temperature ALD SnO_2 layers (Figure 6.3a,b).

The ALD SnO_2 deposits pinhole-free on the FTO substrate as seen in the top-view SEM image in Figure 6.3a supporting the results obtained from cyclic voltammetry (Figure 6.1).

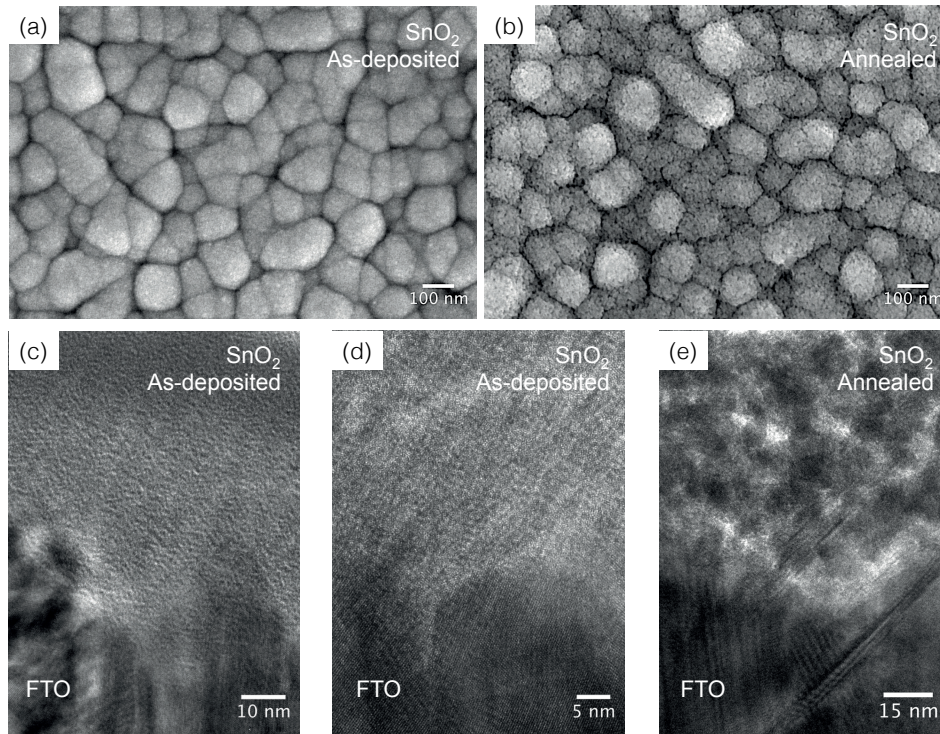


Figure 6.3 Top: Scanning microscopy top views of a) as-deposited and b) annealed ALD SnO_2 films on FTO substrates. Bottom: Bright field transmission electron microscopy cross-sections of c,d) as-deposited and e) annealed ALD SnO_2 films on FTO. Samples stated as 'annealed' were calcined at 450 °C for 30 min in air with heating and cooling ramps of 5 °C/min.

Upon annealing ALD SnO_2 forms a rather porous structure as seen in Figure 6.3b. The TEM micrographs (Figure 6.3c,d) show that the as-deposited SnO_2 layer is rather amorphous and hence, the crystallization upon annealing induces the formation of SnO_2 crystals of 6-8 nm in diameter as seen in Figure 6.3e. This confirms the assumption that the electrochemical similarity of the SnO_2 sample to the uncoated FTO sample (Figure 6.2) is due to the formation of a highly porous structure of SnO_2 upon annealing that is permeable for the electrolyte solution. I note here that, although the SnO_2 layer is amorphous, we can still refer to a band structure similar to the case of amorphous germanium or silicon.³⁰

6.3.2 TIN OXIDE BASED FLAT PEROVSKITE DEVICES

In Figure 6.4, it is illustrated how electron injection is energetically hindered when the bands are mismatched. This is accompanied by a schematic of the planar device architecture of a typical glass/FTO/compact metal oxide/perovskite/hole transporter/gold

stack shown in Figure 6.4a. Figure 6.4b,c show an energy band diagram derived from band gap and ultraviolet photoelectron spectroscopy (UPS) measurements for the two different perovskite materials (MAPbI_3 and mixed halide/cation, i.e. $(\text{FAPbI}_3)_{0.85}(\text{MAPbBr}_3)_{0.15}$, referred to as mixed perovskite throughout the text) atop the TiO_2 and SnO_2 .

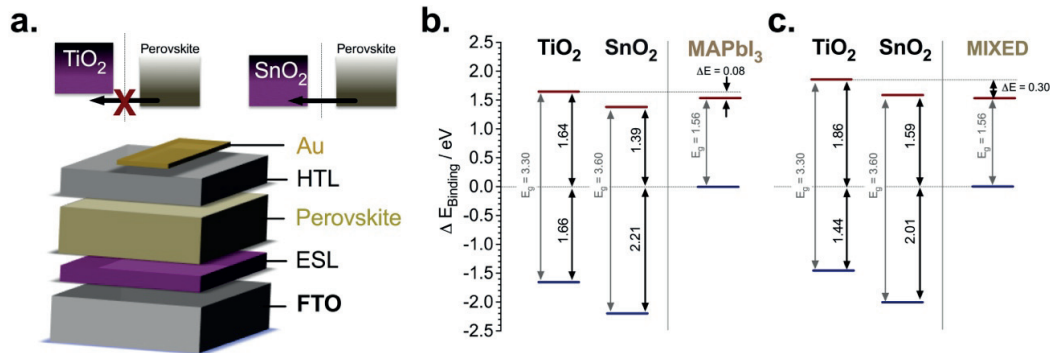


Figure 6.4 Energy level diagrams and electron injection characteristics of SnO_2 and TiO_2 -based planar PSCs. a, Schematic energy level diagram of the perovskite films and the electron selective layers, TiO_2 and SnO_2 grown by ALD for b, MAPbI_3 and c, $(\text{FAPbI}_3)_{0.85}(\text{MAPbBr}_3)_{0.15}$, labelled as 'mixed'.

We calculated the band diagram of the different components using band gap values (Figure 6.5) in combination with the perovskite materials' valence bands as our reference and derived the offset positions from the UPS spectra shown in Figure 6.6. For the band gap estimation of the perovskite materials, I performed diffuse reflectance measurements of each perovskite on a quartz substrate and extracted a band gap of 1.56 eV for both materials from Tauc plots shown in Figure 6.5. The band gaps of the oxides were measured by ellipsometry.

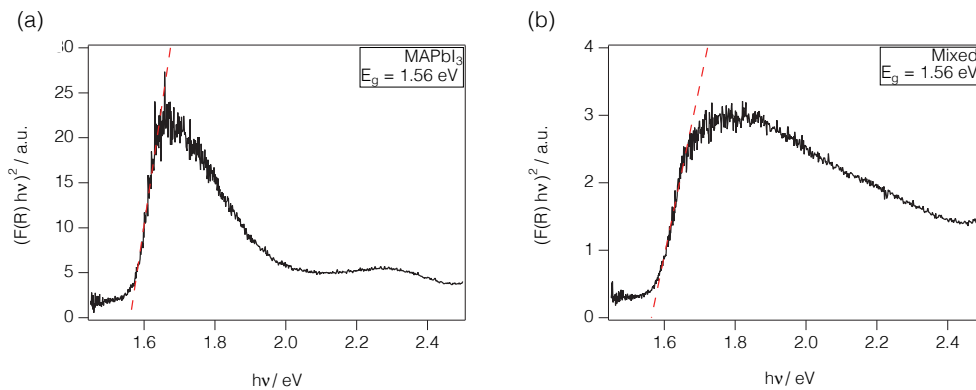


Figure 6.5 Diffuse reflectance measurements in a wavelength range of 300–900 nm for both the mixed (a) and MAPbI_3 (b) perovskites and their respective optical band gap.

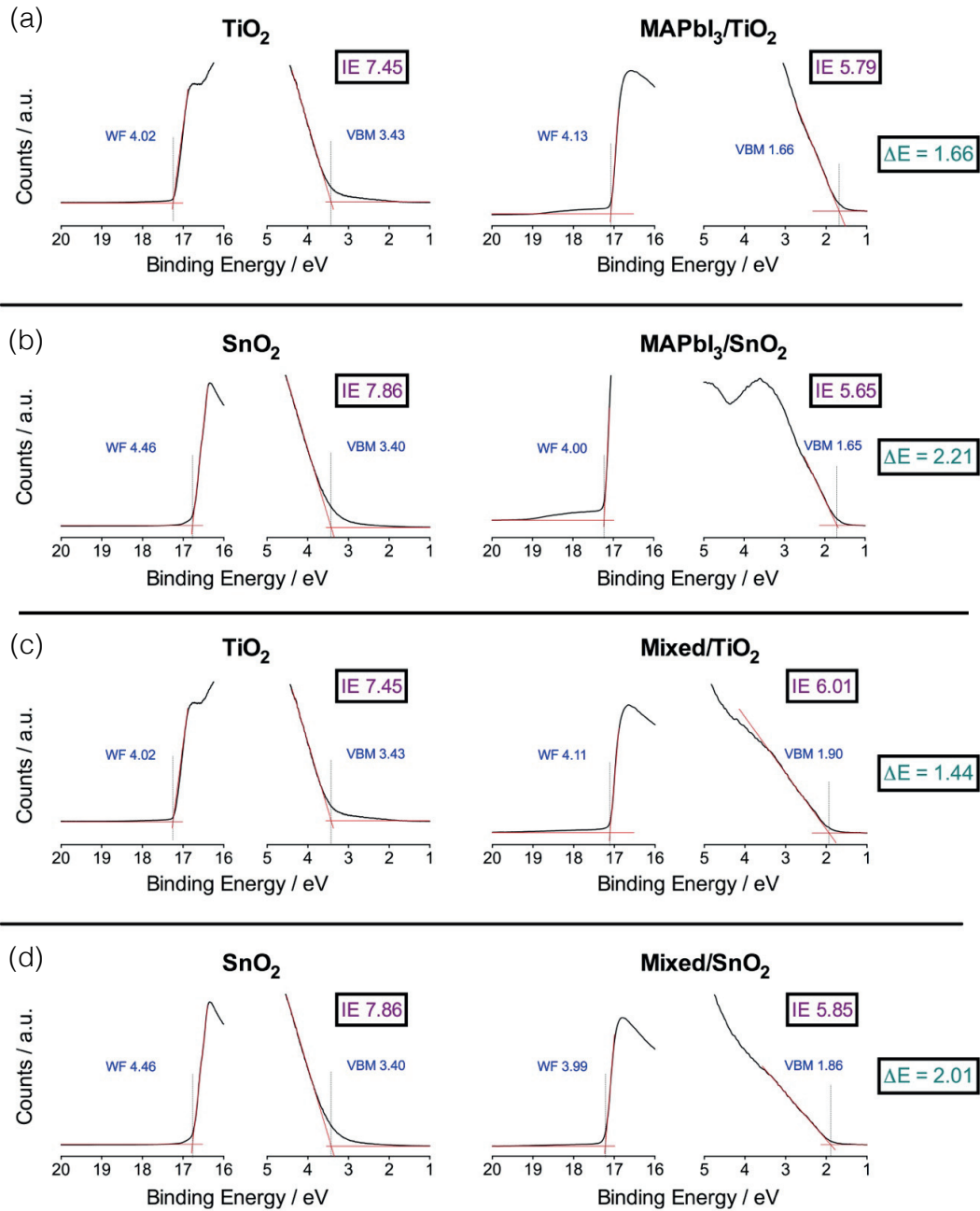


Figure 6.6 UPS spectra (He I) of a) the ALD TiO_2 and MAPbI_3 perovskite, b) the ALD SnO_2 and MAPbI_3 , c) the ALD TiO_2 and the $(\text{FAPbI}_3)_{0.85}(\text{MAPbBr}_3)_{0.15}$ perovskite labelled as 'mixed' and d) the ALD SnO_2 and $(\text{FAPbI}_3)_{0.85}(\text{MAPbBr}_3)_{0.15}$. Ionization energies (IE) and the difference between the valence band energies (ΔE) of the electron selective layers and the perovskite (ΔE) are shown for all materials.

Reconstructing the band energy diagrams shown in Figure 6.4b,c, from the UPS and band gap measurements, we see for both perovskite materials there is a conduction band misalignment with ALD TiO_2 ESLs, in stark contrast to SnO_2 where we have no such

misalignment. The band diagram in Figure 6.4b, shows that the conduction band of MAPbI₃ is ~80 meV below than that of TiO₂ and about 170 meV above that of SnO₂. This inhibits electron extraction by the TiO₂ and facilitates it using SnO₂. Similarly, the conduction band of the mixed perovskite is 300 meV below compared to TiO₂ and only 30 meV below compared to SnO₂. Consequently, this band misalignment with TiO₂ may cause undesirable consequences such as accumulation of photogenerated charges, which could hamper the device performance.

To further investigate this phenomenon, we prepared planar devices of typical stack architecture: glass/FTO/ESL/perovskite/HTL/gold contact as seen in the cross-sectional scanning electron microscopy (SEM) image in Figure 6.7a. I deposited a 15 nm thick ESL of SnO₂, TiO₂ or Nb₂O₅ by atomic layer deposition (ALD).

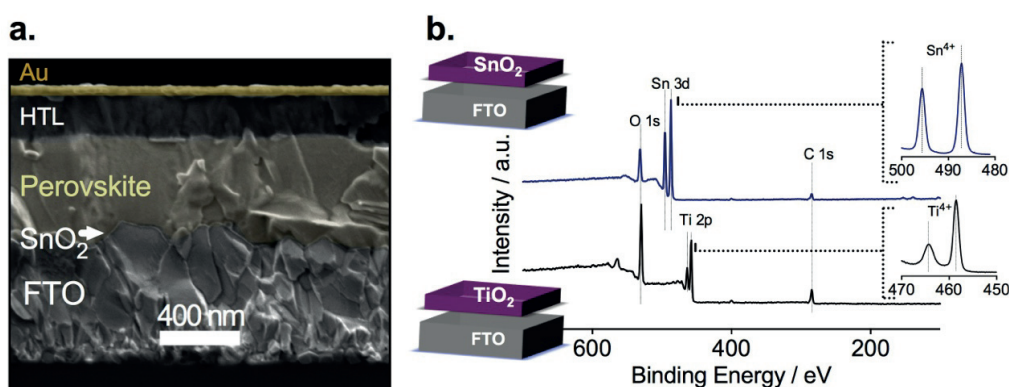


Figure 6.7 Photovoltaic device architecture and elemental composition of the electron selective layers (ESLs). a, Cross-sectional scanning electron micrograph of a typical layered photovoltaic device composed of FTO, SnO₂ as the electron selective layer (ESL), the perovskite film, a hole transporting layer (HTL, Spiro MeOTAD), and a gold top electrode. b, X-ray photoelectron spectroscopy of TiO₂ and SnO₂ thin layers used as ESLs.

The mixed perovskite layer, (FAPbI₃)_{0.85}(MAPbBr₃)_{0.15}, was spin-coated on the electrode using a similar composition as reported by Jeon et al.⁴ A doped spiro-MeOTAD was spin-coated as the HTL and, finally, the gold top electrode was deposited by thermal evaporation.

Figure 6.7b shows the X-ray photoelectron spectroscopy (XPS) of the 15 nm thick ALD TiO₂ and SnO₂ layers. For TiO₂, no peaks other than oxygen O 1s at 528 eV, titanium Ti 2p at 458.5 eV and Ti 2p_{1/2} 464.2 eV were detected confirming the deposition of TiO₂ without traces of cross contamination.³¹ We detect no signal from the underlying FTO indicating conformal and pinhole-free TiO₂ coverage, which we further confirm by SEM

(Figure 6.8a). Similarly, the formation of pure SnO₂ is confirmed observing the oxygen peak O 1s at 530.9 eV and Sn⁴⁺ peaks at 495.6 eV as well as at 487.2 eV in Figure 6.7b. The top-view SEM image in Figure 6.8b also indicates a pinhole-free deposition of SnO₂ as also shown in Section 6.3.1.

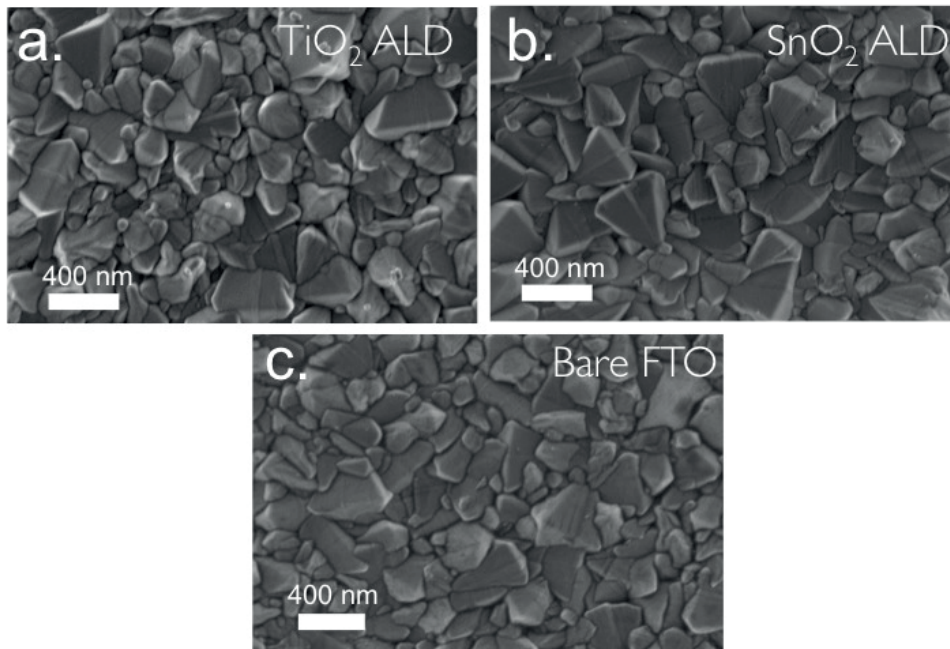


Figure 6.8 Scanning electron micrographs of FTO substrates coated by atomic layer deposition with a, TiO₂ and b, SnO₂ and compared to c, the uncoated FTO.

In order to further understand electron injection dynamics from the perovskite into the ESLs, we performed femtosecond transient absorption (TA) measurements on devices with SnO₂ and TiO₂ and the mixed perovskite under short circuit condition, wherein the charge injection can be resolved in time. In Figure 6.9, we show the TA dynamics taken at a probe wavelength of 750 nm - the peak of the photobleach (PB) of the perovskite.

The PB band, spectrally located at the onset of the absorption spectrum of the semiconductor (Figure 6.5), corresponds to the photo-induced transparency in the material due to the presence of electrons and holes in the bottom and top of the conduction and valence bands, respectively.¹⁷ Hence, the magnitude of this feature is correlated to the photo-induced carrier population and every effect changing the initial population, like electron/hole injection results in its quenching.

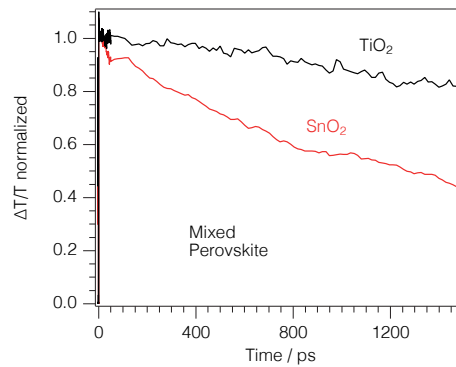


Figure 6.9 Transient absorption measurements of SnO₂ and TiO₂-based planar PSCs. Dynamics of the photo-bleaching bands for photo-excited perovskite measured on a typical working device employing the mixed perovskite (FAPbI₃)_{0.85}(MAPbBr₃)_{0.15} and ALD SnO₂ or TiO₂ as the ESL. The device is held at short circuit condition during the measurement. The probe wavelength is $\lambda = 750$ nm.

We observe a PB decay in the nanosecond timescale for both TiO₂ and SnO₂-based devices. However, while in the TiO₂-based device the dynamic does not strongly differ from the one probed from the pristine perovskite deposited on bare glass,³² in the case of SnO₂ the decay is much faster. In fact, about 60% of the population is gone in about 1.5 ns. As both devices embody the same hole-extracting layer, we conclude that the striking difference observed can be considered as the signature of different electron injection dynamics. This strongly supports our hypothesis of better electron extraction in pristine SnO₂ when compared to TiO₂-based devices, due to favorable energetic alignment.

Poor charge extraction in the TiO₂ based device may appear surprising. However, it must be considered that, in thin film PSCs in presence of planar TiO₂ as electron extracting layer, solar cells generally show J_{SC} comparable to those using a mesoporous TiO₂ layer only when the device is pre-polarized.^{13-15, 24, 33} Indeed, it was recently demonstrated that the PB dynamics becomes faster when it is measured just after keeping the TiO₂-based device at 1 V for a few seconds, suggesting that the electron transfer is suddenly activated.³³ This indicates that upon polarization, the TiO₂/perovskite interface is modified and such modification is needed to allow for an efficient charge transfer as also predicted by De Angelis et al.³⁴

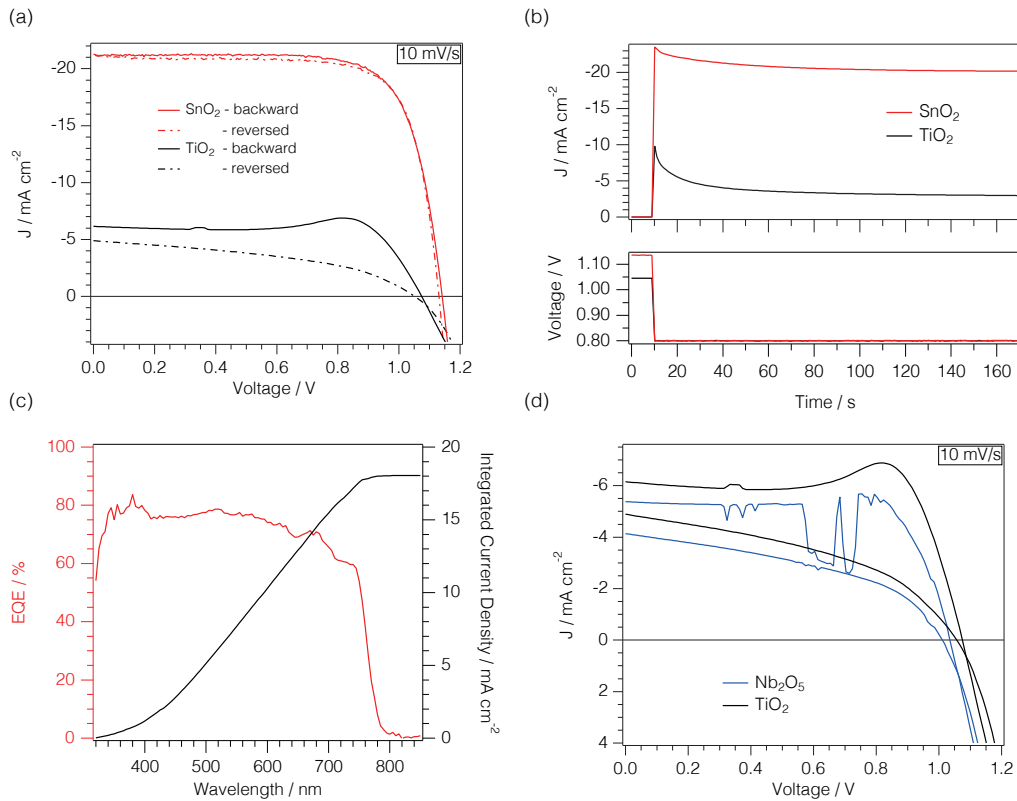


Figure 6.10 Photovoltaic characteristics of planar perovskite devices based on ALD SnO₂ or TiO₂ ESL. a) Current-voltage properties of TiO₂ and SnO₂-based planar mixed halide/cation perovskite devices in backward scan from V_{oc} to J_{sc} and in reversed scan. SnO₂-based devices showed power conversion efficiencies of PCE = 18.4% in forward scan and PCE = 18.1% in reversed scan. b) Transient photocurrents measured from V_{oc} to maximum power point voltage for both planar systems. c) External quantum efficiency and integrated current density ($J_{sc}(int) = 18 \text{ mA cm}^{-2}$) of a SnO₂-based mixed perovskite solar cell. d) Hysteresis behavior of Nb₂O₅ compared to TiO₂-based planar devices.

Table 6.2 Solar cell performance parameters for the SnO₂-based mixed perovskite device for backward and forward scans at a scan rate of 10 mV s^{-1} : short circuit photocurrent (J_{sc}), power conversion efficiency (PCE), open circuit voltage (V_{oc}), and fill factor (FF) as extracted from the data in Figure 6.10a.

ESL	Scan direction	J_{sc} mA cm ⁻²	V_{oc} V	FF	PCE %	Light Intensity mW cm ⁻²
SnO ₂	Backward	21.3	1.14	0.74	18.4	98.4
	Forward	21.2	1.13	0.75	18.1	

We investigated the different electronic properties of devices with ALD TiO₂ or SnO₂ ESLs by analyzing the current density-voltage curves based on the mixed perovskite. In

Figure 6.10a, we observe a representative SnO₂ device with high performance and low hysteresis between the backward and forward scan (Table 6.2). This is indicative of good charge collection independent of voltage. In stark contrast, a representative TiO₂-based device shows strong hysteresis and low current densities ($< 5 \text{ mA cm}^{-2}$) at the same scan rate. This difference can also be seen in Figure 6.10b where we show transient photocurrents recorded at 0.8 V resembling closely operating device conditions at maximum power point. After ~ 50 s, we observe a steady photocurrent when switching from open circuit to 0.8 V. After switching from open circuit to 0.8 V, the current for the TiO₂ device drops by 70% from 10 to stabilized 3 mA cm^{-2} , whereas that for the SnO₂ drops by only 10% from 23 to stabilized 20.2 mA cm^{-2} . The stabilized current is in good agreement with the current seen in the J-V curve at 0.8 V, which is found to be 20.7 mA cm^{-2} (Figure 6.10a).

Small variations were found for 12 devices made in different batches with an average PCE of 16.7%, while the best device is shown in Figure 6.10a. Integrating the external quantum efficiency (EQE) of a typical cell with a PCE of 16.14% yielded a J_{SC} of 18 mA cm^{-2} seen in Figure 6.10c, which is in very good agreement with the measured J_{SC} of 19.6 mA cm^{-2} for this device. We note that for both TiO₂ and SnO₂, we observe open circuit voltages of around 1.14 V, which are close or even exceed most devices prepared with mesoporous interlayers. Additionally, some of our SnO₂ devices yielded stabilized voltages of over 1.19 V approaching the thermodynamic maximum V_{oc} of approx. 1.32 V.³⁵ This suggests exceptionally good charge selectivity and a low degree of charge recombination in our planar perovskite/SnO₂ devices.

As a next step, we investigated devices with ALD Nb₂O₅ as the ESL shown in Figure 6.10d which has a similar conduction band position as TiO₂.³⁶ With this, we can crosscheck if the energy level alignment is indeed critical for high hysteresis and can exclude that other properties of the SnO₂ or TiO₂ are responsible for the above results. Very similar to TiO₂, the Nb₂O₅-based devices exhibited large hysteresis behavior and very low photocurrent densities at sweep rates of 10 mV/s. Faster sweep rates also yield higher photocurrent densities and the transient current measurements also showed a similar behavior to that of TiO₂ with photocurrents decaying to $< 50\%$ of the initial value. We hypothesize that a preconditioning of the TiO₂- and Nb₂O₅-based mixed perovskite devices under forward bias leads to accumulation of negative charge and ion migration at

the ESL-perovskite interface inducing a high electric field and/or dipole formation at this interface.^{12, 24} An elevated electric field or possibly a reduced conduction band offset can facilitate electron injection into the ESL. After releasing the positive bias, this beneficial effect lasts for a few seconds only, which is the time needed for this charge to be removed. Sweep rates in this time range give rise to large hysteresis. For the SnO₂ devices, the energy levels are already well aligned without biasing the device. Thus, charge collection is efficient showing high FF and J_{sc} independent of the scan rate.

Other works^{2, 4} have shown high performance at stabilized currents in thin mesoporous TiO₂ based ESLs, and we note that this may be due to a proper band alignment intrinsic to the mesoporous TiO₂/perovskite interface which is different from the planar configuration with the ALD TiO₂ used in this study.

6.4 CONCLUSION

In summary, we have demonstrated that a barrier-free band alignment between the perovskite light harvester and the charge selective contact is of great importance for an efficient perovskite solar cell. We found that planar PSCs employing the compact and pinhole-free semi-crystalline TiO₂ layer made by ALD exhibit a band misalignment, leading to strong hysteresis behavior and scan rate dependent current densities, indicating capacitive effects at the interface. We chose a layer of SnO₂, due to its deeper conduction band, as the electron selective contact, which achieved voltages and PCEs exceeding 1.14 V and 18%, respectively.

The ALD-grown thin films of SnO₂ were investigated by cyclic voltammetry of Fe(CN)^{3-/4-} as well as by scanning and transmission electron microscopy (SEM and TEM) to detect pinholes, if any, in the blocking layer. The blocking behavior was exceptionally good for the as-grown amorphous SnO₂ films with thicknesses down to 2 nm.

We proved that modifying the conduction band of the ESL can result in planar, high performance PSCs with high voltages and remarkably good stability over time. Furthermore, femtosecond TA measurements clearly show that SnO₂ efficiently extract charges from the mixed (FAPbI₃)_{0.85}(MAPbBr₃)_{0.15} perovskite material but not TiO₂ suggesting a band misalignment at the TiO₂/perovskite interface. From this we can conclude that a barrier-free charge transport across the SnO₂/perovskite interface gives rise to the high and stable current densities – regardless of sweep rate – which are not

observed in TiO₂ based devices. This study highlights the importance of a perfect band alignment for highly efficient PSCs, especially in planar devices with compact charge selective layers.

However, the blocking function of ALD SnO₂ does not persist upon calcination at 450 °C in air, when about 90% of the FTO surface underneath the SnO₂ film seems to be exposed. The SEM and TEM study revealed the formation of a highly porous crystalline SnO₂ film structure for the annealed sample. The sensitivity to thermal formation of pinholes is larger in SnO₂ layers compared to that in ALD TiO₂ layers; and this impediment must be taken into account in the fabrication of electron-selective contacts in combination with mesoporous oxide structures commonly used in photoelectrodes.

6.5 REFERENCES

1. Baena, J. P. C.; Steier, L.; Tress, W.; Saliba, M.; Neutzner, S.; Matsui, T.; Giordano, F.; Jacobsson, T. J.; Kandada, A. R. S.; Zakeeruddin, S. M., *et al.* Highly Efficient Planar Perovskite Solar Cells through Band Alignment Engineering. *Energy & Environmental Science* **2015**, *8*, 2928-2934.
2. Yang, W. S.; Noh, J. H.; Jeon, N. J.; Kim, Y. C.; Ryu, S.; Seo, J.; Seok, S. I. High-Performance Photovoltaic Perovskite Layers Fabricated through Intramolecular Exchange. *Science* **2015**.
3. http://www.nrel.gov/ncpv/images/efficiency_chart.jpg (accessed February 15, 2016)
4. Jeon, N. J.; Noh, J. H.; Yang, W. S.; Kim, Y. C.; Ryu, S.; Seo, J.; Seok, S. I. Compositional Engineering of Perovskite Materials for High-Performance Solar Cells. *Nature* **2015**, *517*, 476-480.
5. Bi, D.; Tress, W.; Dar, M. I.; Gao, P.; Luo, J.; Renevier, C.; Schenk, K.; Abate, A.; Giordano, F.; Correa Baena, J.-P., *et al.* Efficient Luminescent Solar Cells Based on Tailored Mixed-Cation Perovskites. *Science Advances* **2016**, *2*.
6. Kagan, C. R.; Mitzi, D. B.; Dimitrakopoulos, C. D. Organic-Inorganic Hybrid Materials as Semiconducting Channels in Thin-Film Field-Effect Transistors. *Science* **1999**, *286*, 945-947.
7. Kojima, A.; Teshima, K.; Shirai, Y.; Miyasaka, T. Organometal Halide Perovskites as Visible-Light Sensitizers for Photovoltaic Cells. *Journal of the American Chemical Society* **2009**, *131*, 6050-6051.
8. Lee, M. M.; Teuscher, J.; Miyasaka, T.; Murakami, T. N.; Snaith, H. J. Efficient Hybrid Solar Cells Based on Meso-Superstructured Organometal Halide Perovskites. *Science* **2012**, *338*, 643-647.
9. Etgar, L.; Gao, P.; Xue, Z.; Peng, Q.; Chandiran, A. K.; Liu, B.; Nazeeruddin, M. K.; Grätzel, M. Mesoscopic Ch₃nh₃pb₃i₃/TiO₂ Heterojunction Solar Cells. *Journal of the American Chemical Society* **2012**, *134*, 17396-17399.
10. Stranks, S. D.; Eperon, G. E.; Grancini, G.; Menelaou, C.; Alcocer, M. J.; Leijtens, T.; Herz, L. M.; Petrozza, A.; Snaith, H. J. Electron-Hole Diffusion Lengths Exceeding 1 Micrometer in an Organometal Trihalide Perovskite Absorber. *Science* **2013**, *342*, 341-344.
11. Liu, M.; Johnston, M. B.; Snaith, H. J. Efficient Planar Heterojunction Perovskite Solar Cells by Vapour Deposition. *Nature* **2013**, *501*, 395-398.

12. Zhang, Y.; Liu, M.; Eperon, G. E.; Leijtens, T. C.; McMeekin, D.; Saliba, M.; Zhang, W.; de Bastiani, M.; Petrozza, A.; Herz, L. M., *et al.* Charge Selective Contacts, Mobile Ions and Anomalous Hysteresis in Organic-Inorganic Perovskite Solar Cells. *Materials Horizons* **2015**, *2*, 315-322.
13. Xing, G.; Wu, B.; Chen, S.; Chua, J.; Yantara, N.; Mhaisalkar, S.; Mathews, N.; Sum, T. C. Interfacial Electron Transfer Barrier at Compact TiO₂/CH₃NH₃PbI₃ Heterojunction. *Small* **2015**.
14. Wojciechowski, K.; Stranks, S. D.; Abate, A.; Sadoughi, G.; Sadhanala, A.; Kopidakis, N.; Rumbles, G.; Li, C.-Z.; Friend, R. H.; Jen, A. K.-Y. Heterojunction Modification for Highly Efficient Organic-Inorganic Perovskite Solar Cells. *ACS nano* **2014**, *8*, 12701-12709.
15. Wojciechowski, K.; Leijtens, T.; Spirova, S.; Schlueter, C.; Hoerantner, M.; Wang, J. T.-W.; Li, C.-Z.; Jen, A. K. Y.; Lee, T.-L.; Snaith, H. J. C60 as an Efficient N-Type Compact Layer in Perovskite Solar Cells. *The Journal of Physical Chemistry Letters* **2015**.
16. Ke, W.; Fang, G.; Liu, Q.; Xiong, L.; Qin, P.; Tao, H.; Wang, J.; Lei, H.; Li, B.; Wan, J., *et al.* Low-Temperature Solution-Processed Tin Oxide as an Alternative Electron Transporting Layer for Efficient Perovskite Solar Cells. *Journal of the American Chemical Society* **2015**, *137*, 6730-6733.
17. Dong, Q.; Shi, Y.; Wang, K.; Li, Y.; Wang, S.; Zhang, H.; Xing, Y.; Du, Y.; Bai, X.; Ma, T. Insight into Perovskite Solar Cells Based on SnO₂ Compact Electron-Selective Layer. *The Journal of Physical Chemistry C* **2015**, *119*, 10212-10217.
18. Song, J.; Zheng, E.; Bian, J.; Wang, X.-F.; Tian, W.; Sanehira, Y.; Miyasaka, T. Low-Temperature SnO₂-Based Electron Selective Contact for Efficient and Stable Perovskite Solar Cells. *Journal of Materials Chemistry A* **2015**, *3*, 10837-10844.
19. Li, Y.; Zhu, J.; Huang, Y.; Liu, F.; Lv, M.; Chen, S.; Hu, L.; Tang, J.; Yao, J.; Dai, S. Mesoporous SnO₂ Nanoparticle Films as Electron-Transporting Material in Perovskite Solar Cells. *RSC Advances* **2015**, *5*, 28424-28429.
20. Kranz, L.; Abate, A.; Feurer, T.; Fu, F.; Avancini, E.; Löckinger, J.; Reinhard, P.; Zakeeruddin, S. M.; Grätzel, M.; Buecheler, S., *et al.* High-Efficiency Polycrystalline Thin Film Tandem Solar Cells. *The Journal of Physical Chemistry Letters* **2015**, 2676-2681.
21. Azevedo, J.; Steier, L.; Dias, P.; Stefik, M.; Sousa, C. T.; Araujo, J. P.; Mendes, A.; Graetzel, M.; Tilley, S. D. On the Stability Enhancement of Cuprous Oxide Water Splitting Photocathodes by Low Temperature Steam Annealing. *Energy & Environmental Science* **2014**, *7*, 4044-4052.
22. Abate, A.; Leijtens, T.; Pathak, S.; Teuscher, J.; Avolio, R.; Errico, M. E.; Kirkpatrick, J.; Ball, J. M.; Docampo, P.; McPherson, I., *et al.* Lithium Salts as "Redox Active" P-Type Dopants for Organic Semiconductors and Their Impact in Solid-State Dye-Sensitized Solar Cells. *Physical Chemistry Chemical Physics* **2013**, *15*, 2572-2579.
23. Abate, A.; Staff, D. R.; Hollman, D. J.; Snaith, H. J.; Walker, A. B. Influence of Ionizing Dopants on Charge Transport in Organic Semiconductors. *Physical Chemistry Chemical Physics* **2014**, *16*, 1132-1138.
24. Snaith, H. J.; Abate, A.; Ball, J. M.; Eperon, G. E.; Leijtens, T.; Noel, N. K.; Stranks, S. D.; Wang, J. T.-W.; Wojciechowski, K.; Zhang, W. Anomalous Hysteresis in Perovskite Solar Cells. *The Journal of Physical Chemistry Letters* **2014**, *5*, 1511-1515.
25. Kavan, L.; Tetreault, N.; Moehl, T.; Gratzel, M. Electrochemical Characterization of TiO₂ Blocking Layers for Dye-Sensitized Solar Cells. *Journal of Physical Chemistry C* **2014**, *118*, 16408-16418.
26. Moehl, T.; Im, J. H.; Lee, Y. H.; Domanski, K.; Giordano, F.; Zakeeruddin, S. M.; Dar, M. I.; Heiniger, L. P.; Nazeeruddin, M. K.; Park, N. G., *et al.* Strong Photocurrent Amplification in Perovskite Solar Cells with

- a Porous TiO₂ Blocking Layer under Reverse Bias. *Journal of Physical Chemistry Letters* **2014**, *5*, 3931-3936.
27. Amatore, C.; Saveant, J. M.; Tessier, D. Charge-Transfer at Partially Blocked Surfaces - a Model for the Case of Microscopic Active and Inactive Sites. *Journal of Electroanalytical Chemistry* **1983**, *147*, 39-51.
28. Lee, H. J.; Beriet, C.; Ferrigno, R.; Girault, H. H. Cyclic Voltammetry at a Regular Microdisc Electrode Array. *Journal of Electroanalytical Chemistry* **2001**, *502*, 138-145.
29. Sveinbjörnsson, K.; Aitola, K.; Zhang, X.; Pazoki, M.; Hagfeldt, A.; Boschloo, G.; Johansson, E. M. J. Probing Photocurrent Generation, Charge Transport, and Recombination Mechanisms in Mesostuctured Hybrid Perovskite through Photoconductivity Measurements. *The Journal of Physical Chemistry Letters* **2015**, *6*, 4259-4264.
30. Tauc, J.; Grigorovici, R.; Vancu, A. Optical Properties and Electronic Structure of Amorphous Germanium. *physica status solidi (b)* **1966**, *15*, 627-637.
31. Bender, H.; Chen, W. D.; Portillo, J.; Van den Hove, L.; Vandervorst, W. Aes and Xps Analysis of the Interaction of Ti with Si and SiO₂ During Rta. *Applied Surface Science* **1989**, *38*, 37-47.
32. Xing, G.; Mathews, N.; Sun, S.; Lim, S. S.; Lam, Y. M.; Grätzel, M.; Mhaisalkar, S.; Sum, T. C. Long-Range Balanced Electron-and Hole-Transport Lengths in Organic-Inorganic CH₃NH₃PbI₃. *Science* **2013**, *342*, 344-347.
33. Tao, C.; Neutzner, S.; Colella, L.; Marras, S.; Srimath Kandada, A. R.; Gandini, M.; De Bastiani, M.; Pace, G.; Manna, L.; Caironi, M., *et al.* 17.6 % Steady State Efficiency in Low Temperature Processed Planar Perovskite Solar Cells. *Energy & Environmental Science* **2015**.
34. Azpiroz, J. M.; Mosconi, E.; Bisquert, J.; De Angelis, F. Defect Migration in Methylammonium Lead Iodide and Its Role in Perovskite Solar Cell Operation. *Energy & Environmental Science* **2015**.
35. Tress, W.; Marinova, N.; Inganäs, O.; Nazeeruddin, M. K.; Zakeeruddin, S. M.; Graetzel, M. Predicting the Open-Circuit Voltage of CH₃NH₃PbI₃ Perovskite Solar Cells Using Electroluminescence and Photovoltaic Quantum Efficiency Spectra: The Role of Radiative and Non-Radiative Recombination. *Advanced Energy Materials* **2015**, *5*, n/a-n/a.
36. Marschall, R. Semiconductor Composites: Strategies for Enhancing Charge Carrier Separation to Improve Photocatalytic Activity. *Advanced Functional Materials* **2014**, *24*, 2421-2440.

7 CONCLUSIONS AND OUTLOOK

7.1 TRAP STATES IN HEMATITE

In the first part of the work on hematite photoanodes, progress was made towards a better understanding of the electronic processes influencing water oxidation kinetics. Figure 3.9 and Figure 3.11 summarize best the results obtained from Chapter 3:

Firstly, Figure 3.9 shows that the energetic position of the trap level is located 0.8 V more positive of the flat band potential. In other words, the trap level is located *in the middle of the band gap* considering the conduction band located at -4.78 eV.¹ Hence, it is a deep trap level.

Secondly, it shows that the energetic position of the trap level is shifted 200 mV closer to the conduction band upon annealing at 500 °C in air.

Thirdly, it shows that the shift in the energetic position of the trap state correlates well with the shift in the photocurrent onset of these photoanodes. Indeed, the onset of the photocurrent is observed when half of the traps states are emptied (from electrons) while applying a voltage bias that pushes the quasi-Fermi level of electrons to more positive voltages (more negative energies).

Zandi *et al.* obtained exactly the same energetic position of a trap state in ALD hematite samples employing a Ga₂O₃ underlayer after annealing to 500 °C in air at similar heating and cooling rates.² Upon annealing to 800 °C in air they observed a shift in the energetic position of the trap states and a correlated shift of the water oxidation photocurrent onset towards more negative potentials (towards 0.7 V_{RHE}) which is in very good agreement to the results obtained in this work.

While Zandi *et al.* attributed the trap state to water oxidation intermediates, another possible explanation might be that the trap state that was located in the middle of the band gap for samples annealed at 500 °C could be moved during the annealing process at 800 °C. Through the annealing treatment it would become a shallower trap that allows water oxidation to set on with lower applied voltages. This proposed relation will be detailed in the following.

High temperature treatments influence film conductivity

There is evidence in literature that high temperature annealing improves the conductivity of pure hematite films influencing the hole mobility in the temperature range between 450 - 800 °C.³ The results are reprinted in Figure 7.1.

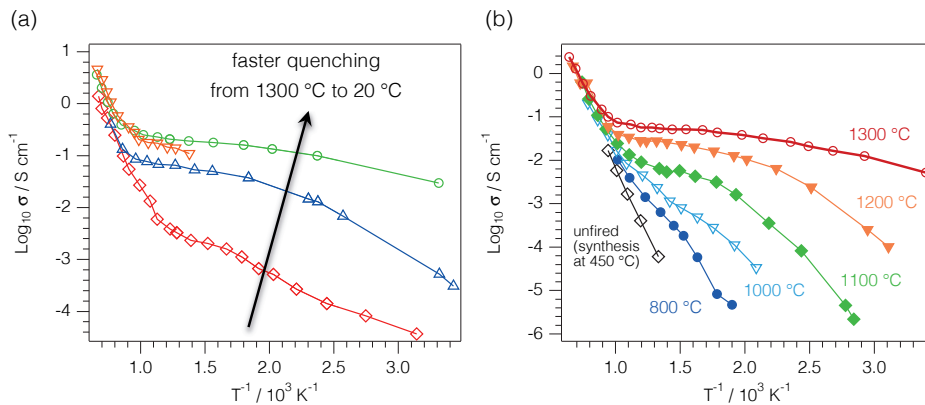


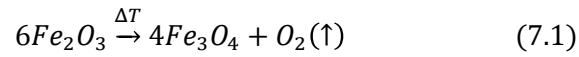
Figure 7.1 a) The conductivity of ferric oxide specimens of high purity as a function of temperature. Prior the temperature dependent conductivity measurements, the specimens were fired at 1300 °C in air and quenched at different rates to room temperature. *Green*: oxidized iron wire, quenched to 20 °C in about 1 s after 5 h at 1300 °C. *Orange*: single crystal of ferric oxide grown from sodium tetraborate; four-probe resistivity along the (111) plane of a specimen quenched after 13 h at 1300 °C. *Blue*: A compact sample (prepared from thick layers (about 1 cm) of oxalate at about 650°C), after quenching from 1300 to 20°C in about 10 s. *Red*: The same compact sample slowly cooled. b) The influence of firing temperature on the conductivity of a compact film of ferric oxide that was synthesized at 450 °C. Black: the unfired compact; blue-red curves obtained for specimen quenched after 20 h at the stated temperatures. Reprinted from reference ³.

Looking in Figure 7.1a at room temperature conductivity measurements (rightmost measurement points), it becomes clear that samples that were rapidly quenched from 1300 °C to 20 °C (green and blue curves) show orders of magnitude higher conductivities than samples that were cooled much slower (red curve). Gardner *et al.* attributed this to donor centers that are *frozen* into the lattice on cooling, which was also observed with NiO and Cr₂O₃.^{4, 5} Furthermore, Figure 7.1b shows, that samples annealed to higher temperatures maintained higher conductivities at room temperature after quenching. Gardner assigned this to the formation of additional carriers due to oxygen loss during annealing in air and also due to positive carriers at temperatures exceeding 1000 °C. This strongly indicates that major electronic changes occur during the annealing step.

Oxygen vacancy formation upon high temperature annealing in air

It is known that hematite becomes oxygen deficient in air at higher temperatures and is

converted to magnetite at temperatures between 900 – 1450 °C depending on the oxygen partial pressure.⁶ Salmon *et al.* showed that at oxygen partial pressures, $p(O_2)$, as low as $10^{-6.5}$ atm a temperature of 900 °C is sufficient for this phase transformation while at $p(O_2) = 1$ atm, hematite has to be heated to 1450 °C for the following reaction to occur:



The defect equilibrium of oxygen vacancy formation is described by Equation (3.7) and their concentration due to oxygen loss for samples equilibrated with air is given by Equation (7.2).^{3, 6}

$$N_D = 4.79 \cdot 10^{26} \text{ cm}^{-3} e^{-\frac{2.03[eV]}{k_B T}} \quad (7.2)$$

Equation (1.18) showed the dependence of conductivity of a semiconductor on charge carrier density, where the carrier density, n , is given by Equation (1.13) and can be simplified to Equation (7.3) for n-type semiconductors.⁷

$$n \approx N_D^+ \quad (7.3)$$

Only ionised donors can contribute to conductivity

The above relationship is important to emphasize at this point as it states that only ionized donors contribute to the conductivity of a semiconductor. In classical semiconductors such as silicon and GaAs mostly shallow donor impurities are introduced to enhance the conductivity. These shallow impurities readily ionize even at room temperature.

However, in hematite this is not necessarily the case because of the deep donor level. Thus, under the assumption that this deep donor level could be related to oxygen vacancies in undoped hematite films, a possible explanation might be related to the change in the energetic position of the trap level after high temperature annealing treatments. This will be elucidated in the following paragraph.

As the trap level moves closer to the conduction band, donors can readily ionize with much less applied bias. This would increase the conductivity in hematite and also influence the electron-hole recombination kinetics. As the conductivity of the film is improved through shallow ionized donor states, electrons can more easily conduct to the back contact. Also, since the ionized oxygen vacancy is positively charged, it does not represent a trap level for the holes. Figure 3.9 shows that the threshold for the

photocurrent onset is reached once half of the donor states become ionized. A possible explanation for this could lie in the higher concentration of holes in the space charge layer due to less recombination leading to a wider Fermi level splitting that finally positions the quasi Fermi level of holes, E_{Fp} , well below the water oxidation potential (+overpotential). Of course, the induced electric field by the applied voltage bias also leads to improved charge separation as stated by Pendlebury *et al.*,⁸ but combining the results obtained in Chapter 3 with the studies in the work of Zandi *et al.*, points to the trap level position being the determining factor for the photocurrent onset potential. Even with the Ga₂O₃ passivation layer, I observed a shift in the trap state energy (Figure 3.8b). Thus, following this train of thought, relocating the trap state closer to the conduction band to become a shallower and more readily ionizable state would be important for the onset of water oxidation due to an increase in conductivity. However, the trap state itself would not necessarily be part of the water oxidation reaction pathway as proposed by the model of Bisquert.⁹⁻¹¹

Also, any surface treatment that reduces electron-hole recombination, such as Co-Pi,^{12, 13} would allow the quasi Fermi levels to split wider as holes actually accumulate at the hematite surface and hence, the thermodynamic potential to oxidize water would be reached with less applied voltage.

Open questions

It is not completely clear what induces the shift in the trap state energy level and neither how surface treatments with Co-Pi or Ga₂O₃ chemically and electronically change the surface to reduce electron-hole recombination. The above-presented assumptions pose many interesting questions to be answered in future work. Also, the differentiation of surface versus bulk recombination and surface versus bulk trap states in such thin (10 nm) hematite films needs to be addressed.

7.2 WITH ALD HEMATITE TOWARDS HOST-GUEST ARCHITECTURES

In the second part of my work on hematite photoanodes, I successfully developed a new low-temperature atomic layer deposition (ALD) route towards crystalline, pure and photoactive hematite thin films that can be deposited on any nanostructured host material.

Towards this goal I installed a home-built ALD setup especially designed for hematite growth. This deposition method has a big potential to realize the host-guest concept (shown in Figure 1.15c) and to overcome the charge extraction barrier in thick hematite films. However, further development on highly conducting host nanostructures with optimized feature size and morphology is needed to minimize resistance and recombination losses in the nanostructure and achieve optimized light absorption.

Meanwhile, ALD provides a better thin film model system for fundamental studies than ultrasonic spray pyrolysis for two reasons: firstly, the photoactive hematite films can be deposited with a much more precise thickness control and secondly, the films are flat and smooth and hence, free of morphology influences. A systematic study on these thin ALD hematite films of precise thicknesses confirmed the effect of doping from the underlayer observed with the USP hematite films. I showed that at a deposition temperature of 230 °C, the underlayer could induce donor impurities diffusing up to 10 nm into the hematite layer. Furthermore, IPCE and APCE measurements indicated that only the space charge region in the hematite thin films contributed to the photocurrent. The optimal thickness with respect to the space charge width was found to be on the order of 10 nm for hematite films on a TiO₂ underlayer (doped hematite) and 12 nm for hematite films on FTO.

Another observation of this study was that light absorbed between 500 – 600 nm is poorly converted to photocurrent as seen in Figure 7.2, which is typical not only for thin ALD hematite layers but for other synthetic methods and morphologies as well. Implementing catalysts can improve reaction kinetics but did not lead to strongly enhanced red light activity in hematite.¹⁴

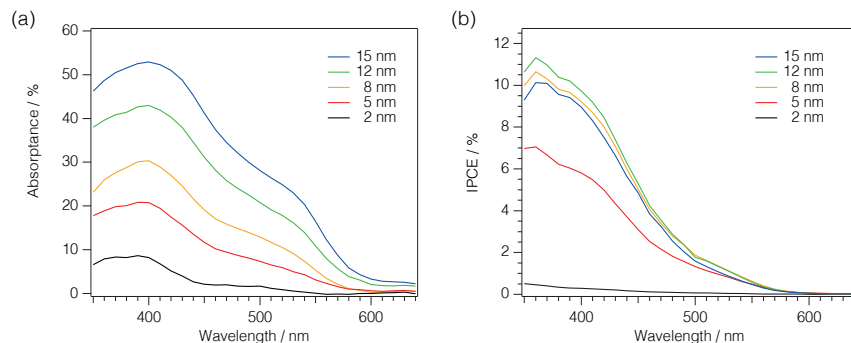


Figure 7.2 Absorbance (a) and incident photon to current conversion efficiencies (b) for air-annealed ALD deposited Ti-doped thin hematite films of different thicknesses (2-15 nm).

The absorption peak at 2.4 eV (517 nm) was assigned to a Fe 3d \rightarrow Fe 3d transition.¹⁵ These d-d transitions are weaker than transitions from the p-orbitals in the valence band. The cauliflower structure in combination with a Co-Pi layer seemed to overcome the poor photon conversion around 517 nm,¹⁶ however, not every nanostructure seems to be as effective as the cauliflower morphology.¹⁷ Optoelectronic modeling will be an important tool in the process of resolving the origin of this conversion loss. In this work a basis for further developments towards a powerful and complete optical and electrical model was created. Hematite and FTO were characterized by ellipsometry and UV-vis spectroscopy providing the necessary optical constants for the model. Also the IPCE, APCE and current voltage measurements from Chapter 4 will be helpful for the development of the electronic model for hematite photoanodes.

7.3 TIN OXIDE ELECTRON-SELECTIVE CONTACT FOR PEROVSKITE SOLAR CELLS

With the implementation of a 15 nm thin SnO₂ electron selective layer deposited by atomic layer deposition, the potential of flat perovskite solar cell device configurations has been demonstrated to be able to reach hysteresis-free power conversion efficiencies of up to 18% for the flat devices based on (FAPbI₃)_{0.85}(MAPbBr₃)_{0.15} perovskite materials. These high efficiencies are the result of precise engineering of the energetic band alignment between all layers in the cell such that electrons and holes can be extracted from the perovskite photoabsorber in the most efficient way. Any band misalignment represents an injection barrier that results in large hysteresis and reduced photovoltaic performance as seen for TiO₂ and Nb₂O₅ oxide layers studied in this work.

Furthermore, the quality of the ALD SnO₂ layer is highly important for the solar cell performance. Any pinhole would lead to recombination processes and result in major performance losses. I could show that ALD yielded amorphous SnO₂ layers that were pinhole-free already for thicknesses as low as 2 nm. Furthermore, the conductivity of the SnO₂ layer is at least 10 times higher than that of MAPbI₃ and hence not limiting electron transport. These results confirm the high quality of the ALD SnO₂ films. Indeed just recently our laboratory obtained power conversion efficiencies approaching 20% and more for flat perovskite devices with SnO₂ as the electron selective layer.

However, since the amorphous SnO₂ deposited by low-temperature ALD undergoes

major morphological changes upon calcination, it is not suitable as a rectifying contact for applications that require sintering treatments.

7.4 REFERENCES

1. Xu, Y.; Schoonen, M. A. A. The Absolute Energy Positions of Conduction and Valence Bands of Selected Semiconducting Minerals. *American Mineralogist* **2000**, 85, 543-556.
2. Zandi, O.; Hamann, T. W. Enhanced Water Splitting Efficiency through Selective Surface State Removal. *Journal of Physical Chemistry Letters* **2014**, 5, 1522-1526.
3. Gardner, R. F. G.; Tanner, D. W.; Sweett, F. Electrical Properties of Alpha Ferric Oxide .2. Ferric Oxide of High Purity. *Journal of Physics and Chemistry of Solids* **1963**, 24, 1183-&.
4. Hagel, W. C.; Seybolt, A. U. Cation Diffusion in Cr₂O₃. *Journal of the Electrochemical Society* **1961**, 108, 1146-1152.
5. Mitoff, S. P. Electrical Conductivity and Thermodynamic Equilibrium in Nickel Oxide. *Journal of Chemical Physics* **1961**, 35, 882-&.
6. Salmon, O. N. High Temperature Thermodynamics of Iron Oxide System. *Journal of Physical Chemistry* **1961**, 65, 550-&.
7. Sze, S. M.; Ng, K. K. *Physics of Semiconductor Devices*. 3rd ed.; Wiley-Interscience: Hoboken, N.J., 2007; p x, 815 p.
8. Pendlebury, S. R.; Wang, X. L.; Le Formal, F.; Cornuz, M.; Kafizas, A.; Tilley, S. D.; Gratzel, M.; Durrant, J. R. Ultrafast Charge Carrier Recombination and Trapping in Hematite Photoanodes under Applied Bias. *Journal of the American Chemical Society* **2014**, 136, 9854-9857.
9. Bertoluzzi, L.; Bisquert, J. Equivalent Circuit of Electrons and Holes in Thin Semiconductor Films for Photoelectrochemical Water Splitting Applications. *Journal of Physical Chemistry Letters* **2012**, 3, 2517-2522.
10. Klahr, B.; Gimenez, S.; Fabregat-Santiago, F.; Bisquert, J.; Hamann, T. W. Photoelectrochemical and Impedance Spectroscopic Investigation of Water Oxidation with "Co-Pi"-Coated Hematite Electrodes. *Journal of the American Chemical Society* **2012**, 134, 16693-16700.
11. Klahr, B.; Gimenez, S.; Fabregat-Santiago, F.; Hamann, T.; Bisquert, J. Water Oxidation at Hematite Photoelectrodes: The Role of Surface States. *Journal of the American Chemical Society* **2012**, 134, 4294-4302.
12. Barroso, M.; Cowan, A. J.; Pendlebury, S. R.; Gratzel, M.; Klug, D. R.; Durrant, J. R. The Role of Cobalt Phosphate in Enhancing the Photocatalytic Activity of Alpha-Fe₂O₃ toward Water Oxidation. *J Am Chem Soc* **2011**, 133, 14868-14871.
13. Ma, Y.; Le, F. F.; Kafizas, A.; Pendlebury, S.; Durrant, J. Efficient Suppression of Back Electron/Hole Recombination in Cobalt Phosphate Surface-Modified Undoped Bismuth Vanadate Photoanodes. *Journal of Materials Chemistry A* **2015**, 3, 20649-20657.
14. Tilley, S. D.; Cornuz, M.; Sivula, K.; Grätzel, M. Light-Induced Water Splitting with Hematite: Improved Nanostructure and Iridium Oxide Catalysis. *Angewandte Chemie International Edition* **2010**, 49, 6405-6408.
15. Debnath, N. C.; Anderson, A. B. Optical Spectra of Ferrous and Ferric Oxides and the Passive Film: A Molecular Orbital Study. *Journal of The Electrochemical Society* **1982**, 129, 2169-2174.

-
16. Zhong, D. K.; Cornuz, M.; Sivula, K.; Graetzel, M.; Gamelin, D. R. Photo-Assisted Electrodeposition of Cobalt-Phosphate (Co-Pi) Catalyst on Hematite Photoanodes for Solar Water Oxidation. *Energy & Environmental Science* **2011**, 4, 1759-1764.
 17. Gurudayal; Sabba, D.; Kumar, M. H.; Wong, L. H.; Barber, J.; Gratzel, M.; Mathews, N. Perovskite-Hematite Tandem Cells for Efficient Overall Solar Driven Water Splitting. *Nano Letters* **2015**, 15, 3833-3839.

8 APPENDIX

8.1 DERIVATION OF MOTT-SCHOTTKY EQUATION**

From Gauss's law of electrostatics

$$\nabla \vec{E} = \frac{\rho}{\epsilon_0 \epsilon_r} \quad (8.1)$$

with ρ being the charge density [C cm^{-3}] and \vec{E} the electric field [V m^{-1}], and the relation of the electric field to the potential, Φ , via

$$\vec{E} = -\nabla \Phi \quad (8.2)$$

the Poisson equation results as:

$$\nabla \nabla \Phi = \frac{d^2 \Phi}{dx^2} = -\frac{\rho}{\epsilon_0 \epsilon_r} \quad (8.3)$$

The Poisson equation can be used to describe the potential and charge distribution in the space charge layer according to

$$\frac{d^2 \Delta \Phi_{SC}}{dx^2} = -\frac{\rho}{\epsilon_0 \epsilon_r} \quad (8.4)$$

with

$$\Delta \Phi_{SC} = \Phi(x) - \Phi_{bulk} \quad (8.5)$$

The charge density in a semiconductor is given by

$$\rho(x) = e_0(p(x) - n(x) + N_D^+ - N_A^-) \quad (8.6)$$

(where trapped charges in states are neglected here and gradient doping is not accounted for). The charge on the semiconductor side is counterbalanced by the charge in the electrolyte. For high ion concentrations in the electrolyte, the diffuse layer can be neglected. Based on the Boltzmann distribution, the charge carriers can be described as

** Derived with the help from references 1 and 2.

$$n(x) = N_C e^{-\frac{(E_C(x)-E_F)}{k_B T}} \quad \text{and} \quad n_{bulk} = N_C e^{-\frac{(E_C^{bulk}-E_F)}{k_B T}}$$

$$\Rightarrow n(x) = n_{bulk} e^{-\frac{(E_C(x)-E_C^{bulk})}{k_B T}} = n_{bulk} e^{-\frac{e_0 \Delta \Phi_{SC}}{k_B T}} \quad (8.7)$$

Similar:

$$p(x) = N_V e^{-\frac{(E_V(x)-E_F)}{k_B T}} = p_{bulk} e^{-\frac{(E_V(x)-E_V^{bulk})}{k_B T}} = p_{bulk} e^{-\frac{e_0 \Delta \Phi_{SC}}{k_B T}} \quad (8.8)$$

Equations (8.4) - (8.8) give

$$\frac{d^2 \Delta \Phi_{SC}}{dx^2} = -\frac{e_0}{\epsilon_0 \epsilon_r} \left(p_{bulk} e^{-\frac{e_0 \Delta \Phi_{SC}}{k_B T}} - n_{bulk} e^{-\frac{e_0 \Delta \Phi_{SC}}{k_B T}} + N_D^+ - N_A^- \right) \quad (8.9)$$

With

$$\frac{d}{dx} \left(\frac{d \Delta \Phi_{SC}}{dx} \right)^2 = 2 \frac{d \Delta \Phi_{SC}}{dx} \cdot \frac{d^2 \Delta \Phi_{SC}}{dx^2} \quad (8.10)$$

Equation (8.9) can be reorganized to

$$2 \frac{d \Delta \Phi_{SC}}{dx} \cdot \frac{d^2 \Delta \Phi_{SC}}{dx^2} = \frac{d}{dx} \left(\frac{d \Delta \Phi_{SC}}{dx} \right)^2 = -\frac{2e_0}{\epsilon_0 \epsilon_r} \left(p_{bulk} e^{-\frac{e_0 \Delta \Phi_{SC}}{k_B T}} - n_{bulk} e^{-\frac{e_0 \Delta \Phi_{SC}}{k_B T}} + N_D^+ - N_A^- \right) \frac{d \Delta \Phi_{SC}}{dx}$$

$$\left(\frac{d \Delta \Phi_{SC}}{dx} \right)^2 = -\frac{2e_0}{\epsilon_0 \epsilon_r} \int \left(p_{bulk} e^{-\frac{e_0 \Delta \Phi_{SC}}{k_B T}} - n_{bulk} e^{-\frac{e_0 \Delta \Phi_{SC}}{k_B T}} + N_D^+ - N_A^- \right) d \Delta \Phi_{SC} \quad (8.11)$$

$$= -\frac{2e_0}{\epsilon_0 \epsilon_r} \left(-\frac{k_B T}{e_0} p_{bulk} e^{-\frac{e_0 \Delta \Phi_{SC}}{k_B T}} - \frac{k_B T}{e_0} n_{bulk} e^{-\frac{e_0 \Delta \Phi_{SC}}{k_B T}} + (N_D^+ - N_A^-) \Delta \Phi_{SC} \right) + C$$

In the bulk of the semiconductor there is no potential difference $\Delta \Phi_{SC} = 0$ and hence $\frac{d \Delta \Phi_{SC}}{dx} = 0$. Thus the constant C is given by

$$C = -\frac{2k_B T}{\epsilon_0 \epsilon_r} (p_{bulk} + n_{bulk}) \quad (8.12)$$

and Equation (8.11) becomes

$$\left(\frac{d \Delta \Phi_{SC}}{dx} \right)^2 = \frac{2e_0}{\epsilon_0 \epsilon_r} \left(\frac{k_B T}{e_0} p_{bulk} e^{-\frac{e_0 \Delta \Phi_{SC}}{k_B T}} + \frac{k_B T}{e_0} n_{bulk} e^{-\frac{e_0 \Delta \Phi_{SC}}{k_B T}} - (N_D^+ - N_A^-) \Delta \Phi_{SC} - \frac{k_B T}{e_0} (p_{bulk} + n_{bulk}) \right)$$

The space charge capacitance is given by

$$C_{SC} = \frac{dQ_{SC}}{d \Delta \Phi_{SC}} \quad (8.13)$$

with Q_{SC} being the charge at the semiconductor surface that is described by the Gauss's law as

$$\nabla \vec{E} = \frac{d\Delta\Phi_{SC}}{dx} = \frac{Q_{SC}}{\epsilon_0 \epsilon_r A} \quad (8.14)$$

and hence

$$C_{SC} = \epsilon_0 \epsilon_r A \frac{d \frac{d\Delta\Phi_{SC}}{dx}}{d\Delta\Phi_{SC}} = \pm \epsilon_0 \epsilon_r A \frac{d}{d\Delta\Phi_{SC}} \sqrt{\frac{2e_0}{\epsilon_0 \epsilon_r} \left(\frac{k_B T}{e_0} p_{bulk} e^{-\frac{e_0 \Delta\Phi_{SC}}{k_B T}} + \frac{k_B T}{e_0} n_{bulk} e^{\frac{e_0 \Delta\Phi_{SC}}{k_B T}} - (N_D^+ - N_A^-) \Delta\Phi_{SC} - \frac{k_B T}{e_0} (p_{bulk} + n_{bulk}) \right)}$$

$$C_{SC} = \pm \frac{\epsilon_0 \epsilon_r A}{2} \cdot \frac{2e_0}{\epsilon_0 \epsilon_r} \sqrt{\frac{-p_{bulk} e^{-\frac{e_0 \Delta\Phi_{SC}}{k_B T}} + n_{bulk} e^{\frac{e_0 \Delta\Phi_{SC}}{k_B T}} - N_D^+ + N_A^-}{\frac{2e_0}{\epsilon_0 \epsilon_r} \left(\frac{k_B T}{e_0} p_{bulk} e^{-\frac{e_0 \Delta\Phi_{SC}}{k_B T}} + \frac{k_B T}{e_0} n_{bulk} e^{\frac{e_0 \Delta\Phi_{SC}}{k_B T}} - (N_D^+ - N_A^-) \Delta\Phi_{SC} - \frac{k_B T}{e_0} (p_{bulk} + n_{bulk}) \right)}}} \quad (8.15)$$

$$\left(\frac{A}{C_{SC}} \right)^2 = \frac{\frac{2}{e_0 \epsilon_0 \epsilon_r} \left(\frac{k_B T}{e_0} p_{bulk} \left(e^{-\frac{e_0 \Delta\Phi_{SC}}{k_B T}} - 1 \right) + \frac{k_B T}{e_0} n_{bulk} \left(e^{\frac{e_0 \Delta\Phi_{SC}}{k_B T}} - 1 \right) - (N_D^+ - N_A^-) \Delta\Phi_{SC} \right)}{\left(-p_{bulk} e^{-\frac{e_0 \Delta\Phi_{SC}}{k_B T}} + n_{bulk} e^{\frac{e_0 \Delta\Phi_{SC}}{k_B T}} - N_D^+ + N_A^- \right)^2} \quad (8.16)$$

In the C_{SC} vs. $\Delta\Phi_{SC}$ plot there are 3 different regions.

For a n-type semiconductor:

- Accumulation ($-\Delta\Phi_{SC} < 0$; $n_{surface} \gg n_{bulk}$)
- Depletion ($n_{surface} < n_{bulk}$, $n_{surface} \gg p_{surface}$). In this region, the capacitance is determined by the linear terms and not the exponential terms.
- Inversion ($p_{surface} > n_{surface}$; $n_{bulk} \gg n_{surface}$). In this region, the capacitance is fully controlled by the minority carriers if $p_{surface} \gg n_{intrinsic}$

For a p-type semiconductor this behavior is mirrored.

For an n-type semiconductor in the depletion region, with $n_{bulk} \approx N_D^+$ and $N_A^-, p_{bulk} \approx 0$, $\Delta\Phi_{SC} < 0$, $e \frac{e_0 \Delta\Phi_{SC}}{k_B T} \ll 1$

$$\left(\frac{A}{C_{SC}}\right)^2 = \frac{2}{e_0 \epsilon_0 \epsilon_r N_D^+} \left(-\Delta\Phi_{SC} - \frac{k_B T}{e_0}\right) \quad (8.17)$$

with $\Delta\Phi_{SC} = \Phi_{surface} - \Phi_{bulk}$

and $V_{bias} = \Phi_{bulk} - \Phi_{Ref.el.}$

and at $V_{bias} = V_{fb}$ $\Phi_{surface} = \Phi_{bulk} \rightarrow V_{fb} = \Phi_{surface} - \Phi_{Ref.el.}$

and $\rightarrow \Delta\Phi_{SC} = V_{fb} - V_{bias}$

Thus, the Mott-Schottky equation for an n-type semiconductor is given by

$$\left(\frac{A}{C_{SC}}\right)^2 = \frac{2}{e_0 \epsilon_0 \epsilon_r N_D^+} \left(V_{bias} - V_{fb} - \frac{k_B T}{e_0}\right) \quad (8.18)$$

For a p-type semiconductor in the depletion region, with $p_{bulk} \approx N_A^-$ and $N_D^+, n_{bulk} \approx 0$, $\Delta\Phi_{SC} < 0$, $e \frac{e_0 \Delta\Phi_{SC}}{k_B T} \ll 1$, the Mott-Schottky equation is given by

$$\left(\frac{A}{C_{SC}}\right)^2 = \frac{2}{e_0 \epsilon_0 \epsilon_r N_A^-} \left(+\Delta\Phi_{SC} - \frac{k_B T}{e_0}\right) = \frac{2}{e_0 \epsilon_0 \epsilon_r N_A^-} \left(V_{fb} - V_{bias} - \frac{k_B T}{e_0}\right) \quad (8.19)$$

8.2 REFERENCES

1. Gelderman, K.; Lee, L.; Donne, S. W. Flat-Band Potential of a Semiconductor: Using the Mott-Schottky Equation. *Journal of Chemical Education* **2007**, *84*, 685.
2. Memming, R. d. *Semiconductor Electrochemistry*. Wiley-VCH: Weinheim ; New York, 2001; p x, 399 p.

ACKNOWLEDGEMENTS

First, I would like to thank Prof. Michael Grätzel for the opportunity to perform 5 years of research on solar energy conversion in his top-notch research group. I am thankful for having acquired a broad and simultaneously deep understanding of electrochemistry, semiconductor physics and various deposition and analysis techniques that I could learn during my research on dye-sensitized solar cells, perovskite solar cells and especially photoelectrochemical water splitting. I greatly appreciated working under your supervision profiting from the rich knowledge of you and the LPI but also enjoyed the freedom and flexibility to discover different fields through various collaborations that you always supported and encouraged.

I would like to thank Prof. Kevin Sivula for his co-supervision. I highly appreciated the brainstorming sessions we had as I was designing the ALD system and your good advice. I would also like to thank your group for their patience, as I was occupying the equipment in your lab. ☺

I kindly thank my PhD exam committee, namely, Prof. Sophia Haussener, Prof. James Durrant, Prof. Roel van de Krol, Prof. Frank Nüesch as well as my supervisors for a fair and enjoyable PhD exam with interesting questions and discussions.

I deeply thank the “old” and “new” LPI for the highly stimulating, motivating and fun environment. I am lucky to have met so many interesting co-workers that very quickly became very good friends. To start with the “old LPI”, I thank Dr. Nicolas Tétreault, Dr. Joël Teuscher, Dr. Jérémie Brillet, Dr. Philippe Labouchère, Dr. Maurin Cornuz, Dr. Jelissa Risse, Dr. Florian Le Formel, Dr. Adriana Paracchino and Dr. Arianna Marchioro for their patience while I was learning French. Merci d’avoir enduré chaque fois quand ça m’a pris 5 minutes pour sortir une phrase de 3 mots en français. Sans vous, je n’aurais jamais appris aussi vite et aussi bien. Merci! Merci aussi à Dr. Leo-Philipp Heiniger, Dr. Jan Brauer, Dr. Hauke Harms et Dr. Thomas Moehl pour les conversations en allemand pendant ce temps-là - ça m’a beaucoup aidé à connecter. J’étais très chanceuse de travailler avec vous et d’avoir gagné votre amitié. Thomas, danke auch, dass du dein Wissen und deine langjährige Erfahrung in Impedanzspektroskopie mit mir geteilt hast.

As I was half through my PhD the group dynamic changed a bit towards the “new LPI”

and I would like to thank Dr. Wolfgang Tress, Dr. Michael Saliba, Dr. Antonio Abate and especially Dr. Fabrizio Giordano and Dr. Juan Pablo Correa Baena for interesting scientific discussions that led to fruitful ideas and projects - suspiciously often at Sat or during dinner ☺. Thanks my friends for our productive collaboration, great time and good laughs!

A special thanks to the water splitting group, namely Prof. David Tilley, Dr. Jingshan Luo, Dr. Matthew Mayer, Dr. Minkyu Son and Marcel Schreier for highly valuable scientific and geopolitical discussions, interesting and multifaceted projects, good advice and a good time.

I thank Dr. Robin Humphry-Baker for valuable scientific discussions, always a good advice and a good time on the slopes of Verbier. I became very interested in transient measurements and absorption spectroscopy after having worked with you during my Master's project and this finally even influenced my next scientific step. Thanks for sharing your knowledge on spectroscopy and Igor programming with me.

I thank Dr. Nicolas Tétreault for proof-reading most of my thesis as well as Dr. Juan Pablo Correa Baena, Dr. Matthew Mayer, Dr. Peter Cendula, Dr. Wolfgang Tress and Dr. Michael Saliba for proof-reading selected chapters.

Un grand merci à l'atelier mécanique pour la construction de mon ALD, surtout à Guillaume Francey, André Fattet et Yves Morier. Mais aussi à Gil Corbaz, Vladan Jankovic, Cédric Mora et Roger Mottier pour m'avoir aidé à chaque fois quand je suis arrivée avec des soucis mécaniques. Je remercie aussi Frédéric Gummy et Patrick Favre pour le développement du programme basé sur Labview et d'alimentation de l'ALD.

I would like to thank Mme Gourdou, Heidi Francelet and Carmen Biagini for their administrative support that made life easier and allowed me to attend numerous conferences with a good financial planning.

Neben den guten Freunden, die ich in Lausanne gefunden habe, möchte ich auch meinen Freunden aus der Schul- und Studienzeit danken. Insbesondere Katrin Tücking, Charlotte Müller, Jan Sauer, Eugenie Geringer und Stephanie Müller. A big thank you to Christina Sáez Martínez and Andreas Hakansson for being crazy, fun, spontaneous and such good friends. Every moment with you is memorable and fun!

Ich danke von Herzen meiner Familie für ihre stetige Unterstützung und Liebe. Mama,

Papa, ich verdanke euch, dass ich hier am Ende meines Doktorats stehe und bin für all eure Bemühungen die mich bis hierher gebracht haben unendlich dankbar.

Un grand merci du cœur à mon amour, Dr. Nicolas Tétreault, pour son énorme soutien pendant mon doctorat. Nos discussions entre autres de la science, de la vie et de la politique m'ont montré plusieurs nouvelles perspectives. Avec ton humour et ton amour tu as fais paraître chaque jour comme le meilleur - même pendant des moments moins faciles. Merci !

Ludmilla STEIER

Av. Récordon 16, 1004 Lausanne, Switzerland

steier.ludmilla@gmail.com

NATIONALITY: German

Born 16th April 1987 in Tashkent (Uzbekistan)

EDUCATION

- 2012 – May 2016 **PhD student, EPFL (Lausanne, Switzerland)**
Thesis: “*FABRICATION AND CHARACTERIZATION OF FUNCTIONAL ALD METAL OXIDE THIN FILMS FOR SOLAR APPLICATIONS*” supervised by Prof. M. Grätzel and co-supervised by Prof. K. Sivula.
GLOBAL YOUNG SCIENTIST SUMMIT (NTU, Singapore) focused on “Advancing Science, creating technologies for a better world”
23RD JYVÄSKYLÄ SUMMER SCHOOL (Jyväskylä, Finland) on “Elemental Depth Profiling of Nanometer Thick Films”
- 2009 –2011 **M.Sc in Chemistry, University of Siegen (Siegen, Germany)**
Thesis: “*INVESTIGATION OF LIQUID DYE-SENSITIZED SOLAR CELLS BASED ON COBALT REDOX SHUTTLES*” supervised by Prof. H. Schönherr and Prof. M. Grätzel.
- 2006 – 2009 **B.Sc in Chemistry, University of Siegen (Siegen, Germany)**
Thesis: “*SYNTHESIS AND ELECTROCHEMICAL RESEARCH ON OSMIUM REDOX POLYMERS FOR APPLICATION IN AMPEROMETRIC BIOSENSORS AND BIOFUEL CELLS*” supervised by Dr. G. Nöll
- 1998 – 2006 **Abitur, Gymnasium der Stadt Lennestadt (Lennestadt, Germany)**

SKILLS

- Expertise in device physics of amperometric biosensors, liquid dye-sensitized solar cells, perovskite solar cells and especially of photoelectrodes for PHOTOELECTROCHEMICAL WATER SPLITTING
- Expert in ATOMIC LAYER DEPOSITION of crystalline highly photoactive Fe₂O₃ THIN FILMS as well as of a variety of wide band gap semiconductors used as electron selective contacts, anti-corrosion layers or transparent conductive oxides.
- Expert on ELECTROCHEMICAL IMPEDANCE SPECTROSCOPY, PHOTO-ELECTROCHEMISTRY Electron Microscopy (SEM, TEM, +EDX), UV-vis Spectroscopy, Ellipsometry, Clean Rooms.
- Technically skilled in IGORPRO, SOLIDWORKS (3D), MS OFFICE. Basic knowledge in Labview and Latex.
- Fluent in GERMAN (2nd mother tongue), ENGLISH and FRENCH. Mother tongue Russian (rusty). Learning Spanish

PUBLICATIONS

- **Cu₂O Nanowire Photocathodes for Efficient and Durable Solar Water Splitting**
J. Luo, L. Steier, M. Son, M. Schreier, M. T. Mayer, M. Grätzel *NANO LETTERS* 2016.
- **Monolithic Perovskite/Silicon-Heterojunction Tandem Solar Cells Processed at Low Temperature**
S. Albrecht, M. Salina, J. P. Correa Baena, F. Lang, L. Kegelmann, M. Mews, L. Steier, A. Abate, J. Rappich, L. Korte, R. Schlattmann, M. K. Nazeeruddin, A. Hagfeldt, M. Grätzel, B. Rech *ENERGY AND ENVIRONMENTAL SCIENCE* 2015.
- **Low-Temperature Atomic Layer Deposition of Crystalline and Photoactive Ultrathin Hematite Films for Solar Water Splitting**
L. Steier, J. Luo, M. Schreier, M. T. Mayer, T. Sajavaara, M. Grätzel *ACS NANO* 2015.
- **Highly Efficient Planar Perovskite Solar Cells through Band Alignment Engineering**
J. P. Correa Baena, L. Steier, W. Tress, M. Saliba, S. Neutzner, T. Matsui, F. Giordano, J. Jacobsson, A. R. S. Kandada, S. M. Zakeeruddin, A. Petrozza, A. Abate, M. K. Nazeeruddin, M. Grätzel, A. Hagfeldt *ENERGY AND ENVIRONMENTAL SCIENCE* 2015.
J.P. Correa Baena and myself contributed equally to this work.
- **Efficient photosynthesis of carbon monoxide from CO₂ using perovskite photovoltaics**
M. Schreier, L. Curvat, F. Giordano, L. Steier, A. Abate, S. M. Zakeeruddin, J. Luo, M. T. Mayer, M. Grätzel *NATURE COMMUNICATIONS* 2015.
- **Solution Transformation of Cu₂O into CuInS₂ for Solar Water Splitting**
J. Luo, S. D. Tilley, L. Steier, M. Schreier, M. T. Mayer, H. J. Fan, M. Grätzel *NANO LETTERS* 2015
- **On the Stability Enhancement of Cuprous Oxide Water Splitting Photocathodes by Low Temperature Steam Annealing**
J. Azevedo, L. Steier, P. Dias, M. Stefik, C. T. Sousa, J. P. Araujo · A. Mendes · M. Grätzel · D. Tilley *ENERGY AND ENVIRONMENTAL SCIENCE* 2014.
- **Understanding the Role of Underlayers and Overlayers in Thin Film Hematite Photoanodes**
L. Steier, I. Herranz-Cardona, S. Gimenez, F. Fabregat-Santiago, J. Bisquert, S. D. Tilley, M. Grätzel *ADVANCED FUNCTIONAL MATERIALS* 2014.

Active Participation in CONFERENCES and PROJECT MEETINGS

- Dec. 2015 **MRS Fall Meeting – Conference of the Materials Research Society (Boston, MA, USA)**
Oral presentation entitled “A Charge Collection Study on Ultrathin Hematite Films Made by Low-Temperature Atomic Layer Deposition”
- July 2015 **SFN International Discussion Meeting - Moving from Materials to Devices (Royal Society, London, UK)**
Poster entitled “A low-temperature ALD route towards ultrathin and highly photoactive hematite photoanodes
- April 2015 **Solar Fuels 15 – Conference for Photoelectrochemical Water Splitting (Uppsala, Sweden)**
Oral presentation entitled “Low-temperature Atomic Layer Deposition of *In Situ* Crystalline and Photoactive Hematite Films”
- June 2014 **Solar Fuels 14 – Conference for Photoelectrochemical Water Splitting (Montréal, Canada)**
Oral presentation entitled “On the nature of interfacial layers in hematite thin films for solar water splitting”
Poster entitled “Photoelectrochemical hydrogen production through hybrid organic/inorganic interfaces”
- Jan. 2014 **Organization and active participation in the PHOCS 12 month project meeting (Lausanne, Switzerland)**
Topic: Photogenerated Hydrogen by Organic Catalytic Systems
- July 2013 **4th European PEFC & H₂ Forum (Lucerne, Switzerland)**
Oral presentation entitled “Improving photocurrent onset potential in ultrathin hematite films using a combination of Nb₂O₅-, SiO_x-underlayers and a Ga₂O₃-overlayer”
- June 2013 **PHOCS 6 month project meeting (Castelló, Spain)**
Topic: Photogenerated Hydrogen by Organic Catalytic Systems
- August 2012 **IPS-19, 19th International Conference on Photochemical Conversion and Storage of Solar Energy (Pasadena, CA, USA)**
Oral presentation entitled “Improving photocurrent onset potential in ultrathin hematite films using a combination of Nb₂O₅-, SiO_x-underlayers and a Ga₂O₃-overlayer”
- June 2012 **ALD 2012 + workshop (Dresden, Germany)**

TEACHING ACTIVITIES

- Mar. 2015 **Invited lecture** on “Electrochemical Impedance Spectroscopy as a Tool for the Analysis of LaTiO₂N Photoanodes” in the group of Dr. Simone Pokrant (EMPA, Dübendorf, Switzerland)
- Jan. - June 2012 **Supervision of a high school student** from Basel during his research project on natural dyes for dye-sensitized solar cells in the framework of the national competition “Schweizer Jugend Forscht”. Felix Läderach won the third prize that allowed him to visit the United States for higher degrees of competition worldwide.
- Jan. 2012 - Dec. 2015 **Teacher of in-class exercises** for Bachelor and Master students in “General Chemistry” and “Chemistry and Physics of Interfaces” (classes held in French and English)
- Student research assistant** in lab courses for General and Physical Chemistry
- June 2008 – Dec. 2010 **Tutor** in mathematics (courses I and II for chemists)

SOCIAL and OUTREACH ACTIVITIES/ SCHOLARSHIPS/ AWARDS

- Mar. 2012- Feb. 2016 **Several outreach activities** for school children, high school students and university students on solar energy and the working principle as well as fabrication of dye-sensitized solar cells. Contribution to international media outreach (*FUTUREMAG*, *ARTE* and “*RUST BRINGS BOOST TO SOLAR ENERGY POTENTIAL: SCIENTISTS*”, *REUTERS*)
- June 2012 **ACS-Prize 2012** by the Alumni Chemistry at the University of Siegen
for achievements during the Master’s degree awarded yearly to the graduate student with the best diploma.
- June 2010 **ACS-Prize 2010** by the Alumni Chemistry at the University of Siegen
for achievements during the Bachelor’s degree awarded yearly to the Bachelor graduate student with the best diploma.
- Dec. 2008 –Sept. 2011 **Students Representative** in the Student Representatives Council of the Chemistry Department at the University of Siegen
- Oct. 2008 –Sept. 2011 **Fellow** of the *GERMAN NATIONAL SCHOLARSHIP FOUNDATION*
(Studienstiftung des Deutschen Volkes)
- Oct. 2006 **Award** by the *DIETER MENNEKES-UMWELTSTIFTUNG* for school attainments during the Abitur and **Award** by the *GESELLSCHAFT DEUTSCHER CHEMIKER* for attainments in Chemistry

